Integrated Ocean Drilling Program Expedition 323 Preliminary Report

Bering Sea Paleoceanography

Pliocene–Pleistocene paleoceanography and climate history of the Bering Sea

5 July–4 September 2009

Expedition 323 Scientists

Published by
Integrated Ocean Drilling Program Management International, Inc.,
for the Integrated Ocean Drilling Program

Publisher’s notes

Citation:

Expedition 323 Scientists, 2009. Bering Sea paleoceanography: Pliocene–Pleistocene paleoceanography and climate history of the Bering Sea. *IODP Prel. Rept.,* 323. doi:10.2204/iodp.pr.323.2010

Distribution:
Electronic copies of this series may be obtained from the Integrated Ocean Drilling Program (IODP) Scientific Publications homepage on the World Wide Web at **www.iodp.org/scientific-publications/.**

This publication was prepared by the Integrated Ocean Drilling Program U.S. Implementing Organization (IODP-USIO): Consortium for Ocean Leadership, Lamont Doherty Earth Observatory of Columbia University, and Texas A&M University, as an account of work performed under the international Integrated Ocean Drilling Program, which is managed by IODP Management International (IODP-MI), Inc. Funding for the program is provided by the following agencies:

National Science Foundation (NSF), United States

Ministry of Education, Culture, Sports, Science and Technology (MEXT), Japan

European Consortium for Ocean Research Drilling (ECORD)

Ministry of Science and Technology (MOST), People’s Republic of China

Korea Institute of Geoscience and Mineral Resources (KIGAM)

Australian Research Council (ARC) and New Zealand Institute for Geological and Nuclear Sciences (GNS), Australian/New Zealand Consortium

Ministry of Earth Sciences (MoES), India

Disclaimer

February 2010

Expedition 323 participants

Expedition 323 Scientists

Christina Ravelo
Co-Chief Scientist
Ocean Sciences Department
University of California
1156 High Street
Santa Cruz CA 95064
USA
acr@pmc.ucsc.edu

Kozo Takahashi
Co-Chief Scientist
Department of Earth and Planetary Sciences
Kyushu University
Hakozaki 6-10-1, Higashi-ku
Fukuoka 812-8581
Japan
kozo@geo.kyushu-u.ac.jp

Carlos Alvarez Zarikian
Expedition Project Manager/Staff Scientist
Integrated Ocean Drilling Program
Texas A&M University
1000 Discovery Drive
College Station TX 77845-9547
USA
zarikian@iodp.tamu.edu

Gilles Guèrin
Logging Staff Scientist
Borehole Research Group
Lamont-Doherty Earth Observatory of Columbia University
PO Box 1000, 61 Route 9W
Palisades NY 10964
USA
guerin@ldeo.columbia.edu

Tanzhuo Liu
Logging Staff Scientist
Borehole Research Group
Lamont-Doherty Earth Observatory of Columbia University
PO Box 1000, 61 Route 9W
Palisades NY 10964
USA
tanzhuo@ldeo.columbia.edu

Ivano Aiello
Sedimentologist
Geological Oceanography
Moss Landing Marine Laboratories
8272 Moss Landing Road
Moss Landing CA 95039-9647
USA
iaiello@mlml.calstate.edu

Hirofumi Asahi
Sedimentologist
Ocean Research Institute
University of Tokyo
1-15-1 Minamidai
Nakuano-ku 164-8639
Japan
hiroasa@ori.u-tokyo.ac.jp

Gretta Bartoli
Sedimentologist
Department of Geology
Eidgenössische Technische Hochschule-Zentrum
NOG47, Sonneggstrasse 5
CH-8092 Zurich
Switzerland
gretta.bartoli@erdw.ethz.ch

Beth Caissie
Sedimentologist
Department of Geosciences
University of Massachusetts
233 Morrill Sciences Center
611 North Pleasant Street
Amherst MA 01003
USA
bethc@geo.umass.edu

Muhong Chen
Paleontologist (radiolarians)
South China Sea Institute of Oceanology
Chinese Academy of Sciences
164 West Xingang Road
Guangzhou
PR China
mhchen@scsio.ac.cn

Elena Colmenero-Hidalgo
Paleontologist (nannofossils)
Departamento de Geología
Universidad de Salamanca
37008 Salamanca
Spain
elecolme@usal.es

Mea Cook
Sedimentologist
Geosciences Department
Williams College
947 Main Street
Williamstown MA 01267
USA
Mea.S.Cook@williams.edu

Kelsie Dadd
Sedimentologist
Earth and Planetary Sciences
Macquarie University
Sydney NSW 2109
Australia
kelsie.dadd@mq.edu.au

Youngsook Huh
Inorganic Geochemist
School of Earth and Environmental Sciences
Seoul National University
Sillim-dong, Gwanak-gu
Seoul 151-747
Korea
yhuh@snu.ac.kr

Katrine Husum
Paleontologist (foraminifers)
Department of Geology
University of Tromso
Dramsveien 201
9037 Tromso
Norway
katrine.husum@uit.no

Akira Ijiri
Sedimentologist
Earth and Life History Research Program
Japan Agency for Marine-Earth Science
and Technology
2-15 Natsushima-Cho
Yokosuka 237-0061
Japan
ijiri@jamstec.go.jp

Minoru Ikehara
Organic Geochemist
Center for Advanced Marine Core Research
Kochi University
B200 Monobe, Nankoku
Kochi 783-8502
Japan
ikehara@kochi-u.ac.jp

Sev Kender
Paleontologist (foraminifers)
Department of Climate Change
British Geological Survey
Keyworth
NG12 5GG Nottingham
United Kingdom
Sev.kender@bgs.ac.uk

Douglas LaVigne
Teacher at Sea
South Cobb High School
1920 Clay Road
Austell GA 30106
USA
arsonor@mindspring.com

Steve Lund
Paleomagnetist
Department of Earth Sciences
University of Southern California
273 Zumberge Hall of Science
University Park
Los Angeles CA 90089-0740
USA
slund@usc.edu

Christian März
Sedimentologist
Institut für Chemie und Biologie
Des Meeres (ICBM)
Carl von Ossietzky Universität Oldenburg
Strasse 9-11
26111 Oldenburg
Germany
cmaerz@icbm.de

Alan Mix
Stratigraphic Correlator
College of Oceanic and Atmospheric Sciences
Oregon State University
COAS Administration Building 104
Corvallis OR 97331-5503
USA
mix@coas.oregonstate.edu

Maheswar Ojha
Downhole Tools/Physical Properties Specialist
Gas-Hydrate Division
National Geophysical Research Institute
Uppal Road, Cyber Building
Hyderrabad 500 606
India
maheswar_ojha@yahoo.com

Makoto Okada
Paleomagnetist
Department of Earth Sciences
Ibaraki University
2-1-1 Bunkyo, Mito
Ibaraki 310-8512
Japan
okada@mx.ibaraki.ac.jp

Yusuke Okazaki
Paleontologist (radiolarians)
Institute of Observational Research
for Global Change (IORGC)
Japan Agency for Marine-Earth Science
and Technology
2-15 Natsushima-Cho
Yokosuka 237-0061
Japan
okazakiy@jamstec.go.jp

Jonaotaro Onodera
Paleontologist (diatoms)
Center for Advanced Marine Core Research
Kochi University
B200 Monobe
Nankoku 783-8502
Japan
jm-jo@kochi-u.ac.jp

Catherine Pierre
Physical Properties Specialist
Laboratoire d'Océanographie et du Climat:
Expérimentation et Approches Numériques
Université Pierre et Marie Curie
4 Place Jussieu
Case Courrier 100
75252 Paris
France
catherine.pierre@locean-ipsl.upmc.fr

Taoufik Radi
Paleontologist (dinoflagellates)
GEOTOP
Université du Québec, Montréal
CP 8888
Succursale Centre-ville
H3C 3P8 Montréal
Canada
radi.taoufik@courrier.uqam.ca

Nils Risgaard-Petersen
Microbiologist
Center for Geomicrobiology
Institute of Biological Sciences
Aarhus Universitet
Ny Munkegade Building 1540
8000 Aarhus C
Denmark
nils.risgaard-petersen@biology.au.dk

Tatsuhiko Sakamoto
Stratigraphic Correlator
Earth and Life History Research Program
Institute of Biogeosciences
Japan Agency for Marine-Earth Science
and Technology
Natsushima-cho 2-15
Yokosuka 237-0061
Japan
tats-ron@jamstec.go.jp

David Scholl
Downhole Tools/Physical Properties Specialist
Department of Geology and Geophysics
College of Natural Science and Mathematics
University of Alaska Fairbanks
Fairbanks AK 99775-7320
USA
dscholl@usgs.gov

Heather Schrum
Inorganic Geochemist
Graduate School of Oceanography
University of Rhode Island
South Ferry Road
Narragansett RI 02882
USA
hschrum@gso.uri.edu

Zuzanna N. Stroynowski
Paleontologist (diatoms)
Departamento de Geologia Marinha (DGM)
INETI
Estrada da Portela, Apartment 7586
2721-866 Alfragide
Portugal
zuzia.stroynowski@ineti.pt

Emily A. Walsh
Microbiologist
Graduate School of Oceanography
University of Rhode Island
South Ferry Road
Narragansett RI 02882
USA
ewalsh@gso.uri.edu

Laura Wehrmann
Microbiologist
Max Planck Institute for Marine Microbiology
Celsiusstrasse 1
28359 Bremen
Germany
lwehrman@mpi-bremen.de

Shipboard personnel and technical representatives

Grant Banta
Marine Computer Specialist

Chris Bennight
Chemistry Laboratory

Christopher Beveridge
Physical Properties Laboratory

Gerald Bode
Curator

Tim Bronk
Assistant Laboratory Officer

Trevor Buys
Marine Instrumentation Specialist

Trevor Cobine
Paleomagnetism Laboratory

William Crawford
Imaging Specialist

Lisa Crowder
Assistant Laboratory Officer

Clayton Furman
Schlumberger Logging Engineer

Randy Gjesvold
Marine Instrumentation Specialist

Kristin Hillis
Underway Geophysics Laboratory

Michael Hodge
Marine Computer Specialist

Sarah-Jane Jackett
Core Laboratory

Eric Jackson
X-Ray/Microbiology Laboratory

Kazushi Kuroki
Downhole Tools/Thin Section Laboratory

Mike Meiring
Drilling Engineer

Stephen Midgley
Operations Superintendent

Bill Mills
Laboratory Officer

Algie Morgan
Applications Developer

Jamie Smidt
Publications Specialist

Yulia Vasilyeva
Chemistry Laboratory

Stephanie Zeliadt
Applications Developer

Abstract

Paleoclimate and paleoceanographic studies present opportunities to study the dynamics of the climate system by examining how it responds to external forcing (e.g., greenhouse gas and solar radiation changes) and how its interacting components generate climate oscillations and abrupt changes. Of note is the amplified recent warming of the high latitudes in the Northern Hemisphere, which is presumably related to sea ice albedo feedback and teleconnections to other regions; both the behavior of sea ice–climate interactions and the role of large-scale atmospheric and oceanic circulation in climate change can be studied with geologic records of past climate change in the Bering Sea.

Over the last 5 m.y., global climate has evolved from being warm with only small Northern Hemisphere glaciers to being cold with major Northern Hemisphere glaciations every 100–40 k.y. The ultimate reasons for this major transition are unknown. Over the last hundreds of thousands of years, Milankovitch- and millennial-scale climate oscillations have occurred. Although the regional environmental changes reflected in the sediment are known in some regions, the mechanisms by which they propagate globally are not understood. Possible mechanisms responsible for both the long-term evolution of global climate as well as the generation of high-frequency climate oscillations involve processes such as intermediate water ventilation and sea ice formation in the North Pacific. However, the paucity of data in critical regions of the Pacific such as the Bering Sea has prevented an evaluation of the role of North Pacific processes in global climate change. Because North Pacific Intermediate Water (NPIW) has the potential to be influenced by dense water forming in the Bering Sea and because of the potential far-field impacts of sea ice, the Bering Sea may be critically involved in causing major climate changes. Thus, drilling in the Bering Sea may help answer questions not only about the global extent of climate trends and oscillations but about the mechanisms that produce them.

In addition to having important sedimentary records of past climate change, the Bering Sea is also a region of relatively high surface productivity, elevated intermediate and deepwater nutrient concentrations, and, presumably, microbial-mediated biogeochemical cycling. Thus, Integrated Ocean Drilling Program (IODP) Expedition 323 was also dedicated to examining subseafloor biomass and microbial processes in high-productivity regions for the first time.

The major objectives of Expedition 323 in the Bering Sea are

1. To elucidate a detailed evolutionary history of climate and surface ocean conditions since the earliest Pliocene in the Bering Sea, where amplified high-resolution changes of climatic signals are recorded;
2. To shed light on temporal changes in the origin and intensity of NPIW and possibly deeper water mass formation in the Bering Sea;
3. To characterize the history of continental glaciation, river discharges, and sea ice formation in order to investigate the link between continental and oceanic conditions of the Bering Sea and adjacent land areas;
4. To investigate linkages through comparison to pelagic records between ocean/climate processes that occur in the more sensitive marginal sea environment and processes that occur in the North Pacific and/or globally. This objective includes an evaluation of how the ocean/climate history of the Bering Strait gateway region may have affected North Pacific and global conditions; and
5. To constrain global models of subseafloor biomass and microbial respiration by quantifying subseafloor cell abundance and pore water chemistry in an extremely high productivity region of the ocean. We also aim to determine how subseafloor community composition is influenced by high productivity in the overlying water column.

During Expedition 323 in the Bering Sea, 5741 m of sediment (97.4% recovery) was drilled at seven sites covering three different areas: Umnak Plateau, proximal to the modern Alaskan Stream entry; Bowers Ridge, proximal to the glacial Alaskan Stream entry; and the Bering Sea shelf region, proximal to the modern sea ice extent. Four deep holes were drilled that ranged in depth from 600 to 745 m below seafloor, spanning 1.9 to 5 Ma in age. The water depths ranged from 818 to 3174 m in order to characterize past vertical water mass distribution and circulation. The highlights of our findings include the following:

1. An understanding of the long-term evolution of surface water mass distribution during the past 5 m.y., including the expansion of seasonal sea ice to Bowers Ridge between 3.0 and 2.5 Ma and the intensification of seasonal sea ice at both Bowers Ridge and the Bering slope at ~1.0 Ma, the mid-Pleistocene Transition.
2. The characterization of intermediate and deep water masses, including evidence from benthic foraminifers and sediment laminations, for episodes of low-oxygen conditions in the Bering Sea throughout the last 5 m.y.
3. The terrigenous and biogenic sedimentary history of the Bering Sea, including evidence for strong climatological and sea level control of siliciclastic deposition

at all sites. Records of lithostratigraphic variations indicate that Bering Sea environmental conditions were strongly linked to global climate change; this is apparent both in long-term million year trends and in the orbital, millennial, and shorter oscillations within the lithostratigraphic records generated at sea.

4. A large range of inferred microbial activity with notable site-to-site variations, including significant activity as deep as 700 m core depth below seafloor (CSF) at the Bering slope sites, and, in contrast, very low rates of microbial-mediated sulfate reduction at Bowers Ridge.

Introduction

The rate and regional expression of recent global warming is difficult to understand and even more difficult to predict because of the complex nature of the climate system, whose components interact nonlinearly with various time lags and timescales. Paleoclimate and paleoceanographic studies present opportunities to study the dynamics of the climate system by examining how it responds to external forcing (e.g., greenhouse gas and solar radiation changes) and how it generates internal variability due to interacting Earth-system processes. Of note is the amplified recent warming of the high latitudes in the Northern Hemisphere (Solomon et al., 2007), which is presumably related to sea ice albedo feedback and teleconnections to other regions; both the behavior of sea ice–climate interactions and the role of large-scale atmospheric and oceanic circulation in climate change can be studied with geologic records of past climate changes in the Bering Sea.

Prior to Integrated Ocean Drilling Program (IODP) Expedition 323, little was known about the sedimentology and climate history of the Bering Sea outside of a few piston core studies (e.g., Cook et al., 2005; Okazaki et al., 2005; Tanaka and Takahashi, 2005; Takahashi et al., 2005) and Sites 188 and 185 (Scholl and Creager, 1973), which were drilled by the Deep Sea Drilling Project (DSDP) in 1971 with old drilling technology and poor recovery. Past studies using piston cores in the Bering Sea indicated that, while current conditions in the Bering Sea promote seasonal sea ice formation, during the Last Glacial Maximum (LGM) conditions sustained perennial or nearly perennial sea ice cover (Katsuki and Takahashi, 2005), attesting to the potential utility of sedimentary records in the Bering Sea to examine sea ice distributions. In paleoceanographic studies in the North Pacific, the Bering and Okhotsk seas have been implicated as sources of dense oxygenated intermediate water that possibly impacted oceanic and climate conditions throughout the Pacific on glacial–interglacial (e.g., Gorbarenko, 1996; Matsumoto et al., 2002) and millennial (e.g., Hendy and Kennett, 2003) timescales. In addition, changes in Bering Sea conditions could be related to sea level and circulation changes, which alter flow through small straits that connect the Bering Sea to the Arctic Ocean to the north and the Pacific Ocean to the south. The lack of Bering Sea material has so far prevented the evaluation of these and other ideas.

Seven sites whose terrigenous and biogenic components capture the spatial and temporal evolution of the Bering Sea through the Pliocene and Pleistocene were successfully drilled during Expedition 323 (Fig. **F1;** Tables **T1, T2**). Additionally, Expedition 323 collected a rich archive of information regarding the role of microbes on biogeochemical cycles in ultra-high-productivity environments, the postdepositional processes that impact geochemical, lithologic, and physical properties of the sediment, and past oceanic chemistry preserved in pore waters. This preliminary report presents background on environmental setting and important scientific questions in the Bering Sea, followed by highlights of the scientific findings of Expedition 323.

Background

Geological and physical setting

With an area of 2.29×10^6 km^2 and a volume of 3.75×10^6 km^3, the Bering Sea is the third largest marginal sea in the world, surpassed only by the Mediterranean and South China seas (Hood, 1983). Approximately one-half of the Bering Sea is a shallow (0–200 m) neritic environment, with the majority of the continental shelf spanning the eastern side of the basin off Alaska from Bristol Bay to the Bering Strait (Fig. **F1**). The northern continental shelf is seasonally ice covered, but little ice forms over the deep southwest areas. In addition to the shelf regions, two significant topographic highs have better $CaCO_3$ preservation than the deep basins: Shirshov Ridge, which extends south of the Koryak Range in eastern Siberia along 170°E and separates the southwestern part of the Bering Sea into two basins, Komandorski (to the west) and Aleutian (to the east); and Bowers Ridge, which extends 300 km north from the Aleutian Island arc (Fig. **F1**). The Aleutian Basin is a vast plain 3800–3900 m deep with occasional gradually sloping depressions as deep as 4151 m (Hood, 1983).

Three major rivers flow into the Bering Sea: the Kuskokwim and Yukon rivers drain central Alaska and the Anadyr River drains eastern Siberia (Fig. **F1**). The Yukon is the longest of the three rivers and supplies the largest discharge into the Bering Sea. Its discharge peaks in August because of meltwater and is about equal to that of the Mississippi. It has a mean annual flow of 5 × 10^3 m^3/s, which is about two-thirds the annual flow of the Columbia River (Hood, 1983).

Today, a substantial amount of water is transported in and out of the Bering Sea across the Aleutian Island arc and the Bering Strait through passes (Figs. **F1, F2, F3**). Water mass exchange with the Pacific through the Aleutian Islands, such as through the Kamchatka Strait, is significant, linking Bering Sea conditions to the Pacific climate. The Alaskan Stream, an extension of the Alaskan Current, flows westward along the Aleutian Islands and enters the Bering Sea mainly through the Amchitka Strait and to some extent through the Near Strait west of Attu Island in the eastern Aleutian Islands (Fig. **F1**). A part of the Subarctic Current also joins the Alaskan Stream, resulting in a combined volume transport of 11 Sv (Ohtani, 1965).

Bottom and intermediate depth water in the Bering Sea originates from the North Pacific. After flowing into the Bering Sea it is slightly modified by the mixing of relatively fresh, warm water with very small amounts of bottom water formed within the Bering Sea today (Warner and Roden, 1995). Nutrient concentrations of North Pacific origin are high compared to all other regions in the global oceans; this explains the very low oxygen concentrations in the Bering Sea today (Fig. **F4**). The oxygen and nutrient composition of these waters is further modified by denitrification (Lehmann et al., 2005) and respiration of organic matter in the water column (Nedashkovskiy and Sapozhnikov, 1999). Respiration and the development of an oxygen minimum zone (OMZ) is particularly intense at water depths of ~1000 m (Fig. **F4**).

Much of the Pacific water entering the Bering Sea is matched by outflow through the Aleutian Islands. The most significant outflow is through the Kamchatka Strait, which has a maximum depth of 4420 m (Stabeno et al., 1999) (Figs. **F1, F3**). If some component of North Pacific Intermediate Water (NPIW) or deep water formed in the Bering Sea in past times, particularly when sea level was lower, it would have flowed out through the Kamchatka Strait or a secondary outlet near the Commander–Near Strait at 2000 m (Fig. **F1**).

The unidirectional northward transport of water mass (0.8 Sv) from the Bering Sea through the Bering Strait to the Arctic Ocean contributes to the salinity and biogeochemical contrast between the Pacific and the Atlantic. The Bering Strait region is one of the most biologically productive regions in the world (324 g $C/m^2/y$ over a wide area [2.12 × 10^4 km^2]) (Sambrotto et al., 1984). Much of this biologically produced organic matter and the associated nutrients flow into the Arctic Ocean because of the northward current direction. This may profoundly influence the present dominance of carbonate production in the Atlantic versus opal production in the Pacific, as described by models of basin-to-basin fractionation (Berger, 1970) and "carbonate ocean vs. silica ocean" (Honjo, 1990). Flow through the Bering Strait, which is ~50 m deep today (fig. 5 in Takahashi, 2005), was certainly different at times of lower sea level or enhanced perennial sea ice cover. The closing of this gateway and the accompanying changes in ocean and river flow through time could have caused changes in global patterns of circulation or in nutrient and salinity distributions.

Relationship to previous drilling in the Bering Sea, the subarctic North Pacific, and the Arctic Ocean

During DSDP Leg 19 in 1971, six sites were drilled in the Bering Sea and four were drilled just south of the Aleutian Islands in order to generally characterize the sedimentary units and tectonic and structural evolution of the Bering Sea (Scholl and Creager, 1973). Although much of the sediment section was washed away and not cored, DSDP Leg 19 provided basic information on the types and ages of sediments in two of the regions (Umnak Plateau and Bowers Ridge) that were targeted by Expedition 323. Expedition 323 marks the first deployment of advanced piston corer (APC) technology in the region and thus the first collection of continuous high-resolution records of the past 5 m.y. from the Bering Sea. Specifically, drilling of DSDP Sites 184 and 185 on Umnak Plateau revealed a Pleistocene to upper Miocene clay-rich diatomaceous ooze (Unit A) above clayey siltstone with sparse fossils (Unit B). At DSDP Site 188 on Bowers Ridge, sedimentary units similar in lithology and age to those found at the Umnak Plateau sites were found. Although Sites 190 and 191 were drilled close to Shirshov Ridge and the Kamchatka Strait, they were located in the deep basins around Shirshov Ridge (water deeper than 3800 m) and sediments recovered were mainly turbidite sequences with reworked microfossils, making paleoceanographic interpretations difficult. Expedition 323 to the Bering Sea did not include drilling in the deep basins; rather, it targeted topographic highs above the basin floors where deposition of reworked sediments was expected to be minimal.

In 1992, several important sites adjacent to the Bering Sea were explored during Ocean Drilling Program (ODP) Leg 145: Sites 881, 882, 883, and 884 (Rea et al., 1995; Rea, Basov, Janecek, Palmer-Julson, et al., 1993; Rea, Basov, Scholl, and Allen, 1995). Maslin et al. (1996) observed a dramatic increase in ice-rafted debris (IRD), a decrease in sea-surface temperature (>7.5°C) and opal mass accumulation rates (MARs) (fivefold decrease), and a decrease in both total organic carbon (TOC) and $CaCO_3$ MARs at Site 882 (50°22′N, 167°36′E; 3244 m) at 2.75 Ma, which is coeval with the IRD change found in the Norwegian Sea and suggests that the Arctic and northeast Asia were significantly glaciated from 2.75 Ma onward. Furthermore, they suggested that the onset of Eurasian Arctic and northeast Asia glaciation occurred ~100 k.y. before the Alaskan glaciation and 200 k.y. before the glaciation of Greenland and the northeast American continent. Both McKelvey et al. (1995) and Krissek (1995) suggest that the provenance of IRD in the northwest Pacific Ocean and the Gulf of Alaska is the Bering Sea off the Kamchatka Peninsula and southeastern Alaska, respectively. By studying the Bering Sea in relation to other regions we can uncover details of the inception of glaciation in the Arctic and North Pacific regions at ~2.75 Ma. Furthermore, the reasons for differences in the timing of glaciation can be investigated in detail using the sections from the Bering Sea, which are much higher resolution than those available in the open ocean pelagic realm.

IODP Expedition 302 (Arctic Coring Expedition [ACEX]) to Lomonosov Ridge in the central Arctic Ocean took place in 2004, and the scientific community anticipated the acquisition of new information regarding the age and effects of the Bering Strait gateway to the Arctic. However, despite the expedition’s success in acquiring sediments spanning the Holocene to the Cretaceous (Backman, Moran, McInroy, Mayer, et al., 2006; Moran et al., 2006), it has been difficult to advance understanding of the significance of flow changes through the Bering Strait gateway on global or regional climate change without being able to compare these new Arctic records to those on the Pacific side of the Bering Strait. Thus, the cores recovered during Expedition 323 in the Bering Sea are essential to deciphering the history of the Bering Strait gateway and its potential impact on global and regional climatic and oceanic processes. The role of the exchange of heat and chemical constituents through the Bering Strait on Arctic and North Pacific environments as well as the influence of changes in this exchange on Northern Hemisphere glaciation (NHG) and higher frequency climate oscillations can only be assessed by comparing results from Bering Sea drilling with the results from Expedition 302.

Millennial-scale climate changes

The Bering Sea contains sediments with high accumulation rates appropriate for the reconstruction of surface and deep water conditions and for the validation of climate/ocean hypotheses that call on these regions as a variable source of open Pacific intermediate and deep water. In addition, climate change in the Bering Basin tends to be extremely sensitive to high-frequency changes due to the semi-isolated nature of the marginal sea. Sea level drop, for example, may produce a profound effect on water mass circulation, sea ice formation, salinity, and biological productivity in the basin (e.g., Takahashi, 1999). The pelagic signals of the open Pacific do not adequately provide the high-frequency climatic history of the northwest Pacific Rim.

Changes in ventilation of subsurface water in the North Pacific may also influence climate downstream and be tied to North Atlantic climate changes on millennial timescales. Interestingly, millennial cycles in climate proxy records are apparently correlative across the North Pacific, for example in the Bering Sea (Cook et al., 2005), the Sea of Okhotsk (Sakamoto et al., 2005; Ono et al., 2005), the California margin (e.g., Behl and Kennett, 1996), and the Sea of Japan (e.g., Tada et al., 1999). Although the mechanisms for strong teleconnections between different sides of the North Pacific are not known, it has been proposed that changes in the Okhotsk (Ono et al., 2005) or Bering seas' source(s) of NPIW could reach the California margin and influence the depth or strength of the OMZ (Cannariato and Kennett, 1999; Zheng et al., 2000), thereby connecting climate/ocean changes across the Pacific Ocean. The fact that millennial-scale records from the Pacific margins also appear to correlate to changes in North Atlantic climate (e.g., Behl and Kennett, 1996; Tada et al., 1999) indicates that processes that link Atlantic and Pacific climate could play an important role in global climate change.

A number of possible theories explain paleoceanographic data from North Pacific marginal seas by implicating changes in NPIW formation due to changes in flow through the Bering Strait (Hasumi, 2002; De Boer and Nof, 2004; Shaffer and Bendtsen, 1994) and teleconnections from the tropics (Niebauer and Day, 1989; Alexander et al., 2002; Niebauer, 1998; Zhao et al., 2004; Gloersen, 1995). Our capacity to test these theories will benefit from documentation of surface and deep water conditions in the Bering Sea. Drilling has allowed us to obtain long sequences of sediments for the reconstruction of the climate cycles and for the evaluation of whether the patterns observed in the last glacial cycle are characteristic of all glacial–interglacial cycles. Long records will also be used to compare millennial climate oscillations in the Bering Sea in the Pleistocene, when there were large Northern Hemisphere ice sheets, to those in the Pliocene warm period, when there were only small Northern Hemisphere ice sheets, thereby shedding light onto whether the generation of these oscillations is related to NPIW ventilation, ice sheet size and dynamics, ocean circulation, and/or rapid reorganization of atmospheric circulation.

Glacial–Interglacial climate change

In the last glacial cycle, enhanced dense water formed, probably from the Okhotsk and Bering seas (e.g., Zahn et al., 1991; Gorbarenko, 1996). In fact, the degree of ventilation of deep and intermediate Pacific waters appears to have fluctuated during the cold and warm periods, implying changes in the configuration of Pacific Ocean circulation (Keigwin, 1995; Matsumoto et al., 2002). However, the use of different nutrient proxies ($\delta^{13}C$ vs. Cd/Ca in benthic foraminifers) provides some contradictory results. Furthermore, the limited spatial coverage of sites in the open Pacific prevents detailed identification of the exact source of intermediate and deep water as well as the exact circulation path of subsurface water masses. Observations of glacial records from the Bering Sea and just outside the Bering Sea on the Detroit Seamount in the North Pacific suggest a source of ventilated intermediate water coming from the Bering Sea and/or the Detroit Seamount region (Gorbarenko, 1996).

Two examples of the prospective reconstructions of Bering Sea paleoceanography by Bering Sea drilling are reported in recent studies performed on the piston cores collected during the 1999 *Hakuhou-Maru* site survey cruise (Takahashi et al., 2005). Sea ice distribution during the glacial period was modulated by surface water circulation partially governed by the topography that resulted from the sea level drop. Note that the distribution of sea ice and water masses is significantly different in the two basins west and east of Bowers Ridge because of the pattern of surface ocean circulation (Katsuki and Takahashi, 2005). Past sources of NPIW formation during the four different time slices have been inferred from the intermediate water–dwelling radiolarian species *Cycladophora davisiana* (Tanaka and Takahashi, 2005). The degree of ventilation of intermediate and deep water will be fully scrutinized with more detailed information from Expedition 323.

Despite evidence that Pacific circulation was different in the last glacial cycle, little is known about what caused circulation to change or what role the Pacific played in determining extreme climate conditions. Extensive studies of the North Atlantic clearly show that ice-sheet dynamics and changes in meridional overturning circulation in the Atlantic can readily influence climate, yet no widely accepted paradigm explains how the North Pacific participates in and possibly impacts global climate change. Construction of long records of glacial–interglacial changes by drilling, especially under a range of boundary conditions over the Pliocene–Pleistocene, will contribute critical information needed to formulate a new North Pacific climate change paradigm.

Pliocene–Pleistocene trends

Compelling evidence shows that North Pacific mid-depth water (~2500 m) had much lower nutrient concentrations in the warm Pliocene (~4.5 to 3.0 Ma) than today, indicating that it was more strongly ventilated (Kwiek and Ravelo, 1999; Ravelo and Andreasen, 2000). Although increased subsurface ventilation in the cold LGM and the warm Pliocene could be interpreted in a number of different ways and is likely not explained by the same processes, only data that directly reflect conditions in the Bering Sea (and the Sea of Okhotsk) can help constrain interpretations.

The end of the early Pliocene warm period is characterized by the development of modern density stratification in the surface and deep North Pacific. IRD recovered at DSDP and ODP sites indicates that increased water mass stratification coincided with more extensive glaciation (Haug et al., 1999; Kwiek and Ravelo, 1999; Ravelo and Andreasen, 2000; Rea and Schrader, 1985). Furthermore, more IRD is found along the Aleutian Islands (DSDP Site 192) than farther north in the Bering Sea (Sites 186 and 191) due to more extensive ice cover in the north compared to more seasonal ice cover at the Aleutian site (McKelvey et al., 1995; Krissek, 1995). The fact that this North Pacific climate reorganization occurred synchronously with the onset of significant NHG as recorded in the Atlantic Ocean highlights the importance of studying North Pacific climate evolution as part of a comprehensive investigation of the regional expression of global climate trends.

The emergence of the Bering Land Bridge (Beringia) prior to the Neogene is not well understood. However, Pliocene climate change—and perhaps the onset of NHG, specifically—could have been affected by changes in the marine gateway connection through the Bering Strait region. The connection may have developed in the late Miocene or the early Pliocene based on the occurrences of Atlantic-type mollusks in Hokkaido, Kamchatka, and the Alaska Peninsula in the late Miocene and early Pliocene. The oldest ages for these occurrences range from 6.3–5.1 to 2.2 Ma (e.g., Uozumi et al., 1986), but a recent study documented that the age of first occurrence was 5.5–5.4 Ma (Gladenkov, 2006). One of the aims of drilling was to recover better records of oceanographic evolution related to the Miocene/Pliocene gateway history. The oldest sediment recovered was ~5 Ma, and long-term trends in Pliocene circulation will be documented to assess the possible influence of the tectonic opening of the Bering Sea if it happened as late as the Pliocene.

Flow through the Bering Strait is likely controlled mainly by sea level change and changes in the amount of perennial sea ice. Pacific to Arctic flow through the Bering Strait (~0.8 Sv) (Coachman and Aagaard, 1981) significantly influences the Pacific–Atlantic partitioning of physical and nutrient properties in the modern ocean and was possibly quite sensitive to past changes in sea level change due to its shallow sill of ~50 m (see Takahashi, 2005, for an illustration of the cross section). During glacial intervals, Atlantic Ocean biogenic sedimentation and preservation became more Pacific-like, and vice versa, and there were major changes in nutrient distributions. Drilling near the Bering Strait will help resolve whether major changes in Pacific–Atlantic partitioning of oceanographic properties were related to changes in flow through the Bering Sea. *Neodenticula seminae*, a dominant extant subarctic Pacific diatom, was found recently in Atlantic waters, possibly because recent warming and melting sea ice in the Arctic Ocean provided a passage from the Pacific to the Atlantic (Berard-Therriault et al., 2002; Corbyn, 2007). This species has been extinct in the Atlantic since 0.8 Ma (Baldauf, 1987), and thus its recent reemergence in the Atlantic appears to be a significant indication that climate change in the Arctic influenced the distribution of this species.

Scientific objectives

The objectives of Expedition 323 are as follows:

1. To elucidate a detailed evolutionary history of climate and surface ocean conditions since the earliest Pliocene in the Bering Sea, where amplified high-resolution changes of climatic signals are recorded;
2. To shed light on temporal changes in the origin and intensity of NPIW and possibly deeper water mass formation in the Bering Sea;
3. To characterize the history of continental glaciation, river discharges, and sea ice formation in order to investigate the link between continental and oceanic conditions of the Bering Sea and adjacent land areas;
4. To investigate linkages through comparison to pelagic records between ocean/climate processes that occur in the more sensitive marginal sea environment and processes that occur in the North Pacific and/or globally. This objective includes evaluating how the ocean/climate history of the Bering Strait gateway region may have affected North Pacific and global conditions; and
5. To constrain global models of subseafloor biomass and microbial respiration by quantifying subseafloor cell abundance and pore water chemistry in an ex-

tremely high productivity region of the ocean. We also aim to determine how subseafloor community composition is influenced by high productivity in the overlying water column.

Summary of expedition results

Overview of ages and sedimentation rates

Expedition 323 in the Bering Sea focused on analyzing long-term ocean and climate trends and the evolution of higher frequency glacial–interglacial to millennial-scale oscillations through the Pliocene and Pleistocene. As such, our primary drilling objective was to obtain sediments whose components could be used to elucidate the detailed evolutionary history of climate, surface ocean, and intermediate water conditions since the earliest Pliocene in the Bering Sea, where amplified high-resolution changes of climatic signals are recorded. In addition, we sought to explore subseafloor microbial activity in the Bering Sea because of its extremely high surface productivity.

Our objectives, in terms of acquiring the sediment core samples as well as conducting shipboard research, have been adequately met because our targeted drill sites had extremely high sedimentation rates (Fig. **F5**) containing abundant microfossils and other paleoceanographic proxies.

Among the three drill sites explored in the Bowers Ridge region, both of the deepest holes drilled, Holes U1340A (605 m uncompressed core depth below seafloor [CSF]) and U1341B (600 m CSF), represent the time spans between the Holocene to ~5 Ma in the Pliocene (Fig. **F5**). The expedition's initial goal of penetrating to ~5 Ma was adequately accomplished at both sites despite the failure of the extended core barrel (XCB) cutting shoe spacing sub in Hole U1340A, whose target depth of penetration was 700 m. In the gateway region sites (at the Bering slope), two deep holes were drilled: Holes U1343E (744 m CSF) and U1344A (745 m CSF). Hole U1343E reached ~2.1 Ma, whereas Hole U1344A reached ~1.9 Ma (Fig. **F5**). At other drill sites, the bottom ages or the sedimentary sequences based on biomagnetostratigraphy are as follows: Site U1339 (Umnak Plateau: 0.74 Ma), Site U1342 (Bowers Ridge: 1.2 Ma [with the exception of the middle Miocene sediments just above the basement]), and Site U1345 (gateway: 0.5 Ma).

The sediments recovered from Bowers Ridge display high sedimentation (~12 cm/k.y. at Sites U1340 and U1341) without apparent hiatuses and are generally appropriate for high-resolution Pliocene–Pleistocene paleoceanography with adequate calcareous benthic foraminiferal preservation in the Pleistocene but lower preservation in the Pliocene. On the other hand, sediments at these sites are generally barren of planktonic foraminifers and calcareous nannofossils except in the section between ~2.5 and ~3 Ma. The abundance of all siliceous microfossils is generally high, enabling good biostratigraphy and paleoceanographic reconstruction. Furthermore, the upper part of Site U1340 (~20–150 m uncompressed core composite depth [CCSF-A]) had obvious soft-sediment deformation due to mass movement possibly caused by local seismic activity. Although such deformation hinders the continuous reconstruction of late Pleistocene high-resolution paleoceanography at this site, information from other drill sites can readily fill the gap.

In the region of the Arctic gateway sites proximal to the Bering slope, the observed sedimentation rates were overwhelmingly high: Hole U1343E had sedimentation rates of 21–58 cm/k.y. and Hole U1344A had rates of 29–50 cm/k.y. Sedimentation rates were so high, in fact, that drilling reached ages of only 2.1 and 1.9 Ma, respectively, despite penetration to 745 m CSF at each site. Such high sedimentation rates stem from the deposition of silt and clays transported by the Yukon and other rivers as well as the terrigenous sediments once deposited on the shelf. In spite of the high percentage of terrigenous materials, pertinent biotic proxies including benthic foraminifers and siliceous microfossils are adequately preserved, enabling future studies. Therefore, the overall coverage of excellent cores to ~5 Ma in the Bowers Ridge region and ~2 Ma in the gateway region makes detailed, continuous high-resolution paleoceanographic studies relevant to global climate change possible.

Lithostratigraphic summary

The seven sites drilled during Expedition 323 provide a continuous high-resolution record of the evolution of marine sedimentation in the marginal Bering Sea (Fig. F6). Onboard, lithologic, and sedimentologic analysis of the core sediments was carried out with a combination of visual core description, smear slide analysis, and, only for selected samples, X-ray diffractometry. Overall, the sediments recovered in the Bering Sea are a mixture of three components: biogenic (mainly diatom frustules with varying proportions of calcareous nannofossils, foraminifers, silicoflagellates, and radiolarians), siliciclastic (mainly silt and, secondarily, sand and isolated IRD clasts of pebble to cobble size), and volcaniclastic (mainly fine ash). Other accessory lithologies identified include authigenic carbonates (dolomite and aragonite) and sulfides. The most prominent sedimentary features observed were decimeter- to meter-scale bedded alternations of sediment color and texture reflecting alternations in lithology. The sediments were generally highly bioturbated. However, fine-scale lamination preserving alternations between millimeter-scale laminae of biogenic and terrigenous material was also present in several of the drilled sites (Fig. **F6**).

The distributions of the sedimentary components and sedimentary structures and their variability both within and between the Expedition 323 sites account for changes of the biogenic, glaciomarine, terrigenous, and volcanogenic sediment sources and the environmental conditions present during sediment deposition. The scales of these lithologic variations indicate that sedimentation in the Bering Sea has recorded long-term trends that include the critical period of reorganization of Earth's climate from the warm early Pliocene and the transition into the ice ages. Milankovitch-scale (bedding) and sub-Milankovitch-scale (lamination) variability is also recorded. The physiographic setting of the different sites, their depths, and their location relative to the sediment source areas (continents, ice sheets, volcanoes, and upwelling centers) account for the marked regional differences in sediment composition, especially between the Pleistocene sections of the Bowers Ridge and Bering slope sites.

The preliminary results of Expedition 323 suggest that the history of sedimentation in the Bering Sea is broadly characterized by three main sedimentary phases that occurred between ~5 and ~2.7 Ma, ~2.7 and ~1.74 Ma, and ~1.74 Ma to recent (Fig. **F6**).

The oldest portion of the sedimentary record (between ~5 and ~2.7 Ma) was retrieved only at Bowers Ridge Sites U1340 and U1341. Sedimentation during the early middle Pliocene was relatively high (Fig. **F5**) and characterized by biogenic diatom ooze with minor amounts of diatom silt, sponge spicules, and vitric ash. Although the Pliocene sediment is commonly bioturbated, distinct intervals characterized by extensive lamination also occur. The oldest laminated intervals (<3.8 Ma) were observed at Site U1341. Stratigraphic intervals where laminations are concentrated are indicative of the depth of the OMZ. Isolated IRD pebbles were observed in sediments older than 3.8 Ma only at Site U1340. Limited dropstone occurrence prior to 2.7 Ma was also reported at two sites drilled in the northern Pacific during Leg 145 (ODP Sites 881 and 883) and in the Yakataga Formation in Alaska (Lagoe et al., 1993), which suggests the development of ice sheets prior to the onset of NHG (Krissek, 1995).

The middle section of Sites U1340 and U1341 (between ~2.7 and 1.74 Ma) is characterized by beds of diatom ooze with minor amounts of calcareous nannofossils and foraminifer ooze alternating with diatom silt beds. The latter are composed of subequal proportions of siliciclastic (silt-sized quartz, feldspar, and rock fragments and/or clay) and biogenic (mainly diatom and, secondarily, calcareous nannofossils, foraminifers, silicoflagellates, and sponge spicules) components and minor volcaniclastic components. Dropstone occurrence is common—indicating a peak in siliciclastic deposition that has also been observed at Leg 145 sites—and coincides with the beginning of NHG. However, the dramatic drop in paleoproductivity recorded at Site 882 (Haug et al., 1999) is not present at the Bowers Ridge sites where, conversely, the biogenic component is high throughout the late Pliocene and Pleistocene.

All sites drilled during Expedition 323 preserve a record of sedimentation ranging from the late Pliocene through the Holocene (between 1.74 Ma and recent). Lithologies and sedimentation rates vary between the different sites, as indicated by a basin-wide comparison of the evolution of sedimentation in the Bering Sea during this period (Fig. **F6**). The slowest sedimentation rates (only 4.5 cm/k.y.) were observed at Site U1342, where laminated foraminifer-rich diatom ooze beds alternate with silty clay beds at scales ranging in the Milankovitch band. The same temporal interval corresponds to a much thicker section at Sites U1340 and U1341, where the bedding alternations are less distinct and the abundance of IRD is higher. Although lamination is common at Sites U1342 and U1340, laminae are virtually absent at the deeper Site U1341, suggesting a shallowing of the depth of the OMZ during most of the Pleistocene. At the Bering Sea slope site, sedimentation rates are about three times higher than at the Bowers Ridge sites. At Sites U1339, U1343, and U1344, siliciclastic-rich beds (mostly diatom-rich silt clay) and mixed siliciclastic-biogenic beds (clay, silt, and diatom ooze with varying abundance of foraminifers, nannofossils, and sponge spicules) alternate rhythmically. The sections are pervasively bioturbated and laminated intervals are rare. Overall, sedimentation on the Bering slope is characterized by higher influence of both siliciclastic material delivered by ice sheets as well as terrigenous sedimentation derived from the continental shelf and slope, which are indented by some of the largest submarine canyons in the world. However, because of their proximity to the continents, it is not clear whether the sediments characterized by high siliciclastic content are recording periods of ice sheet expansion (stadials) or increased runoff (interstadials). IRD is a common feature at all sites during this time period and increases significantly around 1 Ma, as is also observed in coeval sediments from the North Pacific based on the results of Leg 145 (Krissek, 1995).

Cyclical siliciclastic deposition and its relationship to climate change

Expedition 323 in the Bering Sea is the first expedition to recover deep continuous sections of sediment, providing an opportunity to study sediment distributions in time and space in the Bering Sea. The plethora of climatic and sedimentary structure information in the cores will allow us to develop an understanding of the influence of climate changes on sedimentation. Clearly, siliciclastics are a dominant component of all Bering slope sites and are less dominant at the Bowers Ridge sites. At all sites, because the sediments are primarily comprised of mixtures of siliciclastics and diatom frustules, the physical magnetic properties and natural gamma ray (NGR) measurements made on the tracks and with the logging tools generally provide information on the relative proportions of clays/silts versus diatoms (although ash is a significant component of the sediment at Site U1339). The NGR records (Fig. **F6**) indicate clear cyclicity; the amplitude and wavelength change markedly with depth at the Bering slope site but not at the Bowers Ridge sites. Specifically, at the Bering slope sites (Sites U1339, U1343, U1344, and U1345) in sediment younger than ~1 Ma the NGR record appears to vary with lower amplitude and across a wide range of frequencies higher than 1/40 k.y., than it does in sediment older than 1 Ma (Fig. **F6;** see NGR records of Sites U1343 and U1344). Because Sites U1339 and U1345 are short records younger than 1 Ma, longer term trends in the character of the variability can only be evaluated in the longer NGR records of Sites U1343 and U1344; however, the relatively high frequency variability of the NGR data from the younger sediment is evident at all four sites.

This change in the character of the variability is also apparent in the logging data from Sites U1343 and U1344 (Fig. **F7**). The downhole logging data provide our only opportunity to derive continuous records of lithologic variability in the deeper sections where only one hole was drilled and where continuous composites of data generated on the cores cannot be spliced together as they are in the sections with multiple drill holes. The potassium concentrations (K%) measured by the logging tool are generally related to the terrigenous clay concentrations, although variations in mineralogy of the terrigenous fraction could have a secondary influence. In this sedimentary environment, it appears that NGR represents the amount of terrigenous material relative to biogenic material in the sediment. Although much more research is needed, the shipboard data indicate that high siliciclastic relative to biogenic deposition probably occurred during colder periods or possibly during deglaciations.

Applying the shipboard age model to the K% record at Site U1343 and performing spectral analyses on the record (not shown) indicate that variability in K% dominantly occurs with 40 k.y. periodicity in periods older than ~1 Ma. In the portion of the record younger than 1 Ma, the variance is dispersed among many frequencies; 40 k.y. periodicity does not dominate the spectrum. Benthic $\delta^{18}O$ records (Lisiecki and Raymo, 2005) indicate that variability of ice volume and therefore of eustatic sea level occurs primarily with 40 k.y. periodicity prior to ~1 Ma (referred to as the "40 K world"). As such, it appears that sea level may control the timing of pulses of sedimentation at the Bering slope sites. Sea level highstands in warm periods may be times when deposition of sediments on shelves occurred at the expense of sediment deposition on the slope. As ice volume increased, sea level fell, the coastline moved seaward, and the flux of terrigenous material to the slope may have increased. This simple explanation of how sea level controlled long-lived pulses of sediment at Sites U1343 and U1344 may explain how global climate change indirectly controlled the timing of sediment deposition at the slope sites during the 40 K world. After 1 Ma the variability of the sediment composition changed, as reflected by logging K%. NGR core measurements do not appear to be simply related to sea level change, which occurred dominantly with ~100 k.y. variability; rather, the pulses of sedimentation appear to occur with much higher frequency. It is unclear why this happened, but the increase in sea ice diatom and sea ice dinoflagellate forms (discussed in the next section) at ~1 Ma may indicate that high-frequency variability in siliciclastic deposition related to sea ice processes may be an important process—perhaps more important than global ice volume and concomitant sea level changes, which occur with lower frequency.

A close look at magnetic (Fig. **F8**) and density (not shown) data provides additional details about processes that may dictate terrigenous deposition. At first glance the record of relative magnetic paleointensity of the sediment at Sites U1343 and U1344 agrees with the K% records and indicates a change in depositional style and cyclicity at ~1 Ma (Fig. **F8**), with lower frequency and higher amplitude changes prior to 1 Ma at the Bering slope sites. Natural remanent magnetization (NRM)/Chi is an index that attempts to normalize intensity by the concentration of magnetic grains. However, changes in grain size distributions may also impact this ratio; low NRM/Chi values indicate that magnetic grains are coarser than those in sediment with higher NRM/Chi values. Grain-size differences can be related to a variety of climatically controlled factors as well as to diagenetic dissolution of the smallest clay-sized grains. The fact that NRM and Chi each show distinct variability with the same length scale representing 40 k.y. cycles suggests that the primary factor controlling the magnetic susceptibility and paleointensity records is related to the relative amount of terrigenous material. This also indicates that diagenetic overprints may alter but not obliterate the primary signal. The fact that the amplitude of changes in the paleointensity record (Fig. **F9**) downcore are even more extreme than those seen in the NGR and K% data suggests that, if anything, diagenetic overprints may amplify the contrast between sediments with varying amounts of siliciclastics grains.

After 1 Ma, during the time period of large 100 k.y. ice volume cycles, gamma ray attenuation (GRA) bulk density records vary across a spectrum of frequencies. However, they more clearly show long-period variance characteristic of the 100 k.y. ice age cycles than they do other physical parameter properties. For example, after 1 Ma paleointensity (Fig. **F8**) and NGR (Fig. **F6**) variability have power distributed across low (orbital) and suborbital frequencies. This indicates that terrigenous deposition at the Bering slope sites in the late Pleistocene was likely a combination of many processes such as bottom water current deposition of fine-grained material (drift), IRD from sea ice and icebergs, and mass sediment transfer from the shelf to the lower slope and abyss. Superimposed on this are possibly independent or nonlinearly related changes in biogenic fluxes and postdepositional processes such as diagenesis and precipitation of authigenic minerals. The periodic and stochastic forces that drive each of these processes could be different, resulting in rich records of lithologic variability in the latest Pleistocene.

On Bowers Ridge at Sites U1340, U1341, and U1342, the trends and variability in siliciclastics appear to be notably different than at the Bering slope sites, as indicated by the NGR (Fig. **F6**), K% (Fig. **F7**), and NRM/Chi (Fig. **F8**) records. Unlike the Bering slope sites, there are some marked long-term trends in the Bowers Ridge records. A notable change in Site U1341 logging K% data occurs at ~425 m depth (Fig. **F7**) along with an increase in the observed silt content and dropstones in the sediment in smear slides (Fig. **F6**). This level in the section is equivalent in time to ~3 Ma and may signify that the Bering Sea regional expression of NHG includes an increase in clays and silts delivered via sea ice or icebergs to Bowers Ridge. The fact that K% decreases above this level in the section even while the ice ages persisted is difficult to explain. One possibility is that the warmer climate of the Pliocene facilitated the formation of K-rich clays on land that were shed into the Bering Sea once the ice ages began. K-rich clay formation could have then decreased when the climate cooled. The NGR, magnetic susceptibility, and sedimentological smear slide and descriptive data indicate increasing amounts of terrigenous material upsection with a pronounced increase at ~1 Ma, probably due to a greater supply of ice-rafted siliciclastics to Bowers Ridge once large 100 k.y. glaciations occurred.

As at the Bering slope sites, the variability of physical properties in sediments younger than 1 Ma at Bowers Ridge appears to include higher frequency variability than the 100 k.y. ice volume cycles. Again, higher frequency climate variability, including changes in the distribution of sea ice and icebergs delivering sediment to Bowers Ridge, may dominate the mode of sediment deposition in the Bering Sea after 1 Ma. However, unlike at the Bering slope sites the variability of all lithologic parameters studied—NGR, magnetic susceptibility, and GRA bulk density—in sediment older than 1 Ma at Bowers Ridge is not dominantly paced by 40 k.y. ice volume cycles. One explanation is that even in the 40 K world sediment delivery to Bowers Ridge was paced at least in part by processes other than sea level change. Spectral analyses of K% data from Site U1341 at Bowers Ridge indicate that variability occurs across a spectrum of frequencies, with notable concentrations of variance at 40 k.y. and 23 k.y. periodicities. During the 40 K world, cycles and episodes of deposition of IRD on Bowers Ridge were possibly impacted by regional climate changes responding to both obliquity (40 k.y.) and precession (23 k.y.) solar radiation changes. In contrast, at the Bering slope, sea level variations that occur dominantly with 40 k.y. periodicity were the main factor controlling the transport of sediment from the continent/shelf to the slope. The observation that high-latitude climate was responding to precession forcing during the 40 K world has important implications, not only for theories that explain ice volume changes, but ultimately for our understanding of ice sheet dynamics and our ability to predict ice sheet response to radiative forcing.

History of sea ice development

The investigation of the evolutionary history of climate and surface ocean conditions is primarily approached by studying microfossils, sedimentology, and physical properties of sediments. This is particularly true for the influence of sea ice formation and the flow of the relatively warm oligotrophic Pacific surface waters into the Bering Sea.

One of the most striking findings of Expedition 323 is the general sea ice distribution history of the Bering Sea for the past 5 m.y. As described in **"Overview of ages and sedimentation rates,"** the first sign of sea ice is the presence of pebbles, which are thought to be transported as IRD starting at >3.8 Ma at Site U1340 (Fig. **F6**), indicating the formation of sea ice or iceberg transportation to the Bowers Ridge region. The bulk of the evolution of sea ice distribution has been interpreted from shipboard analyses of sea ice diatoms and sea ice–related dinoflagellate taxa and to a lesser extent by other diatom taxa and intermediate water–dwelling radiolarians (see below for details).

The details of sea ice evolution are derived from changes in the relative abundance of sea ice diatom taxa, which are represented mainly by *Thalassiosira antarctica* spores (Abelmann, 1992a) and sea ice dinoflagellates (Fig. **F9**). The first signs of sea ice diatoms and dinoflagellates are subtle increases in their abundance at Bowers Ridge at Site U1340, starting at ~3.4 Ma for dinoflagellates and ~2.7 Ma for diatoms, coincident with NHG (Maslin et al., 1996). After ~2 Ma the sea ice assemblage signals become progressively stronger into the present, up to values of ~10%–20%. In contrast to the Bowers Ridge sites, sea ice cover at the Bering slope sites is markedly severe, indicated by sea ice assemblage percentages significantly higher than the values observed at Bowers Ridge. Sea ice diatom values range from ~10% to 50% during the latest Pliocene and increase from ~30% to 70% during the Pleistocene. The abundance of sea ice dinoflagellates also increases but not to the same extent as sea ice diatoms. Notably, sea ice diatom and sea ice dinoflagellate assemblages clearly show a significant increase in both abundance and amplitudes of variability at around the mid-Pleistocene Transition (MPT) (Fig. **F9**). Analogous to sea ice–associated diatom and dinoflagellate taxa, a clear increasing trend in abundance of intermediate water–dwelling radiolarian taxa at the MPT is also observed at Sites U1343 and U1344. This is consistent with the interpretation that the surface water became gradually more affected by the formation of sea ice as climate progressively cooled; in the presence of sea ice, surface-dwelling radiolarians disappeared, and, as a consequence, the relative percentages of intermediate water dwellers such as *Cycladophora davisiana* were higher (Abelmann, 1992b; Okazaki et al., 2003).

At Sites U1343 and U1344, which are located closer than the Bowers Ridge sites to the southern boundary of today's seasonal sea ice maximum extent, a dramatic change in the dominance of dinoflagellate cyst assemblages from autotrophic to heterotrophic taxa is evident at ~1.2–1.5 Ma. This suggests that sea ice formation occurred well before the time when the abundance of sea ice taxa significantly increased at ~1 Ma. Heterotrophic dinoflagellates feed mainly on diatoms (Jacobson and Anderson, 1986) and their abundance is most likely the result of food availability; hence, they can persist in ice-laden environments. On the other hand, the low production of their autotrophic counterparts, which dwell mainly in open waters without sea ice, could be related to these taxa being out-competed in the presence of blooming diatom populations in regions of seasonal sea ice cover. Furthermore, heterotrophic dinoflagellate cysts dominate the assemblages in polar areas where sea ice occurs up to 12 months per year (e.g., Rochon et al., 1999). The sea ice–associated species *Islandinium minutum*, known to be very abundant or dominant in the Arctic Ocean and subarctic regions with pronounced sea ice cover (Head et al., 2001; Hamel et al., 2002), appeared to increase at ~1 Ma at both Sites U1343 and U1344 (Fig. **F9**). Along with significant increases of both sea ice dinoflagellates and sea ice diatoms (e.g., *Thalassiosira antarctica* spores) at ~1 Ma at both sites, a rather significant drop in the abundance of *Neodenticula seminae*, a typical pelagic diatom, is also seen. All of these biotic events are within the time interval of the MPT, which spans from ~1.2 to 0.8 Ma and marks the transition from 41 k.y. obliquity ice volume cycles to larger ice age cycles that vary at ~100 k.y.

As noted above, the Bowers Ridge and Bering slope regions show distinct differences in the extent of sea ice cover throughout the last ~2.1 m.y., the time period covered by the sedimentary records of both regions. The extent of sea ice cover of the latter is substantially greater than that of the former because of the distal locations of the three Bering slope sites, which are most prone to perennial sea ice cover in the Bering Sea. The spatial differences in sea ice cover today are mainly attributed to the surface water circulation pattern (Fig. **F2**); this spatial difference appears to have persisted since at least 2.1 Ma, implying that the surface water circulation patterns have also persisted (see below for details with *N. seminae* and other taxa). This is further supported by the fact that at Site U1339 on Umnak Plateau, the site closest to an entry point of Alaskan Stream subarctic Pacific water, the sea ice taxa suggest lower levels of sea ice cover compared to the Bering slope sites farther north, which are not as heavily impacted by Alaskan Stream water. Furthermore, Katsuki and Takahashi (2005) illustrated that during the low sea level stand of the Last Glacial Maximum, the relatively warm subarctic Alaskan Stream water entered into the Bering Sea through the western Aleutian passes rather than the eastern passes because of their shallow water depth. After entry it turns eastward, flowing counter-clockwise around Bowers Ridge, and consequently reaches the southeast corner of the Bering Sea, close to Site U1339 on Umnak Plateau, before turning northwest. It is surprising that the spatial pattern of sea ice and surface water circulation observed in the last glacial period, including the stronger influence of warm Alaskan Stream water at Umnak Plateau compared to at the northern Bering slope, persists over long timescales.

Changes in biological productivity and the influence of subarctic Pacific surface water mass flowing into the Bering Sea

Based on the spatial distributions of long-term temporal changes of three diatom taxa (*Coscinodiscus marginatus*, *Neodenticula*, and *Actinocyclus curvatulus*), it is clear that the influence of subarctic Pacific waters, which are relatively warm and less eutrophic than Bering Sea waters, has typically been strongest at the Bowers Ridge sites, followed by the Umnak site; the weakest influence of this warm water mass has occurred at the Bering slope sites (Fig. **F10**). This is the same pattern found by Katsuki and Takahashi's (2005) study of past water mass circulation patterns, which they inferred from sea ice distributions from the last glacial period. The longer records from Expedition 323 indicate that as climate cooled through the Pleistocene, pelagic water influence at all the sites progressively weakened. Furthermore, the sites closest to straits through which pelagic water flows into the Bering Sea have consistently higher abundances of subarctic diatom species than those downstream in the counter-clockwise circulation pattern of the surface water masses.

From the bottom of the holes upward in the Bowers Ridge sites, a marked drop in *Coscinodiscus marginatus* was seen at ~3 Ma at Site U1341 and at ~2.6 Ma at Site U1340 (Fig. **F10**). This can be interpreted as resulting from a sharp reduction in supply of nutrients due to the development of upper layer stratification. It is apparent that the diatom taxon *C. marginatus* requires a relatively high nutrient supply and tolerates low light intensity. This is substantiated by the fact that (1) today this diatom taxon dwells in the lower euphotic zone off Spain (Nogueira et al., 2000; Nogueira and Figueiras, 2005), and (2) it occurs during early winter (~November–January) in the subarctic Pacific and the Bering Sea based on time-series sediment trapping (Takahashi, 1986; Takahashi et al., 1989; Onodera and Takahashi, 2009). Thus, high demand of nutrient supply and low demand of light intensity is apparent for this taxon. This timing of 3–2.6 Ma coincides approximately with the so-called end of "opal dump" observed in the subarctic Pacific at ~2.7 Ma, which is coincidental with the onset of NHG (Maslin et al., 1996). Although the reduction in *C. marginatus* around the time of NHG persisted, an overwhelmingly continuous presence of diatom ooze and interbedded diatom ooze and silt sediments accumulated throughout the Pliocene–Pleistocene in the Bering Sea. This clearly suggests that a high amount of opal sedimentation continued after the onset of NHG well into the Pleistocene.

The 5 m.y. long-term trend of *Neodenticula (N. kamtschatica*, *N. koizumii*, *N. seminae*, and *Neodenticula* sp.) in the Bowers Ridge region shows the following two patterns.

Generally higher percent values are observed from the hole bottoms up until ~2.9–2.7 Ma, depending on the hole, than are observed for the sections above. From there onward there seems to be a decline in *Neodenticula* with sizable fluctuations that indicate surface water stratification progressively developed as the climate cooled from the Pliocene into the Pleistocene. The general antiphase relationship of this taxon versus *Actinocyclus* spp. (Fig. **F10**) suggests subtle and perhaps periodic changes in stratification/water mass circulation as the colder climate developed. This is generally true for Sites U1340 and U1341 at Bowers Ridge and Site U1343 off the Bering slope. The data from Site U1344, however, provide a more complicated picture than this and do not show a clear antiphase relationship trend, probably because of the overwhelmingly high abundance of sea ice–associated diatoms such as *Thalassiosira antarctica* spores (Abelmann, 1992a) (~25% during 4–0.9 Ma; ~40% during 0.9–0 Ma) (Fig. **F10**). Furthermore, an even more clearly visible antiphase relationship of *Actinocyclus* spp. versus *N. seminae* is seen during ~1.9 Ma and 1.1 Ma at Site U1343. Their percentages increased at ~1.9 Ma. Marked declines are seen for both taxa at slightly different times (*Actinocyclus* spp. at ~1.1 Ma and *N. seminae* at 0.9 Ma), both of which are around the MPT (Fig. **F10**). The upheaval of both taxa during this time interval is identical. During intervals of high eutrophic levels suggested by high *Actinocyclus* spp., cooler, low trophic subarctic Pacific waters, indicated by *N. seminae*, were introduced into the Bering Sea. This is based on the geographic and seasonal distributions of *Actinocyclus curvatulus*, which appears to be ecologically similar to *Thalassiosira trifulta* and, to a lesser extent, *N. seminae* (Sancetta, 1982; Takahashi, 1986; Takahashi et al., 1989). As surface waters became increasingly stratified, especially after ~0.9 Ma with Milankovitch-scale 100 k.y. climatic cyclic regimes, *N. seminae* declined with the emerging sea ice diatoms.

Changes in bottom and intermediate water conditions

Much of the Pacific water entering the Bering Sea is matched by outflow through the Aleutian Islands. The most significant outflow is through the Kamchatka Strait, which has a maximum water depth of 4420 m. If some component of North Pacific Intermediate or deep water formed in the Bering Sea in the past, particularly when sea level was lower, it would have flowed out through the Kamchatka Strait or a secondary outlet near the Commander–Near Strait at 2000 m. One of the scientific objectives of Expedition 323 was to elucidate the history, temporal variability, and intensity of NPIW and deep water formation in the Bering Sea and its links to surface water processes. This objective was partially fulfilled during the expedition but would have been more adequately addressed had we obtained permission to drill two important sites located in Russian territorial waters, Shirshov Ridge Site SHR-3B at 2232 m water depth and Site KST-1B inside the Kamchatka Strait at 3435 m water depth. The main objective at these sites was to monitor deep water masses flowing out of the Bering Sea to the Pacific Ocean. Nevertheless, seven sites were successfully cored and complete records of environmental variability of intermediate and deep water sites spanning the Pleistocene to the Pliocene were recovered during Expedition 323. The sites ranged from 818 to 3174 m and allow for the characterization of past vertical water mass distribution and for the reconstruction of the history and distribution of the OMZ in the region (Fig. **F4**).

Previous observations made in glacial records from the Bering Sea and just outside the Bering Sea on the Detroit Seamount in the North Pacific suggest a source of ventilated intermediate water coming from the Bering Sea and/or the Detroit Seamount region (Gorbarenko, 1996). Furthermore, other paleoceanographic reconstructions of the Bering Sea, made possible by the R/V *Hakuhou-Maru* piston coring survey cruise in 1999, show past NPIW formation during four different time slices, reconstructed based on the high oxygen indicator and intermediate water–dwelling radiolarian species *Cycladophora davisiana*. According to these studies, the role of the Bering Sea in NPIW formation is apparently visible during the cold intervals.

Shipboard analyses of sediment samples recovered during Expedition 323 show continuous recovery of Pliocene to Holocene deep sea benthic foraminifers and midwater radiolarians at all sites (Figs. **F11, F12**), although calcareous benthic foraminifers appear to be rare in the middle and early Pliocene. The benthic foraminifer faunal composition displays large assemblage changes and shifts in species dominance. These changes are likely related to variability in local oxygen concentration in the bottom waters associated with surface water productivity and/or deepwater ventilation on Milankovitch timescales. For example, *Bulimina* aff. *exilis*, a common species in the Bering Sea samples, is generally regarded as a low oxygen/deep infaunal species and has been found in samples associated with high productivity and low sea ice (e.g., Bubenshchikova et al., 2008; Kaiho, 1994).

Bering Sea benthic foraminifers show affinities to assemblages found within or near the OMZ in the Sea of Okhotsk and also to more common deep Pacific Ocean assemblages. The faunal similarity between the two marginal seas and the deep Pacific Ocean will allow for the reconstruction of the physico-chemical characteristics of deep and intermediate water masses as a result of changes in surface productivity, deepwater ventilation, sea ice coverage, and continental glaciation.

Previous piston core studies showed a large increase in the intensity of the OMZ during the last deglacial at Umnak Plateau (Okazaki et al., 2005), suggesting a relationship between productivity and terrestrial nutrient supply from melting. However, there is no information regarding the longer timescale relationship through the Pleistocene. Analysis of faunas from the newly drilled Bering Sea sites will be particularly important in extending this record through the entire Pliocene (at Bowers ridge) and Pleistocene (at Bowers ridge and the Bering slope) and will allow us to decipher the onset and evolution of the OMZ and provide further insight into NPIW production at the marginal sea. Furthermore, Site U1344 at ~3200 m is presently located below the OMZ and also has the potential to monitor past deepwater changes.

A striking finding of the expedition was the relatively low oxygen content of intermediate water mass conditions at most sites during the last 5 m.y., as indicated by the presence of episodic laminated sediment intervals throughout the entire sections. However, the benthic foraminiferal faunas recovered from deep cored Sites U1340 and U1341 suggest that in general the Bering Sea intermediate and deep waters were better oxygenated in the early Pliocene, as suggested by the presence of the agglutinated foraminifer *Martinottiella communis* (Fig. **F12**), and less oxygenated during the last ~2 m.y., as suggested by the increase in deep infaunal benthic foraminifers (Fig. **F11**). This assemblage is composed of abundant calcareous benthic genera (e.g., *Bulimina*, *Globobulimina*, *Islandiella*, *Nonionella*, and *Valvulineria*) that are typically indicative of reduced oxygen conditions (Bubenshchikova et al., 2008).

High sediment accumulation rate Sites U1339 and U1345, located within the OMZ today (Fig. **F4**), reveal high-amplitude variability in the relative abundance of the deep infaunal assemblage since 0.8 Ma. This appears to be associated with interglacial–deglacial cyclicity, showing higher abundance of deep infaunal species (reflecting the lowest bottom water oxygen conditions) during interglacials, in particular strong interglacials marine isotope Stages (MIS) 1, 5, and 11. Higher bottom water oxygen conditions appear to correlate with glacials. Furthermore, Sites U1340, U1343, and U1344 contain well-preserved foraminifers over the last 2 m.y. with increasing absolute abundances of benthic and planktonic taxa across the MPT (~0.8–1.1 Ma) in association with an increase in abundance of the polar planktonic foraminifer *Neogloboquadrina pachyderma* sinistral. This cooling trend was also observed as an increase in the abundance of sea ice dinoflagellates and diatoms and intermediate water–dwelling radiolarians (e.g., *C. davisiana*). Cooling of the surface waters would have enhanced ventilation of the intermediate waters during glacials and increased density stratification during interglacials, contributing to the drop in oxygen content in the intermediate and bottom waters at these times, which is suggested by the increase in deep infaunal benthic foraminifer taxa.

Microbiology in high surface productivity environments

The microbiological objectives of Expedition 323 were to constrain global models of subseafloor biomass and microbial respiration by quantifying subseafloor cell abundance and pore water chemistry in an extremely high productivity region of the ocean. We also sought to determine how subseafloor community composition is influenced by high productivity in the overlying water column.

To meet these objectives, high-resolution sampling for microbiological analyses and pore water chemistry took place at five sites throughout the Bering Sea. Each site was selected based upon its distance from land and its levels of marine productivity determined by annual chlorophyll-a concentrations in the water column.

Four cores were drilled using the APC system to ~40 m CSF at each microbiology-dedicated hole. Contamination tests using perfluorocarbon tracer (PFT) and fluorescent beads (Smith et al., 2000) were performed in each hole, showing that contamination from the drill fluid was insignificant.

Sediment samples were taken for determination of cell abundance measurements (a proxy for microbial biomass) and diversity and structure of the microbial community. In general, these samples were taken every 25 cm for Sections 1H-1 to 2H-3 (or 2H-6), and every 75 cm for Core 3H. Below Core 3H, the sampling resolution was one per core. Interstitial water whole-rounds were taken with the same resolution adjacent to microbiology whole-rounds. In addition, 10 cm whole-rounds were taken for interstitial water and microbiological analyses at an interval of one per core until APC refusal. Interstitial water sampling continued at this resolution in XCB cores, and microbiology samples for cell abundance, diversity, and community structure were collected at ~400 and ~700 m CSF. PFT analyses showed no drill-fluid contamination at these depths.

Interstitial water samples were squeezed immediately on board and aliquots were fixed for both shore-based and shipboard analysis. The shipboard aliquots were used to determine concentrations of dissolved inorganic carbon (DIC), alkalinity, sulfate, sulfide, ammonium, phosphate, major ions (e.g., Ca, Na, and K), and minor ions (e.g., Fe and Mn). These data along with formation factor data allow for a quantitative determination of microbial respiration rates (D'Hondt et al., 2002).

The geochemical data obtained during the expedition show that the microbial activity along the slope sites (i.e., Sites U1339, U1343, U1344, and U1345) is substantially higher and more diverse in terms of respiration pathways than at Site U1342 at Bowers Ridge. At the slope sites, the concentrations of microbial respiration products such as DIC, ammonium, and phosphate are approximately an order of magnitude higher than at Bowers Ridge (Fig. **F13**). A shallow sulfate–methane transition zone (SMTZ) (~6–11 m CSF) is also present (Fig. **F13**), indicating that both methanogenesis and sulfate reduction based on methane oxidation occur in these sediments. Interstitial water data further suggest the presence of microbial-mediated Fe and Mn reduction. Interestingly, the geochemical profiles even suggest significant microbial activity as deep as 700 m CSF. In contrast, at Bowers Ridge sulfate penetrates to the basement and is almost unaltered with depth, suggesting only very low rates of microbial-mediated sulfate reduction. Methane is below the detection limit. The difference in microbial activity at these sites might be caused by different rates of water column productivity and sedimentation.

We expect that the differences in the geochemical parameters between the slope and ridge sites will be reflected in microbial abundance and diversity. A larger and more diverse microbial community at the slope sites is likely. Specifically, we expect elevated cell abundance and a consortium of bacteria and archaea at the SMTZ. At the slope sites, geochemical profiles suggest that methanogens, iron reducers, manganese reducers, and sulfate reducers exist throughout the sediment column. At Bowers Ridge, geochemical profiles indicate that only sulfate reducers and nitrate reducers are present.

Principal site results

Site U1339

Background and objectives

The primary objective of drilling at Site U1339 (prospectus Site UMK-4D) was to study high-resolution paleoceanography in the easternmost part of the Bering Sea, a marginal sea expected to exhibit large variations during times of global climate change. Umnak Plateau (Fig. **F14**) is located off Bristol Bay and is well situated for the study of past changes in surface water conditions, sea ice extent, and associated biological productivity. Today, parts of the relatively warm Alaskan Stream surface water flow into the Bering Sea through Unimak and Amukta passes and hence sea ice is not formed in this region. However, substantial sea ice coverage has been noted during the LGM, when sea level was ~100 m lower than today, indicating that the influence of relatively warm water from the distal end of the Alaskan Stream was reduced. This may have been because water entering the Bering Sea from the Pacific Ocean through Unimak and Amukta passes was at least partially restricted when sea level dropped; the warm Pacific water could have more easily passed through the deeper passes located in the central and western Aleutians, such as Amchitka Strait (Katsuki and Takahashi, 2005). Thus, monitoring past environmental conditions at Umnak Plateau can provide an understanding of the impact of changes in water exchange between the Pacific and Bering Sea waters. Since these eastern passes are fairly shallow (~50 m and 430 m), little intermediate or deep water flows out to the Pacific in this region. As such, records from Umnak Plateau should provide us with different information than the western sites, which are closer to deep passes where surface water flow may not have been strongly inhibited by sea level changes and where dense water exchange with the Pacific Ocean is more likely to occur (Tanaka and Takahashi, 2005). To make this west–east comparison, records from the drill site on Umnak Plateau (Site U1339) can be compared to those of Site U1341 (water depth = 2177 m) at Bowers Ridge.

The drill site at Umnak Plateau (Site U1339) is situated on the northwest flank of a section of the plateau that is separated from the main shelf by a canyon (Fig. **F15**). This location was selected with the assumption that much of the siliciclastic material from the shelf would have been transported into the canyon during sea level lowstands. As such, this site location would have received more pelagic biogenics relative to terrigenous sediments than a site located on the main shelf. There is clear evidence of continuous horizontal reflectors on the seismic profiles (Fig. **F16**).

The drill site at Umnak Plateau can also be used to study the impact of subseafloor microbes on biogeochemical fluxes in the highest surface ocean productivity areas of the drill sites in the Bering Sea. Organic-fueled subseafloor respiration and its impact on biogeochemistry in such a highly productive region has not previously been quantified. To do this, drilled sediments from Umnak Plateau were used to determine subseafloor cell abundance and to investigate the link between the mass and characteristics of subseafloor microbes and the extent of export productivity from the surface ocean.

Scholl and Creager (1973) found Pleistocene diatomaceous sediments with ash layers in the uppermost 120 m at DSDP Sites 184 and 185, both drilled at Umnak Plateau, followed by Pliocene diatomaceous sediments below. They recorded sedimentation rates of ~67 m/m.y. and indicated that the diatomaceous sediments have neritic components, which were likely influenced from the Bristol Bay region. A piston core study from the same general region provided a sedimentation rate of 262 m/m.y. (Takahashi, 2005). Thus, prior to drilling the predicted age for the bottom of Site U1339 at ~200 meters below seafloor (mbsf) ranged from the mid-Pleistocene to the Pliocene.

Lithostratigraphy

The sediments recovered at Site U1339 are a mixture of three components: biogenic, volcaniclastic, and siliciclastic. Other accessory lithologies identified include authigenic dolomite and pyrite. In general, the color of the sediments reflects their lithologic characteristics. Sediment composed of mixed lithologies of diatom silt or diatom ashy silt is dark greenish gray, whereas diatom ooze is olive-gray to olive. Most of the volcaniclastic ash layers are black. Only one lithologic unit spanning the Pleistocene was defined and it was divided into four subunits (Fig. **F17**). The largest-scale sedimentary features are decimeter- to meter-scale bedded alternations of sediment color and texture reflecting alternations in lithology. Well-preserved lamination caused by alternating millimeter-scale dark and light laminae was mainly observed in five distinct intervals, each ranging from 10 to 40 cm in thickness. Distinct volcaniclastic layers ranging from a few millimeters to 10 cm in thickness occur throughout the unit. Some black volcaniclastic layers are normally graded, indicating either time-transgressive fining of grains or redeposition by gravity flows.

The major sediment component is biogenic and predominantly composed of diatoms with generally good preservation. Diatom frustules hosting pyrite framboids are also observed. Both benthic and planktonic foraminifers are observed, although their abundance levels were low. Thin laminae dominated by foraminifer tests are observed with dominance of benthic foraminifer *Bulimina* sp., which is characteristic of low oxygen content. Calcareous nannofossils, radiolarians, and sponge spicules are rare. Terrigenous grains, which are common sediment components, are composed of silt-sized quartz and feldspar, clay, mica, and rock fragments. Gravel- to pebble-sized, rounded to angular clasts are interpreted as dropstones delivered by melting sea ice or icebergs. Some pebbles are composed of pumice or obsidian, suggesting a volcanic source. Authigenic dolomite was found in five distinctive intervals, mostly in the upper and lower part of the sedimentary record. It occurs either as dolomite rhombohedra scattered in the sediment or as (semi-) lithified layers 5–10 cm thick. Because of the presence of authigenic carbonates at this site, carbonate-stable isotope measurements are potentially contaminated by the isotopic signature of the overgrowths. However, the presence of authigenic carbonates can be detected and screened out of the isotopic records. Depth variations of the color reflectance (CR) parameters a* and b*, GRA porosity, and magnetic susceptibility were compared to the lithologic variations. Overall, these four parameters show distinct short-term variability and longer term trends that can be correlated to lithologic variations at both short- and long-term scales. The depth variations of CR parameter b*, which reflects the yellowness of the sediment, show a remarkably negative correlation with the GRA data, with lower b* values corresponding to denser, more siliciclastic-rich sediments. CR value a* is tentatively correlated to the concentration of diatom ooze. Changes of magnetic susceptibility with depth mainly reflect volcaniclastic content, and a very good correlation exists between the thickest volcanic ash layers and the highest magnetic susceptibility excursions.

Micropaleontology

In contrast to their calcareous counterparts, siliceous microfossil groups had constant presence and relatively high abundance throughout all sections at this site. All age determinations were achieved with the siliceous microfossil groups (Table T3; Figs. F17, F18). Diatoms provided two important last occurrence (LO) datums of *Thalassiosira jouseae* (0.31 Ma) and *Proboscia curvirostris* (0.28 Ma) in the middle section of the four holes studied. The most important datums were derived by studying silicoflagellates, despite the fact that their abundances were generally “trace” to “few” with rare instances of “common.” These are the first occurrence (FO) of *Distephanus octangulatus* (0.741 Ma) and the LO of *Dictyocha subarctios* (0.736 Ma), respectively. These two datums are considered to occur above the Brunhes/Matuyama boundary (0.781 Ma). However, without definite paleomagnetic datums of the Brunhes/Matuyama boundary (see **“Paleomagnetism”** section for detail), the silicoflagellate datums are the only reliable datums at this time. The LO of *Distephanus octonarius* (0.244 Ma), another silicoflagellate datum, provided harmonious age information in concordance with diatoms and radiolarians. Despite their relatively low abundances due to massive occurrences of diatoms in the bulk of samples, radiolarians provided five pertinent datums that span from near the top through the middle part of the drilled sections. These include *Lychnocanoma nipponica sakaii* (50 ka), *Amphimelissa setosa* (80–100 ka), *Spongodiscus* sp. in Ling (1973) (0.28–0.32 Ma), *Axoprunum acquilonium* (0.25–0.43 Ma), and *Stylatractus universus* (0.41–51 Ma).

Because of this site's proximity to the Bering shelf, particularly during the glacial lowstands, coastal water diatoms including *Chaetoceros* spores and freshwater diatoms were observed. Furthermore, the relative abundances of the ubiquitous *Neodenticula seminae*, an indicator species of the Alaskan Stream, fluctuated throughout the sections, indicating change in the Pacific water entry into the Bering Sea. The extent of sea ice–associated diatoms also fluctuated throughout the sections.

Calcareous nannofossils were either barren or sparse throughout the sections. Reworked specimens of calcareous nannofossils were found in the upper section, indicating transport by IRD or other processes. Planktonic foraminifers were present in all but a few samples. Both planktonic and benthic foraminifers were abundant enough to proceed with more detailed studies such as oxygen and carbon isotopic analyses. Abundant benthic calcareous foraminifers with generally low diversity showed close affinities to those recorded in recent sediments within or near the OMZ in the Sea of Okhotsk. The exceptionally high productivity in surface waters greatly expanded the OMZ.

Dinoflagellate assemblages were moderate to abundant with relatively low species diversity. They showed heterotrophic protoperidinial dinoflagellates feeding on diatoms. Such assemblages are related to extremely high diatom production. In the upper section, a taxon indicative of the North Water Polynia condition was noted, implying significant sea ice formation.

Paleomagnetism

Paleomagnetic analyses indicate that all sediments are likely from the Brunhes Chron (0–780,000 y before present [BP]). However, anomalous NRM intensities along with low or negative inclinations in the same intervals may be due to authigenic growth of greigite related to sulfate reduction or methanogenesis. As such, it is possible that the Brunhes/Matuyama boundary was reached at ~180 mbsf but that the reversal in polar intensity was obscured by the presence of greigite. At this time, it is difficult to say which hypothesis is more likely.

Stratigraphic Correlation

Three holes dedicated to paleoceanographic studies were drilled at this site. Cores were drilled at offset depths in order to obtain a continuous sedimentary section. By comparing fast track GRA density and magnetic susceptibility variations, the cores from different holes can be placed into a continuous stratigraphic framework. An affine table indicating offsets for each core in each hole was constructed (Table **T4**). A continuous record mainly using Holes U1339C and U1339D was constructed by splicing together the GRA and magnetic susceptibility records; this splice (Table **T5**) will guide the postcruise sampling strategy designed to generate continuous paleoceanographic records. The splice at Site U1339 is continuous from the mudline to ~200 m CSF (Fig. **F17**).

Geochemistry

Interstitial water samples taken from Hole U1339A at low resolution from 0 to 200 m CSF and at high resolution from Hole U1339B were analyzed for chlorinity, salinity, alkalinity, DIC, pH, sulfate, hydrogen sulfate, ammonium, phosphate, silica, Ca, Mg, Na, K, Fe, Mn, B, and Sr. In addition, ethane and methane were analyzed. Methane is detectable throughout, and at ~10 m CSF, where sulfate is depleted, methane concentrations increase dramatically (Fig. **F18**). The analyses show that the SMTZ at present is relatively shallow at 8–10 m CSF. Notably, alkalinity and DIC increase from 3 to 30 mM in the uppermost 10 m, reaching a maximum at ~120 m CSF (Fig. **F18**). Solid-phase analyses show that calcium carbonate content ranges from 0 to 13.3 wt% (average = 2.1 wt%) and total organic carbon is 0.47 to 1.83 wt% (average = 0.98 wt%).

Physical properties

Whole-round measurements of magnetic susceptibility and GRA bulk density (using the fast track) and magnetic susceptibility, GRA bulk density, and *P*-wave velocity (PWV) (using the whole-round multisensor logger [WRMSL] slow track) were made on each core recovered at Site U1339. One thermal conductivity (Tcon) measurement per core was also analyzed. Discrete samples of cores from Holes U1339A and U1339B were taken to analyze moisture, density, porosity, water content, and grain density. Magnetic susceptibility varied downcore, with the highest peaks likely related to volcanic ash layers and cyclical variations likely due to varying amounts of siliciclastics versus diatoms. Such variations in lithology likely contributed to the variations in GRA bulk density and discrete bulk density measurements, which indicate cyclical variations from 1.6 to 1.3 g/cm^3. Porosity, water content, and grain density measurements exhibit an oscillating cyclicity similar to the wet bulk density record and are likely tracking variations in the concentration of biogenic debris—in particular, highly porous diatom frustules—with respect to lower porosity terrigenous sediment with higher grain density. Discrete bulk density measurements increase gradually with depth at a rate of ~0.1 g/cm^3/100 m, most likely because of sediment compaction. Compaction likely explains the decrease in porosity downhole from a near-surface value of ~85% to ~65% at a depth near 200 m CSF.

NGR counts/s varied rhythmically from highs of 25 to 40 counts/s to a low of ~10 counts/s, evidently tracking clay mineral–bearing sediment in contrast to sediments with more biogenics. Because the PWV measurements were seriously degraded by expansion of hydrate-released methane gas, the *P*-wave logger was turned off for all core sections deeper than ~33 m CSF. Tcon values ranged widely from a low of ~0.5 W/(m·K) to >1 W/(m·K), with lower values presumably reflecting water-rich diatomaceous sections and higher values reflecting abundant terrigenous debris.

Electrical conductivity to determine formation factor was measured every 10 cm in the working half of the first core of Hole U1339A, then every 20 cm in Cores 323-U1339A-2H and 3H. Sediment conductivity ranges from 1.37 to 3.70 µS/cm. The highest values were recorded in ash layers and formation factor generally increased downhole.

Downhole measurements

By employing the deployed triple combination (triple combo) and the Formation MicroScanner (FMS)-sonic tool string combinations, data were recorded below the bottom of the pipe depth. They indicate good hole conditions and only minor excursions from the nominal size of the drill bit. The comparison of the gamma ray and density logs with the NGR and GRA track measurements on cores recovered and with moisture and density (MAD) measurements shows good agreement, which should allow for reliable core-log integration. All logs were referenced to the seafloor depth of 1875 m wireline log depth below rig floor (WRF) identified during the last pass of the FMS-sonic tool string. Comparison of the gamma ray logs measured during the main pass of the two runs shows an excellent repeatability between the two runs. The resistivity values measured by the electrode spherically focused resistivity (SFLU) measurement were lower than those recorded by induction measurements, probably because of current loss at the electrodes. The higher induction resistivities are closer to values typically measured in deep-sea sediments.

The display of the high coherence in sonic waveforms used to derive the compressional velocity suggests that despite the closeness of the formation velocity to the sound velocity in the borehole fluid (~1500 m/h), the Dipole Sonic Imager (DSI) was able to capture compressional wave arrivals and measure a reliable V_P profile over the entire open interval logged. Additional postcruise processing will, however, be necessary to derive V_S logs from the recorded dipole waveforms.

The downhole log measurements of bulk density, porosity, and electrical resistivity correlate very well. Variations in sediment composition result in variations of porosity that affect bulk density and resistivity in a similar manner. The measurements also correlate significantly with the gamma ray logs as a result of the overall uniform mineral matrix of the sediments in the interval logged. In particular, the parallel decrease with depth in gamma ray, density, and resistivity from 86 to 102 m wireline log matched depth (below seafloor) (WMSF) is typical of a retrograding fining-upward sequence.

The downhole variations of gamma ray radioactivity are controlled by the sediment content of naturally occurring radioactive elements (K, U, and Th). The computed gamma ray, or gamma ray without uranium, is a more accurate measure of the clay content than is the total gamma ray, which can be influenced by such factors as organic matter or detrital minerals. The most significant feature in the gamma ray logs is the increase at ~142 m WMSF, which is associated with an increase in the three radioactive components and a peak in uranium. This increase coincides with the transition from lithologic Subunits ID to IE (diatom ooze and diatom fine ash to diatom ooze). The peak in uranium can be related to the occurrence of dolostones observed in the cores in this interval.

The downhole third-generation advanced piston corer temperature tool (APCT-3) measurements show a range of 3.65°C at 23.0 m drilling depth below seafloor (DSF) to 12.83°C at 158.0 m DSF. These closely fit a linear geothermal gradient of 68.0°C/km. The temperature at the seafloor was 2.1°C based on the average of the measurements at the mudline during all the APCT-3 deployments. The obtained heat flow—the product of the geothermal gradient by the average thermal conductivity (0.80 W/[m·K])—gives a value of 54.4 mW/m^2, which is within the range of previous measurement in the area.

Sedimentation rates

The age model for Site U1339 was constructed using biostratigraphic datums (Fig. **F19**). The datums that were selected to constrain the sedimentation rates were the ones judged to be best resolved (Table **T6**). The calculations indicate some variability in rates, which range from 22 to 50 cm/k.y. (Fig. **F19**).

Site U1340

Background and objectives

The primary objective of drilling at Site U1340 (prospectus Site BOW-12B) was to study high-resolution Pliocene and Pleistocene paleoceanography in the southernmost part of the Bering Sea at a topographic high on Bowers Ridge (Fig. **F20**), where relatively good calcium carbonate preservation is expected. Bowers Ridge is well situated to allow study of the past extent of water mass exchange with the Pacific Ocean through the adjacent Aleutian passes such as the Amukta, Amchitka, and Buldir passes. In particular, its location allows examination of the influence of the warm Alaskan Stream water mass entry into this region, which influenced the distribution of past sea ice coverage (Katsuki and Takahashi, 2005). Although productivity in the Bering Sea in general is very high with respect to other parts of the global oceans, the expected productivity at this site was lower than at Site U1339, which has substantially greater influence from the nearby Bering shelf and which was exposed during glacial lowstands. We selected this site at relatively shallow water depth to study physical and chemical changes in upper water mass conditions such as the low dissolved oxygen concentration conditions that caused the formation of laminated sediments at a site on the Bering slope at similar water depths (Cook et al., 2005). The vertical structure of past water masses can be determined by comparing results at this site with those at the other drilling sites on Bowers Ridge (Site U1341, water depth = 2177 m; Site U1342, water depth = 837 m) (Fig. **F20**).

Site U1340 at Bowers Ridge can also be used to study the impact of subseafloor microbes on biogeochemical fluxes in the highest surface ocean productivity areas of the drill sites in the Bering Sea. Samples used to study organic-fueled subseafloor respiration and its impact on biogeochemistry at the highly productive region of the previous Site U1339 were compared to analyses at the Bowers Ridge sites, including Site U1340, although the high-resolution sampling that occurred at Site U1339 was not performed at Site U1340. The Bowers Ridge sediments were used to determine subseafloor cell abundance and to investigate the link between the mass and characteristics of subseafloor microbes and the extent of export productivity from the surface ocean.

Site U1340 is located on the eastern flank of the southern part of Bowers Ridge (Fig. **F20**) in a basin ~10 km east of the ridge crest (Fig. **F21**). Close-ups of the seismic images in the basin (Figs. **F22, F23, F24**) indicate that strata dip to the east (Fig. **F23**). Some shallow sections do not have continuous parallel strata, but most of the rest of the section appears to have continuous features in the seismic images (Figs. **F23, F24**).

The basement age and the age of the deeper sediments are unknown, but at DSDP Site 188 on the western flank of Bowers Ridge (Scholl and Creager, 1973) sediments as old as upper Miocene were found. Specifically, Scholl and Creager (1973) found recent to upper Miocene diatom ooze interbedded with silt-rich diatom ooze and diatomaceous silt. They also found calcareous nannofossils in the upper 120 m and planktonic foraminifers in the upper 300–400 m. In the interval between 580 and 638 mbsf they encountered mudstone. They reported sedimentation rates of ~100 m/m.y. A piston core study from the same general region provided sedimentation rates of 80 m/m.y. (Takahashi, 2005). Thus, prior to drilling sections ranging from the entire Pleistocene to the Pliocene and possibly Miocene were expected.

Lithostratigraphy

The sediments recovered at Site U1340 are a mix of biogenic, volcaniclastic, and siliciclastic sediments. Authigenic dolomite also occurred as an accessory sediment type. In general, the color of the sediments reflects their lithologic characteristics. Sediment composed of siliciclastic sediment or mixed lithologies tends to be very dark greenish gray to dark gray, whereas diatom ooze tends to be olive-gray to olive or dark gray. Volcaniclastic ash layers are dark gray to black or shades of light gray to white and, rarely, weak red. Intervals showing soft-sediment deformation were observed between Core 323-U1340A-3H and Section 8H-2.

Three lithologic units were defined at Site U1340 (Fig. F25). Unit I is composed of alternating beds of diatom ooze and diatom silt with minor amounts of mixed and volcaniclastic sediment from the Pleistocene. The most prominent sedimentary structure in Unit I is soft-sediment deformation of laminated and bedded diatom ooze and diatom silt. Intervals with soft-sediment deformation were observed from Core 323-U1340A-3H to Section 8H-2 and in Cores 11H, 12H, 14H, and 15H; from Cores 323-U1340B-3H to 6H; in Cores 323-U1340C-2H and 3H; and in all cores from Hole U1340D. Folded and tilted bed boundaries are clearly visible in these cores, suggesting the occurrence of synsedimentary slumps as a potential mechanism for the deformation. Distinct volcaniclastic layers ranging in thickness between a few millimeters and 3 cm occur throughout the unit. Volcanic ash is a common secondary or trace lithologic component. A major component of the sediment in Unit I is biogenic and predominantly composed of diatoms with generally good preservation. Diatom frustules hosting pyrite framboids were observed. Terrigenous particles are also a major component in Unit I. The most abundant terrigenous grain types are silt-sized feldspar, quartz, clay, mica, and rock fragments. Some pebbles are composed of basalt and pumice or scoria, indicating a volcanic source. Bioturbation varies from slight to strong throughout all holes and is typically characterized by a mottling defined by color changes. The main lithologies are olive to dark gray diatom ooze and dark gray to dark greenish gray diatom silt with variable amounts of dispersed vitric ash, isolated pebbles, and distinct ash layers as well as bioturbated ash/diatom ooze layers and laminated intervals. The light-colored sediments (olive) tend to contain predominantly biogenic components, whereas the dark-colored sediments (gray) tend to contain subequal proportions of siliciclastic and biogenic components. The volcanic ash layers are typically black, light gray, and, rarely, weak red. Unit II comprises diatom ooze with minor amounts of diatom silt and mixed and volcaniclastic sediment from the Pliocene. Unit II differs from Unit I in having significantly more diatom ooze, less interbedded diatom silt, and fewer laminated intervals. A layer of gravel was recovered at 380 m CSF from Hole U1340A. This is directly below an interval of frequent deposition of gravel-sized clasts at ~220–360 m CSF. This gravel-rich interval overlaps the base of Unit I and the top of Unit II. Unit III, which is further divided into Subunits IIIA and IIIB, comprises diatom-bearing, sponge-spicule-rich ashy sand; sponge-spicule-rich diatom ooze; diatom ooze; and minor amounts of volcaniclastic and siliciclastic sediment from the Pliocene in age. Core disturbance was observed in all sections collected in Unit III. The sediment was described as a slurry with water-rich areas at the core surface and along the liners.

Mixed and siliciclastic lithologies in Unit I correlate well with magnetic susceptibility changes. The increase occurred at ~260 m CSF, dated to around 2.6 Ma, and may reflect an increase in sea ice- or glacial ice-rafted debris delivered to the site after the onset of large glacial–interglacial cycles. The rounded shape of many of the gravel-sized grains suggests that their source was a coastal environment and therefore favors the hypothesis that they were deposited as a consequence of sea ice rafting. Relatively large clasts interpreted as dropstones were observed most frequently between 360 and 220 m CSF (~3.6–1.8 Ma), and their occurrence overlaps with the onset of increased siliciclastic components, coeval with a subtle increase in GRA. This may reflect the onset of NHG after 3.6 Ma (Mudelsee and Raymo, 2005). The occurrence of extensive intervals with soft-sediment deformation related to slumping is somewhat unexpected because the slope of Bowers Ridge is only slightly inclined at the drill sites. An alternative explanation for the triggering of sediment mass movements could be the seismogenic activity of Bowers Ridge, which is representing a buried subduction zone and is relatively close to the volcanic Aleutian arc. Another possibility could be water loss during mineral phase changes in deeper sediments, which may result in less cohesive sediment packages prone to deformation. The primarily biogenic components of Unit II and Subunit IIIB may reflect warmer, highly productive Pliocene conditions or a higher sea level.

Micropaleontology

Core catcher (CC) samples from Site U1340 are dominated by diatom microfossil assemblages with high diversity. Seventeen datums have been identified in Hole U1340A (Table **T7;** Fig. **F26**). Sections 323-U1340A-1H-CC to approximately 34H-CC exhibit a broadly linear sedimentation rate. Thereafter, the sedimentation rate appears to increase drastically, with the last three datums all giving the same age of 3.8–4 Ma. Siliceous microfossils show consistent occurrences throughout the section and are mainly composed of high-latitude pelagic species, indicating changes to surface water productivity. Calcareous microfossils are mostly confined to the top of the section above Section 323-U1340A-23H-CC for nannofossils and 31H-CC for foraminifers. Reworked calcareous nannofossil specimens, mostly of Miocene and Paleogene age, were found in some samples. The planktonic foraminifer fauna does not change radically throughout the Pleistocene (above 200 m CSF), and it is dominated by the subpolar–polar species *Neogloboquadrina pachyderma* (sinistral) together with the subpolar species *Globigerina bulloides*, *Globigerina umbilicata*, and *Neogloboquadrina pachyderma* (dextral). Benthic foraminifers are largely characteristic of those found within or near the OMZ in high-latitude regions. Dinoflagellates consistently occur throughout the section, indicating changes to the productivity and ice cover of the surface waters.

Over 40 species of benthic foraminifers recovered in 83 samples resemble species from oxygen-depleted zones on Umnak Plateau and elsewhere. Abundance and diversity fell markedly below 282.17 m CSF in Hole U1340A, with samples either barren or consisting of a monospecific agglutinated assemblage. Core catcher samples were checked for ostracodes, but no specimens were found.

Diatoms are the dominant microfossil in all holes and they show good preservation throughout. The LOs of *Proboscia curvirostris*, *Thalassiosira jouseae*, and *Proboscia barboi* were identified at 37.60 m CSF for all three species, giving a composite estimated age of 0.3 Ma based on the result from a piston core from Site ES on the northern Emperor Seamount. The age of 0.9 Ma was assigned at 161.24 m CSF by the last common occurrence (LCO) of *Actinocyclus oculatus*, which is followed by the first common occurrence (FCO) of *Proboscia curvirostris* at 1.8 Ma. The LCO of *Neodenticula koizumii* was determined at Section 323-U1340A-25H-CC, giving an age of 2.1 Ma. *Neodenticula koizumii* and *Neodenticula kamtschatica* occur jointly between Sections 323-U1340A-46X-

CC and 57X-CC, corresponding to North Pacific Diatom (NPD) Zone 8 (2.7–3.9 Ma). The FO of *Neodenticula koizumii* and the dominance of *Neodenticula kamtschatica* above Section 323-U1240A-56X-CC defines this zone as NPD Zone 7Bb (3.9 Ma). Diatom assemblages are mainly composed of pelagic species throughout the Pleistocene and upper Pliocene. Several significant abundance peaks of a high-productivity indicator occur throughout the upper and lower Pliocene. In general, few coastal water diatoms, including *Chaetoceros* spores, or freshwater diatoms were observed below the upper Pleistocene, which may be explained by the distant location of this site to continental influence.

Despite the low abundances of silicoflagellates and ebridians, two LOs were obtained. The LO of *Dc. subarctios* (0.74 Ma) fits conformably with those of other siliceous microfossils as well as that of paleomagnetism. The LO of *Ebriopsis antiqua antiqua* (2.47–2.48 Ma) is placed at 305.47 m CSF.

Consistently abundant to common radiolarians with good to moderate preservation occurred in the upper interval (above ~200 m), whereas radiolarians with few abundances and moderate to poor preservation occurred in the lower interval (below ~200 m). The radiolarian stratigraphy spans from the *Botryostrobus aquilonaris* Zone (upper Quaternary) to the *Dictyophimus bullatus* Zone (middle Pliocene). A missing *Stylatractus universus* Zone (between 0.4 and 0.9 Ma) is due to the absence of *S. universus*. Eleven radiolarian datums derived in the subarctic Pacific were identified at this site.

All samples contain poorly to well-preserved palynomorphs. The concentration of terrestrial palynomorphs is low to moderate in most samples. Freshwater palynomorphs (*Pediastrum*, *Botryococcus*, and tintinides) occur only in the upper part of the sequence from 42 to 186 m CSF. Reworked palynomorphs are generally accompanied by a high number of wood microfragments. Very abundant dinoflagellate cysts occur only in the uppermost 200 m CSF and lower abundance occurs below. The LO of *Filisphaera filifera* (1.7 Ma) was determined at 216 m CSF. The Gonyaulacale *Operculodinium centrocarpum* co-dominates the assemblage together with *Brigantedinium* spp. in the core catcher samples from the uppermost cores. *O. centrocarpum* is closely related to seasonal sea ice cover. All accompanying taxa except extinct species (*Filisphaera filifera* and *Batiacasphaera minuta*) are known to be abundant in polar and circumpolar regions.

Paleomagnetism

The inclinations measured in Site U1340 sediments average almost 70° over the entire depth range of the cores. The site axial dipole inclination is ~72°. Several distinct intervals of reversed inclinations are interpreted to be polarity epochs. The declinations, after correction with the FlexIt tool to orient the declination data with North, suggest that there are multiple polarity intervals in the uppermost 17 cores from Hole U1340A; however, the FlexIt corrections are too poor to be of much detailed use in assigning polarity boundaries. The inclinations provide an initial guide to polarity zonation in Hole U1340A; we could discern the Brunhes, Jaramillo, Olduvai, and Gauss normal polarity chrons (Fig. **F25**). Polarity boundaries and paleontological age estimates are generally in agreement (Fig. **F26**).

The NRM intensities largely remain at the same level throughout most of Hole U1340A. The NRM and Chi intensities vary over more than an order of magnitude on a meter scale. We interpret this to stem mostly from variable flux of detrital sediment versus biogenic sediment flux (mostly diatoms at this site). The large changes in NRM intensity also appear to be associated with notable detrital (and presumably magnetic) grain size changes. Both of these variations make the relative paleointensity estimates, determined by normalizing the cleaned NRM (20 mT) by magnetic susceptibility, questionable in interpretation. The relative paleointensity variability is quite large, but most of it is strongly correlated with NRM and magnetic susceptibility variability and is probably not due mostly to geomagnetic field variability. As at our last site, we see no notable evidence for the presence of magnetic field excursions in any of the cores.

Stratigraphic correlation

The composite depth scale and splice at Site U1340 is complete from 0.0 to 47.7 m CCSF-A (Tables **T8, T9**). This splice is tentative because of some evidence for soft-sediment deformation in some of the cores based on observed sedimentary structures, data features that do not appear to correlate between holes, and in some cases sections that appear repeat within a single hole. An interval that contains a distinctive pink ash appears to be present three times in Hole U1340C: twice in Core 323-U1340C-2H and once in Core 3H. This appearance of the same sedimentary interval at different subseafloor depths as well as the replication of a section within a single hole is consistent with visual evidence for tilted beds and nonconformable surfaces. We suggest that sediment deformation has produced thickened and noncorrelative intervals in the depth interval from ~20 to ~45 m CCSF-A in Holes U1340B and U1340C and perhaps also in Holes U1340A and U1340D. We are not confident that the full sedimentary sequence is represented in the composite splice. We tentatively splice Core 323-U1340B-4H as the bottom interval of the splice, which includes the least disturbed intervals through the interval of inferred slumping. Affine growth factors in the spliced interval have values of 1.14 in Hole U1340A and 1.18 in Hole U1340B, which are within the normal range typical of many drill sites. The remaining cores at Site U1340 are not tied to the splice but are appended to the bottom of the splice with a constant affine value of 7.31.

Geochemistry

In Hole U1340B, nine interstitial water samples ranging from 2.9 to 53.3 m CSF were retrieved by the whole-round squeezing technique. Interstitial water chloride concentrations varied between 528 and 570 mM, but downhole salinity remained constant at 36. Alkalinity increased from 2.9 to 18 m CSF, whereas only a subtle increase was seen below. DIC showed a similar trend as alkalinity with a maximum concentration at 42.3 m CSF. pH remained unchanged throughout, averaging 7.7. The dissolved sulfate concentrations slightly decreased. Hydrogen sulfide was detected at low concentrations, averaging 4.4 µM. Ammonium concentrations increased as depth increased. Phosphate concentrations gradually increased throughout the uppermost ~12 m, followed by a gradual decrease to 53 m CSF.

Methane was the only hydrocarbon gas detected in Holes U1340A and U1340B. Concentrations of methane in Holes U1340A and U1340B ranged from 0 to 3.1 ppmv and from 2.2 to 6.6 ppmv, respectively. Ethane and other volatile hydrocarbons were not detected. Fourteen core catchers from Hole U1340A were used for the preliminary analysis of solid-phase total inorganic carbon (TIC), TOC, total nitrogen, and total sulfur. Calcium carbonate contents in Hole U1340A ranged from 0 to 3.6 wt%. A part of increased $CaCO_3$ contents between 300 and 400 m CSF corresponds to the intervals where authigenic dolomite and calcite were observed in sediments. Because of the presence of authigenic carbonates at this site, carbonate-stable isotope measurements are potentially contaminated by the isotopic signature of the overgrowths. However, the presence of authigenic carbonates can be detected and screened out of the isotopic records. TOC and total nitrogen contents range from 0.25 to 1.19 wt% and from 0.02 to 0.09 wt%, respectively. TOC decreased below 400 m CSF. Total sulfur contents ranged from 0.09 to 0.42 wt%. Undetectable methane, deep SO_4^{2-} penetration, and low values of DIC, alkalinity, NH_4^+, and PO_4^{3-} suggest extremely low microbial activity compared to Site U1339 despite similar TOC content.

Microbiology

Samples for abundance of prokaryotes were collected adjacent to interstitial water whole-rounds at the same resolution. Samples were fixed for further shore-based analyses.

Physical properties

Cores from all holes were placed on the fast or Special Task Multisensor Logger (STMSL) track and scanned for magnetic susceptibility and GRA bulk density and on the WRMSL for GRA, magnetic susceptibility, and *P*-wave scanning. Because of noisy data, noncontact resistivity values were not recorded. *P*-wave velocity and sediment shear strength measurements were not determined on working section halves. Magnetic susceptibility values spike irregularly, with values ranging from 500 to 1300 SI units in the uppermost 250 m CSF, but values were relatively low and invariant below ~250 m CSF until 525 m CSF, when they increased sharply to above 1000 SI units, registering a thick tephra unit. Bulk density determinations reveal high excursions and an apparent rhythmic pattern of higher values alternating with lower ones. The average reading in the tephra-bearing diatom silt of Unit I (surface to ~360 m CSF) is ~1.4 g/cm^3. Within Unit I, bulk density decreases with depth to ~1.38 g/cm^3 at ~360 m CSF. Below ~384 m CSF and a shift to XCB coring, values lowered additionally to ~1.32 g/cm^3. In Hole U1340A, NGR counts/s, which principally reflect clay mineral abundance, decrease with depth from near-surface readings averaging ~20 counts/s to ~10 counts/s at ~380 m CSF and below. Presumably the downhole decrease in NGR counts reflects increasing relative abundance of siliceous biogenic tests and debris of lithologic Unit II.

The *P*-wave velocity profile for Hole U1340A is variable but generally increases from a near-surface velocity of ~1.52 to ~1.55 km/s at ~280 m CSF. This section corresponds to lithologic Unit I. In the underlying Unit II, and in particular below the transition from APC to XCB coring at ~384 m CSF, average *P*-wave readings exhibit only a subtle continuation of a downsection increase in velocity of ~10 m/s (from ~1.55 to ~1.56 km/s) at the bottom of Hole U1340A (~604 m CSF), possibly because the diatomaceous ooze section of Unit II that included tephra beds is mechanically stronger and less yielding to compaction than the overlying diatomaceous silt beds of lithologic Unit I.

The depth distribution of MAD wet bulk density is similar to that traced by the WRMSL GRA sensor. The MAD profile documents a slight downhole trend of decreasing density from ~1.42 g/cm^3 near the seafloor to ~1.40 g/cm^3 at ~360 m CSF. Below this depth, which marks a switch to XCB drilling and a ~25 m thick section of poor core recovery (~360 to 384 m CSF), a low average density of ~1.32 g/cm^3 is recorded. However, bulk density increases farther downhole to ~1.4 g/cm^3 at the bottom of Hole U1340A at ~604 m CSF. Perhaps a water-rich and partially load-bearing section signaled by the recovery of gravelly and sandy beds in the upper part of lithologic Unit II separates the upper decreasing and lower increasing trends in bulk density.

Porosity and water content profiles in Hole U1340A are similar and exhibit three contrasting trends. For porosity, the upper trend from seafloor to ~350 m CSF displays an average value near 74% that remains virtually constant with depth. The middle trend, which begins below the transition from APC to XCB drilling at ~384 m CSF and the zone of poor recovery from ~360 to 384 m CSF, documents a shift to a higher average porosity value near 80%, below which the average decreases progressively to ~66% at ~550 m CSF. Porosity measurements decrease to ~75% at the base of Hole U1340A at ~604 m CSF (Fig. F22). Hydraulically, the middle porosity sections appear to be separated from the upper ones by a permeability barrier in the zone of poor core recovery between ~360 and 384 m CSF. This inferred barrier occurs at the level of a gravel-bearing sequence within the diatom ooze section of lithologic Unit II. Isolation of the middle trend from the basal one is coincident with lithologic Unit III, a coarse ashy layer overlying the diatom ooze of Unit IV.

The average grain density decreases downsection from near-surface values of ~2.61 g/cm^3 to ~2.5 g/cm^3 at the bottom of Hole U1340A at ~604 m CSF. Wide excursions, some of which are so low (<1.5 g/cm^3) or high (>2.9 g/cm^3) that measuring error is suspected, occur about the mean, which is ~2.45 g/cm^3. The downsection decreasing values appear to reflect an increase in biogenic silica (chiefly diatom frustules) with respect to terrigenous mineral debris and tephra.

Downhole measurements

The measured temperatures ranged from 5.67°C at 70.4 m DSF to 9.79°C at 165.4 m DSF, and they closely fit a linear geothermal gradient of 43.4°C/km. The temperature at the seafloor was 2.8°C based on the average of the measurements at the mudline during all the APCT-3 deployments. A simple estimate of the heat flow can be obtained from the product of the geothermal gradient by the average thermal conductivity (0.851 W/[m·K]), which gives a value of 36.9 mW/m^2, within the range of previous measurement in the area. Alternatively, if the thermal regime is purely conductive, then the resulting linear fit of the temperature gives a slightly higher heat flow value of 37.8 mW/m^2.

Sedimentation rates

Sedimentation rates in the upper Pleistocene section appear to be 13–17 cm/k.y. (Fig. **F26;** Table **T10**). However, below ~30 m CSF there is evidence of soft-sediment deformation, which could have caused postdepositional thickening of the section. From ~150 m CSF to ~330 m CSF, sedimentary structures indicative of deformation were almost completely absent and the sedimentation rate was 15–24 cm/k.y. Below 330 m CSF to ~500 m CSF the sedimentation rate was as high as 32 cm/k.y. From ~500 m CSF to the bottom of the hole the sedimentation rates appeared to be quite low (~4 cm/k.y.)

Site U1341

Background and objectives

The primary objective of drilling at Site U1341 (prospectus Site BOW-14B) was to study high-resolution Pliocene–Pleistocene paleoceanography in the southern part of the Bering Sea at a western flank location of Bowers Ridge. Previous DSDP coring (Site 188) and other piston core studies in the region documented relatively high sedimentation rates of 100–138 m/m.y., respectively, and the presence of appropriate microfossils for paleoceanographic studies. Bowers Ridge is well situated to allow study of the past extent of water mass exchange with the Pacific Ocean through the adjacent Aleutian passes such as Amukta, Amchitka, and Buldir passes. In particular, its location allows for examination of the influence of the warm Alaskan Stream water mass entry into this region and presumable impact the distribution of past sea ice coverage. Although the productivity in the Bering Sea in general is very high with respect to other parts of the global oceans (Takahashi et al., 2002), the expected productivity at this site is lower than at Site U1339, which experienced substantially greater influence from the adjacent Bering shelf, which was subaerially exposed during the glacial low sea level stands. Drilling at this site—located at a relatively deep water depth of 2177 m—provides us with past intermediate water conditions, including chemical compositions. For example, this site is located just below the modern dissolved OMZ, which causes the formation of laminated sediments. Slight fluctuations in the intensity or depth of the OMZ should be captured by proxy records of past oxygenation measured at this site and compared to other, shallower sites. This site and the shallower drill sites at Bowers Ridge (Site U1340, water depth = 1295 m; Site U1342, water depth = 819 m) will be used to compare the vertical extent of water mass conditions.

This drill site at Bowers Ridge also allowed for study of the impact of subseafloor microbes on biogeochemical fluxes in the highest surface ocean productivity areas of the drill sites in the Bering Sea. Organic-fueled subseafloor respiration and its impact on biogeochemistry in such a highly productive region has not previously been quantified. To do this, sediments drilled at Bowers Ridge were used to determine subseafloor cell abundances and then subjected to intensive geochemical analysis to investigate the link between the mass and characteristics of subseafloor microbes and the extent of export productivity from the surface ocean.

Site U1341 is located on the western flank of the central part of Bowers Ridge (Fig. **F20**) in a depression (Fig. **F27**) ~40 km west of the ridge crest. Close-ups of the seismic images in the basin (Figs. **F27, F28, F29, F30**) indicate that strata dip gently to the west (Figs. **F27, F29**). Some shallow sections do not have continuous parallel strata, but most of the rest of the section appears to have continuous features in the seismic images (Figs. **F29, F30**). The basement age and the age of the deeper sediments are unknown, but at DSDP Site 188 on the western flank of Bowers Ridge (Scholl and Creager, 1973) sediments as old as upper Miocene were found. Specifically, Scholl and Creager (1973) found recent to upper Miocene diatomaceous silt as well as diatom ooze interbedded with silt-rich diatom ooze. They also found calcareous nannofossils in the uppermost 120 m and planktonic foraminifers in the uppermost 300–400 m. In the interval between 580 and 638 m they encountered mudstone. They reported sedimentation rates of ~100 m/m.y. A piston core study from the same general region provided a sedimentation rate of 138 m/m.y. (Takahashi, 2005), permitting the study of high-resolution paleoceanography. Thus, prior to drilling, recovery of Pleistocene to Pliocene sections was expected.

Lithostratigraphy

Three holes were drilled at Site U1341; the deepest, Hole U1341B, reached 604.5 m CSF. The sediments recovered are a mix of biogenic and siliciclastic sediments, whereas volcaniclastic material was of minor importance, perhaps reflecting the more distal location of Site U1341 to the Aleutian arc. The most abundant terrigenous grain types are silt-sized feldspar, quartz, clay, mica, and rock fragments. Some pebbles are composed of basalt, pumice, or scoria, indicating a volcanic source. Dolostones and micrometer-scale crystals of dolomite occur in high concentrations at various depths but particularly at the bottom of Hole U1341B. Authigenic carbonate patches, nodules, and layers are light olive-gray and olive-gray and often characterized by a granular texture and a stronger induration than the surrounding sediments. Because of the presence of authigenic carbonates, carbonate-stable isotope measurements in sediments from this and other sites where authigenic carbonates occur are potentially contaminated by the isotopic signature of the overgrowths. However, the presence of authigenic carbonates can be detected and screened out of the isotopic records. Sediment composed of siliciclastic sediment or mixed lithologies tends to be very dark greenish gray to dark gray, whereas diatom ooze tends to be dark gray to olive-gray to light olive. Boundaries between different sediment colors and/or lithologies are dominantly gradational and bioturbated, but occasional sharp contacts occur as well. Sharp contacts are occasionally coeval with distinct changes in magnetic susceptibility, with higher values corresponding to mixed biogenic-siliciclastic sediments and lower values corresponding to diatom ooze. Intervals with thin, distinct parallel laminations were relatively rare and confined to the upper part of the record (0–20 m CSF). At lower depths, thickly laminated to thinly bedded material with wavy boundaries occurred more frequently. Site U1341 sediments are indicative of low oxygen conditions, as implied by the decrease in the benthic foraminifer diversity index below 200 m and by the occurrence of laminated intervals throughout the cores. Also, today an OMZ impinges on parts of the western Bowers Ridge.

Two lithologic units were defined at Site U1341 by a change from alternating diatom silt, diatom clay, and diatom ooze to solely diatom ooze (Fig. **F31**). The boundary between the two units, dated at 1.6 Ma, is paralleled by a significant change in the intensity of the magnetic susceptibility record (208 m CSF in Hole U1341B), in the abundances of calcareous tests, and in interstitial water pH and Ca values. The two units are further divided into Subunits IA to ID and Subunits IIA to IIE, respectively.

Whole-round density (GRA) (Fig. **F31**) correlates well with the abundance of diatoms recorded in smear slide data, with a high percentage of diatoms correlating with low GRA values and low siliciclastic components. Diatom ooze may reflect interglacial conditions, whereas mixed diatom-siliciclastic lithologies may reflect glacial conditions. This is consistent with the pattern of biogenic opal MARs observed in piston cores from the Bering Sea. Interestingly, sediment intervals rich in nannofossils were observed at this site.

Biostratigraphy

Core catcher samples from Site U1341 are dominated by highly diverse diatoms together with radiolarian, calcareous nannofossil, foraminiferal, and organic-walled microfossils with medium to high diversity and preservation ranging from moderate to very good. Biostratigraphic datums are derived from diatom, radiolarian, dinoflagellate, ebridian, silicoflagellate, and calcareous nannofossil bioevents and show that Site U1341 contains early Pliocene to Pleistocene sediments (Table **T11;** Fig. **F31**). However, the presence of early Pliocene species indicates that some reworking has occurred within the uppermost ~20 m.

Cores from Holes U1341A and U1341B exhibit a broadly linear sedimentation rate. Siliceous microfossils show consistent occurrences throughout the section and are mainly composed of high-latitude pelagic species, indicating changes to surface water productivity. Calcareous microfossils are mostly confined to the top of sections from cores at ~250 m CCSF-A for nannofossils and 280 m CCSF-A for planktonic foraminifers. Thereafter, only sporadic occurrences of calcareous fossils and calcareous cemented agglutinated foraminifers are detected, which may be linked to changes in preservation. Benthic foraminifers are largely characteristic of those found within or near the OMZ in high-latitude regions. Dinoflagellates consistently occur throughout the section, indicating changes to the productivity and ice cover of the surface waters.

Calcareous foraminifers and nannofossils show greatest preservation in the upper part of the section from ~240 m CCSF-A. This broadly coincides with the greatest abundances of sea ice diatoms and radiolarians living in cold and oxygen-rich intermediate water masses. As the preservation of carbonate in deep-sea sediments is hindered by high productivity and associated low oxygen in the bottom waters, productivity may have been reduced by a direct seasonal sea ice coverage and an enhanced stratification. Sea ice diatoms, intermediate water–dwelling radiolarians, and calcite preservation all increase markedly again at ~110 m CCSF-A.

The first occurrence datum of *Emiliania huxleyi* at 0.29 Ma provided the zonal assignment of calcareous nannofossil Zone NN21 in the upper section of this site. Calcareous nannofossil Zone NN20 and the top of calcareous nannofossil Zone NN19 can only be well constrained in Hole U1341C, establishing an age older than 0.44 Ma.

The late Pleistocene fauna at Site U1341 is dominated by *Neogloboquadrina pachyderma* (sinistral) and reflects late Pleistocene cooling. Additional fauna are the subpolar species *Globigerina bulloides*, *Globigerina umbilicata*, and *Neogloboquadrina pachyderma* (dextral), which appear in low numbers. Around 2.5 Ma only the subpolar species are present. Around 60 species of benthic foraminifers were recovered in 140 samples from three holes at this site. Assemblages in the top of the section from Sample 323-U1341B-11H-CC are of relatively high diversity and abundance and show affinities to assemblages within or near the OMZ in the Sea of Okhotsk and also more common deepwater Pacific Ocean species. In the remainder of the holes foraminifers become less abundant and the agglutinated species *Eggerella bradyi* and *Martinottiella communis* become more important components of the assemblages.

Cores above 41.2 m CSF in Hole U1341A are assigned to the *Neodenticula seminae* Zone (0.3 Ma and younger). This datum was closely matched in Hole U1341B at 37.7 m CSF. The following age of 0.9 Ma in Hole U1341A is defined by the LCO of *Actinocyclus oculatus* at 79.6 m CSF. The top of the *A. oculatus* Zone is constrained by the LCO of *Neodenticula koizumii* (1.7 ± 0.1 Ma). The LCO of *Neodenticula kamtschatica* at 366.2 m CSF in Hole U1341B defines the base of the next biostratigraphic zone at 2.7 ± 0.1 Ma. The age of 3.9 Ma is assigned between 458.3 and 458.8 m CSF by the FO of *N. koizumii*.

The LO of silicoflagellate *Dictyocha subarctios* was found between 50.95 and 60.41 m CSF in Hole U1341A. The LO of ebridian *Ammodochium rectangulare*, with the age of 1.9 Ma, was assigned to 233.21–241.4 m CSF in Hole U1341A and 228.52–238.11 m CSF in Hole U1341B. The LO of ebridian *Ebriopsis antiqua antiqua* was found between 328.09 and 332.81 m CSF in Hole U1341A and between 325.83 and 335.28 m CSF in Hole U1341B. The LO of silicoflagellate *Distephanus jimlingii* lies between 332.71 and 342.26 m CSF in Hole U1341A and between 335.18 and 345.78 m CSF in Hole U1341B. Silicoflagellate assemblages were mainly composed of *Distephanus speculum*, *Distephanus medianoctisol*, and *Distephanus octonarius* in most core catcher samples in both holes.

The radiolarian stratigraphy at Site U1341 spans from the *Botryostrobus aquilonaris* Zone (upper Quaternary) to the *Dictyophimus bullatus* Zone (middle Pliocene) in the subarctic Pacific. At the bottom of Hole U1341B, the LO of *Dictyophimus bullatus* (3.8–4.0 Ma) is identified by the occurrence of several specimens of the species. Changes in abundances of *Cycladophora davisiana* intermediate water–dwelling species showed antiphase patterns with abundances of calcareous microfossils (calcareous nannoplanktons and planktonic foraminifers) in each hole of Site U1341. This suggests the relationship between intermediate water formation in the subarctic Pacific and carbonate preservation. *Cycladophora sakaii* is thought to be an ancestor species of *Cycladophora davisiana*. Occurrences of *Cycladophora sakaii* were very low at Site U1340 (water depth = ~1300 m). On the other hand, *Cycladophora sakaii* was consistently found below the 1000 m interval at Site U1341 (water depth = ~2200 m), implying *Cycladophora sakaii* dwelled mainly in deep water below 1000 m water depth.

The polar and subpolar dinoflagellate taxa *Islandinium minutum*, *Operculodinium centrocarpum* (arctic morphotype), and *Impagidinium pallidum*—which are known to be abundant in regions where sea ice cover occurs up to 12 months per year and winter sea-surface temperature is <0°C—occur only in the upper part of the sequence starting at ~371 m CSF. Below 300 m CSF the diversity decreases and the assemblages are dominated by the Protoperidinial *Brigantedinium* spp. and *Trinovantedinium variabile* or by the extinct species *Filisphaera filifera*. *T. variabile* appears below 300 m CCSF-A and dominates the assemblage of Sample 323-U1341A-60X-CC.

Paleomagnetism

Archive halves of all APC cores recovered at Site U1341 were measured on the three-axis cryogenic magnetometer at 2.5 cm intervals. NRM was measured before (NRM step) and/or after stepwise alternating-field (AF) demagnetization (demagnetization step) in peak fields of up to 20 mT. Cores 323-U1341A-1H through 12H and Sections 323-U1341C-5H-3 through 11H-5 were measured at NRM step and 20 mT demagnetization step; other cores from Site U1341 were measured only at 20 mT demagnetization step to maintain core flow. The obtained inclinations average nearly 70° over the entire depth range of the cores, whereas the site axial dipole inclination is ~72°. The inclinations show several distinct intervals of reversed inclinations that we interpret to be polarity epochs (Table **T11;** Fig. **F31**). The declinations, after correction with the FlexIt tool to orient the declination data with North, suggest that there are multiple polarity intervals in the uppermost 17 cores in Holes U1341A and U1341B. The FlexIt tool appears to show the declination change of ~180° at the Brunhes/Matuyama boundary in Hole U1341A but it does not seem to identify older polarity changes (Jaramillo onset or termination) or the Brunhes/Matuyama boundary in Hole U1341B. Within the Matuyama reversed polarity interval, approximately a dozen previously identified excursions are discernible. Relative paleointensity variations (Chi or INT/Ms) show good correlation with benthic foraminifer diversity related to dissolved oxygen contents of the bottom waters. This indicates that extensive reducing conditions near the sediment/water interface, especially in the lower half of the hole, were responsible for the degradation of paleointensity.

Geochemistry

Undetectable methane, deep SO_4^{2-} penetration, and low values of DIC, alkalinity, NH_4^+, and PO_4^{3-} suggest low present-day microbial activity compared to Site U1339 despite similar TOC contents (Fig. **F32**). Preliminary model estimates based on the measured DIC profiles suggest that microbial respiration at Site U1341 in the uppermost 30 m is ~20% of the activity estimated for Site U1339. This difference may partly be attributed to differences in sedimentation rates. The major metabolic pathway in the sections studied is organoclastic sulfate reduction, and according to the DIC, alkalinity, and sulfate profiles this process is mainly confined to the upper 30 m.

The most striking feature of Site U1341 is the unusual shape of the DIC, alkalinity, and phosphate profiles as well the pattern of the SO_4^{2-} profile (Fig. **F32**). DIC, phosphate, and alkalinity profiles indicate either nonsteady state caused by recent changes in microbial activity or unusually high net consumption of DIC and PO_4^{3-} in strata below 50 m. The SO_4^{2-} profile suggests a curiously high net consumption in the 300–400 m depth interval despite the lack of CH_4 and the presence of a presumable, rather refractory, organic carbon pool. It is possible that the interstitial water chemistry still to a large extent shows the overprint by past events such as sulfate removal by extreme high rates of organic matter mineralization during high productivity periods. The present-state interstitial water chemistry thus reflects the transition toward a new steady state.

Microbiology

Seventy-three microbiological samples were collected adjacent to interstitial water whole-rounds for postcruise analyses for abundance of prokaryotes.

Physical properties

The uppermost ~210 m CSF of the sediment section at Site U1341 exhibits rapid single-point excursions to readings >200–400 SI units of whole-core magnetic susceptibility measurements. Below this depth magnetic susceptibility readings are subdued and rapid deflections to values >100 SI units are uncommon except at ~575 m CSF, where a broad band of high susceptibility occurs between 565 and 575 m CSF. The upper section of rapidly varying and high values is coincident with lithologic Unit I. Although ash layers occur in this unit, they are equally abundant in the underlying Unit II, which displays only background variations in readings. The contrast in the profiles of magnetic susceptibility readings between Units I and II is thought to reflect the occurrence in the diatom silt of Unit I of presently unidentified alteration products having magnetic susceptibility properties.

The GRA sensor records a trend of slightly decreasing average values of wet bulk density from a near-surface reading of ~1.35 g/cm³ to ~1.32 g/cm³ at the base of Hole U1341B at ~605 m CSF (Fig. **F31**). At ~220 m CSF, which is below the transition from Unit I to Unit II, a discernible but small shift to lower density near ~125 g/cm³ is evident. The entire vertical profile of bulk density undulates broadly from average values of ~1.30 g/cm³ to ~1.45 g/cm³. The wavelength of fluctuations narrows downhole. Measurement of *P*-wave velocity by the slow track WRMSL documents a downhole trend of increasing velocity. The gradient of average *P*-wave velocity values ranges from ~1.51 km/s for near-surface sediment to ~1.56 km/s at the base of the hole at 605 m CSF. A slight shift to lower readings (0.02 km/s) appears to occur across the transition from lithologic Unit I to Unit II. The low overall gradient in downhole velocity, which is estimated at only 0.08 km/s/km, demonstrates the ability of diatomaceous sediment to resist compaction.

Downhole NGR readings show spiking to high values >40 counts/s above an undulatory and generally decreasing trend of values from near-surface averages of ~15 counts/s to less than ~5 counts/s at the base of Hole U1341B (Fig. **F31**). A shift to slightly lower values is just perceptible near the boundary between Units I and II. The implication of the overall decreasing trend and broad superimposed oscillations is that the clay mineral content decreases irregularly downhole, an interpretation that is consistent with the decreasing terrigenous content of the drilled section from the diatom silt of Unit I to the dominantly siliceous ooze of Unit II.

The MAD downhole trend clearly reveals the contrasting density characteristics of the diatom silt of lithologic Unit I and the siliceous microfossil ooze of Unit II. The sediment in Unit I shows a higher fluctuation in values ranging from 1.62 to 1.2 g/cm³ superimposed on a perceptible but slight increase with depth to the unit's boundary with underlying Unit II. The lower overall bulk density of Unit II appears to reflect a higher concentration of low-density siliceous microfossils than that found in the diatom silt of overlying Unit I. Just beneath the surface, porosity values average ~80% and the corresponding water content is ~60%. At the bottom of Hole U1341B water content decreases only slightly to ~58% and, correspondingly, porosity decreases to ~75%. Similar to the depth profiles of most other physical properties, the downhole distribution of sediment porosity exhibits undulations or excursions to higher and lower values. The downhole variation in grain density is prominently offset, from an average density of ~2.39 g/cm^3 to 2.23 g/cm^3 at the boundary between Units I and II. The average density also decreases with depth from a near-surface value of ~2.50 g/cm^3 to as low as 2.10 g/cm^3 at the base of Hole U1341B. These trends are interpreted as tracking the downhole increase in relative abundance of low-density diatoms. The depth distribution of thermal conductivity decreases overall from a near-surface value of 0.85 W/(m·K) to 0.80 W/(m·K) at the base of Hole U1341B. This profile thus parallels the downhole decreasing values of most other physical properties measured on cores recovered in Hole U1341B.

Stratigraphic correlation

The composite depth scale and splice at Site U1341 is constructed from 0.0 to 374.40 m CCSF-A (Tables **T12, T13**). The splice consists of one continuous splice from the mudline to 141.30 m CCSF-A and two appended "floating" splices, the first from 141.3 to 326.43 m CCSF-A and the second from 326.44 to 374.40 m CCSF-A. The continuous splice ranges from the top of Core 323-U1341A-1H to Section 323-U1341B-14H-7, 88 cm. The first floating splice ranges from Section 323-U1341B-15H-1, 0 cm, to Section 323-U1341A-34H-7, 64 cm. The second floating splice ranges from Section 323-U1341A-35H-1, 0 cm, to the base of Section 323-U1341B-39H-7. These appended intervals are supported by wireline logging data compared to core logging of natural gamma radiation. Additional cores below the splice are included in the composite depth framework by appending them with a constant affine value specific to each hole.

The cumulative offset between CSF and CCSF-D depth scales is approximately linear. The affine growth factor (a measure of the fractional stretching of the composite section relative to the drilled interval) at Site U1341 is 1.06 between 0 and 374.4 m CSF. Cores deeper than the spliced interval, that is, Cores 323-U1341A-41H and 323-U1341B-40H through 71X, are not tied to the splice but are appended with a constant affine value of 19.95. MARs in this interval should not be divided by the affine growth factor because their depths are a linear transformation of drilling depths.

Downhole measurements

Two downhole logging tool strings were deployed in Hole U1341B to the total depth of 600 m DSF (2750 m drilling depth below rig floor [DRF]): the triple combo and the FMS-sonic combination. Overall, the caliper of the density sonde on the triple combo tool string indicated an enlarged and irregular borehole with many intervals with hole diameter >20 inches. During the runs, the tool encountered significant drag in many places above 260 m wireline log depth below seafloor (WSF), producing a stick-slip motion that was detrimental to the quality of the data. As a result, the logging speed was increased from 900 ft/h to 1200 ft/h, and the tools were reconfigured to prevent any impact on the vertical resolution of the data.

The readings of the two orthogonal FMS calipers suggest that the borehole section was far from circular, probably elliptical. One caliper read <10 inches over most of the lower half of the interval logged, while the other one kept close to ~14 inches, near the limit of its range. The fact that the curves display variability over most of the hole suggests that both sets of arms were making some kind of contact with the formation, possibly with one pad only in some places. The larger Hostile Environment Litho-Density Sonde (HLDS) caliper readings show that this single-arm caliper was likely following the longest axis of the hole and that the stronger and skinnier arm was actually pushing inside the formation.

The large hole size had an effect mostly on measurements that require good contact with the formation, namely density and porosity. The very high neutron porosity values above ~275 m WMSF indicate that porosity readings are erroneous above this depth. Similarly, the anomalously low density values between 180 and 210 m WMSF also indicate poor tool contact and are also erroneous. Even if the FMS arms seem to have been in contact with the formation over most of the interval logged, this contact was likely only partial in places, resulting in blurry or featureless images in many intervals. It is still possible to identify many fine layers, mostly in the deeper part of the hole.

Logging Unit 1 (80–220 m WMSF) is characterized mainly by decreasing trends with depth in gamma radiation and resistivity, accompanied with several high peaks in these measurements (Fig. F33). It coincides mostly with lithologic Unit I, which consists of diatom ooze and diatom silt. Most of the peaks in gamma radiation are related to high uranium content. The coincidence of these higher uranium values with higher resistivity, and to some extent with higher density, is an indication that they are due to authigenic carbonate, which was observed at many of these depths. Logging Unit 2 (220–350 m WMSF) is defined by increasing trends with depth in gamma radiation and density measurements, whereas resistivity mostly decreases. Several peaks in gamma radiation can be observed in this unit as well, again generally due to higher uranium content and often associated with authigenic carbonate observed in the core. The top of logging Unit 3 (350–425 m WMSF) is defined by a sharp drop in density at ~350 m WMSF and by similar changes in gamma radiation and density. Because velocity does not display any significant change at this depth, the change in density is likely responsible for the strong reflector that can be observed in seismic Line Stk5-1 at 3340 ms two-way traveltime. The top of logging Unit 4 (425–600 m WMSF) is defined by a drop in resistivity, which decreases with depth over the entire unit. It coincides also with an inflection in the overall increase with depth of shear velocity and, to a lesser extent, of compressional velocity.

Formation temperature measurements were successfully made with the APCT-3 tool at three depths in Hole U1341A. The measured temperatures ranged from 4.68°C at 41.0 m DSF to 11.12°C at 136.0 m DSF and closely fit a linear geothermal gradient of 67.8°C/km. The temperature at the seafloor was 1.95°C based on the average of the measurements at the mudline during all the APCT-3 deployments. A simple estimate of the heat flow can be obtained from the product of the geothermal gradient by the average thermal conductivity (0.825 W/[m·K]), which gives a value of 55.9 mW/m^2, within the range of previous measurement in the area.

Age model and sedimentation rates

Only two relatively deep holes in Expedition 323 reached the bulk of the Pliocene age: Holes U1340A (cored to 604.6 m CSF) and U1341B (cored to 600.0 m CSF). Stratigraphic efforts using diatoms, silicoflagellates, ebridians, radiolarians, and paleomagnetism were employed to determine a correct age model; however, this method proved difficult. Among the many parameters examined on board the R/V *JOIDES Resolution*, the percentage counts of three species of abundant diatoms—*Neodenticula kamtschatica*, *Neodenticula koizumii*, and *Neodenticula seminae*—were very useful in constructing tie points between the two holes in question.

The total percentage of each of these species exceeds 50% during the Pliocene (Fig. **F34**). Because of their high abundances, higher reliability on the tie points was given to their rapid increase (RI) or rapid decrease (RD) than was given to the LO or FO of taxa with only a single or few specimen counts (Fig. **F35**). These taxa were interpreted to have occurred to a similar extent at about the same times because Holes U1340A and U1341B are not too far apart in the Bowers Ridge region. Detailed compilation of all the pertinent biostratigraphic and paleomagnetic datums clearly suggests that the tie points are more or less in agreement, with the exception of *Ebriopsis antiqua antiqua,* whose abundance is very rare (Fig. **F35**). Especially note that the agreed paleomagnetic datums are in line with the tie points illustrated. Six reliable tie points were assigned from the Pliocene and Pleistocene section: the FO of *N. koizumii*, the top of the Gauss, the RI of *N. seminae*, the bottom of the Jaramillo, the top of the Jaramillo, and the Brunhes/Matuyama boundary (Fig. **F35**).

Sedimentation rates in the upper Pleistocene section appear to be 10–11 cm/k.y. (Fig. **F36;** Table **T14**). During the Jaramillo the sedimentation rate is very high, 46 cm/k.y., but more work is needed to refine the depth of the polarity reversals at the top and bottom of the Jaramillo. Below ~150 m CCSF-A sedimentation rates are at 15 cm/k.y. until the top of the Gauss at 368 m CCSF-A. Below that depth the sedimentation rate is 9 cm/k.y. These age model and sedimentation rate estimates may be altered with postcruise research.

Site U1342

Background and objectives

The primary objective of drilling at Site U1342 (prospectus Site BOW-15A) was to study high-resolution Pliocene–Pleistocene paleoceanography at a relatively shallow water depth on Bowers Ridge, where relatively low sedimentation rates were observed in an earlier site survey piston core study (Takahashi, 2005). Bowers Ridge is well situated for study of the past extent of water mass exchange with the Pacific Ocean through adjacent Aleutian passes such as Amukta, Amchitka, and Buldir passes (Figs. **F37, F38, F39, F40**). As with the other Bowers Ridge sites, the record of changes in the flow of the warm Alaskan Stream water mass into the Bering Sea and its impact on the distribution of past sea ice coverage is of particular interest.

A previous site survey piston core study found more open water conditions during the LGM at Site BOW-8A, which is practically the same location as Site U1342, than at Site BOW-12A near the ridge crest at the location of Site U1340. Although productivity in the Bering Sea in general is very high with respect to other parts of the global oceans, the expected productivity at this site, along with the other Bowers Ridge sites, is lower than at Site U1339 on Umnak Plateau, which experiences substantially greater influence from the adjacent Bering Sea shelf. Site U1342, with its relatively shallow water depth of 818 m, serves as the shallow end site in comparison to the other Bowers Ridge sites (Site U1340, water depth = 1295 m; Site U1341, water depth = 2140 m); therefore, Site U1342 provides an important constraint on the intensity and depth of the water column OMZ. A previous site survey piston core study reported sedimentation rates of ~32 m/m.y., and Pliocene-age sediments at the bottom of the sedimentary section are expected.

This drill site at Bowers Ridge can also be used to study the impact of subseafloor microbes on biogeochemical fluxes. Organic-fueled subseafloor respiration and its impact on biogeochemistry in such a highly productive region has not previously been quantified. To do this, sediments drilled at Bowers Ridge will be used to determine subseafloor cell abundances and to investigate the link between the mass and characteristics of subseafloor microbes and the extent of export productivity from the surface ocean (Takahashi et al., 2000, 2002). Compared to the other Expedition 323 drill sites where detailed microbiological studies have occurred, Site U1342 is expected to have lower (but still high) surface ocean productivity. As such, because of its more open ocean location farthest away from the high-productivity zone of the shelf, Site U1342 serves as the low-productivity end-member of the expedition's microbiological study.

Lithostratigraphy

The sediments recovered at Site U1342 are a mix of biogenic, volcaniclastic, and siliciclastic sediments. In general, the color of the sediments reflects their lithologic characteristics: sediment composed of siliciclastic sediment or mixed lithologies tends to be very dark greenish gray to dark gray, whereas biogenic sediment is olive-gray to olive. Volcaniclastic ash layers are dark gray to black or shades of light gray to white. The sedimentary sequence can be divided into three lithologic units: Unit I, consisting of silt and laminated ooze; Unit II, consisting of sponge spicule–bearing, diatom-bearing sand; and Unit III, consisting of volcanic rock and volcaniclastic sedimentary rock.

The occurrence of well-preserved laminations in Unit I indicates the absence of bioturbating fauna and thus suggests low oxygen conditions in the bottom waters and the sediment pore water. Burrows or mottles at the gradational tops of laminated sediment intervals indicate an increase in oxygenation of bottom waters after the deposition of the laminated sediments. In contrast, the sharp bottom boundaries suggest either a sudden increase in sedimentation rate at the onset of laminated intervals or a hiatus between the laminated sediments and underlying siliciclastic sediments. The winnowing of sediment by bottom currents may have caused the apparent low average sedimentation rate (3 cm/k.y.), and the sedimentary record might inherit strongly variable sedimentation rates or even phases of nondeposition or erosion. The total number of well-correlated laminated intervals is roughly equal to the total number of interglacial cycles that occurred during the last 1.1 m.y. The occurrence of laminated ooze reflects the interglacial times, which is consistent with the preliminary paleomagnetic age model.

Moderately to well-rounded and mixed volcaniclastic and metamorphic mineral or rock fragments in the sand encountered in Unit II indicate a terrestrial source. Although the base of Unit I is dated to only 1.2 Ma, several Miocene diatom species were observed in Unit II. This suggests the following possible processes: extremely low sedimentation, a hiatus, or reworking by sediment gravity flows.

The basement volcanic rock (basalt) was most likely deposited as lava, as indicated by the flow alignment of the plagioclase laths and the vesicular texture. The volcaniclastic rocks beneath have a mafic volcanic source and contain both lava fragments and tephra fragments (scoria).

Biostratigraphy

Eighteen biostratigraphic datum events indicating an upper to middle Quaternary sequence were identified based on radiolarians, diatoms, silicoflagellates, and calcareous nannofossils. The sedimentation rate at Site U1342 is relatively low (3 cm/k.y.), as implied by the estimated age of 1.2 Ma for the bottom of Unit I based on biostratigraphic markers. Calcareous microfossils reflect a high-latitude environment, indicating variations of sea-surface temperatures. The benthic foraminifers generally reflect environments within or near the OMZ in high-latitude regions. The preserved siliceous microfossils are mainly composed of high-latitude pelagic species, which indicates changes to surface water productivity. Dinoflagellates consistently occur throughout the record with poor preservation in the lower part. The dinoflagellate assemblages show changes between low and high primary productivity together with general low sea-surface temperatures and low seasonal sea ice coverage.

Both dinocyst assemblages and sea ice diatoms suggest low seasonal sea ice coverage. In general, dinocysts suggest high primary productivity, low sea-surface temperature, and seasonal sea ice coverage. However, the co-dominance of the autotrophic *Operculodinium centrocarpum* and the heterotrophic *Brigantedinium* spp. at 20.96 m CSF in Hole U1342A could be associated with relatively low primary productivity and/or an incursion of oceanic/oligotrophic waters. Planktonic foraminifers are present throughout the section from ~36 m CSF, showing polar–subpolar conditions. Benthic foraminifers generally exhibit high abundances, and variation in species dominance is probably related to changes in oxygen levels and/or organic fluxes.

The uppermost one or two cores, depending on the hole, are assigned to calcareous nannoplankton Zone NN21 (0.29 Ma to the present) (Martini, 1971; Lourens et al., 2004), characterized by *Emiliania huxleyi*. Sample 323-U1342A-3H-CC contains *Pseu-*

doemiliana lacunosa and is therefore assigned to calcareous nannofossil Zone NN19 (>0.44 Ma). Planktonic foraminifers are present only in the uppermost four cores of each hole except Hole U1342D, where they also occur in Core 323-U1342D-5H. The fauna is dominated by *Neogloboquadrina pachyderma* (sinistral) in all samples. More than 20 species of benthic foraminifers were recovered from this site. Occasionally dominant species are *Cassidulina* sp. and *Uvigerina peregrina*. Persistently occurring species include *Brizalina pygmaea*, *Brizalina spathulata*, *Bulimina* aff. *exilis*, *Globobulimina pacifica*, and *Valvulineria* spp. This assemblage shows similarities to those in the uppermost ~100 m CSF of Sites U1339, U1340, and U1341 and also to those within or near the OMZ in the Sea of Okhotsk (Bubenshchikova et al., 2008). This assemblage does not appear to reflect shallow-water (shelfal) deposition.

The LO of *Proboscia curvirostris* (0.3 Ma) is observed at the base of Cores 323-U1342A-3H and 323-U1342C-3H, which is consistent with Sites U1340 and U1341, also located on Bowers Ridge. Because of poor diatom preservation below Core 5H in each hole, the biostratigraphic zonation was constrained by one species, *P. curvirostris*, which places the *N. seminae* Zone 12 at 0–11.41 m CSF in Hole U1342A and 0–17.04 m CSF in Hole U1342C, respectively. Based on the observed silicoflagellate species the age of the uppermost four cores in Holes U1342A and U1342D is probably Pleistocene. Cores 323-U1342A-5H and below may possibly be older than 2.5 Ma given the occurrence of *Ebriopsis antiqua antiqua,* assuming it is not reworked.

Six radiolarian datums derived in the subarctic Pacific were identified at this site. These datums showed relatively low sedimentation rates (~5 cm/k.y.) in the uppermost 20 m of each hole compared to the other Bowers Ridge sites (Sites U1340 and U1341). Although radiolarian datums are scarce in the lower intervals, the LO of *E. matuyamai* (0.9–1.5 Ma) was found at the base of Core 323-U1342B-4H. This datum provides a constraint for the age estimation for the lower intervals and an average sedimentation rate in Hole U1342B of 2–4 cm/k.y.

Poor preservation of organic-walled dinoflagellate cysts in the lower part of the sequence and particularly in the sandy layer suggests significant oxygen concentrations in the bottom water. The dinoflagellate assemblage composition is modern, suggesting Pleistocene age for all analyzed samples.

Paleomagnetism

The average inclination value is nearly 70° over all normal polarity intervals, which is close to the site axial dipole inclination of ~72° (Table **T15**). This indicates that we can effectively remove overprint magnetization caused by drill pipes and/or core barrels from the NRM records. We defined a polarity zonation from the inclination record and correlated the zonation to the polarity timescale based on micropaleontology datums (Fig. **F41**). The Brunhes/Matuyama boundary and the base of the Jaramillo Subchron are clearly identified through Holes U1342A, U1342C, and U1342D. The top of the Jaramillo Subchron and both the top and base of the Cobb Mountain Subchron are identified in Holes U1342C and U1342D but not in Hole U1342A. We also tentatively note the existence of three excursions visible in all three holes: the Kamikatsura, Santa Rosa, and Punaruu excursions.

It is possible to see a correlatable pattern of relative paleointensity at the present site and at Site U1341, as indicated by the relative numbering scheme within the Brunhes Chron (the last 780,000 y). Note, however, that the relative paleointensity estimates are both significantly influenced by lithologic variability and should not be considered high-resolution estimates of true geomagnetic field intensity variations. We estimate that fine-grained hemipelagic marine sediments were deposited over the last 1 m.y. with essentially a constant sediment accumulation rate. Note the discrete intervals where both magnetic parameters undergo more than order-of-magnitude decreases. These indicate the intervals of significant magnetic mineral dissolution. They appear to be closely related to the laminated sediment intervals, and both are probably related to enhanced rates of reduction diagenesis during those selected time intervals. Our chronostratigraphic estimates suggest that these dissolved intervals (and the associated laminations) occur in the interglacial sediments. Note that a few narrow intervals have significantly stronger remanence because of authigenic greigite. They are interpreted to always occur within the glacial-stage sediments with lower porosity.

Stratigraphic correlation

The composite depth scale and splice at Site U1342 is complete and continuous from 0.0 to 46.71 m CCSF-A (Tables **T16, T17**). Sediment cores below the splice are included in the composite depth framework by appending them with a constant affine value of 2.783 m. Color reflectance data were examined: the b* parameter is considered useful for correlation, but L* and a* do not appear to correlate between holes. Within the splice the composite CCSF-A depth scale is defined as the CCSF-D depth scale. Note that CCSF-D rigorously applies only to the spliced interval. Intervals outside the splice, although available with CCSF-A composite depth assignments, should not be expected to correlate precisely with fine-scale details within the splice or with other holes because of normal variation in the relative spacing of features in different holes. Such apparent depth differences may reflect coring artifacts or fine-scale variations in sediment accumulation and preservation at and below the seafloor. The cumulative offset between CSF and CCSF-D depth scales is approximately linear. The affine growth factor at Site U1342 is 1.06 between 0 and 44.0 m CSF. Calculation of MARs based on the CCSF-A or CCSF-D scales should account for this affine growth factor by dividing apparent depth intervals by the appropriate growth factor. After dividing by the growth factor this scaled depth scale should be referred to as CCSF-B.

Geochemistry

Interstitial water sulfate, DIC, PO_4^{3-}, and NH_4^+ profiles indicate that sediments at Site U1342 are characterized by low rates of anaerobic carbon mineralization predominantly driven by organoclastic sulfate reduction (Fig. **F42**). Additionally, small increases in Mn concentration might indicate microbial Mn reduction as a further mineralization pathway. It is more likely, however, that dissolved Mn is released during reaction of hydrogen sulfide with Fe/Mn (oxyhydr)oxides. Comparison with Site U1341, also located on Bowers Ridge, reveals that the present site has one order of magnitude lower NH_4^+ concentrations and ~50% lower phosphate concentrations. This highlights the extremely low mineralization rates at Site U1342 despite its shallower depth and the similar TOC at both sites. The low extent of anaerobic carbon mineralization at the present site can be attributed to the extremely low sedimentation rates. Very low sedimentation rates probably prolong the time that organic matter is degraded via oxic respiration and nitrate reduction in the oxic/suboxic sediment zone. This leaves rather refractory organic material, which is only inefficiently degraded during anaerobic carbon mineralization (Hulthe et al., 1998).

Solid-phase data, however, suggest that the present-day geochemistry might only give a limited picture of past conditions. High TOC concentrations that correlate strongly with high total sulfur concentrations in several laminated intervals discovered throughout the sediment column indicate events of high organic carbon input that probably resulted in high sulfate reduction rates during these periods and hence elevated hydrogen sulfide production, which is reflected in high pyrite (total sulfur) concentrations. However, the contents of $CaCO_3$ are not always high in the laminated layers.

Another interesting feature of Site U1342 is the inverse relationship of the (almost linear) calcium and magnesium profiles, which indicates the influence of signals linked to the alteration of the underlying basalt on the interstitial water calcium and magnesium concentrations. Most likely, both profiles are the result of diffusion between the seawater and the relatively shallow basaltic basement. Low-temperature interactions of seawater with the basaltic basement (e.g., the dissolution of basaltic glass, calcic plagioclase, and olivine) result in the liberation of calcium, whereas the precipitation of smectite leads to the consumption of magnesium (see, for example, Gieskes, 1981; Staudigel and Hart, 1983; Thompson, 1983; Lyons et al., 2000).

Microbiology

Samples for abundance of prokaryotes were collected adjacent to interstitial water whole-rounds in sections drilled using the APC. High-resolution sampling took place in the microbiology-dedicated cores and in additional samples taken once per core to APC refusal in Hole U1342A. These additional samples were taken to evaluate cell abundance and community structure in the deepest portion of Site U1342. PFT analyses performed on these cores showed no contamination from the drill fluid. Samples from all cores were fixed. These analyses assist the understanding of global distribution and abundance of subseafloor life in a highly productive oceanic regime. Special focus will be directed toward the function of Archaea in the sulfate reduction zone, the SMTZ, and the methanogenesis zone.

Physical properties

The downhole-decreasing trend of magnetic susceptibility ranges from a near-surface value of ~100 SI units to about half this value at ~35 m CSF, which is the base of lithologic Unit I. Below this depth magnetic susceptibility readings in Unit II increase in steps to as high as 400 SI units at 40 m CSF. The higher values in Unit II likely track the downward-increasing abundance of sandy material derived from the underlying volcanic basement, which was wave-based leveled sometime in the early late Miocene. Magnetic susceptibility values are much higher in Hole U1342D at ~73–74 m CSF (29–30 m below the sediment/basement contact), averaging ~1500 SI units, and decrease deeper in the section to ~750 SI units at ~116–117 m CSF (~72–73 m into basement).

A prominent downhole profile of increasing average wet bulk density is noted. The higher gradient of the lower trend is within the sandy sediment of Unit II, which is presumably granular material derived during the wave-beveling final stage of destruction of a stratavolcano that formerly rose above Ulm Plateau. *P*-wave velocity increases downhole from near-surface readings of just over 1.45 km/s to ~1.55 km/s in Unit II near the contact with basement rock at ~45 m CSF (Fig. **F39**). In the sandy sediment of Unit II in Hole U1342D, *P*-wave velocity increased to ~1.65 km/s and somewhat higher.

NGR readings increase irregularly downhole from a near-surface average of ~18 counts/s to ~24 counts/s at the base of Unit I. The gradient of increasing counts/s steepens within the sandy beds of Unit II to reach ~33 counts/s just above basement contact at ~44 m CSF. Presumably, the elevated NGR readings record a downhole increase in clay minerals and, at least within Unit II, clay minerals derived from the underlying bedrock of arc lava and volcaniclastic deposits. Rock clasts recovered in core sections exhibit evidence of oxidation. Clay minerals that account for the higher readings in the basal sediment of Unit II presumably reflect subaerial weathering of the stratavolcano that formerly towered above Ulm Plateau prior to its early late Miocene destruction.

In general, MAD values of discrete samples track those of gamma ray attenuation but with a much greater spacing of measurements. The contrast between Unit I and denser Unit II sediments is nonetheless well shown by MAD data. The near-surface porosity is ~80% but decreases to ~55% in the sandy sediment of Unit II and just above basement at 44 m CSF. The downhole trend of overall decreasing porosity and water content presumably reflects compaction of the section, with notable excursions to higher values in the basal 10–12 m of Unit I that may identify a higher relative content of siliceous microfossils. The relatively elevated grain density in Unit I in comparison to the upper beds of Site U1341 on the deeper flank of Bowers Ridge can be attributed to the availability of nearby bedrock sources for Site U1342 deposits.

Downhole measurements

The temperatures measured with the APCT-3 tool in Hole U1342C were 4.46°C at 26.2 m DSF and 5.32°C at 35.0 m DSF. From these two measurements the geothermal gradient should be 97.7°C/km. The estimated heat flow is 96.9 m W/m^2, which is significantly higher than existing measurements in the area. Alternately, considering the variations in thermal conductivity with depth, a more accurate measure of the heat flow in a conductive regime can be given by a Bullard plot, which gives a heat flow value of 80.9 m W/m^2, which is closer to other measurements in the Bowers Ridge area.

Sedimentation rates

The apparent sedimentation rate in the uppermost section between the mudline and 3.6 m CCSF-A (marked by the LO of *Amphimelissa setosa*) was 5 cm/k.y. with relatively high water contents and hence may not be significantly different from those below it (Fig. **F43;** Table **T18**). Sedimentation rates stayed at fairly constant values of 2–3 cm/

k.y. between 3.6 m CCSF-A and the magnetic Kamikatsura Excursion at ~29 m CCSF-A. This is followed by an increasing trend up to 9 cm/k.y. down to the bottom of magnetic Cobb Mountain at ~43 m CCSF-A. The presence of Miocene diatoms in lithologic Unit II warrants further refinement of the age model.

Site U1343

Background and objectives

The primary objective of drilling at Site U1343 (prospectus Site GAT-4C) was to study high-resolution Pliocene–Pleistocene paleoceanography at a location proximal to the gateway to the Arctic Ocean. Additionally, this site is closer to the current seasonal sea ice limit and because of its 2 km water depth it provides information regarding the history of mid-depth water in the Aleutian Basin. This site is located at a topographic high clearly separated from the Bering shelf (Figs. **F44, F45, F46, F47, F48**). Hence, it was anticipated to have received fewer reworked terrigenous sediments from the shelf during the interglacials or the subaerially exposed land during the glacials than a location directly downslope of the Bering shelf.

Site U1343 is in the area of high biological productivity called the Green Belt. The Green Belt is formed by the Bering Slope Current (BSC), which originates from the Alaskan Stream water that flows into the Bering Sea through the western Aleutian Islands. The water that enters the Bering Sea moves eastward along the Aleutian Islands and consequently encounters the Bering shelf. The base of the BSC is at ~300 m water depth and its flow is forced to turn to the northwest once it meets the slope and shelf; eddies and instabilities in its flow cause upwelling along the shelf break. Moreover, tidal mixing causes further vertical mixing of the water masses along the BSC, enhancing biological productivity within the Green Belt, which is adjacent to the northwest-trending shelf break where high primary productivity in the surface waters and high organic carbon accumulation at the seafloor take place. Because of the expected high organic carbon supply to the seafloor, especially during the interglacial sea level highstands, it is possible the OMZ previously expanded down to the depth of this site. In order to compare the vertical extent of water mass conditions across the basin and relate the OMZ to paleoproductivity, the records from the shallower drill sites on Bowers Ridge (Site U1340, water depth = 1295 m; Site U1342, water depth = 818 m) as well as the other slope sites will be used. This site is also located close to the maximum extent of the present-day seasonal sea ice cover. Thus, this site was expected to have been covered by seasonal or perennial sea ice during the glacial sea level lowstands.

This drill site in the gateway region to the Arctic Ocean can also be used to study the impact of subseafloor microbes on biogeochemical fluxes in the highest surface ocean productivity areas of the Bering Sea drill sites. Organic-fueled subseafloor respiration and its impact on biogeochemistry in such a highly productive region has not previously been quantified. To do so, the drilled sediments in the gateway region were used to determine subseafloor cell abundance and to investigate the link between the mass and characteristics of subseafloor microbes and the extent of export productivity from the surface ocean.

Sedimentation rates at this site were not previously known because of a lack of piston cores. However, rates of ~180 m/m.y. were observed at Site U1344 (proposed Site GAT-3A) in an earlier site survey piston core study (Takahashi, 2005). Thus, prior to drilling, recovery of Pleistocene to Pliocene sections was expected at this site.

Lithostratigraphy

Sediments at Site U1343 are primarily composed of silt with varying amounts of clay and diatoms and minor amounts of sand, ash, foraminifers, calcareous nannofossils, and sponge spicules. The sediment is predominantly dark/very dark greenish gray to dark/very dark gray. One lithologic unit spanning the early Pleistocene to the Holocene is defined at this site. Six laminated intervals are observed and can be correlated between the holes based on lithologic, reflectance, and magnetic susceptibility data. Unit I encompasses a time period comparable to Unit I defined at Bowers Ridge Sites U1340 and U1341. However, Site U1343 is distinct in having a higher proportion of siliciclastic grains and a higher occurrence of sand-sized grains. This is probably related to the location of this site on the continental slope and the relative proximity to the source of terrigenous sediments. During glacial sea level lowstands, and in particular during early stages of deglaciations, significant amounts of coarser grained detrital material might have been mobilized from the exposed Bering Sea shelf and redeposited farther down the continental slope. Unlike Site U1339, drilled on the slope at Umnak Plateau, volcaniclastic material is only a minor component of sediment at Site U1343 because it is more distant from the Aleutian arc. There is a shallow SMTZ and abundant methane in the sediment column at Site U1343, like at the other slope sites. Benthic and planktonic foraminifers encrusted with yellow minerals are common, and they often coincide with samples in which authigenic carbonates are found. Association of authigenic carbonates and apparent overgrowths implies that authigenic carbonates nucleated on the foraminifer tests. In this case the stable isotope records from this site are potentially contaminated by the isotopic signature of the overgrowths; however, pristine foraminifer shells were also observed, and the generation of uncontaminated isotope stratigraphies should be possible after careful screening for authigenic carbonates.

Biostratigraphy

The composite age model derived from all five holes shows that the sediment record recovered at Site U1343 spans the last 2.0–2.4 m.y., yielding a broadly linear trend in sedimentation rates, with values around 26 cm/k.y. in the uppermost 400 m CCSF-A that increase to ~56 cm/k.y. in the bottom 350 m CCSF-A. Siliceous, calcareous, and organic fossils show the greatest abundances in the uppermost 300–250 m CCSF-A relative to the section below. In the upper section all microfossil groups show distinct large and frequent oscillations, indicating fluctuations in the sea ice cover and productivity in the upper water column and in the deepwater environment. All major microfossil groups show distinct changes, occurring gradually or abruptly between 200 and 300 m CCSF-A (0.8 to 1.1 Ma), in their general trend of abundances and/or assemblage composition. These changes are thus linked to the MPT. Benthic foraminifers indicate high-frequency changes in bottom water oxygen content over the entire sequence, probably related primarily to surface water productivity, but possibly also to bottom water ventilation changes and methane seeps. The cooling trend observed after the MPT is reflected in the increase of abundances of sea ice dinoflagellate and diatom taxa and in the decrease of the predominance of pelagic/open water conditions evidenced in the decline of subpolar planktonic foraminifers and the diatom species *Neodenticula seminae*.

The occurrence of calcareous nannofossil *Emiliania huxleyi* at the base of Core 323-U1343A-3H assigns an age for this core to calcareous nannofossil Zone NN21, which is defined by the FO datum of *E. huxleyi* (0.29 Ma) to the present. However, the occurrence of a barren interval below this level made it impossible to constrain the FO of *E. huxleyi* and the boundary with Zone NN20. The LO datum of *Pseudoemiliania lacunosa* (0.44 Ma) in Sample 323-U1343A-12H-7, 46 cm, which defines the upper limit of calcareous nannofossil Zone NN19, is well constrained because it takes place within an interval rich in calcareous nannofossils. Although the trace amount of planktonic foraminifer *Neogloboquadrina atlantica* (sinistral) with the LO (2.4–2.5 Ma) is present, the age derived by this taxon appears too old when compared to other datums. Benthic foraminiferal assemblages have a similar species composition to the assemblages found at Site U1339 and are within or near the OMZ in the Sea of Okhotsk.

High-frequency variation in oxygenation is apparent throughout the section, but initial results show generally higher oxygen indicators such as *Elphidium* cf. *batialis* and *Islandiella norcrossi* are dominant in and below Core 323-U1343E-24H.

The LO datum of diatom *Proboscia curvirostris* (0.3 Ma) and the LO datum of *Thalassiosira jouseae* (0.3 Ma) were observed at ~70–77 m CSF in three holes at Site U1343. This is consistent with results from Site U1339 at Umnak Plateau. The cored interval above the LO of *P. curvirostris* (0.3 Ma) is assigned to *Neodenticula seminae* Zone NPD12. The interval between the LCO datum of *Actinocyclus oculatus* observed at 296.4 m CSF and the LO datum of *P. curvirostris* at 69.4 m CSF in Hole U1343E is assigned to *P. curvirostris* Zone NPD11. The interval below this datum above the FO of *Neodenticula koizumii* is *A. oculatus* Zone NPD10. The FO of *P. curvirostris* (1.85 ± 0.1 Ma) was defined in Sample 323-U1343E-50X-CC and assigned to the age in the *A. oculatus* Zone. The LO of *Pyxidicula horridus* (1.9–2.0 Ma) was estimated in Core 323-U1343E-61X. The LCO of *N. koizumii* (2.1 Ma) was observed in Sample 323-U1342E-77X-CC. The interval between this datum and the bottom of Hole U1343E is assigned to *N. koizumii* Zone NPD9. The LO of silicoflagellate *Distephanus octonarius* (0.2–0.3 Ma) is estimated to be between 64.0 and 74.9 m CSF. The LO of *Dictyocha subarctios* (0.6–0.8 Ma) is estimated to be between 196.2 and 205.35 m CSF (Hole U1343C) and between 196.1 and 205.45 m CSF (Hole U1343E). The bottom age in Hole U1343E is younger than 2.5 Ma because of the absence of ebridian *Ebriopsis antiqua antiqua*. In Sample 323-U1343E-27H-CC relatively warm water taxa belonging to *Dictyocha* spp. are observed in high numbers (30%), indicating a possible increase of subarctic Pacific water entry into the Bering Sea. Six radiolarian datums common in the subarctic Pacific were identified at this site. The LO and FO datums of *E. matuyamai* (0.9–1.5 Ma and 1.7–1.9 Ma, respectively) were identified in samples from Hole U1343E. In the uppermost 250 m CSF changes in dinoflagellate assemblages are observed, indicating surface water conditions that vary from high productivity and upwelling to conditions with pronounced sea ice cover. Such a high variability above 250 m CSF is also observed in pollen and spore abundances, suggesting changing vegetation in adjacent land masses as well.

Paleomagnetism

The Brunhes/Matuyama boundary is clearly identified in Holes U1343A, U1343C, and U1343E between 180 and 185 m CSF, and both the termination and onset of the Jaramillo Subchron were identified below this (Table T19). Deeper in the section, whereas inclination tends to cluster around normal polarity values making it difficult to identify polarity zonation, the top boundary of the normal polarity zone at ~292 m CSF has been tentatively identified as the termination of the Cobb Mountain Subchron (Fig. **F49**). The paleointensity variation has quite a large amplitude and obviously shows a coherent change with the magnetic susceptibility, suggesting that NRM intensity has been largely influenced by environmental changes.

Geochemistry

Interstitial water SO_4^{2-}, DIC, PO_4^{3-}, and NH_4^+ concentration profiles indicate that the sediments at Site U1343 are characterized by high rates of carbon turnover compared to sites at Bowers Ridge (Fig. **F50**). Values are, in general, at least one order of magnitude higher than at Site U1342 on Bowers Ridge. Profiles of CH_4 and SO_4^{2-} suggest that sulfate reduction is largely driven by the diffusion of CH_4 into the sulfate zone. The SO_4^{2-} profile is nearly linear in the uppermost 8 m CSF, indicating no significant consumption there. The CH_4 flux into the SO_4^{2-} zone, as calculated from the concentration gradient between 8 and 11 m CSF, is ~50%–60% of the SO_4^{2-} flux into the SMTZ. Hydrogen sulfide is also at a maximum in the SMTZ. The ratio between autotrophic and organoclastic sulfate reduction is higher at Site U1343 than at the Bowers Ridge or Umnak Plateau sites. A relatively high flux of Ca^{2+} into the SMTZ further stresses the importance of anaerobic methane oxidation (AOM), which commonly leads to the formation of $CaCO_3$. The Ca^{2+} flux into the SMTZ is ~35% of the methane flux, indicating that an equivalent fraction of the DIC produced through AOM is deposited as $CaCO_3$.

The curvature of the NH_4^+ profile suggests NH_4^+ production from organic matter degradation throughout the sediment column. This is confirmed through preliminary modeling exercises and suggests organic matter degradation and hence microbial activity even at depths below 400 m CSF. Organic matter degradation also leads to the accumulation of DIC and PO_4^{3-} in the interstitial water. The accumulation of these species, however, is much lower than predicted by the NH_4^+ profile assuming steady state and a constant ratio between C, N, and P of remineralized organic matter. This suggests both production and consumption of DIC and PO_4^{3-} in the sediment. Consumption of these species is most likely due to formation of apatite and calcium carbonates (e.g., dolomite). The pore water profiles suggest that rates of net consumption of PO_4^{3-} are highest between 180 and 200 m CSF and net DIC consumption is highest between 300 and 350 m CSF.

The decrease in salinity and pore water chloride concentrations indicate freshening of the pore fluids with depth. A possible explanation for this trend is the dissociation of gas hydrates during core recovery, which releases fresh water and causes depletions in dissolved ion concentrations. Alternatively, decreases in pore water salinity and chloride concentrations can result from meteoric water input, clay membrane ion filtration, and clay mineral dehydration.

Microbiology

Samples for abundance of prokaryotes were collected adjacent to interstitial water whole-rounds in sections cored using the APC. High-resolution sampling took place in the microbiology-dedicated cores from Hole U1343B as well as in samples taken in each core to APC refusal in Hole U1343A. Additional samples were taken from XCB Cores 323-U1343E-78X to 80X to evaluate cell abundance and community structure in the deepest portion of Hole U1343E. PFT analyses performed on all cores from Hole U1343B and in the deeper cores from Hole U1343E show no contamination from the drill fluid. Samples from all cores were fixed. These analyses will assist with understanding the global distribution and abundance of subseafloor life in a highly productive oceanic regime. A special focus will be directed toward the function of Archaea in the sulfate reduction zone, the SMTZ, and the methanogenesis zone.

Physical properties

Downhole from the uppermost ~10 m CSF, wet bulk density increases slightly from an average of ~1.60 g/cm^3 to ~1.65 g/cm^3 at ~100 m CSF. The average value below this depth, although oscillatory, does not seem to change until ~360 m CSF, the calculated depth (~360 m) of the bottom-simulating reflector (BSR), where a shift to a lower average of ~1.60 g/cm^3 occurs. This shift coincides with the change from APC to XCB coring and the consequent recovery of drilling-disturbed core sections. Magnetic susceptibility exhibits cyclicity from lower values averaging ~20–25 SI units to higher readings of ~250 SI units. Peak readings, which are roughly separated by 30–50 m, are prominent to ~360 m CSF. Below this depth the wavelength increases and average values decrease.

Sonic velocities, V_P and V_S, recorded by the downhole FMS-sonic logging tool increase with depth from a near-surface value of ~1550 m/s to ~1840 m/s at the bottom of Hole U1343E at ~744 m CSF. Three gradients of increasing V_P can be recognized: the first gradient extends to ~360 m CSF, increasing at ~110 m/s/km; the second extends from 360 to 520 m CSF, increasing at ~550 m/s/km; and the third gradient extends from 530 to ~744 m CSF, increasing at ~890 m/s/km. NGR counts generally track abundance of clay minerals and their absorbed radioactive nuclei. Evidently, in Hole U1343E higher bulk density sediment is also richer in clay and other siliciclastic minerals. Siliceous microfossils that resist compaction and sediment consolidation are not the dominant component constructing the stratigraphic section. Perhaps because of this circumstance, NGR readings appear to track compaction-driven densification of clay-rich beds, an observation consistent with the progressive downhole increase in logging-tool-measured V_P.

In general, cores collected above the BSR at ~360 m CSF exhibit higher variability of thermal conductivity values, and these are also the most gas-disrupted sections measured. In cores collected below the transition at ~520 m CSF to higher carbonate bearing, V_P and bulk density display the highest range of thermal conductivity values. Average values of discrete sample density increase downhole in Hole U1343A from a near-surface measurement of ~1.50 g/cm^3 to near 1.70 g/cm^3 at ~100 m CSF. Below this subsurface level the average MAD bulk density changes little. Similar profiles of water (moisture) content and sediment porosity are recorded in Holes U1343A and U1343E. Near-surface porosity is ~70%, noticeably lower than that measured at Sites U1339 (~80%), U1340 (~75%), U1341 (~78%), and U1342 (~80%). This difference is ascribed to the lower overall content of siliceous microfossils constructing the sedimentary section. Porosity and water content decrease sharply downhole to ~60% at ~80 m CSF, below which porosity only gradually decreases to ~56% at ~744 m CCSF-D. Average grain density seems to show three density-fluctuating groupings: an upper group from the seafloor to ~100 m CSF with an average density of ~2.68 g/cm^3; a middle group between ~100 and 540 m CSF with an average density ~2.65 g/cm^3; and a basal group that shifts to a lower density of ~2.55 g/cm^3 at ~540 m CSF but that increases to 2.70 g/cm^3 at 744 m CSF.

Stratigraphic correlation

The composite depth scale and splice at Site U1343 is constructed from 0 to 779.18 m CCSF-A (Tables T20, T21). The splice consists of one complete and continuous interval from the mudline to 270.47 m CCSF-A. The continuous splice ranges from the top of Core 323-U1343C-1H to Section 323-U1343E-29H-7, 79 cm, and below this are appended cores ranging from Sections 323-U1343E-29H-1, 0 cm, to 83X-7, 31 cm, (779.18 m CCSF-A), with a constant affine value of 35.62 m. Within the splice the CCSF-A depth scale is defined as the CCSF-D depth scale. CCSF-D rigorously applies only to the spliced interval. The cumulative offset between CSF and CCSF-D depth scales is nonlinear. The affine growth factor at Site U1343 between 0 and 36.4 m CSF is 1.03. At greater depths all cores have an affine growth factor of 1.15. Calculation of MARs based on the CCSF-A or CCSF-D scales should account for the affine growth factor by dividing apparent depth intervals by the appropriate growth factor for the depth interval. After dividing by the growth factor (accounting for the different depth intervals) this scaled depth scale should be referred to as CCSF-B. MARs calculated for the interval of appended cores deeper than the spliced interval should not be divided by the affine growth factor because their depths are a linear transformation of drilling depths.

Downhole measurements

Two tool strings were deployed in Hole U1343E: the triple combo and the FMS-sonic combination. Although both runs indicated an irregular hole, particularly above 430 m WSF, all of the calipers showed that the tools were making contact with the formation over most of the interval logged, suggesting that the overall quality of the data is good. Although the HLDS caliper suggested that the tools made good contact between 300 and 360 m WSF and that the hole was even smaller than the nominal bit size in part of this interval, the density and neutron porosity data in this interval seem questionable. The anomalously low density readings between 307 and 322 m WSF and the very high neutron porosity values between 300 and 360 m WSF suggest that the tool was not properly measuring formation properties. Comparison with the density measurements made with the GRA track sensor on cores recovered from Hole U1343E and with the MAD measurements made on samples from Site U1343 shows generally good agreement except in this interval, where logging data are significantly lower than core measurements.

Logging Unit 1 (100–330 m WMSF) is characterized mainly by a steady increase with depth in velocity, whereas the other log data remain mostly uniform despite some variability, such as in gamma radiation. The velocity increase at the bottom of logging Unit 1 is likely responsible for the strong reflector observed at 2860 ms two-way traveltime in the seismic data. A synthetic seismogram was produced using a wavelet extracted from the seafloor reflection in traces adjacent to Shotpoint 350 and Site U1343 in Line Stk-1. Although we speculated this reflector might be a BSR, indicating the existence of gas hydrate overlying free gas, no conclusive indication from the logs supported the occurrence of gas hydrate. However, slightly higher velocity and resistivity trends and lower dipole waveform amplitudes above the reflector, as well as low chlorinity values measured on several interstitial water samples, suggest that some amount of gas hydrate might be present. Logging Unit 2 (330–510 m WMSF) is defined by slightly decreasing trends with depth in resistivity and by gamma ray values slightly higher than the shallower and deeper units. The top of logging Unit 3 (510–745 m WMSF) is defined by a drop in gamma radiation, an increase in V_P, and a change in the trends of all the logs. The gamma ray, potassium, thorium, density, resistivity, V_P, and V_S logs all display higher amplitude and lower frequency variability than in the upper units, suggesting a significant change in the deposition history and rates. A dolostone recovered in this unit can be recognized in the FMS images.

The APCT-3 tool was successfully deployed three times in Hole U1343A. The measured temperatures ranged from 4.34°C at 43.5 m DSF to 8.53°C at 129.0 m DSF and closely fit a linear geothermal gradient of 49.0°C/km. A simple estimate of the heat flow can be obtained from the product of the geothermal gradient and the average thermal conductivity (0.985 W/[m·K]), which gives a value of 48.2 mW/m^2, within the range of previous measurement in the area.

Sedimentation rates

Very high sedimentation rates were observed throughout the drilled depths at Site U1343 (Fig. **F51;** Table **T22**). From the seafloor to the top of the Jaramillo Subchron (0.998 Ma; 267.6 m CCSF-A) sedimentation rates were relatively constant within the range of 25–29 cm/k.y. An increase in the rate to 46 cm/k.y. was observed between the top and the bottom of the Jaramillo Subchron (1.072 Ma; 302.0 m CCSF-A). Farther down at 407.7 m CCSF-A, or 1.55 Ma as indicated by the LO of dinoflagellate *F. filifera*, sedimentation rates are ~21–25 cm/k.y. Sedimentation rates increase to 54–58 cm/k.y. between 408 and 716 m CCSF-A. The age at this depth is estimated at 2.1 Ma by the LCO of diatom *Neodenticula koizumii*.

Site U1344

Background and objectives

The primary objective of drilling at Site U1344 (prospectus Site GAT-3C) was to study high-resolution Pliocene–Pleistocene paleoceanography at a proximal gateway location to the Arctic Ocean at the deepest water depth of Expedition 323. The site is located ~3200 m along the small summit of a canyon interfluve ~10–15 km southeast of Pervenets Canyon, a large submarine canyon that deeply and widely incises the Beringian continental slope (Figs. **F1**, **F52, F53, F54, F55**) (Normark and Carlson, 2003). Pervenets Canyon, along with companion Zhemchug Canyon adjacent to Site U1343, was discovered in the early 1960s by the Soviet fishing industry and named after one of the discovering trawlers. At times of glacially lowered sea level the head of Pervenets Canyon is commonly presumed to have been one of the outfall locations for the Anadyr River, which presently drains the Russian northeast and enters the Bering Sea at the Gulf of Anadyr. It is anticipated to have received a supply of terrigenous sediments from the shelf during both the interglacials and the glacials.

This is also the area of high biological productivity called the Green Belt. The Green Belt is formed by the BSC, which originates from the Alaskan Stream water that flows into the Bering Sea through the western Aleutian Islands. The water that enters the Bering Sea moves eastward along the Aleutian Islands and consequently encounters the shallow blocking Bering shelf. The bottom depth of the BSC is at ~300 m, and its flow is forced to turn to the northwest once it meets the slope and shelf; eddies and instabilities in its flow cause upwelling along the shelf break. Moreover, tidal mixing causes further vertical mixing of the water masses along the BSC, enhancing biological productivity within the Green Belt (Taniguchi, 1984; Springer et al., 1996), a zone adjacent to the northwest-trending shelf break where high primary productivity in the surface waters and high organic carbon accumulation at the seafloor take place (Springer et al., 1996). However, we anticipated finding a lower organic carbon supply to the seafloor than at the other gateway sites or at Site U1339 because of the deeper water depth of Site U1344. Thus, expectation of the impingement by the dissolved OMZ in the past is relatively small at this site. Nevertheless, it is important to compare the vertical extent of water mass conditions on a basin-wide scale that includes this site. Hence, the records from the shallower drill sites on Bowers Ridge as well as the other gateway sites can be fully employed for the comparison.

This site is also located close to the maximum extent of the present-day seasonal sea ice cover. Thus, this site was expected to have been covered by seasonal or perennial sea ice during the glacial low sea level stands. Since it is adjacent to the Bering shelf, a high amount of terrigenous sediment supply was expected, especially during the glacial lowstands.

This relatively deep drill site in the gateway region to the Arctic Ocean can also be used to study the impact of subseafloor microbes on biogeochemical fluxes in the highest surface ocean productivity areas of the drill sites in the Bering Sea. Organic-fueled subseafloor respiration and its impact on biogeochemistry in such a highly productive region has not previously been quantified. To do this, the drilled sediments in the gateway region were used to determine subseafloor cell abundances and to investigate the link between the mass and characteristics of subseafloor microbes and the extent of export productivity from the surface ocean.

Sedimentation rates at this site have been estimated at 170–180 m/m.y. based on earlier site survey piston core studies (Takahashi, 2005; T. Sakamoto et al., unpubl. data). Neither of the piston cores taken in these studies recovered the Holocene section, possibly indicating erosion during the recent past. Prior to drilling, recovery of sections from the Pleistocene to Pliocene were expected.

Lithostratigraphy

One lithologic unit spanning the early Pleistocene to the Holocene was defined at this site. Unit I at Site U1344 encompasses a time period comparable to Unit I defined at Bowers Ridge Sites U1340 and U1341, and it is in general very similar to Unit I at the other Bering Sea margin Sites U1339 and U1343. However, Site U1344 is distinct in that it has an even higher proportion of siliciclastic components and a higher occurrence of sand-sized grains than Site U1343. This is probably related to the location of this site on the continental slope and its relative proximity to sources of terrigenous sediments from the continental margin. Sandy lithologies are concentrated in three relatively distinct intervals at Site U1344. These can be correlated not only between the holes at Site U1344 but also to Site U1343, where three distinctly sandy intervals occur. Whereas lithologies dominated by diatoms are associated with changes in color reflectance and are analogous to those at other sites, the lithology changes here are more subtle because of overall higher abundances of siliciclastic detritus. Higher abundances of diatoms may reflect high diatom flux during interglacials, as previously observed in the Bering Sea (Okazaki et al., 2005).

Only one diatom-rich laminated interval was observed. All other laminations are defined by faint color changes with gradational boundaries with the surrounding lithologies. It appears that well-oxygenated bottom water conditions probably prevailed throughout most of the Pleistocene, preventing preservation of laminations. Almost all dropstones are well rounded, indicating a period of reworking prior to incorporation in the ice. The rounding therefore favors a coastal provenance and sea ice rafting rather than icebergs (Lisitzin, 2003). Unlike most other sites (though similar to Site U1343) volcaniclastic material is only a minor component of the sediment at Site U1344 because it is more distant from the Aleutian arc. Authigenic carbonate occurs throughout the sediment and is not constrained to deeper parts of the sequence as it was at Site U1343. The shallowest appearance in Hole U1344A is at 63 m CSF. The presence of gas in the sediments caused several types of coring disturbance—mostly cracks as wide as several centimeters. In some cases, this affected the stratigraphic integrity of the sediment sequence, similar to Sites U1339 and U1343.

Biostratigraphy

The water depth of Site U1344 is ~3200 m and has a potential to reconstruct past deepwater changes because it is presently located below the OMZ. Benthic foraminiferal fauna indicate high-frequency changes in the bottom water oxygen content over the entire section, probably related primarily to surface water productivity but possibly to bottom water ventilation changes and methane seeps as well. There is a general increase in abundance and bottom water oxygen variability from ~300 m CSF to the top of the section. The low-oxygen indicator *Bulimina* aff. *exilis* is more abundant at both Sites U1343 and U1344 after ~0.8 Ma, as is benthic foraminifer abundance maxima. Both high-abundance and low-oxygen benthic fauna were found to be common during the last deglacial at Bowers Ridge (Okazaki et al., 2005), and the increase in such characteristics from 0.8 Ma may mark the onset of more intense deglacials, greater nutrient availability, and higher surface water productivity. Similarly to Site U1343, the increases of planktonic foraminifers also coincide with the highest numbers of sea ice diatoms and sea ice dinoflagellate cysts after 1 Ma. The change from low to high abundances of planktonic foraminifers coincides with the increased abundances of dinoflagellate cysts, calcareous nannofossils, benthic foraminifers, and the number of low-oxygen benthic foraminifers, analogous to the data shown by Okazaki et al. (2005) for the $CaCO_3$ preservation peaks during the last deglaciation in the Bering Sea.

This site is characterized by very low abundance of calcareous nannofossils. Only samples from the uppermost cores to the base of Core 323-U1344D-4H can be assigned to calcareous nannofossil Zone NN21 with an estimated age of <0.29 Ma. The planktonic foraminifer faunal assemblage found during the late Pleistocene is dominated by *Neogloboquadrina pachyderma* (sinistral) throughout. Below 260 m CCSF-A, *N. pachyderma* (sinistral) is reduced or absent from the assemblage and the fauna is replaced by subpolar assemblage dominated by *G. bulloides*. The occurrence of this species is mainly ruled by sea-surface temperature (Asahi and Takahashi, 2007), indicating that the late Pliocene–early Pleistocene was warmer than the late Pleistocene at this site.

The drilled interval above the LO of diatom *P. curvirostris* (ranging from 107.2 to 122.3 m CSF, depending on the hole) is assigned to *Neodenticula seminae* Zone NPD12. Because of the absence of *Actinocyclus oculatus* in Holes U1344D and U1344E, the bottom of each hole is assigned to Zone NPD 11. The FO datum of *P. curvirostris* was defined in Sample 323-U1344A-56X-CC and assigned the age of 1.85 ± 0.1 Ma in the

A. oculatus Zone. The LO of *Pyxidicula horridus* (1.9–2.0 Ma) was estimated at the base of Core 323-U1344A-63X. The LO of silicoflagellate *Dictyocha subarctios* was assigned to Cores 323-U1344A-30H (270.25–280.31 m CSF) and 323-U1344D-26H (224.41–234.09 m CSF). The LO of ebridian *Ammodochium rectangulare* appears to be located in Core 323-U1344A-78X (733.13–739.75 m CSF). The radiolarian ages at Site U1344 span from the *Botryostrobus aquilonaris* Zone (upper Quaternary) to the *Eucyrtidium matuyamai* Zone (middle Quaternary) in the subarctic Pacific. Five radiolarian datums derived from the subarctic Pacific were identified at this site. Estimated sedimentation rates in the uppermost 150 m in Holes U1344A, U1344D, and U1344E are >30 cm/k.y., which is slightly higher than at neighboring Site U1343 (~20 cm/k.y.). The LO of *E. matuyamai* (0.9–1.5 Ma) was identified in samples from Hole U1344A. The occurrence of dinoflagellate *Filisphaera filifera* at the base of Core 323-U1244A-50X (473.4 m CSF) suggests an age of 1.41–1.7 Ma, according to its LO datum in the North Pacific and North Atlantic. This species dominates the assemblages in a few samples above this depth, quite similarly to Site U1343. The occasional occurrence of the autotrophic species *Operculudinium centrocarpum* may be related to oceanic conditions with relatively low productivity.

Paleomagnetism

The Brunhes/Matuyama boundary is clearly identified at ~280 m CSF. The Jaramillo, Cobb Mountain, and Olduvai Subchrons might be correlatable with the extracted normal polarity zones placed at ~380, 420, and 680 m CSF, respectively (Fig. **F56;** Table **T23**). The paleointensity variation has large amplitude and obviously shows a coherent change with magnetic susceptibility, suggesting that NRM intensity has been largely influenced by environmental changes. The relative paleointensity pattern seen at this site is consistent with those observed at Sites U1340, U1341, U1342, and U1343. Based on the correlations, MIS 1–19 have been assigned to ~280 m CSF. The dramatic changes in NRM indicate notable effects of early sediment diagenesis. Significant magnetic mineral dissolution starts within 10 m CSF due to AOM–sulfate reduction processes, which are also evident at Sites U1343 and U1339.

Geochemistry

The rate of carbon turnover in the sediment at Site U1344 is similar to or slightly higher than at Site U1343, as evidenced by similar SO_4^{2-}, DIC, PO_4^{3-}, and NH_4^+ concentration profiles (Fig. **F57**). Similar to Site U1343, profiles of CH_4 and SO_4^{2-} at Site U1344 suggest that sulfate reduction is largely driven by CH_4 diffusion into the sulfate zone. The CH_4 flux into the SO_4^{2-} zone, as calculated from the concentration gradient between 8 and 13 m CSF, is ~70%–80% of the SO_4^{2-} flux into the SMTZ. The importance of AOM for overall carbon turnover is also stressed by the curvature in the DIC profile. The steepest concentration gradient in the uppermost 10 m CSF is observed directly above the SMTZ, suggesting that the highest DIC flux occurs from this zone. Preliminary modeling of the DIC profile suggests that net DIC production in the SMTZ accounts for 80% of the DIC production in the uppermost 30 m CSF of sediment. Hydrogen sulfide is also at a maximum in the SMTZ, most likely because sulfate reduction rates are the highest and the content of oxidized iron is the lowest in this zone. Magnetic susceptibility data obtained during fast scan of the cores confirm a low content of oxidized iron in the SMTZ.

AOM is well known to favor the deposition of carbonates in the SMTZ. At Site U1344 a relatively high flux of Ca^{2+} into the SMTZ is observed, which indicates the formation of calcium carbonate. There were also indications for Mg^{2+} flux into the SMTZ, which may suggest dolomite formation. The curvature of the NH_4^+ profile suggests production from organic matter degradation throughout the sediment column. Microbial-mediated degradation is either conducted via a respiratory or fermentative pathway. According to the classical reduction scheme in sediments, only fermentation and hydrogenotrophic methanogenesis occur below the SMTZ; however, at this site the Fe profile suggests that Fe reduction occurs below the SMTZ. Organic matter degradation also leads to the accumulation of DIC and PO_4^{3-} in the interstitial water. The accumulation of these species, however, is much lower than that predicted by the NH_4^+ profile, assuming steady state and a constant ratio between C, N, and P of remineralized organic matter. This suggests both production and consumption of DIC and PO_4^{3-} in the sediment. Consumption of these species is most likely due to formation of apatite and calcium carbonates (e.g., dolomite). The interstitial water profiles suggest that rates of net consumption of PO_4^{3-} and DIC are the highest between 300 and 350 m CSF. Ca^{2+} and Mg^{2+} concentration profiles likewise indicate net consumption of these species between 300 and 350 m CSF.

Microbiology

Samples for abundance of prokaryotes were collected adjacent to interstitial water whole-rounds in sections drilled using the APC. High-resolution sampling took place in the microbiology-dedicated cores as well as in additional samples taken once per core to APC refusal in Hole U1344A. Additional samples were taken from XCB Cores 323-U1344A-78X to 80X to evaluate cell abundance and community structure in the deepest portion of Hole U1344A. PFT analyses performed on these cores show no contamination from the drill fluid. Samples from all cores were fixed.

It is of interest to examine the relationship between microbial productivity and diversity in the uppermost 25 m of the sediment column. Special attention will be directed toward the function of Archaea in the sulfate reduction zone, the SMTZ, and the methanogenesis zone. The sulfate-methane transition is a hot spot for microbial activity and abundance within deep-sea sediments (D'Hondt, Jørgensen, Miller, et al., 2003), and we will expect an increase in the abundance and activity of microbial life, while the remainder of the core should see a significant decrease with depth in both active and benign microbial life.

Physical properties

The downhole profile of density for Hole U1344A is remarkably similar to that of Hole U1343E. The overall downhole increase in bulk density is interpreted to record compactive dewatering in a generally lithologically uniform sequence of fine-grained sediment. Magnetic susceptibility, as measured by the WRMSL, exhibits little change in average value and character with depth. Based on what was learned at previous sites, the rhythmic oscillations are presumed to be a function of lithologic composition and patterns of in situ sediment alteration.

Except for the uppermost three cores in Hole U1344A, *P*-wave velocity readings for the sedimentary section penetrated at this hole were only collected by the FMS-sonic downhole logging tool. Sonic *P*-wave velocity data reveal a profile similar to that recorded in Hole U1343E in that the average velocity increases downsection in steplike sectors. Except for the uppermost ~80–100 m CSF, across which NGR readings increase from a near-surface measurement of ~25 count/s to ~34 counts/s, NGR values at deeper depths oscillate around this average to the base of the Hole U1344A at 745 m CSF. Presumably, variations in counts per second reflect downhole changes in content of clay and siliciclastic minerals.

Thermal conductivity measurements can be grouped into an upper and lower sequence. The upper vertical sequence displays an estimated average reading of ~0.905 W/(m·K) and extends downhole from the near surface to ~260 m CSF, below which APC refusal caused a change to XCB coring and V_P shifts abruptly to higher readings. In Hole U1344A porosity decreases most rapidly in the upper part of the drilled section, falling to an average value of ~60% at 80–100 m CSF. Below this depth, other than oscillating readings, there are no notable shifts in average value or changes in trend. The overall downhole decrease in porosity tracked by MAD and logging data is presumably a manifestation of compaction dewatering.

The upper group of dry grain density, extending from the surface to ~160 m CSF, is ~2.70 g/cm^3. The middle sequence, from ~160 to 620 m CSF, exhibits an average density of 2.65 g/cm^3, and the underlying basal group has a lower density of ~2.62 g/cm^3. It appears that an overall uphole increase in deposition of denser siliciclastic mineral debris is recorded.

Stratigraphic correlation

The complete and continuous composite depth scale and splice at Site U1344 is constructed from 0.0 to 332.02 m CCSF-A (Tables T24, T25). The continuous splice ranges from the top of Core 323-U1344A-1H to Section 323-U1344A-31X-5, 50 cm. The appended cores range from Cores 323-U1344A-32X to 79X (790.37 m CCSF-A), with a constant affine value of 43.78 m. All splice points in the interval of 0–50 m CCSF-A are clear and convincing based on multiple data types. The splice tie point between Sections 323-U1344A-5H-7, 4.44 cm, and 323-U1344D-6H-3, 79.88 cm (51.99 m CCSF-A), is uncertain and could be moved ~2.4 m shallower in Core 323-U1344D-6H with equal uncertainty. This is a point to be resolved with postcruise data. The splice tie points between Sections 323-U1344E-6H-6, 112.47 cm, and 323-U1344A-6H-4, 122.06 cm (60.40 m CCSF-A), between Sections 323-U1344E-14H-1, 10.92 cm, and 323-U1344D-14H-2, 136.02 cm (140.43 m CCSF-A), and Sections 323-U1334A-16H-7, 1.04 cm, and 323-U1334D-17H-4, 1.34 cm (175.52 m CCSF-A), are uncertain because of low signal amplitude in magnetic susceptibility.

Downhole measurements

Two tool strings were deployed in Hole U1344A: the triple combo and the FMS-sonic combination. Overall, the caliper of the density sonde shows an irregular borehole with a particularly large-diameter interval between 170 and 260 m WSF but with very good conditions in the lower section. Deeper in the borehole, small enlargements regularly spaced every ~9.5 m indicate where the bit was sitting whenever a core was recovered. However, all the calipers show that the tools made at least partial contact with the formation over most of the interval logged, suggesting that the overall quality of the data is good. Irregular hole size has an effect on measurements that require good contact with the formation, namely density and porosity. The anomalously low density values between 230 and 250 m WSF within the 100 m interval with the largest hole size are probably erroneous, as are most neutron porosity measurements in this entire interval. The quality of the logs can also be assessed by comparison with the NGR and GRA track data and with the MAD measurements made on cores recovered from Hole U1344A. Except for two short intervals with lower density logging data

(230–250 and 420–430 m WSF), all density data sets are in good agreement, confirming overall good data quality despite the enlarged hole. Comparison of the gamma ray logs measured during the main pass of the two runs shows excellent repeatability.

Logging Unit 1 (100–330 m WMSF) is characterized mainly by a steady increase with depth in V_P and V_S, whereas the other log data remain mostly uniform despite some variability such as in gamma radiation. The bottom of this unit is defined by a noticeable drop in V_P, V_S, gamma radiation, density, and resistivity immediately above a sharp peak in these measurements, particularly in V_S and resistivity, indicating a fine, stiff layer. This sequence corresponds to a core with poor recovery. Logging Unit 2 (330–460 m WMSF) is almost uniquely defined by the V_P and V_S logs, both of which increase steadily through the unit. Gamma radiation and density also increase with depth in this unit in a more subdued manner. The top of logging Unit 3 (460–620 m WMSF) is defined by an inflection in the velocity profiles, which, combined with a decreasing trend in density, generates the strong reflector at 4.83 s two-way traveltime. The variability with depth in gamma radiation and in most logs displays a cyclicity more clearly defined than in the upper units. Finally, the top of logging Unit 4 (620–745 m WMSF) is defined by a sharp increase in V_P, V_S, gamma radiation, and density, as well as by a significant change in the trends of all the logs. As in the deepest unit of Site U1343, the gamma ray, potassium, thorium, density, resistivity, V_P, and V_S logs all display a variability with depth of wider amplitude and lower frequency than in the upper units, suggesting a significant change in deposition history and rates.

The APCT-3 tool was successfully deployed three times in Hole U1344A. The measured temperatures ranged from 4.51°C at 47.1 m DSF to 9.57°C at 142.1 m DSF and closely fit a linear geothermal gradient of 53.3°C/km. The temperature at the seafloor was 1.65°C based on the average of the measurements at the mudline during all the APCT-3 deployments. A simple estimate of the heat flow can be obtained from the product of the geothermal gradient and the average thermal conductivity (0.911 W/[m·K]), which gives a value of 48.5 mW/m^2, within the range of previous measurement in the area

Sedimentation rates

Sedimentation rates observed at Site U1344 are mostly similar to values within a narrow range of 29–50 cm/k.y. throughout Holes U1344A, U1344D, and U1344E (Table T26). One exception is the interval between the top and the bottom of the Cobb Mountain Subchron (459.0–469.6 m CCSF-A), which resulted in 89 cm/k.y. Based on sedimentation rates, the bottom age of Hole U1344A was determined to be ~1.9 Ma (Fig. **F58**).

Site U1345

Background and objectives

The primary objective of drilling at Site U1345 (prospectus Site NAV-1B) was to study high-resolution Holocene–late Pleistocene paleoceanography at a proximal gateway location to the Arctic Ocean at a water depth of ~1008 m. The drill site is located on an interfluve ridge near the large, broad head of Navarin submarine channel off the Bering Sea shelf (Figs. **F1, F59, F60, F61, F62**) (Normark and Carlson, 2003). We anticipated that this site received an ample supply of terrigenous sediments from the shelf during the glacials. This is also in the area of high biological productivity called the Green Belt. The Green Belt is formed by the BSC, which originates in the incoming Alaskan Stream water that flows through the western Aleutians into the Bering Sea (Taniguchi, 1984; Springer et al., 1996). Farther northwest, higher primary productivity and organic carbon is observed at the seafloor (Springer et al., 1996). Thus, past impingement by the dissolved OMZ was highly expected at this site. Because the expected sedimentation rates were high with intermittently laminated sediment of millimeter to submillimeter thickness (see below), we expected to be able to reconstruct detailed climate change of submillennial timescales. Therefore, we anticipated comparing data from this site with those of other pertinent high-resolution records from such places as the Santa Barbara Basin, the Cariaco Basin, and GISP2. It is also important to compare the vertical extent of water mass conditions on a basin-wide scale that includes the Bowers Ridge, gateway, and Umnak sites.

Furthermore, this site is located close to the maximum extent of the present-day seasonal sea ice cover. Thus, we expected this site to have been extensively covered by seasonal or perennial sea ice during the glacial low sea level stands. Due to its proximity to the location of sea ice formation, where cold and dense brine is expelled when sea ice is formed, this site, as well as Site U1344, provides crucial information regarding the formation of the North Pacific Intermediate Water.

This relatively shallow drill site in the gateway region to the Arctic Ocean can also be used to study the impact of subseafloor microbes on biogeochemical fluxes in the highest surface ocean productivity areas of the drill sites in the Bering Sea. Organic-fueled subseafloor respiration and its impact on biogeochemistry in such a highly productive region has not previously been quantified. To do this, the drilled sediments in the gateway region were used to determine subseafloor cell abundance and to investigate the link between the mass and characteristics of subseafloor microbes and the extent of export productivity from the surface ocean (Takahashi et al., 2000).

Reports of sedimentation rates at this site location vary significantly, ranging from 14 cm/k.y. during the Holocene and 91 cm/k.y. during the LGM to as much as 242 cm/k.y. during the deglaciation (Cook et al., 2005). Prior to drilling, recovery of sections from the Holocene to late Pleistocene were expected at this site.

Lithostratigraphy

Only one lithologic unit was recognized at Site U1345. Unit I comprises the same time period as Unit I at the other sites: the middle Pleistocene to the Holocene. Site U1345 is distinct among the near-shelf sites due to the abundance and generally coarser texture of the siliciclastic component in the sediments as well as the higher frequency of laminated intervals. Intervals characterized by >25% sand and by thin sandy layers occur at all depths in all the holes drilled at this site. The laminations and thin-bedded sediments are numerous and well correlated between holes.

Site U1345 is located in the central portion of the modern OMZ. The sediments deposited at this site can provide important information concerning Pleistocene to Holocene variability of bottom water oxygen concentrations. The preservation of laminated and thinly bedded sediments (beds <10 cm thick) could be interpreted as the result of a reduction of the activity of benthic macrofauna due to low oxygen concentrations in the bottom waters and surface sediments. Laminations do not have a clear signature in the physical property or reflectance data as observed at Site U1342.

The laminated intervals can be divided into two categories based on the abundance of biogenic grains: (1) couplets or triplets of diatom oozes, mixed siliciclastic/biogenic sediments, and siliciclastic sediments, or (2) couplets of siliciclastic sediments of alternating textures that may include minor (<40%) amounts of diatoms. Laminated sediments of the first category are similar to laminated intervals at other sites, which are typically biogenic rich, olive-green, dark olive-gray, and very dark greenish gray. This category of lamination seems to occur mainly during interglacials. This relationship supports previous observations of higher flux of diatoms during interglacial compared to glacial periods (Okazaki et al., 2005). The second category of laminated sediments is mainly siliciclastic and unique to Site U1345. This type of lamination occurs in sediments that are tentatively identified as deposited during glacial conditions. Since these sediments are not biogenic rich, changes in intermediate water ventilation may have been the controlling parameter for bottom water oxygen concentrations during these periods.

We observed intermittent finely disseminated authigenic carbonates deeper than ~30 m CSF in all holes at this site. The SMTZ is at ~6.5 m CSF, the shallowest observed during Expedition 323. Calcium and magnesium concentrations in the pore water decrease toward the SMTZ, suggesting active authigenic carbonate precipitation at and below this depth today.

Few ash layers were observed at Site U1345. The ashes that do appear are light colored, suggesting that their source is explosive rhyolitic volcanism. This site is distant from the nearest likely source of volcaniclastic grains, the Aleutian arc, so the transport mechanism must have been one capable of widespread dissemination.

The lithologies at Site U1345 are sandier than at any other site from Expedition 323. Lithologies with >25% sand and thin sandy layers occur throughout all holes. The presence of this coarse material is probably related to the position of Site U1345 at the crest of an interfluve at the mouth of Navarin Canyon. The siliciclastic grain sizes at Site U1345 contrast even more strongly with Site U1339, located on a submarine plateau isolated from the continental shelf. At the latter site virtually no sand-sized grains were recorded. This may be due either to decreased transport of terrigenous material to the site or to a high biogenic flux to Site U1339 sediments.

Biostratigraphy

High-frequency variations can be seen in the abundance and composition of all microfossil groups. The decrease in sea ice diatoms, the increase in dinoflagellates, planktonic foraminifers, and calcareous nannofossils, and the percent of open ocean diatoms *Neodenticula* and *Actinocyclus* and the high-productivity dinoflagellate *Islandinium minutum*, which are associated with increases in the low-oxygen benthic foraminifer *Bulimina* aff. *exilis*, indicate the approximate depth intervals of distinct interglacials (at ~5, 40, 130, and 145 m CCSF-A). These intervals also coincide with low GRA bulk density and are consistent with the age model.

Overall, the distribution of calcareous nannofossils at Site U1345 seems to follow glacial–interglacial cyclicity with higher numbers during interglacials. Changes in their abundances generally reflect changes in environmental factors such as temperature and nutrients. Calcareous nannofossils do not become dominant components of the biota in areas of sea ice coverage. Elevated content of subpolar planktonic foraminifer species with *G. bulloides* appear at ~5, 40, 90, 130, and 145 m CCSF-A, largely coinciding with the inferred interglacials. This shows increased sea-surface temperatures during these intervals. *G. bulloides* is controlled by temperature rather than food availability in the Bering Sea (Reynolds and Thunell, 1985; Asahi and Takahashi, 2007). These periods of elevated sea-surface temperatures probably reflect interglacial conditions.

As at the previous Bering Sea sites, the benthic foraminifer assemblage faunal composition shows large changes in species dominance. These changes are interpreted as shifts in local oxygen concentrations associated with surface productivity and/or deepwater ventilation on Milankovitch timescales. *Bulimina* aff. *exilis* is generally regarded as a low-oxygen/deep infaunal species (Bubenshchikova et al., 2008; Kaiho, 1994) and occurs in samples associated with high productivity and low sea ice. This suggests that higher productivity during some interglacials may have caused an expansion and intensification of the OMZ.

The LO of *Proboscia curvirostris* and the LO of *Thalassiosira jouseae* were observed from 71.1 to 73.3 m CSF, depending on the hole, giving an age of 0.3 Ma. In general, diversity is lower for this site than at the other gateway sites. The diatom assemblage for this zone (NPD11) is dominated by *Thalassiosira antarctica* spores, *Fragilariopsis* spp., *Paralia sol*, *P. sulcata, Thalassiothrix longissima, Thalassionema nitzschioides, T. latimarginta* s.l., and to a lesser extent *Neodenticula seminae*, *Bacteriosira fragilis*, and *Actinocyclus curvatulus*. The core interval above the LO of *P. curvirostris* to the recent is assigned to *Neodenticula seminae* Zone NPD12. This zone is dominated by *T. antarctica* spores, *T. latimarginta* s.l., *P. sulcata*, *T. hyalina*, *B. fragilis*, and the minor presence of *N. seminae* and *A. curvatulus*. In general, this site reveals a higher proportion of coastal neritic diatoms, together with freshwater species, than the other gateway sites (Sites U1343 and U1344). Low proportions of sea ice diatoms and high proportions of open water diatoms correspond well with the interglacial horizons. The last occurrence of silicoflagellate *Distephanus octonarius* (0.2–0.3 Ma) was observed in Core 323-U1345A-9H (71.01–80.64 m CSF).

Radiolarian zones at Site U1345 could not be established due to the absence of *Stylatractus universus*. Four radiolarian datums derived in the subarctic Pacific were identified at this site. The LO of *Lychnocanoma nipponica sakaii* (50 ka) and *Spongodiscus* sp. (280–320 ka) were determined. The LOs of *Amphimelissa setosa* (70–90 ka) and *Axoprunum aquilonium* (250–410 ka) were supported only by seldom occurrences, indicating uncertain top positions of the stratigraphic age. Estimated sedimentation rates between the LO of *L. nipponica sakaii* and *Spongodiscus* sp. are ~25 cm/k.y. in each hole. Among all radiolarian species, *C. davisiana* shows high fluctuations in abundance, possibly relating to ventilation changes with glacial–interglacial cycles. The *Sphaeropyle langii/robusta* group, which are commonly found at Sites U1343 and U1344, show very low abundances. Because abundances of *Sphaeropyle langii/robusta* group at the shallower Sites U1339, U1340, and U1342 were also very low, their dwelling depth might be in deep water below 1000 m.

The dinoflagellate species *Brigantedinium* spp. is one of the most ubiquitous taxa among protoperidinials, and its distribution in modern sediments is closely related to primary productivity in temperate regions and also to polar and subpolar regions of the North Atlantic and Arctic oceans with seasonal sea ice coverage (Rochon et al., 1999). *Islandinium minutum* is one of the principal, if not the dominant, component of assemblages in the modern Arctic Ocean (Rochon et al., 1999; Head et al., 2001). The overall abundance of dinocysts and particularly the above-mentioned species suggests high productivity and upwelling during prominent interglacials. Extremely high abundances of dinocysts, especially at the mudline in Hole U1345B and Sections 323-U1345A-5H-CC (44.4 m CCSF-A) and 13A-CC (130.6 m CCSF-A) suggest interglacial periods. This coincides with relatively low pollen and spore concentrations.

Paleomagnetism

No polarity reversal boundary was observed in the cores at Site U1345; therefore, the whole sequence is assigned to the Brunhes normal polarity zone (Fig. **F63;** Table **T27**). The relative paleointensity pattern is consistent with that seen at all other sites. Based on the correlations, MIS 1–12 were assigned. The significant changes in NRM indicate notable effects of early sediment diagenesis, as this has also been seen at the previous sites. Significant magnetic mineral dissolution starts within 5 m CSF due to processes related to AOM and sulfate reduction. This is also evident at Sites U1344, U1343, and U1339. The active zone of dissolution appears to be limited to the top 10 m so that magnetization does not change significantly at deeper depths.

Geochemistry

Of all the sites investigated, Site U1345 shows the shallowest SMTZ at ~6.25 m CSF (Fig. **F64**). Likewise, this site is characterized by the steepest flux of methane into this zone and the highest interstitial water hydrogen sulfide concentrations. Similar to the other shelf sites (Sites U1343 and U1344), the almost linear sulfate and methane profiles suggest that AOM coupled with sulfate reduction accounts for most of the sulfate consumption in the sediment. Preliminary modeling of the DIC profile suggests that net DIC production in the SMTZ accounts for 70% of the DIC production in the top sediment layers. The organic matter degradation products phosphate and ammonium show accumulation in the pore water, with the distinct minimum in phosphate concentration between 22.25 and 27.25 m CSF. However, this also indicates that the consumption of this species is most likely due to the formation of phosphate-bearing minerals such as apatite.

The occurrence of high concentrations of interstitial water hydrogen sulfide in the SMTZ can be attributed to very high sulfate reduction rates at this depth and probably also to a lack of a sufficient pool of reactive Fe mineral phases (e.g., Fe [oxhydr]oxides) that can react with hydrogen sulfide on short timescales. Distinct peaks in dissolved Fe and Mn concentrations immediately below the SMTZ are the result of microbial dissimilatory Fe reduction. Calcium and magnesium profiles show depletion at the depth of the present SMTZ, suggesting the formation of authigenic Mg-rich carbonate (e.g., dolomite) driven by the production of DIC during AOM and an increase in pH leading to oversaturation of the pore water with respect to carbonate. Interestingly, the dissolved calcium profile shows a further decrease with depth and a minimum concentration at ~40 m CSF. This depth corresponds to a dolostone layer found at 40.27 m CSF. Sites U1343, U1344, and U1345 furthermore show high concentrations of dissolved Ba in the pore water and indicate a sink of this ion just above the SMTZ. The distribution of Ba at these sites can be attributed to diagenetic remobilization of Ba deposited as biogenic barite into the sulfate-depleted pore water (von Breymann et al., 1992). The upper end of the SMTZ where the sulfate and dissolved Ba profiles overlap marks the present front of authigenic barite formation.

Microbiology

Samples for abundance of prokaryotes were collected adjacent to interstitial water whole-rounds. High-resolution sampling took place in the microbiology-dedicated cores as well as in additional samples taken once per core to APC refusal. It is of interest to examine the relationship between microbial productivity and diversity in the uppermost 25 m of sediment dedicated for microbial ecology. A special focus will be directed toward the function of Archaea in the sulfate reduction zone, the SMTZ, and the methanogenesis zone. The sulfate–methane transition is a hot spot for microbial activity and abundance within deep-sea sediments (D’Hondt, Jørgensen, Miller, et al., 2003), and we will thus expect an increase in the abundance and activity of microbial life; the remainder of the core should see a significant decrease with depth in both active and benign microbial life. To obtain an estimate of active subseafloor life, samples were also taken in low resolution for catalyzed reporter deposition-fluorescence in situ hybridization (CARD-FISH) at all aforementioned zones and at depth.

We will rely on estimates generated by shipboard participants (cell counts and geochemical profiles) and shore-based participants (amino acid and amino sugar composition) as indicators of productivity. We will examine overall bacterial and archaeal diversity by a combination of conventional 16S ribosomal ribonucleic acid (rRNA) clone libraries and quantitative polymerase chain reaction (qPCR) and/or a new quantitative community fingerprinting method involving automated ribosomal intergenic spacer analysis (ARISA) (Ramette, 2009).

Physical properties

Wet bulk densities in Hole U1345A appear to be higher by 0.1–0.2 g/cm^3 than those measured in Hole U1344A in the uppermost 150 m of the sedimentary section; the higher densities of sediment in Hole U1345A probably reflect their higher sand content.

Similar to stratigraphic sections drilled at Beringian margin sites (Sites U1343 and U1344), GRA density values in Hole U1345A also document rhythmic fluctuations. Magnetic susceptibility measurements seem to have realistically recorded the downhole contour of changing values that are functions of many factors. An explanation for the higher counts for the Hole U1345A section is its coarser and higher content of siliciclastic mineral debris. In the downhole profile the contour of NGR readings is broadly similar to that of GRA bulk density. The downhole distribution of thermal conductivity readings displays an overall trend of increasing conductivity. Downsection profiles of MAD-measured porosity and water content record a progressive decrease in average values. The downhole distribution of water content and porosity is rhythmic. Little change is seen in average grain density with depth. The higher average grain density (2.75 g/cm^3) of Unit I in Hole U1345A is interpreted to be a consequence of its greater abundance of coarse siliciclastic grains.

Stratigraphic correlation

The composite depth scale and splice at Site U1345 is complete and continuous from 0.0 to 167.6 m CCSF-A (Tables T28, T29). The splice ranges from the top of Core 323-U1345A-1H to Section 323-U1345D-16H-7, 146.6 cm. There are no appended intervals. Most of the splice points are clear and convincing based on the multiple copies of the section recovered in five holes. The splice tie point between Sections 323-U1345A-10H-4, 50.0 cm, and 323-U1345C-10H-1, 100.18 cm (93.02 m CCSF-A), is uncertain because Core 323-U1345A-10H contains disturbed flow-in starting approximately in the middle of Section 10H-4 and extending through the bottom of Section 10H-7. The disturbed section is not included in the splice. The splice tie point between Sections 323-U1345D-10H-7, 58.4 cm, and 323-U1345A-11H-3, 115.4 cm (103.284 m CCSF-A), and between Sections 323-U1345D-13H-6, 138.4 cm, and 323-U1345A-14H3, 94.7 cm (133.637 m CCSF-A), are tentative because of low signal amplitudes in MS477. The cumulative offset between CSF and CCSF-D depth scales is roughly linear. The affine growth factor at Site U1345 is 1.11.

Downhole measurements

The only downhole measurements made at Site U1345 were three deployments of the APCT-3 tool in Hole U1345A. The measured temperatures ranged from 4.92°C at 42.4 m DSF to 8.15°C at 108.9 m DSF, indicating a local geothermal gradient of 48.5°C/km. A simple estimate of the heat flow can be obtained from the product of the geothermal gradient and the average thermal conductivity, which gives a value of 51.6 mW/m^2, in agreement with existing measurements in the area.

Sedimentation rates

Based on the four holes studied, the following two mean radiolarian biostratigraphic datums were employed for the determination of sedimentation rates: the LO of *Lychnocanoma nipponica sakaii* and the LO of *Spongodiscus* sp. (Ling, 1973). Only one sedimentation rate of 28 cm/k.y. appears to be applicable to this site (Fig. F65; Table T30). This sedimentation rate is lower than that of the adjacent, deeper Site U1344 (~39 cm/k.y.).

Operations

Site U1339

We arrived at Site U1339 early on 16 July 2009 after a 6.5 day, 1782 nmi transit from Victoria, British Columbia, Canada, and operations officially began.

Four holes were drilled at Site U1339 (Table T2) employing the APC at a water depth of 1867 m on Umnak Plateau, with the deepest Hole U1339D reaching a maximum depth of 200 m DSF. One relatively shallow and three relatively deep holes were drilled and cored as follows: Hole U1339A, cored to 34 m DSF; Hole U1339B, cored to 196 m DSF; Hole U1339C, cored to 195 m DSF; and Hole U1339D, cored to 200 m

DSF. The first four cores of Hole U1339B (Cores 323-U1339B-1H to 4H) were primarily used for subseafloor microbial study with both PFTs and whirlpacks deployed. The remainder of the cores were used for paleoceanographic studies. Most of the cores had nearly 100% or greater recovery because of gas expansion except for two short cores (Cores 323-U1339B-13H, 2 m, and 323-U1339C-16H, 4.5 m) that were recovered when the APC fired into an unknown object, most likely a glacial dropstone.

Hole U1339A

Hole U1339A was spudded at 0430 h on 17 July 2009. The first core was shot with the bit at 1873 m DRF and recovered the mudline and 4.94 m of core. The hole was terminated after Core 323-U1339A-4H with a suspected bottom-hole assembly (BHA)/coring system problem resulting in almost 100,000 lb of overpull on the last core. The drill string was tripped out of the hole, the coring system components were inspected, and several parts were changed. No conclusive evidence of the encountered mechanical problem was found. The BHA was run and the coring system was tested successfully in the water column.

Hole U1339B

The vessel was offset 20 m, the rest of the string was tripped to the seafloor, and Hole U1339B was spudded at 2315 h on 17 July 2009. The first four cores (Cores 323-U1339B-1H to 4H) were dedicated to microbiology with both PFTs and whirlpacks deployed. The remainder of Hole U1339B recovered the sedimentary sequence from the total depth of Hole U1339A down to 196 m DSF, with one short core (Core 323-U1339B-13H) recovered when the APC fired into an unknown object, most likely a glacial dropstone. The nonmagnetic core barrel was switched to a steel core barrel when the resistance became exceedingly high with Core 323-U1339B-19H. Hole U1339B was cored to 196 m DSF, and coring ended at 2010 h on 18 July 2009 when the bit cleared the seafloor.

Hole U1339C

The vessel was offset 28 m and Hole U1339C was spudded at 2230 h on 18 July 2009. The first core was more than 9.5 m long but contained the mudline at its top. Core advance was a continuous 9.5 m except for Core 323-U1339C-16H, which contacted an apparent dropstone at 4.5 m. The nonmagnetic core barrel was used through Core 323-U1339C-17H, and APC coring proceeded with a steel core barrel through Core 21H to 195.8 m DSF. The drill string cleared the seafloor at 1610 h on 19 July 2009, officially ending Hole U1339C.

Hole U1339D

The vessel was offset 28.3 m and Hole U1339D was spudded at 1724 h on 19 July 2009. Core 323-U1339D-1H was 6.6 m long. All cores taken below the first one were 9.5 m long with the exception of one short core resulting from premature firing of the APC. The nonmagnetic core barrel was used through Core 323-U1339D-17H, and APC coring proceeded with a steel core barrel through Core 22H to 200.0 m DSF. Rig-up for wireline logging in Hole U1339D started at 1130 h on 20 July 2009. The triple combo and FMS-sonic tool strings were deployed; both obtained good data. The drill string was pulled and secured for transit. Transit to the next site, Site U1340 (BOW-12B), began at 0745 h on 21 July 2009. In all, APC coring for Site U1339 totaled 69 cores, 642.2 m penetrated, and 643.67 m recovered, for 103.1% recovery.

Site U1340

We arrived at Site U1340 at 2300 h on 22 July 2009 after a 1.5 day, 344 nmi transit from Site U1339. Hole U1340A was spudded at 0520 h. A total of four holes, one relatively deep and three shallow, were drilled and cored employing the APC and XCB at a water depth of 1306 m on Bowers Ridge (Table T2). A complete set of site-specific tide tables was provided by the science party for Site U1340 and were used to make adjustments relative to initial mudline core and for each successive core in each hole. The APCT-3 temperature tool was deployed four times, and three out of four of the data points fell on a linear curve describing a temperature gradient of +4.34°C per 100 m of depth. Overall recovery for Site U1340 using the APC and XCB coring systems was 91.0%.

Hole U1340A

Hole U1340A was spudded at 0520 h on 23 July 2009. Hole U1340A was cored to 603.6 m DSF, employing both the APC and XCB. APC recovery was 100%, whereas XCB recovery averaged 61%. APC coring continued through Core 323-U1340A-17H to 1461.9 DRF using nonmagnetic coring assemblies with the FlexIt orientation tool installed. The standard steel coring assemblies were used from Cores 323-U1340A-18H through 42H. APC coring was terminated after Core 323-U1340A-42H after two successive short, incomplete strokes of the core barrel. The XCB coring system was then deployed at Core 323-U1340A-43X and coring continued with the XCB system until Core 62X. After three straight zero-recovery runs, the APC coring system was redeployed. Coring with the APC system through Core 323-U1340A-67H was successful in recovering ~25 m of very sandy sediment. The XCB system was redeployed and the hole was terminated after Core 323-U1340A-71X when the XCB cutting shoe spacer sub failed, leaving a portion of the sub and the XCB cutting shoe at the bottom of the hole. The drill string was pulled back to the seafloor at 2103 h on 25 July 2009, officially ending the hole. Shear pressures were consistent throughout the coring process at 2800 psi. Recovery for Hole U1340A using the APC coring system was 105.0% with 398.8 m recovered. Recovery for Hole U1340A using the XCB coring system was 61.0% with 136.7 m recovered. Combined recovery for Hole U1340A using both the APC and XCB coring systems was 88.7%.

Hole U1340B

Hole U1340B officially began when the bit cleared the seafloor at 2103 h on 25 July 2009, ending Hole U1340A. The vessel was offset 350 m east of Hole U1340A. The top drive was picked up and the drill string was spaced out, placing the bit at 1305.4 m DRF or 5 m above the “corrected” precision depth recorder (PDR) depth of 1310.4 m DRF. The first APC barrel was pressured up and fired, the barrel recovered 6.4 m of core, and an official seafloor depth was established at 1308.5 m DRF. Hole U1340B was spudded at 2340 h on 25 July 2009. Nonmagnetic coring assemblies and the FlexIt core orientation system were used through Core 323-U1340B-6H. Hole U1340B ended at 0400 h on 26 July 2009 when the bit cleared the seafloor. Shear pressures were consistent throughout the coring process at 2800 psi. Average core recovery for the APC was 103.0%. Total depth of Hole U1340B was 1362.4 m DRF or 53.9 m CSF.

Hole U1340C

Hole U1340C officially began when the drill string cleared the seafloor at 0400 h 26 July 2009. The ship was offset 300 m south from Hole U1340A. A new PDR depth was established and the bit was placed at 1313 m DRF to optimize the core breaks between Holes U1340A and U1340B. The APC was deployed and Hole U1340C was spudded at 0620 h on 26 July 2009. Unfortunately, a mistake in the corrected PDR depth resulted in the first core being taken well below mudline. The 9.5 m of core recovered with the APC (Core 323-U1340C-1H) failed to establish the seafloor depth. APC coring continued through Core 323-U1340C-3H to 1341.5 m DRF using the FlexIt core orientation system and nonmagnetic coring assemblies. With the exception of the first core, shear pressures were consistent throughout the coring process at 2800 psi. Overall core recovery for the APC was 105.3%. The drill string was pulled clear of the seafloor at 0835 h on 26 July, officially ending Hole U1340C.

Hole U1340D

Hole U1340D officially began when the drill string cleared the seafloor at 0835 h 26 July. The ship was offset 20 m from Hole U1340C at 180°. This hole was spudded at 0905 h on 26 July, and the 7.3 m recovered with Core 323-U1339D-1H established a seafloor depth of 1304.7 m DRF. Three APC cores were shot to 26.3 m CSF. APC coring through Core 323-U1340D-3H used the nonmagnetic coring assemblies with FlexIt orientation. Shear pressures were consistent throughout the coring process at 2800 psi. APC core recovery was 103.5%. The drill string was then pulled clear of the seafloor and secured for transit. Once the drill collars were racked back and the rig floor was secured for transit, control was transferred from dynamic positioning (DP) to the bridge. The ship was placed in cruise mode at 1534 h on 26 July for the scheduled 6 h (65 nmi) transit to Site U1341 (BOW-14B). Official APC coring totals for Site U1340 included 83 total cores, 712.3 m penetrated, and 648.1 m recovered, for 91.0% recovery.

Site U1341

A positioning beacon was deployed at 2311 h on 26 July after our arrival at Site U1341. Three holes were drilled at this site (Table T2). A complete set of site-specific tide tables was provided by the science party for Site U1341, and these were used to make adjustments relative to initial mudline core and for each successive core on each hole. A new continuous APC coring depth record was established when Hole U1341B reached 458.4 m DSF. APC coring totals for Site U1341 included 148 total cores, 1189.4 m penetrated, and 1201.54 m recovered, for 101% recovery. The time spent at Site U1341 was 170.5 h or 7.1 days.

Hole U1341A

Hole U1341A was spudded at 0510 h on 27 July. The first APC barrel recovered 3.04 m of core and an official seafloor depth was established at 2150.9 m DRF. APC coring continued through Core 323-U1341A-20H to 2334.4 m DRF using nonmagnetic coring assemblies and with the FlexIt orientation tool installed. The nonmagnetic coring equipment was changed to the standard APC coring system and coring continued. Coring with the APC system was suspended at Core 323-U1341A-41H after two successive short, incomplete strokes of the core barrel. Overall recovery for Hole U1341A using the APC coring system was 101% with 364.94 m recovered.

Hole U1341B

The vessel was offset 20 m east of Hole U1341A. Hole U1341B was spudded at 2245 h on 28 July. The first APC barrel recovered 8.7 m of core and an official seafloor depth was established at 2150.9 m DRF. APC coring continued through Core 323-U1341B-18H to 166.7 m DSF using nonmagnetic coring assemblies and with the FlexIt orientation tool installed. Coring with the APC system was suspended at Core 323-U1341B-56H after three successive short, incomplete short strokes of the core barrel. A new continuous APC coring record was established with continuous piston cores from the mudline to 458.4 m DSF or CSF. The XCB coring system was then deployed from Cores 323-U1341B-57X through 71X. The hole was terminated after Core 323-U1341A-71X when the total depth of the hole reached 600.0 m DSF. APC core recovery for Hole U1341B was 102% with 467.64 m recovered. XCB core recovery for Hole U1341B was 88.2% with 126.9 m recovered. Total core recovery was 98.7% with 594.5 m recovered. The coring tools were secured and the hole was swept clean and then displaced with 200 bbl of high-viscosity logging mud. No fill was identified at total depth. The top drive was set back and the drill pipe was tripped to 80 m DSF while monitoring the hole for problems. The end-of-pipe (EOP) was placed at ~80.0 m DSF. Rig-up for wireline logging began at 1930 h on 31 July. Two logging strings were deployed. The triple combo tool string reached a total hole depth of 600 m WSF and good quality logs were obtained. The FMS-sonic tool string also reached total depth of 600 m WSF and also obtained good data on both passes. Wireline logging in Hole U1341B was successfully concluded and all logging equipment was rigged down by 1530 h on 1 August.

Hole U1341C

Operations in Hole U1341C commenced at 1555 h on 1 August. The vessel was moved 20 m east of Hole U1341B. Hole U1341C was spudded at 1810 h. The first APC barrel recovered 5.5 m of core and an official seafloor depth was established at 2150.9 m DRF. APC coring continued through Core 323-U1341C-17H to 147 m DSF using nonmagnetic coring assemblies and with the FlexIt orientation tool installed. Standard steel core barrels were then installed and coring continued through Core 323-U1341C-27H (230 m DSF). Overall core recovery for the APC was 242.06 m (106.2%).

Site U1342

Four holes were drilled at this site. The first was cored using the APC system to refusal. When refusal was met early, the XCB system was deployed to confirm formation material. The XCB recovered 0.5 m of basalt, effectively ending Hole U1342A. The second hole, U1342B, was dedicated to microbiology. Hole U1342C was cored with the APC system to 45.4 m DSF. The last hole, U1342D, was APC cored to 44.0 m DSF. At that point, a center bit was dropped and the hole was drilled ahead for 18.6 m to determine if the basalt was continuous or not. At a drilling break, the XCB system was deployed and used to take 13 cores of hard rock to the total hole depth of 127.4 m DSF. A complete set of site-specific tide tables was provided by the science party for Site U1342. The tide tables were used to make adjustments relative to initial mudline core and for each successive core in each hole. APC coring totals included 182 m penetrated with 194.11 m recovered (a recovery of 106.7%). XCB coring totals for Site U1342 included 66.1 m of penetration with 41.54 m recovered (62.8% recovery). The total cored interval was 248.1 m with 235.65 m of core recovered for a 95% total recovery. The time spent at Site U1342 was 33.25 h or 1.4 days.

Hole U1342A

Hole U1342A was spudded at 1320 h on 3 August, recovering 1.8 m of sediment in the first APC barrel and establishing an official seafloor depth of 829.7 m DRF. APC coring continued through Core 323-U1342A-8H to 49.3 m DSF. Coring with the APC system was suspended after two successive short, incomplete strokes of the core barrel and apparent refusal. Three meters were then drilled with the APC/XCB bit and the XCB system was deployed; a short core (1 m) was drilled to identify the material at APC refusal. Basalt was recovered and Hole U1342A was terminated. Overall recovery for Hole U1342A using the APC coring system was 115.5% with 56.93 m recovered. Recovery for the XCB core was 0.46 m or 46% recovery.

Hole U1342B

The vessel was offset 20 m east of Hole U1342A. Hole U1342B was spudded at 2315 h on 3 August. The barrel recovered 5.33 m of core, and an official seafloor depth was established at 830.4 m DRF. APC coring continued through Core 323-U1342B-5H to 43.3 m DSF.

Hole U1342C

The vessel was moved 20 m east of Hole U1342B. The first APC barrel recovered 7.2 m of core and an official seafloor depth was established at 830.3 m DRF. Hole U1342C was spudded at 0235 h on 4 August. APC coring continued through Core 323-U1342C-6H to refusal. Overall recovery for Hole U1342C using the APC coring system was 103.7% with 47.06 m recovered.

Hole U1342D

The vessel was moved 20 m east of Hole U1342C. The first APC barrel recovered 6.0 m of core and an official seafloor depth was established at 829.7 m DRF. Hole U1342D was spudded at 0830 h on 4 August. APC coring continued through Core 323-U1342D-5H to 873.7 m DRF. On reaching refusal, the center bit was dropped and the hole was drilled 18.6 m to see if there were sediments under the layer of hard rock (basalt). After a drilling break was observed, the XCB coring system was deployed and used successfully to core an additional 65.10 m into the formation. Overall recovery for Hole U1342A using the APC coring system was 102.9% with 45.29 m recovered. Recovery with the XCB core was 41.08 m or 63.1% recovery.

Site U1343

Five holes were cored at Site U1343. Hole U1343A was cored with the APC system and drilled to 201.5 m DSF. Hole U1343B was dedicated to microbiology and cored to 35.5 m DSF. Hole U1343C was cored with the APC system to 234.2 m DSF. Only a single mudline core was taken in Hole U1343D and a decision was made to attempt another mudline core for stratigraphic correlation. Hole U1343E was cored with the APC and XCB systems to 744.3 m DSF. The XCB system was used for Cores 323-U1343E-42X through 45X, where we encountered dry sediment and retrieved a destroyed core liner (42X), and for the deepest cores (Cores 323-U1343-50X through 83X). The shallower interval cored with the XCB system coincided with a BSR. Generally, coring was routine except for biogenic methane encountered in the cores, which complicated the curation of all cores at this site. APC coring totals for Site U1343 included 98 cores, 860.4 m penetrated, and 859.8 m recovered for 99.9% recovery. XCB coring totals for Site U1343 included 37 cores, 360.6 m penetrated, and 318.14 m recovered for 62.8% recovery. The total cored interval for Site U1343 was 1221.0 m, with 1178.23 m of core recovered for a 96.5% total recovery. The time spent at Site U1343 was 6.7 days.

Hole U1343A

Hole U1343A was spudded at 0305 h on 7 August. The first mudline core recovered 5.5 m of sediment and the seafloor was calculated at 1962.4 m DRF. APC coring continued through Core 323-U1343A-22H to 201.5 m DSF using nonmagnetic coring assemblies. Temperature measurements were taken on Cores 323-U1343A-5H, 9H, and 14H with the APCT-3 temperature tool. Core orientation was taken on all cores with the FlexIt orientation tool, but the data were lost when the computer running the download software was accidentally switched off during the FlexIt operations, causing the program to lose its synchronization with the tool. Overall recovery for Hole U1343A using the APC system was 101.2% with 203.86 m recovered.

Hole U1343B

The vessel was offset 30 m north and Hole U1343B was spudded at 2240 h on 7 August. The first mudline core recovered 6.85 m of sediment and the seafloor was calculated at 1962.4 m DRF. Both PFT and microsphere contamination testing methods were deployed. A total of four APC cores were recovered for microbiological sampling to 35.5 m DSF. Average APC core recovery for Hole U1343B was 97.4% with 34.56 m recovered.

Hole U1343C

The ship was offset 30 m west from the proposed site position. The APC was deployed and Hole U1343C was spudded at 0305 h on 8 August. The first mudline core recovered 7.2 m of sediment and the seafloor was calculated at 1964.2 m DRF. APC coring continued through Core 323-U1343C-26H to 234.2 m DSF using nonmagnetic coring assemblies. Overall recovery for Hole U1343C using the APC coring system was 98.7% with 231.04 m recovered.

Hole U1343D

Hole U1343D was spudded 30 m south of Hole U1343C at 0135 h on 9 August. Based on the stratigraphic correlation of the first and only core, Hole U1343D was terminated at 0135 h. Overall recovery for Hole U1343D using the APC coring system was 100.0% with 8.5 m recovered.

Hole U1343E

There was no offset from Hole U1343D. Hole U1343E was spudded at 0215 h on 9 August. The first core barrel recovered 8.2 m of core and an official seafloor depth was established at 1967.5 m DRF. APC coring continued through Core 323-U1343E-15H using standard steel core barrels. At Core 323-U1343E-16H, the nonmagnetic barrels were put in service and used for the rest of the hole. Coring with the APC system was suspended after Core 323-U1343E-41H was pulled with a ruptured core liner. Core 41H had to be hydraulically pressed out of the core barrel. This coincided with a BSR observed in the seismic data. The core was also noticeably drier and harder at this depth. The XCB coring system was then deployed from Cores 323-U1343E-42X through 45X with good recovery. The APC coring system was then put back in service for Cores 323-U1343E-46H to 49H. At that time we began to get partial strokes of the piston and were having to drill over every core. The XCB system was redeployed and coring continued through Core 323-U1343E-83X to 744.3 m DSF. The coring tools were secured and the hole was swept clean and then displaced with 200 barrels of prepared high-viscosity logging mud. No fill was identified at total depth. Two logging strings were deployed. The triple combo tool string reached total depth of 745 m DSF and good quality logs were obtained. The second logging string consisted of the FMS-sonic tool, which reached total depth of 745 m DSF and also obtained good data on both passes. Wireline logging in Hole U1343E was successfully concluded and all logging equipment was rigged down by 0745 h on 13 August. APC core recovery for Hole U1343E was 100.3% with 381.86 m recovered. XCB core recovery for Hole U1343E was 88.3% with 318.41 m recovered. Total core recovery for Hole U1343E was 94.47% with 700.27 m recovered.

Site U1344

Five holes were cored at Site U1344. The first hole was cored with the APC/XCB systems to 745.0 m DSF. Hole U1344A was then successfully logged with the triple combo and FMS-sonic logging tool strings. The second hole, planned as a dedicated microbiology hole, was cut short due to contamination when the core liner split during mudline coring. Therefore, the third hole was assigned to microbiology. Hole U1344D was cored with the APC system to 286.5 m DSF. The last hole, Hole U1344E, was cored with the APC system to 202.8 m DSF. A complete set of site-specific tide tables provided by the science party was used to make adjustments relative to initial mudline core and for each successive core in each hole. Coring in general was routine except for biogenic methane encountered in the cores, which complicated the curation of all cores at this site. APC coring totals for Site U1344 included 87 cores, 781.8 m penetrated, and 791.1 m recovered for 101.2% recovery. XCB coring totals for Site U1344 included 52 cores, 489.9 m penetrated, and 384.1 recovered for 78.4% recovery. The total cored interval for Site U1344 was 1271.7 m with 1175.19 m of core recovered for a 92.4% total recovery. The time spent at Site U1344 was 8.5 days.

Hole U1344A

The first APC barrel recovered 9.1 m of core and an official seafloor depth was established at 3183.4 m DRF. Hole U1344A was spudded at 0932 h on 14 August. APC coring continued through Core 323-U1344A-26H to 245.6 m DSF using nonmagnetic coring assemblies. The XCB system was deployed and coring continued through Core 323-U1344A-79X to 745.0 m DSF. The coring tools were secured and the hole was swept clean and then displaced with 200 barrels of prepared high-viscosity logging mud. No fill was identified at total depth. The EOP was placed at ~100.0 m DSF. Two logging strings were deployed. The triple combo tool string reached total hole depth of 745 m CSF and good quality logs were obtained. The second logging string consisted of the FMS-sonic tool. This tool string also reached total depth of 745 m CSF on the first pass but reached only 725 m CSF on the second pass as hole conditions began to deteriorate. Good data were obtained on both passes. APC core recovery for Hole U1344A was 103.5% with 264 m recovered. XCB core recovery for Hole U1344A was 78.4% with 384.1 m recovered. Total core recovery for Hole U1344A was 87% with 648.1 m recovered.

Hole U1344B

The vessel was offset 20 m north of Hole U1344A. Hole U1344B was spudded with the APC at 1335 h on 19 August. One APC core was recovered. Unfortunately, Core 323-U1344B-1H came to the surface with a split/damaged core liner and was unfit for microbiological studies.

Hole U1344C

The first APC barrel recovered 7.12 m of core and an official seafloor depth was established at 3184.4 m DRF. Hole U1344C was spudded at 1505 h on 19 August. Both PFT and microsphere contamination testing methods were deployed. A total of four APC cores were recovered for microbiological studies to a depth of 35.6 m. Average core recovery for the APC in Hole U1344B was 94.13% with 33.5 m recovered.

Hole U1344D

The ship was offset 20 m north from Hole U1344C. The APC was deployed and Hole U1344C was spudded at 1940 h on 19 August. The first mudline core recovered 2.73 m of sediment and the seafloor was calculated at 3185.8 m DRF. APC coring continued through Core 323-U1344C-25H to 224.5 m DSF using nonmagnetic coring assemblies. The nonmagnetic coring equipment was changed to the standard APC coring system and coring continued. Coring with the APC system was suspended after Core 323-U1344D-32H at 286.5 m DSF. Only two cores, Cores 323-U1344D-30H and 32H, required drill over. Overall recovery for Hole U1344D using the APC coring system was 99.9% with 286.1 m recovered.

Hole U1344E

The ship was offset 20 m north from Hole U1344D. The first APC barrel recovered 5.3 m of core and an official seafloor depth was established at 3185.7 m DRF. Hole U1344E was spudded at 0750 h on 21 August. APC coring continued through Core 323-U1344E-23H using nonmagnetic coring assemblies. Coring was uneventful and continuous except for a 3 m section at 3276.5 m DRF, which was drilled at the request of the stratigraphic correlator. APC core recovery for Hole U1344E was 101.4% with 202.7 m recovered.

Site U1345

Five holes were cored at this site. With the exception of Hole U1345B, which was cored to 36.7 m DSF for microbiological sampling, four holes were cored to ~150 m DSF. A complete set of site-specific tide tables was provided by the science party for making coring adjustments relative to the initial mudline core and for each successive core in each hole. Coring in general was routine except for biogenic methane encountered in the cores, which complicated the curation of all cores at this site. Two complete splices were obtained at Site U1345 to ~150 m CSF. APC coring totals for Site U1345 included 68 cores, 632.1 m penetrated, and 648.35 m recovered for 102.6% recovery. The time spent at Site U1345 was 2.2 days.

Hole U1345A

Hole U1345A was spudded at 0045 h on 23 August. The first APC core barrel recovered 4.39 m of sediment, establishing a seafloor depth of 1019.1 m DRF. APC coring continued through Core 323-U1345A-16H to 146.9 m DSF using nonmagnetic coring assemblies. Temperature measurements were taken in Cores 323-U1345A-5H, 8H, and 12H with the APCT-3 temperature tool. APC core recovery for Hole U1345A was 101.1% with 148.49 m recovered.

Hole U1345B

The ship was offset 20 m northwest of Hole U1345A. Both PFTs and microspheres were deployed for contamination testing. A total of four APC cores were recovered for use as microbiology samples to 36.7 m. Average core recovery for the APC in Hole U1345B was 104.2% with 38.24 m of sediment recovered.

Hole U1345C

The ship was offset 20 m northwest of Hole U1345B. APC coring continued through Core 323-U1345C-16H to 148.5 m DSF using nonmagnetic coring assemblies. APC core recovery for Hole U1345C was 102.9% with 152.85 m recovered.

Hole U1345D

The ship was offset 20 m northwest of Hole U1345C. APC coring continued through Core 323-U1345D-16H to 150.0 m DSF using nonmagnetic coring assemblies. APC core recovery for Hole U1345D was 103.1% with 154.62 m recovered.

Hole U1345E

The ship was offset 20 m northwest of Hole U1345D. APC coring continued through Core 323-U1345E-16H to 150.0 m DSF using nonmagnetic coring assemblies. APC core recovery for Hole U1345E was 102.8% with 154.15 m recovered.

References

Abelmann, A., 1992a. Diatom assemblages in Arctic sea ice—indicator for ice drift pathways. *Deep-Sea Res., Part A,* 39(2–1):S525–S538. **doi:10.1016/S0198-0149(06)80019-1**

Abelmann, A., 1992b. Radiolarian flux in Antarctic waters (Drake Passage, Powell Basin, Bransfield Strait). *Polar Biol.,* 12(3–4):357–372. **doi:10.1007/BF00243107**

Alexander, M.A., Bladé, I., Newman, M., Lanzante, J.R., Lau, N.-C., and Scott, J.D., 2002. The atmospheric bridge: the influence of ENSO teleconnections on air–sea interaction over the global oceans. *J. Clim.,* 15(16):2205–2231. **doi:10.1175/1520-0442(2002)015<2205:TABTIO>2.0.CO;2**

Asahi, H., and Takahashi, K., 2007. A 9-year time-series of planktonic foraminifer fluxes and environmental change in the Bering Sea and the central subarctic Pacific Ocean, 1990–1999. *Prog. Oceanogr.,* 72(4):343–363. **doi:10.1016/j.pocean.2006.03.021**

Backman, J., Moran, K., McInroy, D.B., Mayer, L.A., and the Expedition 302 Scientists, 2006. *Proc. IODP,* 302: Edinburgh (Integrated Ocean Drilling Program Management International, Inc.). **doi:10.2204/iodp.proc.302.2006**

Baldauf, J.G., 1987. Diatom biostratigraphy of the middle- and high-latitude North Atlantic Ocean, Deep Sea Drilling Project Leg 94. *In* Ruddiman, W.F., Kidd, R.B., Thomas, E., et al., *Init. Repts. DSDP,* 94: Washington, DC (U.S. Govt. Printing Office), 729–762. **doi:10.2973/dsdp.proc.94.115.1987**

Behl, R.J., and Kennett, J.P., 1996. Brief interstadial events in the Santa Barbara Basin, NE Pacific, during the last 60 kyr. *Nature (London, U. K.),* 379(6562):243–246. **doi:10.1038/379243a0**

Berard-Therriault, L., Starr, M., Poulin, M., and Roy, S., 2002. A very unusual spring bloom in the Gulf of St. Lawrence, eastern Canada: the rebirth of diatom *Neodenticula seminae*. Proc. 17th Int. Diatom Symp., 17:9.

Berger, W.H., 1970. Biogenous deep-sea sediments: fractionation by deep-sea circulation. *Geol. Soc. Am. Bull.,* 81(5):1385–1402. **doi:10.1130/0016-7606(1970)81[1385:BDSFBD]2.0.CO;2**

Bubenshchikova, N., Nürnberg, D., Lembke-Jene, L., and Pavlova, G., 2008. Living benthic foraminifera of the Okhotsk Sea: faunal composition, standing stocks and microhabitats. *Mar. Micropaleontol.,* 69(3–4):314–333. **doi:10.1016/j.marmicro.2008.09.002**

Cannariato, K.G., and Kennett, J.P., 1999. Climatically related millennial-scale fluctuations in strength of California margin oxygen-minimum zone during the past 60 k.y. *Geology,* 27(11):975–978. **doi:10.1130/0091-7613(1999)027<0975:CRMSFI>2.3.CO;2**

Coachman, L.K., and Aagaard, K., 1981. Re-evaluation of water transports in the vicinity of the Bering Strait. *In* Hood, D.W., and Calder, J.A. (Eds.), *The Eastern Bering Sea Shelf: Oceanography and Resources:* Seattle (Univ. Washington Press), 95–110.

Cook, M.S., Keigwin, L.D., and Sancetta, C.A., 2005. The deglacial history of surface and intermediate water of the Bering Sea. *Deep-Sea Res., Part II,* 52(16–18):2163–2173. **doi:10.1016/j.dsr2.2005.07.004**

Corbyn, Z., 2007. Atlantic invaders. *Nature Rep. Clim. Change,* 6(711):82. **doi:10.1038/climate.2007.61**

D'Hondt, S., Rutherford, S., and Spivack., A.J., 2002. Metabolic activity of the subsurface life in deep-sea sediments. *Science,* 295(5562):2067–2070. **doi:10.1126/science.1064878**

D'Hondt, S.L., Jørgensen, B.B., Miller, D.J., et al., 2003. *Proc. ODP, Init. Repts.,* 201: College Station, TX (Ocean Drilling Program). **doi:10.2973/odp.proc.ir.201.2003**

De Boer, A.M., and Nof, D., 2004. The Bering Strait's grip on the Northern Hemisphere climate. *Deep-Sea Res., Part I,* 51(10):1347–1366. **doi:10.1016/j.dsr.2004.05.003**

Gieskes, J.M., 1981. Deep-sea drilling interstitial water studies: implications for chemical alteration of the oceanic crust, Layers I and II. *In* Warme, J.E., Douglas, R.G., and Winterer, E.L. (Eds.), *The Deep Sea Drilling Project: A Decade of Progress.* Spec. Publ.—Soc. Econ. Paleontol. Mineral., 32:149–167.

Gladenkov, A.Y., 2006. Neogene diatoms from the Sandy Ridge section, Alaska Peninsula: significance for stratigraphic and paleogeographic reconstructions. *Stratigr. Geol. Correl.,* 14(1):73–90. **doi:10.1134/S0869593806010059**

Gloersen, P., 1995. Modulation of hemispheric sea-ice cover by ENSO events. *Nature (London, U. K.),* 373(6514):503–506. **doi:10.1038/373503a0**

Gorbarenko, S.A., 1996. Stable isotope and lithological evidence of late glacial and Holocene oceanography of the northwestern Pacific and its marginal seas. *Quat. Res.,* 46(3):230–250. **doi:10.1006/qres.1996.0063**

Hamel, D., de Vernal, A., Gosselin, M., and Hillaire-Marcel, C., 2002. Organic-walled microfossils and geochemical tracers: sedimentary indicators of productivity changes in the North Water and northern Baffin Bay during the last centuries. *Deep-Sea Res., Part II,* 49(22–23):5277–5295. **doi:10.1016/S0967-0645(02)00190-X**

Hasumi, H., 2002. Sensitivity of the global thermohaline circulation to interbasin freshwater transport by the atmosphere and the Bering Sea throughflow. *J. Clim.,* 15(17):2516–2526. **doi:10.1175/1520-0442(2002)015<2516:SOTGTC>2.0.CO;2**

Haug, G.H., Sigman, D.M., Tiedemann, R., Pedersen, T.F., and Sarnthein, M., 1999. Onset of permanent stratification in the subarctic Pacific Ocean. *Nature (London, U. K.),* 401(6755):779–782. **doi:10.1038/44550**

Head, M.J., Harland, R., and Matthiessen, J., 2001. Cold marine indicators of the late Quaternary: the new dinoflagellate cyst genus *Islandinium* and related morphotypes. *J. Quat. Sci.,* 16(7):621–636. **doi:10.1002/jqs.657**

Hendy, I.L., and Kennett, J.P., 2003. Tropical forcing of North Pacific intermediate water distribution during late Quaternary rapid climate change? *Quat. Sci. Rev.,* 22(5–7):673–689. **doi:10.1016/S0277-3791(02)00186-5**

Honjo, S., 1990. Particle fluxes and modern sedimentation in the polar oceans. *In* Smith, W.O., Jr. (Ed.), *Polar Oceanography* (Pt. B): *Chemistry, Biology, and Geology:* New York (Academic), 687–739.

Hood, D.W., 1983. The Bering Sea. *In* Ketchum, B.H. (Ed.), *Estuaries and Enclosed Seas:* The Netherlands (Elsevier), 337–373

Hulthe, G., Hulth, S., and Hall, P.O.J., 1998. Effect of oxygen on degradation rate of refractory and labile organic matter in continental margin sediments. *Geochim. Cosmochim. Acta,* 62(8):1319–1328. **doi:10.1016/S0016-7037(98)00044-1**

Jacobson, D.M., and Anderson, D.M., 1986. Thecate heterotrophic dinoflagellates: feeding behavior and mechanisms. *J. Phycol.,* 22(3):249–258. **doi:10.1111/j.1529-8817.1986.tb00021.x**

Kaiho, K., 1994. Benthic foraminiferal dissolved-oxygen index and dissolved-oxygen levels in the modern ocean. *Geology,* 22(8):719–722. **doi:10.1130/0091-7613(1994)022<0719:BFDOIA>2.3.CO;2**

Katsuki, K., and Takahashi, K., 2005. Diatoms as paleoenvironmental proxies for seasonal productivity, sea-ice and surface circulation in the Bering Sea during the late Quaternary. *Deep-Sea Res., Part II,* 52(16–18):2110–2130. **doi:10.1016/j.dsr2.2005.07.001**

Keigwin, L.D., 1995. Northwest Pacific paleohydrography. *In* Tsunogai, S., Iseki, K., Koike, I., and Oba, T. (Eds.), *Global Fluxes of Carbon and Its Related Substances in the Coastal Sea-Ocean-Atmosphere System: Proceedings of the 1994 Sapporo IGBP Symposium:* Yokohama (M and J Int.), 473–478.

Krissek, L.A., 1995. Late Cenozoic ice-rafting records from Leg 145 sites in the North Pacific: late Miocene onset, late Pliocene intensification, and Pliocene–Pleistocene events. *In* Rea, D.K., Basov, I.A., Scholl, D.W., and Allan, J.F. (Eds.), *Proc. ODP, Sci. Results,* 145: College Station, TX (Ocean Drilling Program), 179–194. **doi:10.2973/odp.proc.sr.145.118.1995**

Kwiek, P.B., and Ravelo, A.C., 1999. Pacific Ocean intermediate and deep water circulation during the Pliocene. *Palaeogeogr., Palaeoclimatol., Palaeocol.,* 154(3):191–217. **doi:10.1016/S0031-0182(99)00111-X**

Lagoe, M.B., Eyles, C.H., Eyles, N., and Hale, C., 1993. Timing of late Cenozoic tidewater glaciation in the far North Pacific. *Geol. Soc. Am. Bull.,* 105(12):1542–1560. **doi:10.1130/0016-7606(1993)105<1542:TOLCTG>2.3.CO;2**

Lehmann, M.F., Sigman, D.M., McCorkle, D.C., Brunelle, B.G., Hoffmann, S., Kienast, M., Cane, G., and Clement, J., 2005. Origin of the deep Bering Sea nitrate deficit: constraints from the nitrogen and oxygen isotopic composition of water column nitrate and benthic nitrate fluxes. *Global Biogeochem. Cycles*, 19(4):GB4005. **doi:10.1029/2005GB002508**

Ling, H.Y., 1973. Radiolaria: Leg 19 of the Deep Sea Drilling Project. *In* Creager, J.S., Scholl, D.W., et al., *Init. Repts. DSDP,* 19: Washington, DC (U.S. Govt. Printing Office), 777–797. **doi:10.2973/dsdp.proc.19.128.1973**

Lisiecki, L.E., and Raymo, M.E., 2005. A Pliocene–Pleistocene stack of 57 globally distributed benthic δ^{18}O records. *Paleoceanography,* 20(1):PA1003. **doi:10.1029/2004PA001071**

Lisitzin, A.P., 2003. *Sea-Ice and Iceberg Sedimentation in the Ocean: Recent and Past:* New York (Springer).

Lyons, T.W., Murray, R.W., and Pearson, D.G., 2000. A comparative study of diagenetic pathways in sediments of the Caribbean Sea: highlights from pore-water results. *In* Leckie, R.M., Sigurdsson, H., Acton, G.D., and Draper, G. (Eds.), *Proc. ODP, Sci. Results,* 165: College Station, TX (Ocean Drilling Program), 287–298. **doi:10.2973/odp.proc.sr.165.020.2000**

Maslin, M.A., Haug, G.H., Sarnthein, M., and Tiedemann, R., 1996. The progressive intensification of Northern Hemisphere glaciation as seen from the North Pacific. *Geol. Rundsch.* 85(3):452–465. **doi:10.1007/BF02369002**

Matsumoto, K., Oba, T., Lynch-Stieglitz, J., and Yamamoto, H., 2002. Interior hydrography and circulation of the glacial Pacific Ocean. *Quat. Sci. Rev.,* 21(14–15):1693–1704. **doi:10.1016/S0277-3791(01)00142-1**

McKelvey, B.C., Chen, W., and Arculus, R.J., 1995. Provenance of Pliocene–Pleistocene ice-rafted debris, Leg 145, northern Pacific Ocean. *In* Rea, D.K., Basov, I.A., Scholl, D.W., and Allan, J.F. (Eds.), *Proc. ODP, Sci. Results,* 145: College Station, TX (Ocean Drilling Program), 195–204. **doi:10.2973/odp.proc.sr.145.120.1995**

Moran, K., Backman, J., Brinkhuis, H., Clemens, S.C., Cronin, T., Dickens, G.R., Eynaud, F., Gattacceca, J., Jakobsson, M., Jordan, R.W., Kaminski, M., King, J., Koc, N., Krylov, A., Martinez, N., Matthiessen, J., McInroy, D., Moore, T.C., Onodera, J., O'Regan, M., Pälike, H., Rea, B., Rio, D., Sakamoto, T., Smith, D.C., Stein, R., St. John, K., Suto, I., Suzuki, N., Takahashi, K., Watanabe, M., Yamamoto, M., Farrell, J., Frank, M., Kubik, P., Jokat, W., and Kristoffersen, Y., 2006. The Cenozoic palaeoenvironment of the Arctic Ocean. *Nature (London, U. K.),* 441(7093):601–605. **doi:10.1038/nature04800**

Mudelsee, M., and Raymo, M.E., 2005. Slow dynamics of the Northern Hemisphere glaciation. *Paleoceanography,* 20(4):PA4022. **doi:10.1029/2005PA001153**

Nedashkovskiy, A.P., and Sapozhnikov, V.V., 1999. Variability in the components of the carbonate system and dynamics of inorganic carbon in the western Bering Sea in summer. *In* Loughlin, T.R., and Ohtani, K. (Eds.), *Dynamics of the Bering Sea:* Fairbanks (Univ. Alaska Sea Grant), 311–322.

Niebauer, H.J., 1998. Variability in Bering Sea ice cover as affected by a regime shift in the North Pacific in the period 1947–1996. *J. Geophys. Res.,* 103(C12):27717–27737. **doi:10.1029/98JC02499**

Niebauer, H.J., and Day, R.H., 1989. Causes of interannual variability in the sea ice cover of the eastern Bering Sea. *GeoJournal,* 18(1):45–59. **doi:10.1007/BF00722385**

Nogueira, E., and Figueiras, F.G., 2005. The microplankton succession in the Ria de Vigo revisited: species assemblages and the role of weather-induced, hydrodynamic variability. *J. Mar. Syst.,* 54(1–4):139–155. **doi:10.1016/j.jmarsys.2004.07.009**

Nogueira, E., Ibanez, F., and Figueiras, F.G., 2000. Effect of meteorological and hydrographic disturbances on the microplankton community structure in the Ría de Vigo (NW Spain). *Mar. Ecol.: Prog. Ser.,* 203:23–45. **doi:10.3354/meps203023**

Normark, W.R., and Carlson, P.R., 2003. Giant submarine canyons: is size any clue to their importance in the rock record? *In* Chan, M.A., and Archer, A.W. (Eds.), *Extreme Depositional Environments: Mega end Members in Geologic Time*. Spec. Pap.—Geol. Soc. Am., 370:175–190. **doi:10.1130/0-8137-2370-1.175**

Ohtani, K., 1965. On the Alaskan Stream in summer. *Bull. Fac. Fish., Hokkaido Univ.,* 15:260–273. (In Japanese).

Okazaki, Y., Takahashi, K., Asahi, H., Katsuki, K., Hori, J., Yasuda, H., Sagawa, Y., and Tokuyama, H., 2005. Productivity changes in the Bering Sea during the late Quaternary. *Deep-Sea Res., Part II,* 52(16–18):2150–2162. **doi:10.1016/j.dsr2.2005.07.003**

Okazaki, Y., Takahashi, K., Yoshitani, H., Nakatsuka, T., Ikehara, M., and Wakatsuchi, M., 2003. Radiolarians under the seasonally sea-ice covered conditions in the Okhotsk Sea: flux and their implications for paleoceanography. *Mar. Micropaleontol.,* 49(3):195–230. **doi:10.1016/S0377-8398(03)00037-9**

Ono, A., Takahashi, K., Katsuki, K., Okazaki, Y., and Sakamoto, T., 2005. The Dansgaard–Oeschger cycles discovered in the up stream source region of the North Pacific Intermediate Water formation. *Geophys. Res. Lett.,* 32(11):L11607. **doi:10.1029/2004GL022260**

Onodera, J., and Takahashi, K., 2009. Long-term diatom fluxes in response to oceanographic conditions at Stations AB and SA in the central subarctic Pacific and the Bering Sea, 1990–1998. *Deep-Sea Res., Part I,* 56(2):189–211. **doi:10.1016/j.dsr.2008.08.006**

Ramette, A., 2009. Quantitative community fingerprinting methods for estimating the abundance of operational taxonomic units in natural microbial communities. *Appl. Environ. Microbiol.,* 75(8):2495–2505. **doi:10.1128/AEM.02409-08**

Ravelo, A.C., and Andreasen, D.H., 2000. Enhanced circulation during a warm period. *Geophys. Res. Lett.,* 27(7):1001–1004. **doi:10.1029/1999GL007000**

Rea, D.K., Basov, I.A., Janecek, T.R., Palmer-Julson, A., et al., 1993. *Proc. ODP, Init. Repts.,* 145: College Station, TX (Ocean Drilling Program). **doi:10.2973/odp.proc.ir.145.1993**

Rea, D.K., Basov, I.A., Krissek, L.A., and the Leg 145 Scientific Party, 1995. Scientific results of drilling the North Pacific transect. *In* Rea, D.K., Basov, I.A., Scholl, D.W., and Allan, J.F. (Eds.), *Proc. ODP, Sci. Results,* 145: College Station, TX (Ocean Drilling Program), 577–596. **doi:10.2973/odp.proc.sr.145.146.1995**

Rea, D.K., Basov, I.A., Scholl, D.W., and Allan, J.F. (Eds.), 1995. *Proc. ODP, Sci. Results,* 145: College Station, TX (Ocean Drilling Program). **doi:10.2973/odp.proc.sr.145.1995**

Rea, D.K., and Schrader, H., 1985. Late Pliocene onset of glaciation: ice-rafting and diatom stratigraphy of North Pacific DSDP cores. *Palaeogeogr., Palaeoclimatol., Palaeoecol.,* 49(3–4):313–325. **doi:10.1016/0031-0182(85)90059-8**

Reynolds, L., and Thunell, R.C., 1985. Seasonal succession of planktonic foraminifera in the subpolar North Pacific. *J. Foraminiferal Res.,* 15:282–301.

Rochon, A., de Vernal, A., Turon, J.L., Mathiessen, J., and Head, M.J., 1999. Distribution of recent dinoflagellate cysts in surface sediments from the North Atlantic Ocean and adjacent seas in relation to sea-surface parameters. *Am. Assoc. Strat. Palynol. Found. Contrib. Ser.,* Vol. 35.

Sakamoto, T., Ikehara, M., Aoki, K., Iijima, K., Kimura, N., Nakatsuka, T., and Wakatsuchi, M., 2005. Ice-rafted debris (IRD)-based sea-ice expansion events during the past 100 kyrs in the Okhotsk Sea. *Deep Sea Res., Part II,* 52(16–18):2275–2301. **doi:10.1016/j.dsr2.2005.08.007**

Sambrotto, R.N., Goering, J.J., and McRoy, C.P., 1984. Large yearly production of phytoplankton in the western Bering Strait. *Science,* 225(4667):1147–1150. **doi:10.1126/science.225.4667.1147**

Sancetta, C., 1982. Distribution of diatom species in surface sediments of the Bering and Okhotsk Seas. *Micropaleontology,* 28(3):221–257. **doi:10.2307/1485181**

Scholl, D.W., and Creager, J.S., 1973. Geologic synthesis of Leg 19 (DSDP) results; far North Pacific, and Aleutian Ridge, and Bering Sea. *In* Creager, J.S., Scholl, D.W., et al., *Init. Repts. DSDP,* 19: Washington, DC (U.S. Govt. Printing Office), 897–913. **doi:10.2973/dsdp.proc.19.137.1973**

Shaffer, G., and Bendtsen., J., 1994. Role of the Bering Strait in controlling North Atlantic ocean circulation and climate. *Nature (London, U. K.),* 367(6461):354–357. **doi:10.1038/367354a0**

Smith, D.C., Spivack, A.J., Fisk, M.R., Haveman, S.A., Staudigel, H., and the Leg 185 Shipboard Scientific Party, 2000. Methods for quantifying potential microbial contamination during deep ocean coring. *ODP Tech. Note,* 28. **doi:10.2973/odp.tn.28.2000**

Solomon, S., Qin, D., Manning, M., Marquis, M., Averyt, K., Tignor, M.M.B., Miller, H.L., Jr., and Chen, Z. (Eds.), 2007. *Climate Change 2007: The Physical Science Basis:* Cambridge (Cambridge Univ. Press).

Springer, A.M., McRoy, C.P., and Flint, M.V., 1996. The Bering Sea Green Belt: shelf-edge processes and ecosystem production. *Fish. Oceanogr.,* 5(3–4):205–223. **doi:10.1111/j.1365-2419.1996.tb00118.x**

Stabeno, P.J., Schumacher, J.D., and Ohtani, K., 1999. The physical oceanography of the Bering Sea. *In* Loughlin, T.R., and Ohtani, K. (Eds.), *Dynamics of the Bering Sea: A Summary of Physical, Chemical, and Biological Characteristics, and a Synopsis of Research on the Bering Sea*: Fairbanks (Univ. Alaska Sea Grant), 1–28.

Staudigel, H., and Hart, S.R., 1983. Alteration of basaltic glass: mechanisms and significance for the oceanic crust-seawater budget. *Geochim. Cosmochim. Acta,* 47(3):337–350. **doi:10.1016/0016-7037(83)90257-0**

Tada, R., Irino, T., and Koizumi, I., 1999. Land-ocean linkages over orbital and millennial timescales recorded in late Quaternary sediments of the Japan Sea. *Paleoceanography,* 14(2):236–247. **doi:10.1029/1998PA900016**

Takahashi, K., 1986. Seasonal fluxes of pelagic diatoms in the subarctic Pacific, 1982–1983. *Deep-Sea Res., Part A,* 33:1225–1251. **doi:10.1016/0198-0149(86)90022-1**

Takahashi, K., 1999. Paleoceanographic changes and present environment of the Bering Sea. *In* Loughlin, T.R., and Ohtani, K. (Eds.), *Dynamics of the Bering Sea:* Fairbanks (Univ. Alaska Sea Grant), 365–385.

Takahashi, K., 2005. The Bering Sea and paleoceanography. *Deep-Sea Res., Part II,* 52(16–18):2080–2091. **doi:10.1016/j.dsr2.2005.08.003**

Takahashi, K., Fujitani, N., and Yanada, M., 2002. Long term monitoring of particle fluxes in the Bering Sea and the central subarctic Pacific Ocean, 1990–2000. *Prog. Oceanogr.,* 55 (1–2), 95–112. **doi:10.1016/S0079-6611(02)00072-1**

Takahashi, K., Fujitani, N., Yanada, M., and Maita, Y., 2000. Long-term biogenic particle fluxes in the Bering Sea and the central subarctic Pacific Ocean, 1990–1995. *Deep-Sea Res., Part I,* 47(9):1723–1759. **doi:10.1016/S0967-0637(00)00002-9**

Takahashi, K., Honjo, S., and Tabata, S. 1989. Siliceous phytoplankton flux: interannual variability and response to hydrographic changes in the northeastern Pacific. *In* Peterson, D. (Ed.), *Aspects of Climate Variability in the Pacific and Western Americas*. Geophys. Monogr., 151–160.

Takahashi, K., Jordan, R.W., and Boltovskoy, D. (Eds.), 2005. Preface. *Deep-Sea Res., Part II,* 52(16–18):2079. **doi:10.1016/j.dsr2.2005.08.002**

Tanaka, S., and Takahashi, K., 2005. Late Quaternary paleoceanographic changes in the Bering Sea and the western subarctic Pacific based on radiolarian assemblages. *Deep-Sea Res., Part II,* 52(16–18):2131–2149. **doi:10.1016/j.dsr2.2005.07.002**

Taniguchi, A., 1984. Microzooplankton biomass in the arctic and subarctic Pacific Ocean in summer. *In* Hoshiai, T., and Fukuchi, M., *Proc. Sixth Symp. Polar Biol.* Mem. Natl. Inst. Polar Res. Spec. Issue (Jpn.), 32:63–76.

Thompson, G., 1983. Basalt-seawater interaction. *In* Rona, P.A., Boström, K., Laubier, L., and Smith, K.L., Jr. (Eds.), *Hydrothermal Processes at Seafloor Spreading Centers:* New York (Plenum), 225–278.

Uozumi, S., Akamatsu, M., and Takagi, T., 1986. Takikawa-Honbetsu and Tatsunokuchi faunas (*Fortipecten takahashii*-bearing Pliocene faunas). *Spec. Pap.—Palaeontol. Soc. Japan,* 29:211–226.

von Breymann, M.T., Brumsack, H., and Emeis, K.C., 1992. Depositional and diagenetic behavior of barium in the Japan Sea. *In* Pisciotto, K.A., Ingle, J.C., Jr., von Breymann, M.T., Barron, J., et al., *Proc. ODP, Sci. Results,* 127/128 (Pt. 1): College Station, TX (Ocean Drilling Program), 651–665. **doi:10.2973/odp.proc.sr.127128-1.168.1992**

Warner, M.J., and Roden, G.I., 1995. Chlorofluorocarbon evidence for recent ventilation of the deep Bering Sea. *Nature (London, U. K.),* 373(6513):409–412. **doi:10.1038/373409a0**

Zahn, R., Rushdi, A., Pisias, N.G., Bornhold, B.D., Blaise, B., and Karlin, R., 1991. Carbonate deposition and benthic $\delta^{13}C$ in the subarctic Pacific: implications for changes of the oceanic carbonate system during the past 750,000 years. *Earth Planet. Sci. Lett.,* 103(1–4):116–132. **doi:10.1016/0012-821X(91)90154-A**

Zhao, P., Zhang, X., Zhou, X., Ikeda, M., and Yin, Y., 2004. The sea ice extent anomaly in the North Pacific and its impact on the east Asian summer monsoon rainfall. *J. Clim.,* 17(17):3434–3447. **doi:10.1175/1520-0442(2004)017<3434:TSIEAI>2.0.CO;2**

Zheng, Y., van Geen, A., Anderson, R.F., Gardner, J.V., and Dean, W.E., 2000. Intensification of the northeast Pacific oxygen minimum zone during the Bölling-Alleröd warm period. *Paleoceanography,* 15(5):528–536. **doi:10.1029/1999PA000473**

Table T1. Summary of drilled results for IODP Expedition 323 in the Bering Sea.

IODP site number	Water depth (mbsl)	Depth DSF (m)	Age (Ma)	Average sedimentation rate (cm/k.y.)
Umnak Plateau				
U1339	1911	200	0–0.8	28
Bowers Ridge				
U1340	1324	600	0–5	12
U1341	2177	600	0–5	12
U1342	848	45	0–1.2	4.5
Bering slope				
U1343	1986	745	0–2.1	35
U1344	3220	745	0–1.9	45
U1345	1020	150	0–0.5	30

Table T2. Coring summary.

Hole	Latitude	Longitude	Water depth (mbsl)	Cores (*N*)	Cored (m)	Recovered (m)	Recovered (%)	Time on hole (h)	Time on site (days)
U1339A	54°40.2001′N	169°58.9017′W	1866.7	4	33.4	34.87	104	22.50	
U1339B	54°40.2103′N	169°58.9106′W	1867.6	22	196.0	204.45	104	29.67	
U1339C	54°40.2063′N	169°58.8852′W	1867.6	21	194.8	199.40	102	19.83	
U1339D	54°40.1891′N	169°58.8909′W	1879.4	22	200.0	206.00	103	39.58	
			Site U1339 totals:	67	624.2	644.75	103	111.58	4.65
U1340A	53°24.0008′N	179°31.2973′W	1294.7	71	604.5	535.91	89	69.80	
U1340B	53°24.0002′N	179°30.9815′W	1297.2	6	53.9	55.53	103	6.95	
U1340C	53°23.8113′N	179°31.2975′W	1293.4	3	28.5	30.00	105	4.58	
U1340D	53°23.8004′N	179°31.2974′W	1293.4	3	26.3	27.23	104	6.98	
			Site U1340 totals:	73	713.2	648.67	91	87.86	3.66
U1341A	54°2.0025′N	179°0.4999′E	2139.6	41	359.2	373.23	104	47.93	
U1341B	54°1.9984′N	179°0.5171′E	2139.6	71	600.0	594.98	99	90.08	
U1341C	54°2.0010′N	179°0.5390′E	2139.6	27	230.0	242.06	105	32.58	
			Site U1341 totals:	139	1189.2	1210.27	102	170.59	7.11
U1342A	54°49.6987′N	176°55.0027′E	818.3	9	53.3	57.39	108	13.83	
U1342B	54°49.7004′N	176°55.0232′E	818.9	5	43.3	44.83	104	3.50	
U1342C	54°49.7017′N	176°55.0232′E	818.8	6	45.4	47.06	104	6.17	
U1342D	54°49.6987′N	176°55.0027′E	818.2	19	127.7	86.37	68	33.25	
			Site U1342 totals:	39	269.7	235.70	95	56.75	2.36
U1343A	57°33.3993′N	175°48.9659′W	1950.9	22	201.5	203.86	101	24.87	
U1343B	57°33.4156′N	175°48.9951′W	1950.9	4	35.5	34.56	97	4.25	
U1343C	57°33.3982′N	175°49.0275′W	1952.6	26	234.2	231.04	99	22.92	
U1343D	57°33.3817′N	175°48.9971′W	1954.1	1	8.5	8.50	100	1.42	
U1343E	57°33.3814′N	175°48.9974′W	1956.0	82	744.3	700.27	95	106.82	
			Site U1343 totals:	135	1224.0	1178.00	96.5	160.28	6.68
U1344A	59°3.0005′N	179°12.2011′W	3171.8	79	745.0	684.10	87	129.70	
U1344B	59°3.0112′N	179°12.2051′W	3173.0	1	4.44	4.80	92	2.00	
U1344C	59°3.0116′N	179°12.2052′W	3172.7	4	35.6	33.51	94	5.30	
U1344D	59°3.0224′N	179°12.2030′W	3174.1	32	286.5	286.10	100	35.50	
U1344E	59°3.0339′N	179°12.2029′W	3174.0	23	202.8	202.68	100	31.30	
			Site U1344 totals:	139	1274.7	1174.80	92	203.80	8.49
U1345A	60°9.1917′N	179°28.2036′W	1007.3	16	146.9	148.24	101	16.82	
U1345B	60°9.2003′N	179°28.2127′W	1007.5	4	36.7	38.79	106	3.90	
U1345C	60°9.2097′N	179°28.2229′W	1008.8	16	148.5	152.85	103	9.00	
U1345D	60°9.2175′N	179°28.2283′W	1008.3	16	150.0	154.62	103	9.00	
U1345E	60°9.2264′N	179°28.2407′W	1007.7	16	150.0	154.15	103	14.10	
			Site U1345 totals:	68	632.1	648.65	103	52.82	2.21
			Expedition 323 totals:	660	5927.1	5740.84	97	843.68	35.15

Table T3. Datum events of radiolarians, diatoms, and silicoflagellates, Site U1339. (**See table notes.**)

Datum event	Taxon/ magnetics	Age (ka)	Depth CSF (m)			
			Hole U1339A	Hole U1339B	Hole U1339C	Hole U1339D
LO *Lychnocanoma nipponica sakaii*	Radiolarian	52 ± 5	19.49	18.51	14.60	11.33
LO *Amphimelissa setosa*	Radiolarian	90 ± 10		37.59	34.03	29.54
LO *Distephanus octonarius*	Silicoflagellate	244 ± 47		47.25	71.59	48.16
LO *Proboscia curvirostris*	Diatom	260 ± 1		75.66	90.18	66.89
LO *Spongodiscus* sp.	Radiolarian	300 ± 20		75.66	80.94	75.73
LO *Thalassirosira jouseae*	Diatom	305		75.66	90.18	57.78
LO *Axoprunum acquilonium*	Radiolarian	340 ± 90		125.30	90.18	115.07
LO *Stylatractus universus*	Radiolarian	460 ± 50		163.38	90.18	133.04
FO *Distephanus octangulatus*	Silicoflagellate	741 ± 3				190.10

Notes: For first occurrences (FO), the depth was estimated as the midpoint between the depth at which the species was first observed and the depth of the next sample below. For last occurrences (LO), the depth was estimated as the midpoint between the depth at which the species was last observed and the depth of the next sample above.

Table T4. Affine table indicating the amount that each core in each hole needs to be offset in order to construct a continuous record, Site U1339.

Core	Offset (m)
323-U1339A-	
1H	0.36
2H	0.01
3H	1.17
4H	1.33
323-U1339B-	
1H	0.23
2H	0.38
3H	1.32
4H	1.55
5H	2.30
6H	2.85
7H	3.96
8H	5.52
9H	5.32
10H	8.06
11H	7.81
12H	7.58
13H	9.52
14H	9.74
15H	11.50
16H	13.01
17H	14.63
18H	16.51
19H	18.07
20H	20.32
21H	21.89
22H	22.58
323-U1339C-	
1H	0.00
2H	0.30
3H	1.30
4H	2.10
5H	2.75
6H	5.03
7H	6.13
8H	6.65
9H	7.58
10H	7.79
11H	8.38
12H	9.83
13H	11.26
14H	12.41
15H	14.41
16H	15.57
17H	16.18
18H	18.77
19H	18.09
20H	19.98
21H	20.08
323-U1339D-	
1H	0.30
2H	1.50
3H	1.68
4H	1.62
5H	2.01
6H	3.68
7H	4.70
8H	6.77
9H	6.91
10H	7.36
11H	7.60
12H	8.84
13H	11.68
14H	12.79
15H	16.89
16H	18.24
17H	19.17
18H	20.76
19H	23.14
20H	25.59
21H	25.41
22H	27.03

Table T5. Splice table indicating tie points between holes, Site U1339. Sampling along the splice should be used to construct a continuous record.

Hole, core, section, interval (cm)	Depth (m)			Hole, core, section, interval (cm)	Depth (m)	
	CSF	CCSF-A			CSF	CCSF-A
323-				323-		
U1339C-1H-7, 1.62	8.87	8.87	Tie to	U1339D-2H-1, 95.16	7.40	8.90
U1339D-2H-6, 46.71	14.42	15.92	Tie to	U1339C-2H-4, 148.63	15.74	16.03
U1339C-2H-6, 116.00	18.46	18.76	Tie to	U1339D-3H-1, 95.16	17.00	18.68
U1339D-3H-5, 138.74	23.44	25.12	Tie to	U1339C-3H-4, 6.69	23.78	25.09
U1339C-3H-6, 89.68	27.65	28.95	Tie to	U1339D-4H-2, 30.31	27.35	28.98
U1339D-4H-5, 73.77	32.29	33.91	Tie to	U1339C-4H-3, 4.59	31.80	33.90
U1339C-4H-6, 115.72	37.41	39.51	Tie to	U1339D-5H-3, 104.27	37.49	39.51
U1339D-5H-6, 135.16	42.30	44.32	Tie to	U1339C-5H-3, 29.53	41.45	44.19
U1339C-5H-7, 47.82	47.63	50.37	Tie to	U1339D-6H-3, 84.79	46.70	50.38
U1339D-6H-7, 9.84	51.93	55.62	Tie to	U1339C-6H-3, 99.74	50.69	55.71
U1339C-6H-7, 90.95	56.60	61.62	Tie to	U1339D-7H-3, 145.22	56.80	61.50
U1339D-7H-6, 107.23	60.92	65.62	Tie to	U1339C-7H-2, 84.60	59.45	65.57
U1339C-7H-6, 40.31	65.05	71.18	Tie to	U1339D-8H-2, 106.65	64.39	71.16
U1339D-8H-6, 24.18	69.56	76.33	Tie to	U1339C-8H-3, 3.30	69.69	76.34
U1339C-8H-5, 82.23	73.47	80.12	Tie to	U1339D-9H-2, 34.92	73.30	80.21
U1339D-9H-5, 4.06	77.50	84.41	Tie to	U1339C-9H-1, 60.12	76.85	84.43
U1339C-9H-6, 49.20	84.07	91.65	Tie to	U1339D-10H-3, 28.63	84.24	91.60
U1339D-10H-6, 93.48	89.38	96.75	Tie to	U1339C-10H-3, 118.25	88.88	96.67
U1339C-10H-5, 135.32	91.92	99.71	Tie to	U1339D-11H-2, 142.52	92.15	99.75
U1339D-11H-7, 62.42	98.56	106.17	Tie to	U1339C-11H-2, 105.51	97.81	106.18
U1339C-11H-5, 43.36	101.62	110.00	Tie to	U1339D-12H-2, 80.54	101.16	110.00
U1339D-12H-6, 97.62	107.21	116.05	Tie to	U1339C-12H-1, 145.23	106.20	116.03
U1339C-12H-5, 137.70	112.10	121.93	Tie to	U1339D-13H-2, 0.39	110.15	121.83
U1339D-13H-7, 59.43	118.09	129.77	Tie to	U1339C-13H-4, 3.59	118.49	129.75
U1339C-13H-6, 8.53	121.59	132.84	Tie to	U1339D-14H-2, 74.88	120.06	132.85
U1339D-14H-7, 48.93	127.25	140.04	Tie to	U1339C-14H-4, 7.84	127.66	140.07
U1339C-14H-6, 147.70	132.08	144.49	Tie to	U1339B-16H-2, 116.72	131.39	144.39
U1339B-16H-6, 131.59	137.31	150.31	Tie to	U1339C-15H-2, 134.43	136.04	150.46
U1339C-15H-6, 56.72	141.26	155.67	Tie to	U1339B-17H-3, 17.59	140.98	155.61
U1339B-17H-6, 66.19	145.91	160.54	Tie to	U1339D-16H-3, 144.22	142.35	160.59
U1339D-16H-6, 92.12	146.33	164.57	Tie to	U1339C-17H-2, 4.11	148.40	164.58
U1339C-17H-6, 147.83	155.67	171.84	Tie to	U1339D-17H-5, 1.66	152.71	171.88
U1339D-17H-7, 102.58	156.72	175.88	Tie to	U1339C-18H-2, 3.64	157.05	175.82
U1339C-18H-7, 57.33	164.97	183.75	Tie to	U1339D-18H-5, 64.46	163.05	183.82
U1339D-18H-7, 39.54	165.81	186.57	Tie to	U1339C-19H-3, 49.59	168.36	186.45
U1339C-19H-5, 123.52	172.09	190.18	Tie to	U1339D-19H-2, 3.73	167.10	190.24
U1339D-19H-7, 3.83	174.47	197.62	Tie to	U1339C-20H-2, 49.39	177.69	197.67
U1339C-20H-7, 17.26	184.71	204.69	Tie to	U1339D-20H-3, 72.43	179.09	204.69
U1339D-20H-7, 15.30	184.18	209.77	Tie to	U1339C-21H-3, 11.00	189.66	209.74
U1339C-21H-6, 110.20	193.85	213.93	Tie to	U1339D-21H-3, 67.20	189.10	214.52

Table T6. Sedimentation rates and their control points, Site U1339. (See table note.)

Age (ka)	Depth CCSF-A (m)	Control point	Sedimentation rate (cm/k.y.)
52 ± 5	16.6	Average depth of LO *Lychnocanoma nipponica sakaii*	32
90 ± 10	35.5	Average depth of LO *Amphimelissa setosa*	50
300 ± 20	83.9	Average depth of LO *Spongodiscus* sp.	23
460 ± 50	118.5	Hole U1339C depth of LO *Stylatractus universus*	22
740 ± 3	215.6	Hole U1339D depth of FO *Distephanus octangulatus* and LO *Dictyocha subarctios*	35

Note: LO = last occurrence, FO = first occurrence.

Table T7. Datum events of radiolarians, diatoms, silicoflagellates, ebridians, dinoflagellates, and paleomagnetics, Hole U1340A. (**See table notes.**)

Datum event	Taxon/ magnetics	Age (Ma)	Depth CSF (m)
LO *Lychnocanoma nipponica sakaii*	Radiolarian	0.05	8.9
LO *Amphimelissa setosa*	Radiolarian	0.08–1	8.9
LO *Spongodiscus* sp.	Radiolarian	0.28–0.32	18.7
LO *Axoprunum acquilonium*	Radiolarian	0.25–0.43	18.7
LO *Proboscia curvirostris*	Diatom	0.3	37.6
LO *Dichtyocha subarctios*	Silicoflagellate	0.6–0.8	118.4
Brunhes/Matuyama	Paleomagnetic	0.781	117.9
LCO *Actinocyclus oculatus*	Diatom	0.9	161.2
LO *Eucyrtidium matuyamai*	Radiolarian	0.9–1.5	161.2
Jaramillo top	Paleomagnetic	0.998	146.4
Jaramillo bottom	Paleomagnetic	1.072	155.9
LO *Filisphaera filifera*	Dinoflagellate	1.4–1.7	206.0
FO *Eucyrtidium matuyamai*	Radiolarian	1.7–1.9	201.3
Olduvai top	Paleomagnetic	1.778	260.7
Olduvai bottom	Paleomagnetic	1.945	300.7
FO *Proboscia curvirostris*	Diatom	1.7–2.0	201.2
LO *Pyxidicula horridus*	Diatom	1.9–2.0	229.9
Reunion top	Paleomagnetic	2.128	343.2
LO *Thecosphaera akitaensis*	Radiolarian	2.4–2.7	267.9
LO *Ebriopsis antiqua antiqua*	Ebridian	2.47–2.48	305.5
Gauss top	Paleomagnetic	2.581	486.2
LO *Phormostichoartus fistula*	Radiolarian	2.8–4.4	314.4
FO *Neodenticula koizumii*	Diatom	3.7–3.9	531.0
LO *Dictyophimus bullatus/Dictyophimus* sp. B	Radiolarian	3.8–4.0	531.0

Notes: For first occurrences (FO), the depth was estimated as the midpoint between the depth at which the species was first observed and the depth of the next sample below. For last occurrences (LO), the depth was estimated as the midpoint between the depth at which the species was last observed and the depth of the next sample above. LCO = last common occurrence.

Table T8. Affine table indicating the amount that each core in each hole needs to be offset in order to construct a continuous record, Site U1340.

Core	Offset (m)
323-U1340A-	
1H	–0.06
2H	1.05
3H	1.30
4H	1.61
5H	7.27
6H	7.31
7H	7.31
8H	7.31
9H	7.31
10H	7.31
11H	7.31
12H	7.31
13H	7.31
14H	7.31
15H	7.31
16H	7.31
17H	7.31
18H	7.31
19H	7.31
20H	7.31
21H	7.31
22D	7.31
23H	7.31
24H	7.31
25H	7.31
26H	7.31
27H	7.31
28H	7.31
29H	7.31
30H	7.31
31H	7.31
32H	7.31
33H	7.31
34H	7.31
35H	7.31
36H	7.31
37H	7.31
38H	7.31
39H	7.31
40H	7.31
41H	7.31
42H	7.31
43X	7.31
44X	7.31
45X	7.31
46X	7.31
47X	7.31
48X	7.31
49X	7.31
50X	7.31
51X	7.31
52X	7.31
53X	7.31
54X	7.31
55X	7.31
56X	7.31
57X	7.31
58X	7.31
59X	7.31
60X	7.31
61X	7.31
62X	7.31
63H	7.31
64H	7.31
65H	7.31
66H	7.31
67H	7.31
68X	7.31
69X	7.31
70X	7.31
71X	7.31
323-U1340B-	
1H	–0.21
2H	1.74
3H	1.48
4H	6.81
5H	6.77
6H	4.71
323-U1340C-	
1H	10.03
2H	25.72
3H	15.29
323-U1340D-	
1H	0.00
2H	2.41
3H	15.80

Table T9. Splice table indicating tie points between holes, Site U1340. Sampling along the splice should be used to construct a continuous record.

Hole, core, section, interval (cm)	Depth (m)			Hole, core, section, interval (cm)	Depth (m)	
	CSF	CCSF-A			CSF	CCSF-A
323-				323-		
U1340D-1H-5, 59.48	6.59	6.59	Tie to	U1340A-2H-2, 14.53	5.55	6.59
U1340A-2H-4, 143.32	9.83	10.88	Tie to	U1340C-1H-1, 85.10	0.85	10.88
U1340C-1H-4, 127.08	5.77	15.80	Tie to	U1340A-3H-1, 112.74	14.53	15.83
U1340A-3H-3, 75.51	17.11	18.41	Tie to	U1340B-3H-1, 105.11	16.95	18.43
U1340B-3H-6, 101.23	24.41	25.89	Tie to	U1340A-4H-1, 137.78	24.28	25.89
U1340A-4H-6, 100.77	31.41	33.02	Tie to	U1340B-4H-1, 80.13	26.20	33.01

Table T10. Sedimentation rates and their control points, Hole U1340A. (**See table note.**)

Age (Ma)	Depth CSF (m)	Control point	Sedimentation rate (cm/k.y.)
0.3	37.6	Depth of LO *Proboscia curvirostris*	13
0.781	117.9	Brunhes bottom	17
0.998	146.4	Jaramillo top	13
1.072	155.9	Jaramillo bottom	13
1.778	260.7	Olduvai top	15
1.945	300.7	Olduvai bottom	24
2.128	343.2	Reunion top	23
2.581	486.2	Gauss top	32
3.8	531.0	FO *Neodenticula koizumii*	4

Note: LO = last occurrence, FO = first occurrence.

Table T11. Datum events of radiolarians, diatoms, calcareous nannofossils, silicoflagellates, ebridians, dinoflagellates, and paleomagnetics, Hole U1341B. (**See table notes.**)

Datum event	Taxon/ magnetics	Age (Ma)	Depth CSF (m)
LO *Lychnocanoma nipponica sakaii*	Radiolarian	0.05	4.4
LO *Amphimelissa setosa*	Radiolarian	0.08–1	13.7
LO *Spongodiscus* sp.	Radiolarian	0.28–0.32	42.4
LO *Axoprunum acquilonium*	Radiolarian	0.25–0.43	61.4
LO *Proboscia curvirostris*	Diatom	0.3	32.9
LO *Thalassirosira jouseae*	Diatom	0.3	32.9
Brunhes/Matuyama	Paleomagnetic	0.781	82.5
LCO *Actinocyclus oculatus*	Diatom	0.9	118.4
LO *Eucyrtidium matuyamai*	Radiolarian	0.9–1.5	108.9
Jaramillo top	Paleomagnetic	0.998	103.7
Jaramillo bottom	Paleomagnetic	1.072	138.0
FO *Eucyrtidium matuyamai*	Radiolarian	1.7–1.9	147.0
RI *Neodenticula seminae*	Diatom	1.778	245.5
FO *Proboscia curvirostris*	Diatom	1.7–2.0	162.5
LO *Pyxidicula horridus*	Diatom	1.9–2.0	204.9
LO *Ammodochium rectangulare*	Ebridian	1.9	233.4
LO *Thecosphaera akitaensis*	Radiolarian	2.4–2.7	414.1
LO *Ebriopsis antiqua antiqua*	Ebridian	2.47–2.48	330.6
LO *Distephanus jimlingii*	Silicoflagellate	2.52	340.5
Gauss top	Paleomagnetic	2.581	367.8
FO *Neodenticula koizumii*	Diatom	3.7–3.9	463.0
LO *Dictyophimus bullatus*/*Dictyophimus* sp. B	Radiolarian	3.8–4.0	597.1

Notes: For first occurrences (FO), the depth was estimated as the midpoint between the depth at which the species was first observed and the depth of the next sample below. For last occurrences (LO), the depth was estimated as the midpoint between the depth at which the species was last observed and the depth of the next sample above. LCO = last common occurrence, RI = rapid increase.

Table T12. Affine table indicating the amount that each core in each hole needs to be offset in order to construct a continuous record, Site U1341. (**Continued on next two pages.**)

Core	Depth CSF (m)		Offset (m)	Depth CCSF-A (m)		Recovered (m)	Recovery (%)
	Top	Bottom		Top	Bottom		
323-U1341A-							
1H	0.00	3.04	0.00	0.00	3.04	3.04	101
2H	3.00	12.64	0.35	3.35	12.99	9.49	100
3H	12.50	22.43	0.46	12.96	22.89	9.75	103
4H	22.00	31.77	0.83	22.83	32.60	9.49	100
5H	31.50	41.32	1.91	33.41	43.23	9.51	100
6H	41.00	50.95	3.42	44.42	54.37	9.75	103
7H	50.50	60.51	3.66	54.16	64.17	9.73	102
8H	60.00	69.41	4.89	64.89	74.30	9.09	96
9H	69.50	79.66	4.84	74.34	84.50	9.89	104
10H	79.00	89.12	5.05	84.05	94.17	10.12	107
11H	88.50	98.51	5.15	93.65	103.66	10.01	105
12H	98.00	108.16	5.36	103.36	113.52	10.16	107
13H	107.50	117.70	4.97	112.47	122.67	10.20	107
14H	117.00	127.10	3.53	120.53	130.63	10.10	106
15H	126.50	136.26	4.58	131.08	140.84	9.76	103
16H	136.00	146.07	10.12	146.12	156.19	10.07	106
17H	145.50	155.63	9.92	155.42	165.55	10.13	107
18H	155.00	165.02	10.89	165.89	175.91	10.02	105
19H	164.50	174.49	10.66	175.16	185.15	9.99	105
20H	174.00	183.92	12.31	186.31	196.23	9.92	104
21H	183.50	193.35	13.81	197.31	207.16	9.85	104
22H	193.00	203.13	17.18	210.18	220.31	10.13	107
23H	202.50	212.63	13.53	216.03	226.16	10.13	107
24H	212.00	221.34	15.50	227.50	236.84	9.44	99
25H	221.50	231.43	13.78	235.28	245.21	9.93	105
26H	231.00	233.21	16.00	247.00	249.21	2.21	100
27H	233.20	241.50	16.15	249.35	257.65	8.30	87
28H	242.70	252.54	16.11	258.81	268.65	9.84	104
29H	252.20	262.24	16.51	268.71	278.75	10.04	106
30H	261.70	271.82	17.37	279.07	289.19	9.84	104
31H	271.20	281.30	17.55	288.75	298.85	9.83	103
32H	280.70	290.61	19.78	300.48	310.39	9.62	101
33H	290.20	300.19	17.20	307.40	317.39	9.71	102
34H	299.70	309.52	17.10	316.80	326.62	9.82	103
35H	309.20	319.02	17.23	326.43	336.25	9.61	101
36H	318.70	328.19	18.29	336.99	346.48	9.49	100
37H	328.20	332.81	18.62	346.82	351.43	4.61	102
38H	332.70	342.26	18.66	351.36	360.92	9.56	101
39H	342.20	352.03	19.16	361.36	371.19	9.83	103
40H	351.70	356.78	18.96	370.66	375.74	5.08	113
41H	356.20	359.12	19.50	375.70	378.62	2.92	97
323-U1341B-							
1H	0.00	8.72	–0.06	–0.06	8.66	8.70	100
2H	8.70	18.58	–0.18	8.52	18.40	9.60	101
3H	18.20	28.18	0.45	18.65	28.63	10.00	105
4H	27.70	37.70	1.25	28.95	38.95	10.00	105
5H	37.20	47.18	2.43	39.63	49.61	10.00	105
6H	46.70	57.12	2.71	49.41	59.83	10.00	105
7H	56.20	66.18	2.79	58.99	68.97	10.00	105
8H	65.70	75.75	4.25	69.95	80.00	10.10	106
9H	75.20	85.24	5.26	80.46	90.50	10.00	105
10H	84.70	94.20	5.72	90.42	99.92	9.50	100
11H	94.20	104.25	5.98	100.18	110.23	9.80	103
12H	103.70	113.59	6.39	110.09	119.98	9.60	101
13H	113.20	123.24	8.39	121.59	131.63	9.70	102
14H	122.70	132.84	8.74	131.44	141.58	9.90	104
15H	132.20	142.36	8.77	140.97	151.13	9.80	103
16H	141.70	151.68	9.74	151.44	161.42	9.60	101
17H	151.20	158.19	8.57	159.77	166.76	6.80	113
18H	157.20	166.81	10.43	167.63	177.24	9.20	97
19H	166.70	176.65	10.34	177.04	186.99	9.90	104
20H	176.20	180.17	11.18	187.38	191.35	3.70	82
21H	180.70	190.72	11.27	191.97	201.99	10.00	105
22H	190.20	199.97	12.47	202.67	212.44	9.80	103
23H	199.70	209.78	12.09	211.79	221.87	10.10	106
24H	209.20	218.93	13.26	222.46	232.19	9.70	102

Table T12 (continued). (Continued on next page.)

	Depth CSF (m)		Offset (m)	Depth CCSF-A (m)		Recovered (m)	Recovery (%)
Core	Top	Bottom		Top	Bottom		
25H	218.70	228.52	14.94	233.64	243.46	9.80	103
26H	228.20	238.21	14.72	242.92	252.93	10.00	105
27H	237.70	247.60	15.44	253.14	263.04	9.90	104
28H	247.20	257.19	15.52	262.72	272.71	10.00	105
29H	256.70	266.02	16.08	272.78	282.10	9.30	98
30H	266.20	276.19	17.07	283.27	293.26	10.00	105
31H	275.70	283.81	17.94	293.64	301.75	8.10	100
32H	283.80	291.66	18.05	301.85	309.71	7.90	83
33H	293.30	301.23	17.33	310.63	318.56	7.70	97
34H	301.20	307.32	17.83	319.03	325.15	6.10	100
35H	307.30	316.75	18.40	325.70	335.15	9.40	99
36H	316.80	325.93	17.90	334.70	343.83	9.10	96
37H	326.30	335.28	18.73	345.03	354.01	9.00	95
38H	335.80	345.78	19.09	354.89	364.87	9.70	102
39H	345.30	355.09	19.62	364.92	374.71	9.80	103
40H	354.80	358.11	19.95	374.75	378.06	3.10	89
41H	358.30	366.24	19.95	378.25	386.19	7.70	81
42H	367.80	375.68	19.95	387.75	395.63	7.90	99
43H	375.80	385.48	19.95	395.75	405.43	9.70	102
44H	385.30	395.12	19.95	405.25	415.07	9.80	103
45H	394.80	403.59	19.95	414.75	423.54	8.80	98
46H	403.80	413.70	19.95	423.75	433.65	9.90	104
47H	413.30	414.53	19.95	433.25	434.48	1.20	92
48H	414.60	422.84	19.95	434.55	442.79	8.20	100
49H	422.80	423.29	19.95	442.75	443.24	0.50	100
50H	423.30	431.18	19.95	443.25	451.13	7.90	100
51H	431.20	439.04	19.95	451.15	458.99	7.80	100
52H	439.00	448.86	19.95	458.95	468.81	9.90	104
53H	448.50	457.80	19.95	468.45	477.75	9.30	100
54H	457.80	458.33	19.95	477.75	478.28	0.50	100
55H	458.30	458.36	19.95	478.25	478.31	0.10	100
56H	458.40	458.42	19.95	478.35	478.37	0.00	0
57X	458.40	467.33	19.95	478.35	487.28	8.90	96
58X	467.70	476.75	19.95	487.65	496.70	9.05	97
59X	477.00	486.77	19.95	496.95	506.72	9.49	98
60X	486.70	496.46	19.95	506.65	516.41	9.76	103
61X	496.20	504.34	19.95	516.15	524.29	7.84	81
62X	505.90	515.72	19.95	525.85	535.67	9.49	98
63X	515.60	525.46	19.95	535.55	545.41	9.49	99
64X	525.20	534.86	19.95	545.15	554.81	9.35	97
65X	534.80	543.02	19.95	554.75	562.97	9.33	97
66X	544.40	549.36	19.95	564.35	569.31	4.50	47
67X	554.00	563.68	19.95	573.95	583.63	9.45	97
68X	563.70	573.48	19.95	583.65	593.43	9.78	102
69X	573.30	573.54	19.95	593.25	593.49	0.24	2
70X	582.90	592.56	19.95	602.85	612.51	9.66	101
71X	592.50	601.87	19.95	612.45	621.82	9.37	125
323-U1341C-							
1H	0.00	5.54	0.06	0.06	5.60	5.54	101
2H	5.50	15.44	0.37	5.87	15.81	9.94	105
3H	15.00	24.92	1.03	16.03	25.95	9.92	104
4H	24.50	34.51	1.63	26.13	36.14	10.01	105
5H	34.00	41.79	1.03	35.03	42.82	7.79	82
6H	43.50	53.62	3.91	47.41	57.53	9.91	104
7H	53.00	62.24	4.41	57.41	66.65	9.24	116
8H	61.00	71.06	5.03	66.03	76.09	10.06	106
9H	70.50	80.62	6.31	76.81	86.93	10.12	107
10H	80.00	90.05	7.35	87.35	97.40	10.05	106
11H	89.50	97.03	6.59	96.09	103.62	7.53	126
12H	95.50	105.74	8.22	103.72	113.96	10.24	108
13H	105.00	115.15	8.49	113.49	123.64	10.15	107
14H	114.50	124.66	3.84	118.34	128.50	9.84	104
15H	124.00	134.06	4.15	128.15	138.21	9.85	104
16H	133.50	139.65	8.61	142.11	148.26	6.15	154
17H	137.50	147.18	10.21	147.71	157.39	9.49	100
18H	147.00	157.10	8.82	155.82	165.92	9.83	103
19H	156.50	166.60	10.67	167.17	177.27	9.90	104
20H	166.00	176.08	11.96	177.96	188.04	9.81	103
21H	175.50	185.55	12.13	187.63	197.68	10.05	106

Table T12 (continued).

Core	Depth CSF (m)		Offset (m)	Depth CCSF-A (m)		Recovered (m)	Recovery (%)
	Top	Bottom		Top	Bottom		
22D	185.00	185.00	12.47	197.47	197.47	0.00	0
23H	187.00	197.06	13.37	200.37	210.43	10.06	106
24H	196.50	201.68	12.13	208.63	213.81	5.18	104
25H	201.50	211.27	14.33	215.83	225.60	9.77	103
26H	211.00	220.92	15.21	226.21	236.13	9.92	104
27H	220.50	230.54	16.33	236.83	246.87	10.04	106
					Total:	1199.7	101

Table T13. Splice table indicating tie points between holes, Site U1341. Sampling along the splice should be used to construct a continuous record.

Hole, core, section, interval (cm)	Depth (m)			Hole, core, section, interval (cm)	Depth (m)	
	CSF	CCSF-A			CSF	CCSF-A
323-				323-		
U1341A-1H-2, 89.04	2.39	2.39	Tie to	U1341B-1H-2, 95.03	2.45	2.39
U1341B-1H-5, 103.83	7.04	6.97	Tie to	U1341C-2H-1, 115.25	6.55	6.92
U1341C-2H-7, 5.79	14.47	14.83	Tie to	U1341A-3H-2, 44.85	14.35	14.80
U1341A-3H-6, 127.76	21.18	21.63	Tie to	U1341B-3H-3, 9.55	21.20	21.65
U1341B-3H-7, 1.89	27.12	27.57	Tie to	U1341C-4H-2, 3.73	26.04	27.67
U1341C-4H-7, 76.78	34.27	35.90	Tie to	U1341A-5H-2, 99.56	34.00	35.91
U1341A-5H-6, 81.05	39.81	41.72	Tie to	U1341B-5H-2, 58.75	39.29	41.71
U1341B-5H-7, 26.09	46.46	48.89	Tie to	U1341C-6H-1, 140.27	44.80	48.71
U1341C-6H-7, 7.79	52.51	56.42	Tie to	U1341A-7H-2, 79.43	52.79	56.46
U1341A-7H-6, 135.02	59.35	63.02	Tie to	U1341B-7H-3, 103.09	60.23	63.02
U1341B-7H-7, 5.01	65.25	68.04	Tie to	U1341C-8H-2, 47.82	62.98	68.01
U1341C-8H-6, 149.80	70.00	75.03	Tie to	U1341A-9H-1, 70.09	70.15	74.99
U1341A-9H-5, 91.79	76.37	81.21	Tie to	U1341B-9H-1, 90.10	76.00	81.27
U1341B-9H-6, 96.05	83.66	88.92	Tie to	U1341C-10H-2, 8.61	81.59	88.94
U1341C-10H-6, 109.75	88.60	95.95	Tie to	U1341B-10H-4, 102.98	90.13	95.85
U1341B-10H-7, 14.79	93.25	98.96	Tie to	U1341C-11H-2, 148.45	92.38	98.97
U1341C-11H-5, 6.00	95.47	102.05	Tie to	U1341B-11H-2, 44.31	96.04	102.03
U1341B-11H-6, 56.64	102.22	108.20	Tie to	U1341C-12H-4, 1.01	99.98	108.19
U1341C-12H-6, 138.93	104.34	112.56	Tie to	U1341B-12H-2, 102.74	106.18	112.57
U1341B-12H-6, 104.59	112.20	118.59	Tie to	U1341C-13H-4, 67.89	110.18	118.67
U1341C-13H-7, 20.44	114.20	122.69	Tie to	U1341A-14H-2, 65.64	119.16	122.69
U1341A-14H-6, 113.52	125.64	129.17	Tie to	U1341C-15H-1, 105.21	125.05	129.20
U1341C-15H-6, 137.25	132.82	136.97	Tie to	U1341B-14H-4, 105.69	128.21	136.95
U1341B-14H-7, 87.56	132.58	141.32	Append to	U1341B-15H-1, 0.03	132.20	140.97
U1341B-15H-6, 130.79	141.01	149.78	Tie to	U1341A-16H-3, 68.87	139.69	149.81
U1341A-16H-7, 21.96	145.22	155.34	Tie to	U1341B-16H-3, 90.85	145.61	155.34
U1341B-16H-5, 30.50	148.01	157.74	Tie to	U1341A-17H-2, 85.49	147.85	157.77
U1341A-17H-6, 117.90	154.18	164.10	Tie to	U1341B-17H-3, 134.25	155.54	164.11
U1341B-17H-5, 77.29	157.97	166.54	Tie to	U1341A-18H-1, 65.08	155.60	166.49
U1341A-18H-4, 33.86	159.79	170.68	Tie to	U1341C-19H-3, 54.56	160.05	170.71
U1341C-19H-7, 2.56	165.53	176.19	Tie to	U1341A-19H-1, 105.11	165.55	176.21
U1341A-19H-5, 103.48	171.53	182.19	Tie to	U1341C-20H-3, 122.48	170.17	182.13
U1341C-20H-6, 145.55	174.91	186.86	Tie to	U1341A-20H-1, 60.07	174.60	186.91
U1341A-20H-5, 52.87	180.53	192.83	Tie to	U1341B-21H-1, 85.10	181.50	192.77
U1341B-21H-4, 121.26	186.36	197.63	Tie to	U1341A-21H-1, 40.06	183.85	197.66
U1341A-21H-6, 119.23	192.14	205.95	Tie to	U1341B-22H-3, 33.94	193.54	206.01
U1341B-22H-6, 128.38	198.98	211.45	Tie to	U1341A-22H-1, 130.14	194.30	211.48
U1341A-22H-5, 97.20	199.97	217.15	Tie to	U1341C-25H-1, 130.26	202.80	217.13
U1341C-25H-6, 144.17	210.44	224.77	Tie to	U1341B-24H-2, 80.14	211.50	224.76
U1341B-24H-6, 3.90	216.74	229.99	Tie to	U1341A-24H-2, 99.48	214.49	229.99
U1341A-24H-6, 28.41	219.78	235.28	Tie to	U1341B-25H-2, 9.44	220.29	235.24
U1341B-25H-5, 10.85	224.81	239.75	Tie to	U1341C-27H-2, 145.16	223.45	239.78
U1341C-27H-6, 33.17	228.33	244.66	Tie to	U1341B-26H-2, 24.11	229.94	244.67
U1341B-26H-6, 138.91	237.09	251.81	Tie to	U1341A-27H-2, 94.01	235.64	251.79
U1341A-27H-5, 70.25	239.90	256.06	Tie to	U1341B-27H-2, 139.89	240.60	256.04
U1341B-27H-6, 46.72	245.67	261.11	Tie to	U1341A-28H-2, 80.09	245.00	261.11
U1341A-28H-5, 82.53	249.53	265.64	Tie to	U1341B-28H-2, 140.35	250.10	265.62
U1341B-28H-6, 106.17	255.76	271.28	Tie to	U1341A-29H-2, 110.06	254.80	271.31
U1341A-29H-6, 117.40	260.87	277.38	Tie to	U1341B-29H-4, 12.93	261.33	277.41
U1341B-29H-6, 30.14	264.50	280.58	Tie to	U1341A-30H-1, 150.16	263.20	280.57
U1341A-30H-7, 0.02	270.70	288.07	Tie to	U1341B-30H-4, 31.33	271.01	288.08
U1341B-30H-6, 130.63	275.01	292.07	Tie to	U1341A-31H-3, 30.03	274.50	292.05
U1341A-31H-6, 126.89	279.97	297.52	Tie to	U1341B-31H-3, 89.41	279.59	297.53
U1341B-31H-6, 41.16	283.51	301.45	Tie to	U1341A-32H-1, 95.10	281.65	301.43
U1341A-32H-4, 82.86	286.03	305.81	Tie to	U1341B-32H-4, 89.77	287.74	305.79
U1341B-32H-6, 51.23	289.74	307.79	Tie to	U1341A-33H-1, 40.06	290.60	307.80
U1341A-33H-6, 112.36	298.82	316.02	Tie to	U1341B-33H-4, 88.02	298.68	316.01
U1341B-33H-5, 56.57	299.87	317.20	Tie to	U1341A-34H-1, 40.06	300.10	317.20
U1341A-34H-7, 63.64	309.34	326.44	Append to	U1341A-35H-1, 0.03	309.20	326.43
U1341A-35H-7, 18.78	318.39	335.61	Tie to	U1341B-36H-1, 90.19	317.70	335.61
U1341B-36H-4, 127.40	322.57	340.48	Tie to	U1341A-36H-3, 49.12	322.19	340.49
U1341A-36H-7, 18.35	327.58	345.88	Tie to	U1341B-37H-1, 85.17	327.15	345.88
U1341B-37H-6, 43.67	334.24	352.96	Tie to	U1341A-38H-2, 9.23	334.29	352.96
U1341A-38H-6, 4.93	340.25	358.91	Tie to	U1341B-38H-3, 99.09	339.79	358.88
U1341B-38H-7, 3.02	344.83	363.92	Tie to	U1341A-39H-2, 110.17	344.80	363.96
U1341A-39H-6, 81.81	350.52	369.67	Tie to	U1341B-39H-4, 23.38	350.03	369.65

Table T14. Sedimentation rates and their control points, Hole U1341B. (**See table note.**)

Age (Ma)	Depth CSF (m)	Control point	Sedimentation rate (cm/k.y.)
0.3	32.9	Depth of LO *Proboscia curvirostris*	11
0.781	82.5	Brunhes bottom	10
0.998	104.0	Jaramillo top	10
1.072	137.8	Jaramillo bottom	46
1.778	245.5	Depth of RI *Neodenticula seminae*	15
2.581	367.8	Gauss top	15
3.8	463.0	Depth of FO *Neodenticula koizumii*	8

Note: LO = last occurrence, RI = rapid increase, FO = first occurrence.

Table T15. Datum events of radiolarians, diatoms, calcareous nannofossils, silicoflagellates, and paleomagnetics, Site U1342. (**See table notes.**)

Datum event	Taxon/ magnetics	Age (Ma)	Depth CSF (m)				Depth CCSF-A (m)			
			U1342A	U1342B	U1342C	U1342D	U1342A	U1342B	U1342C	U1342D
LO *Lychnocanoma nipponica sakaii*	Radiolarian	0.05	0.9	2.7	3.6	3.1	0.9	2.7	3.6	3.0
LO *Amphimelissa setosa*	Radiolarian	0.08–1	—	—	3.6	—	—	—	3.6	—
LO *Spongodiscus* sp.	Radiolarian	0.28–0.32	6.6	10.2	12.1	11.0	6.8	10.1	11.9	11.0
LO *Axoprunum acquilonium*	Radiolarian	0.25–0.43	16.2	19.8	12.1	20.5	16.8	20.0	11.9	21.2
LO *Proboscia curvirostris*	Diatom	0.3	—	—	21.8	—	—	—	22.0	—
LO *Pseudoemiliana lacunosa*	Calcareous nannofossil	0.44	16.2	—	—	—	16.8	—	—	—
LO *Dichtyocha subarctios*	Silicoflagellate	0.73–0.75	25.9	—	—	30.0	26.8	—	—	31.2
Brunhes/Matuyama	Paleomagnetic	0.781	24.9	—	25.1	24.8	26.4	—	26.2	26.1
Kamikatsura Excursion	Paleomagnetic	0.885	27.3	—	27.0	27.0	28.7	—	28.1	28.6
LO *Eucyrtidium matuyamai*	Radiolarian	0.9–1.5	—	29.3	—	—	—	30.3	—	—
Santa Rosa Excursion	Paleomagnetic	0.93	—	—	29.0	28.5	—	—	30.1	30.1
Jaramillo top	Paleomagnetic	0.998	—	—	30.7	30.3	—	—	31.8	31.9
Jaramillo bottom	Paleomagnetic	1.072	33.5	—	34.5	34.0	35.6	—	35.6	35.6
Punaruu Excursion	Paleomagnetic	1.125	35.8	—	36.3	36.3	37.9	—	38.3	38.6
Cobb Mountain top	Paleomagnetic	1.173	40.3	—	40.1	39.9	43.0	—	42.1	42.3
Cobb Mountain bottom	Paleomagnetic	1.185	41.5	—	40.9	40.6	44.3	—	42.9	43.0

Notes: For last occurrences (LO), the depth was estimated as the midpoint between the depth at which the species was last observed and the depth of the next sample above. — = not applicable.

Table T16. Affine table indicating the amount that each core in each hole needs to be offset in order to construct a continuous record, Site U1342. (See table note.)

Core	Depth CSF (m)		Offset (m)	Depth CCSF-A (m)		Recovered (m)	Recovery (%)
	Top	Bottom		Top	Bottom		
323-U1342A-							
1H	0.00	1.80	0.00	0.00	1.80	1.75	97
2H	1.80	11.30	0.55	2.35	11.85	9.61	101
3H	11.30	20.80	1.01	12.31	21.81	9.71	102
4H	20.80	30.30	1.47	22.27	31.77	9.95	105
5H	30.30	39.80	2.20	32.50	42.00	9.92	104
6H	39.80	48.30	2.78	42.58	51.08	8.55	101
7H	48.30	49.30	2.78	51.08	52.08	7.44	744
8D	49.30	52.30	—	—	—	0.00	0
9X	52.30	53.30	—	—	—	0.46	46
323-U1342B-							
1H	0.00	5.30	0.07	0.07	5.37	5.33	101
2H	5.30	14.80	0.04	5.34	14.84	9.78	103
3H	14.80	24.30	0.94	15.74	25.24	10.01	105
4H	24.30	33.80	1.50	25.80	35.30	9.77	103
5H	33.80	43.30	2.27	36.07	45.57	9.94	105
323-U1342C-							
1H	0.00	7.20	–0.03	–0.03	7.17	7.22	100
2H	7.20	16.70	0.01	7.21	16.71	9.84	104
3H	16.70	26.20	1.14	17.84	27.34	9.67	102
4H	26.20	35.70	1.12	27.32	36.82	9.80	103
5H	35.70	45.20	2.03	37.73	47.23	9.98	105
6H	45.20	45.40	—	—	—	0.22	110
323-U1342D-							
1H	0.00	6.00	–0.01	–0.01	5.99	6.11	102
2H	6.00	15.50	0.59	6.59	16.09	9.83	103
3H	15.50	25.00	1.31	16.81	26.31	9.62	101
4H	25.00	34.50	1.61	26.61	36.11	9.83	103
5H	34.50	44.00	2.36	36.86	46.36	9.90	104
6D	44.00	62.60	—	—	—	0.00	0
7X	62.60	66.60	—	—	—	0.55	14
8X	66.60	71.60	—	—	—	1.66	33
9X	71.60	75.60	—	—	—	3.84	96
10X	75.60	82.10	—	—	—	4.66	72
11X	82.10	87.90	—	—	—	3.34	58
12X	87.90	90.10	—	—	—	2.01	91
13X	90.10	94.90	—	—	—	4.64	97
14X	94.90	102.50	—	—	—	3.48	46
15X	102.50	106.10	—	—	—	1.48	41
16X	106.10	115.10	—	—	—	2.49	28
17X	115.10	117.70	—	—	—	5.70	219
18X	117.70	121.70	—	—	—	3.00	75
19X	121.70	127.70	—	—	—	4.23	70

Note: — = not applicable.

Table T17. Splice table indicating tie points between holes, Site U1342. Sampling along the splice should be used to construct a continuous record.

Hole, core, section, interval (cm)	Depth (m)			Hole, core, section, interval (cm)	Depth (m)	
	CSF	CCSF-A			CSF	CCSF-A
323-				323-		
U1342D-1H-4, 75.13	5.25	5.24	Tie to	U1342A-2H-2, 139.58	4.68	5.22
U1342A-2H-7, 16.89	10.96	11.51	Tie to	U1342C-2H-3, 130.27	11.50	11.51
U1342C-2H-7, 27.28	16.46	16.47	Tie to	U1342A-3H-3, 120.38	15.48	16.49
U1342A-3H-6, 124.72	20.04	21.05	Tie to	U1342C-3H-3, 24.38	19.94	21.08
U1342C-3H-7, 39.46	26.07	27.21	Tie to	U1342D-4H-1, 60.10	25.58	27.18
U1342D-4H-7, 4.90	34.05	35.66	Tie to	U1342A-5H-3, 14.51	33.44	35.64
U1342A-5H-6, 104.36	38.83	41.03	Tie to	U1342D-5H-3, 119.73	38.70	41.06

Table T18. Sedimentation rates and their control points, Site U1342. (See table note.)

Age (Ma)	Depth (m) CSF	Depth (m) CCSF-A	Control point	Sedimentation rate (cm/k.y.)
0.05	2.5	2.5	Average depth of LO *Lychnocanoma nipponica sakaii*	5
0.3	10.0	10.0	Average depth of LO *Spongodiscus* sp.	3
0.781	24.9	26.2	Brunhes bottom	3
0.885	27.1	28.5	Kamikatsura Excursion	2
1.072	34.0	35.6	Jaramillo bottom	4
1.125	36.1	38.3	Punaruu Excursion	5
1.173	40.1	42.5	Cobb Mountain top	9

Note: LO = last occurrence.

Table T19. Datum events of radiolarians, diatoms, calcareous nannofossils, silicoflagellates, ebridians, dinoflagellates, planktonic foraminifers, and paleomagnetics, Holes U1343A, U1343C, and U1343E. (See table notes.)

Datum event	Taxon/ magnetics	Age (Ma)	Depth CSF (m) Hole U1343A	Depth CSF (m) Hole U1343C	Depth CSF (m) Hole U1343E	Depth CCSF-A (m) Hole U1343A	Depth CCSF-A (m) Hole U1343C	Depth CCSF-A (m) Hole U1343E
LO *Lychnocanoma nipponica sakaii*	Radiolarian	0.05	10.3	12.0	13.0	10.2	11.9	16.6
LO *Distephanus octonarius*	Silicoflagellate	0.2–0.3	—	—	69.4	—	—	78.8
LO *Spongodiscus* sp.	Radiolarian	0.28–0.32	76.9	83.0	79.5	82.7	89.0	90.2
LO *Axoprunum acquilonium*	Radiolarian	0.25–0.43	86.5	111.4	87.6	93.6	121.8	99.8
LO *Proboscia curvirostris*	Diatom	0.3	—	—	69.4	—	—	78.8
LO *Thalassirosira jouseae*	Diatom	0.3	95.8	—	69.4	93.6	—	78.8
LO *Stylatractus universus*	Radiolarian	0.41–0.51	105.6	129.8	104.2	115.1	143.5	118.9
LO *Pseudoemiliania lacunosa*	Calcareous nannofossil	0.44	109.3	—	—	119.5	—	—
LO *Dichtyocha subarctios*	Silicoflagellate	0.6–0.8	—	210.5	188.6	—	236.6	215.4
Brunhes/Matuyama	Paleomagnetic	0.781	184.4	185.0	181.4	209.0	207.2	207.7
LCO *Actinocyclus oculatus*	Diatom	0.9	—	—	296.4	—	—	332.0
LO *Eucyrtidium matuyamai*	Radiolarian	0.9–1.5	—	—	296.4	—	—	332.0
Jaramillo top	Paleomagnetic	0.998	—	—	232.0	—	—	267.6
Jaramillo bottom	Paleomagnetic	1.072	—	—	266.3	—	—	302.0
Cobb Mountain top	Paleomagnetic	1.173	—	—	291.5	—	—	327.1
LO *Filisphaera filifera*	Dinoflagellate	1.4–1.7	—	—	372.1	—	—	407.7
FO *Eucyrtidium matuyamai*	Radiolarian	1.7–1.9	—	—	612.5	—	—	648.1
LO *Pyxidicula horridus*	Diatom	1.7–1.9	—	—	517.3	—	—	552.9
LO *Ammodochium rectangulare*	Ebridian	1.9	—	—	555.9	—	—	591.5
LCO *Neodenticula koizumii*	Diatom	2.0–2.2	—	—	680.8	—	—	716.4
LO *Neogloboquadrina atlantica*	Planktonic foraminifer	2.4–2.5	—	—	372.1	—	—	407.7

Notes: For first occurrences (FO), the depth was estimated as the midpoint between the depth at which the species was first observed and the depth of the next sample below. For last occurrences (LO), the depth was estimated as the midpoint between the depth at which the species was last observed and the depth of the next sample above. LCO = last common occurrence, — = not applicable.

Table T20. Affine table indicating the amount that each core in each hole needs to be offset in order to construct a continuous record, Site U1343. (**Continued on next two pages.**)

	Depth CSF (m)		Offset	Depth CCSF-A (m)		Recovered	Recovery
Core	Top	Bottom	(m)	Top	Bottom	(m)	(%)
323-U1343A-							
1H	0.00	5.49	–0.10	–0.10	5.39	5.49	100
2H	5.50	15.04	–0.09	5.41	14.95	9.54	100
3H	15.00	24.73	–0.16	14.84	24.57	9.73	102
4H	24.50	34.76	0.46	24.96	35.22	10.26	108
5H	34.00	44.01	2.62	36.62	46.63	10.01	105
6H	43.50	54.02	3.26	46.76	57.28	10.52	111
7H	53.00	62.29	4.97	57.97	67.26	9.29	98
8H	62.50	71.89	5.29	67.79	77.18	9.39	99
9H	72.00	82.00	6.26	78.26	88.26	10.00	105
10H	81.50	91.00	8.03	89.53	99.03	9.50	100
11H	91.00	100.60	8.97	99.97	109.57	9.60	101
12H	100.50	110.52	10.18	110.68	120.70	10.02	105
13H	110.00	119.42	12.13	122.13	131.55	9.42	99
14H	119.50	128.96	13.75	133.25	142.71	9.46	100
15H	129.00	139.16	13.88	142.88	153.04	10.16	107
16H	138.50	147.21	16.41	154.91	163.62	8.71	92
17H	148.00	157.39	17.33	165.33	174.72	9.39	99
18H	157.50	166.22	18.66	176.16	184.88	8.72	92
19H	167.00	173.90	19.93	186.93	193.83	6.90	115
20H	173.00	182.06	21.79	194.79	203.85	9.06	95
21H	182.50	191.60	23.24	205.74	214.84	9.10	96
22H	192.00	201.76	24.64	216.64	226.40	9.76	103
323-U1343B-							
1H	0.00	6.85	0.01	0.01	6.86	6.85	98
2H	7.00	16.87	–0.19	6.81	16.68	9.87	104
3H	16.50	25.08	–0.02	16.48	25.06	8.58	90
4H	26.00	35.26	0.67	26.67	35.93	9.26	97
323-U1343C-							
1H	0.00	7.24	0.00	0.00	7.24	7.24	101
2H	7.20	16.67	–0.04	7.16	16.63	9.47	100
3H	16.70	26.60	–0.11	16.59	26.49	9.90	104
4H	26.20	36.40	0.86	27.06	37.26	10.20	107
5H	35.70	44.75	1.71	37.41	46.46	9.05	95
6H	45.20	55.51	3.03	48.23	58.54	10.31	109
7H	54.70	63.91	4.41	59.11	68.32	9.21	97
8H	64.20	70.68	2.82	67.02	73.50	6.48	162
9H	68.20	78.35	5.26	73.46	83.61	10.15	107
10H	77.70	87.68	6.71	84.41	94.39	9.98	105
11H	87.20	97.54	7.87	95.07	105.41	10.34	109
12H	96.70	106.68	9.79	106.49	116.47	9.98	105
13H	106.20	116.10	11.08	117.28	127.18	9.90	104
14H	115.70	124.65	13.19	128.89	137.84	8.95	94
15H	125.20	135.04	14.04	139.24	149.08	9.84	104
16D	134.70	134.70	13.79	148.49	148.49	0.00	0
17H	144.20	153.40	17.22	161.42	170.62	9.20	97
18H	153.70	163.15	18.24	171.94	181.39	9.45	99
19H	163.20	171.99	20.42	183.62	192.41	8.79	93
20H	172.70	182.21	21.11	193.81	203.32	9.51	100
21H	182.20	192.15	22.24	204.44	214.39	9.95	105
22H	191.70	196.16	23.85	215.55	220.01	4.46	99
23H	196.20	205.45	25.82	222.02	231.27	9.25	97
24H	205.70	215.54	27.60	233.30	243.14	9.84	104
25H	215.20	224.77	28.41	243.61	253.18	9.57	101
26H	224.70	234.72	29.98	254.68	264.70	10.02	105
323-U1343D-							
1H	0.00	8.53	1.16	1.16	9.69	8.53	100
323-U1343E-							
1H	0.00	8.22	3.48	3.48	11.70	8.22	100
2H	8.20	17.80	3.72	11.92	21.52	9.60	101
3H	17.70	26.40	3.82	21.52	30.22	8.70	92
4H	27.20	37.17	5.24	32.44	42.41	9.97	105
5H	36.70	43.06	5.37	42.07	48.43	6.36	67
6H	46.20	55.55	8.42	54.62	63.97	9.35	98
7H	55.70	64.00	8.82	64.52	72.82	8.30	87
8H	65.20	74.89	9.87	75.07	84.76	9.69	102

Table T20 (continued). (Continued on next page.)

Core	Depth CSF (m)		Offset (m)	Depth CCSF-A (m)		Recovered (m)	Recovery (%)
	Top	Bottom		Top	Bottom		
9H	74.70	84.15	11.56	86.26	95.71	9.45	99
10H	84.20	91.08	12.80	97.00	103.88	6.88	72
11H	93.70	101.77	13.89	107.59	115.66	8.07	108
12H	101.20	106.69	15.40	116.60	122.09	5.49	100
13D	106.70	106.70	15.39	122.09	122.09	0.00	0
14H	109.70	116.05	15.37	125.07	131.42	6.35	127
15H	114.70	123.45	17.78	132.48	141.23	8.75	92
16H	124.20	129.56	18.28	142.48	147.84	5.36	107
17H	129.20	138.44	19.16	148.36	157.60	9.24	97
18H	138.70	148.31	20.58	159.28	168.89	9.61	101
19H	148.20	155.97	22.02	170.22	177.99	7.77	100
20H	156.00	164.99	24.59	180.59	189.58	8.99	95
21H	165.50	175.17	25.09	190.59	200.26	9.67	102
22H	175.00	183.86	26.36	201.36	210.22	8.86	104
23H	183.50	193.41	27.21	210.71	220.62	9.91	104
24H	193.00	197.57	29.78	222.78	227.35	4.57	102
25H	197.50	208.09	30.18	227.68	238.27	10.59	111
26H	207.00	217.14	32.61	239.61	249.75	10.14	107
27H	216.50	226.11	34.51	251.01	260.62	9.61	101
28H	226.00	234.82	35.62	261.62	270.44	8.82	100
29H	234.80	245.59	35.62	270.42	281.21	10.79	114
30H	244.30	254.31	35.62	279.92	289.93	10.01	105
31H	253.80	263.85	35.62	289.42	299.47	10.05	106
32H	263.30	272.59	35.62	298.92	308.21	9.29	98
33H	272.80	282.40	35.62	308.42	318.02	9.60	101
34H	282.30	291.28	35.62	317.92	326.90	8.98	100
35H	291.30	301.49	35.62	326.92	337.11	10.19	107
36H	300.80	311.20	35.62	336.42	346.82	10.40	109
37H	310.30	320.29	35.62	345.92	355.91	9.99	105
38H	319.80	329.84	35.62	355.42	365.46	10.04	106
39H	329.30	338.51	35.62	364.92	374.13	9.21	97
40H	338.80	346.84	35.62	374.42	382.46	8.04	100
41H	346.80	354.42	35.62	382.42	390.04	7.62	100
42X	354.40	359.67	35.62	390.02	395.29	5.27	88
43X	360.40	367.42	35.62	396.02	403.04	7.02	73
44X	370.00	376.69	35.62	405.62	412.31	6.69	70
45X	379.60	388.36	35.62	415.22	423.98	8.76	91
46H	389.20	398.67	35.62	424.82	434.29	9.47	100
47H	398.70	406.09	35.62	434.32	441.71	7.39	100
48H	406.10	412.43	35.62	441.72	448.05	6.33	100
49H	412.40	418.54	35.62	448.02	454.16	6.14	101
50X	418.50	428.60	35.62	454.12	464.22	10.10	112
51X	427.50	435.95	35.62	463.12	471.57	8.45	88
52X	437.10	446.21	35.62	472.72	481.83	9.11	94
53X	446.80	455.98	35.62	482.42	491.60	9.18	96
54X	456.40	463.49	35.62	492.02	499.11	7.09	76
55X	465.70	475.70	35.62	501.32	511.32	10.00	104
56X	475.30	482.67	35.62	510.92	518.29	7.37	78
57X	484.80	494.07	35.62	520.42	529.69	9.27	97
58X	494.40	502.98	35.62	530.02	538.60	8.58	89
59X	504.00	512.62	35.62	539.62	548.24	8.62	89
60X	513.70	522.00	35.62	549.32	557.62	8.30	86
61X	523.30	532.51	35.62	558.92	568.13	9.21	96
62X	532.90	541.88	35.62	568.52	577.50	8.98	94
63X	542.50	550.64	35.62	578.12	586.26	8.14	84
64X	552.20	561.15	35.62	587.82	596.77	8.95	93
65X	561.80	568.87	35.62	597.42	604.49	7.07	74
66X	571.40	581.14	35.62	607.02	616.76	9.74	103
67X	580.90	588.60	35.62	616.52	624.22	7.70	80
68X	590.50	599.36	35.62	626.12	634.98	8.86	91
69X	600.20	606.94	35.62	635.82	642.56	6.74	70
70X	609.80	618.00	35.62	645.42	653.62	8.20	85
71X	619.40	628.26	35.62	655.02	663.88	8.86	92
72X	629.00	634.54	35.62	664.62	670.16	5.54	58
73X	638.60	643.89	35.62	674.22	679.51	5.29	55
74X	648.20	657.51	35.62	683.82	693.13	9.31	97
75X	657.80	667.19	35.62	693.42	702.81	9.39	99
76X	667.30	675.06	35.62	702.92	710.68	7.76	81
77X	676.90	686.47	35.62	712.52	722.09	9.57	100

Table T20 (continued).

Core	Depth CSF (m)		Offset (m)	Depth CCSF-A (m)		Recovered (m)	Recovery (%)
	Top	Bottom		Top	Bottom		
78X	686.50	695.30	35.62	722.12	730.92	8.80	92
79X	696.10	705.82	35.62	731.72	741.44	9.72	101
80X	705.70	713.90	35.62	741.32	749.52	8.20	85
81X	715.40	725.06	35.62	751.02	760.68	9.66	101
82X	725.00	734.51	35.62	760.62	770.13	9.51	99
83X	734.60	744.00	35.62	770.22	779.62	9.40	97

Table T21. Splice table indicating tie points between holes, Site U1343. Sampling along the splice should be used to construct a continuous record.

Hole, core, section, interval (cm)	Depth (m)			Hole, core, section, interval (cm)	Depth (m)	
	CSF	CCSF-A			CSF	CCSF-A
323-				323-		
U1343C-1H-5, 8	6.09	6.12	Tie to	U1343E-1H-2, 140	2.60	6.12
U1343E-1H-5, 129	6.89	10.46	Tie to	U1343C-2H-3, 81	10.49	10.46
U1343C-2H-6, 95	15.10	15.08	Tie to	U1343E-2H-3, 44	11.34	15.08
U1343E-2H-5, 142	15.32	19.08	Tie to	U1343A-3H-4, 19	19.20	19.08
U1343A-3H-6, 45	22.40	22.33	Tie to	U1343E-3H-1, 120	18.50	22.33
U1343E-3H-4, 146	23.16	27.07	Tie to	U1343A-4H-2, 111	26.59	27.07
U1343A-4H-6, 97	32.49	32.96	Tie to	U1343E-4H-1, 110	27.70	32.96
U1343E-4H-7, 1	35.56	40.88	Tie to	U1343C-5H-3, 102	39.13	40.88
U1343C-5H-5, 138	42.52	44.24	Tie to	U1343E-5H-2, 119	38.79	44.24
U1343E-5H-5, 10	41.61	47.08	Tie to	U1343A-6H-1, 90	43.80	47.08
U1343A-6H-7, 107	52.65	55.91	Tie to	U1343E-6H-2, 60	47.40	55.91
U1343E-6H-6, 51	53.13	61.61	Tie to	U1343C-7H-3, 35	57.19	61.61
U1343C-7H-5, 100	60.72	65.16	Tie to	U1343E-7H-1, 120	56.30	65.16
U1343E-7H-4, 138	60.83	69.74	Tie to	U1343A-8H-3, 24	64.40	69.74
U1343A-8H-6, 110	69.70	75.00	Tie to	U1343E-8H-1, 50	65.20	75.00
U1343E-8H-6, 87	71.99	81.87	Tie to	U1343A-9H-3, 115	75.59	81.87
U1343A-9H-5, 143	78.79	85.07	Tie to	U1343C-10H-2, 36	78.35	85.07
U1343C-10H-7, 87	86.30	93.01	Tie to	U1343A-10H-4, 36	84.97	93.01
U1343A-10H-7, 24	89.17	97.21	Tie to	U1343C-11H-2, 95	89.30	97.21
U1343C-11H-7, 66	96.47	104.34	Tie to	U1343A-11H-4, 113	95.34	104.34
U1343A-11H-6, 117	98.19	107.19	Tie to	U1343C-12H-1, 80	97.40	107.19
U1343C-12H-6, 25	103.80	113.61	Tie to	U1343A-12H-3, 87	103.40	113.61
U1343A-12H-7, 28	108.84	119.02	Tie to	U1343C-13H-2, 143	107.89	119.02
U1343C-13H-6, 65	113.06	124.18	Tie to	U1343A-13H-3, 87	112.05	124.18
U1343A-13H-6, 111	116.75	128.90	Tie to	U1343C-14H-1, 80	115.70	128.90
U1343C-14H-5, 69	121.24	134.47	Tie to	U1343A-14H-2, 93	120.70	134.47
U1343A-14H-7, 15	126.98	140.75	Tie to	U1343C-15H-2, 19	126.70	140.75
U1343C-15H-7, 55	133.92	147.98	Tie to	U1343A-15H-5, 3	134.05	147.98
U1343A-15H-7, 38	137.36	151.24	Tie to	U1343E-17H-3, 5	132.00	151.24
U1343E-17H-6, 105	137.50	156.67	Tie to	U1343A-16H-2, 138	140.26	156.67
U1343A-16H-6, 70	145.33	161.75	Tie to	U1343E-18H-3, 91	141.10	161.75
U1343E-18H-7, 76	146.53	167.19	Tie to	U1343A-17H-2, 60	149.85	167.19
U1343A-17H-6, 45	155.42	172.79	Tie to	U1343C-18H-2, 58	154.50	172.79
U1343C-18H-6, 70	160.64	178.89	Tie to	U1343A-18H-3, 62	160.20	178.89
U1343A-18H-6, 4	163.88	182.57	Tie to	U1343E-20H-2, 90	157.90	182.57
U1343E-20H-6, 84	163.58	188.22	Tie to	U1343C-19H-4, 30	167.77	188.22
U1343C-19H-6, 79	170.99	191.43	Tie to	U1343E-21H-2, 56	166.30	191.43
U1343E-21H-5, 144	171.56	196.72	Tie to	U1343C-20H-3, 86	175.61	196.72
U1343C-20H-6, 119	180.22	201.36	Tie to	U1343E-22H-1, 40	175.00	201.36
U1343E-22H-4, 128	180.10	206.49	Tie to	U1343A-21H-1, 100	183.25	206.49
U1343A-21H-7, 42	189.84	213.10	Tie to	U1343E-23H-3, 35	185.86	213.10
U1343E-23H-6, 122	190.30	217.55	Tie to	U1343A-22H-2, 25	192.90	217.55
U1343A-22H-6, 134	199.60	224.27	Tie to	U1343C-23H-3, 40	198.42	224.27
U1343C-23H-6, 129	203.14	229.01	Tie to	U1343E-25H-2, 128	198.79	229.01
U1343E-25H-7, 107	206.08	236.28	Tie to	U1343C-24H-4, 50	208.66	236.28
U1343C-24H-7, 89	213.55	241.17	Tie to	U1343E-26H-2, 123	208.49	241.17
U1343E-26H-7, 12	214.55	247.25	Tie to	U1343C-25H-4, 30	218.81	247.25
U1343C-25H-7, 15	223.03	251.53	Tie to	U1343E-27H-1, 90	217.00	251.53
U1343E-27H-5, 150	223.50	258.11	Tie to	U1343C-26H-3, 133	228.10	258.11
U1343C-26H-7, 48	233.05	263.07	Tie to	U1343E-28H-2, 31	227.40	263.07
U1343E-28H-6, 70	234.20	269.83	Append to	U1343E-83X-CC, 40	744.00	779.62

Table T22. Sedimentation rates and their control points, Site U1343. (**See table note.**)

Age (Ma)	Depth (m)		Control point	Sedimentation rate (cm/k.y.)
	CSF	CCSF-A		
0.3	79.8	87.3	Average depth of LO *Spongodiscus* sp.	29
0.781	183.6	208.0	Average depth of Brunhes bottom	25
0.998	232.0	267.6	Jaramillo top	27
1.072	266.3	302.0	Jaramillo bottom	46
1.173	291.5	327.1	Cobb Mountain top	25
1.55	372.1	407.7	LO *Filisphaera filifera*	21
1.8	517.3	552.9	LO *Pyxidicula horridus*	58
2.1	680.8	716.4	LCO *Neodenticula koizumii*	54

Note: LO = last occurrence, LCO = last common occurrence.

Table T23. Datum events of radiolarians, diatoms, silicoflagellates, ebridians, dinoflagellates, and paleomagnetics, Holes U1344A, U1344D, and U1344E. (**See table notes.**)

Datum event	Taxon/ magnetics	Age (Ma)	Depth CSF (m)			Depth CCSF-A (m)		
			Hole U1344A	Hole U1344D	Hole U1344E	Hole U1344A	Hole U1344D	Hole U1344E
LO *Lychnocanoma nipponica sakaii*	Radiolarian	0.05	23.7	26.6	19.9	25.1	30.0	23.6
LO *Spongodiscus* sp.	Radiolarian	0.28–0.32	109.2	102.6	108.0	124.4	118.6	125.5
LO *Axoprunum acquilonium*	Radiolarian	0.25–0.43	118.7	—	117.7	136.1	—	136.7
LO *Proboscia curvirostris*	Diatom	0.3	118.7	93.2	117.7	136.1	107.1	136.7
LO *Thalassirosira jouseae*	Diatom	0.3	118.7	102.6	97.0	136.1	118.6	111.8
LO *Stylatractus universus*	Radiolarian	0.41–0.51	—	150.3	150.3	—	176.0	177.1
LO *Dichtyocha subarctios*	Silicoflagellate	0.6–0.8	275.3	237.4	—	320.1	278.1	—
Brunhes/Matuyama	Paleomagnetic	0.781	276.5	284.1	—	322.1	332.2	—
LCO *Actinocyclus oculatus*	Diatom	0.9	409.3	—	—	455.7	—	—
LO *Eucyrtidium matuyamai*	Radiolarian	0.9–1.5	409.3	—	—	455.7	—	—
Jaramillo top	Paleomagnetic	0.998	348.4	—	—	394.8	—	—
Jaramillo bottom	Paleomagnetic	1.072	373.0	—	—	419.4	—	—
Cobb Mountain top	Paleomagnetic	1.173	412.6	—	—	459.0	—	—
Cobb Mountain bottom	Paleomagnetic	1.185	423.2	—	—	469.6	—	—
LO *Filisphaera filifera*	Dinoflagellate	1.4–1.7	462.6	—	—	509.0	—	—
FCO *Proboscia curvirostris*	Diatom	1.7–2.0	526.1	—	—	572.5	—	—
LO *Pyxidicula horridus*	Diatom	1.7–1.9	592.0	—	—	638.4	—	—
Olduvai top	Paleomagnetic	1.778	669.9	—	—	716.3	—	—
LO *Ammodochium rectangulare*	Ebridian	1.9	731.4	—	—	777.9	—	—

Notes: For last occurrences (LO), the depth was estimated as the midpoint between the depth at which the species was last observed and the depth of the next sample above. LCO = last common occurrence, FCO = first common occurrence, — = not applicable.

Table T24. Affine table indicating the amount that each core in each hole needs to be offset in order to construct a continuous record, Site U1344. (**See table note.**) (**Continued on next two pages.**)

Core	Depth CSF (m)		Offset (m)	Depth CCSF-A (m)		Recovered (m)	Recovery (%)
	Top	Bottom		Top	Bottom		
323-U1344A-							
1H	0.00	9.14	0.00	0.00	9.14	9.14	100
2H	9.10	18.75	0.80	9.90	19.55	9.65	102
3H	18.60	28.72	2.01	20.61	30.73	10.12	107
4H	28.10	38.22	3.86	31.96	42.08	10.12	107
5H	37.60	47.61	5.93	43.53	53.54	10.01	105
6H	47.10	57.29	7.64	54.74	64.93	10.19	107
7H	56.60	66.68	7.66	64.26	74.34	10.08	106
8H	66.10	75.32	9.36	75.46	84.68	9.22	97
9H	75.60	85.21	12.11	87.71	97.32	9.61	101
10H	85.10	95.19	13.20	98.30	108.39	10.09	106
11H	94.60	104.46	14.22	108.82	118.68	9.86	104
12H	104.10	113.96	16.13	120.23	130.09	9.86	104
13H	113.60	123.49	18.69	132.29	142.18	9.89	104
14H	123.10	132.89	20.81	143.91	153.70	9.79	103
15H	132.60	142.45	22.79	155.39	165.24	9.85	104
16H	142.10	152.23	24.67	166.77	176.90	10.13	107
17H	151.60	161.27	26.19	177.79	187.46	9.67	102
18H	161.10	171.34	27.91	189.02	199.26	10.24	108
19H	170.60	180.17	30.52	201.12	210.69	9.57	101
20H	180.10	190.40	32.30	212.40	222.70	10.30	108
21H	189.60	199.28	34.74	224.34	234.02	9.68	102
22H	199.10	208.83	35.85	234.95	244.68	9.73	102
23H	208.60	218.11	38.70	247.30	256.81	9.51	100
24H	218.10	226.67	38.61	256.71	265.28	8.57	101
25H	226.60	236.10	38.21	264.81	274.31	9.50	100
26H	236.10	245.49	40.54	276.64	286.03	9.39	99
27H	245.60	255.83	42.04	287.64	297.87	10.23	108
28X	255.10	263.83	43.06	298.16	306.89	8.73	103
29X	263.60	270.35	44.06	307.66	314.41	6.75	70
30X	273.20	280.31	43.18	316.38	323.49	7.11	74
31X	282.80	288.58	43.78	326.58	332.36	5.78	60
32X	292.40	299.17	43.78	336.18	342.95	6.77	71
33X	302.00	309.23	43.78	345.78	353.01	7.23	75
34X	311.60	318.41	43.78	355.38	362.19	6.81	73
35X	320.90	323.57	43.78	364.68	367.35	2.67	28
36X	330.40	338.89	43.78	374.18	382.67	8.49	88
37X	340.00	346.38	43.78	383.78	390.16	6.38	66
38X	349.60	357.08	43.78	393.38	400.86	7.48	78
39X	359.20	364.23	43.78	402.98	408.01	5.03	52
40X	368.80	373.19	43.78	412.58	416.97	4.39	45
41X	378.50	387.97	43.78	422.28	431.75	9.47	100
42X	388.00	397.51	43.78	431.78	441.29	9.51	99
43X	397.60	403.56	43.78	441.38	447.34	5.96	62
44X	407.20	414.98	43.78	450.98	458.76	7.78	81
45X	416.80	425.93	43.78	460.58	469.71	9.13	95
46X	426.40	434.10	43.78	470.18	477.88	7.70	80
47X	436.00	443.02	43.78	479.78	486.80	7.02	73
48X	445.60	451.69	43.78	489.38	495.47	6.09	64
49X	455.10	461.85	43.78	498.88	505.63	6.75	70
50X	464.70	473.49	43.78	508.48	517.27	8.79	91
51X	474.40	482.67	43.78	518.18	526.45	8.27	87
52X	483.90	493.20	43.78	527.68	536.98	9.30	100
53X	493.20	502.13	43.78	536.98	545.91	8.93	92
54X	502.90	511.96	43.78	546.68	555.74	9.06	95
55X	512.40	521.80	43.78	556.18	565.58	9.40	98
56X	522.00	530.31	43.78	565.78	574.09	8.31	86
57X	531.70	540.28	43.78	575.48	584.06	8.58	89
58X	541.30	549.57	43.78	585.08	593.35	8.27	86
59X	550.90	558.79	43.78	594.68	602.57	7.89	82
60X	560.50	567.42	43.78	604.28	611.20	6.92	72
61X	570.10	578.90	43.78	613.88	622.68	8.80	91
62X	579.80	587.61	43.78	623.58	631.39	7.81	81
63X	589.40	596.29	43.78	633.18	640.07	6.89	72
64X	599.00	607.73	43.78	642.78	651.51	8.73	92
65X	608.50	618.08	43.78	652.28	661.86	9.58	100
66X	618.10	618.10	43.78	661.88	661.88	—	0
67X	627.70	627.70	43.78	671.48	671.48	—	0

Table T24 (continued). (Continued on next page.)

Core	Depth CSF (m)		Offset (m)	Depth CCSF-A (m)		Recovered (m)	Recovery (%)
	Top	Bottom		Top	Bottom		
68X	637.30	646.00	43.78	681.08	689.78	8.70	91
69X	646.90	647.34	43.78	690.68	691.12	0.44	5
70X	656.50	666.45	43.78	700.28	710.23	9.95	104
71X	666.10	675.18	43.78	709.88	718.96	9.08	95
72X	675.70	683.55	43.78	719.48	727.33	7.85	82
73X	685.30	694.70	43.78	729.08	738.48	9.40	98
74X	694.90	703.69	43.78	738.68	747.47	8.79	92
75X	704.50	713.35	43.78	748.28	757.13	8.85	92
76X	714.10	723.11	43.78	757.88	766.89	9.01	94
77X	723.70	733.13	43.78	767.48	776.91	9.43	98
78X	733.30	739.75	43.78	777.08	783.53	6.45	113
79X	739.00	746.59	43.78	782.78	790.37	7.59	126
323-U1344B-							
1H	0.00	4.80	–0.04	–0.04	4.76	4.80	100
323-U1344C-							
1H	0.00	7.12	0.04	0.04	7.16	7.12	100
2H	7.10	14.24	1.26	8.36	15.50	7.14	75
3H	16.60	26.40	2.70	19.30	29.10	9.80	103
4H	26.10	35.55	3.66	29.76	39.21	9.45	99
323-U1344D-							
1H	0.00	2.73	–0.02	–0.02	2.71	2.73	101
2H	2.70	12.25	2.20	4.90	14.45	9.55	101
3H	12.20	21.62	2.84	15.04	24.46	9.42	99
4H	21.70	31.67	3.80	25.50	35.47	9.97	105
5H	31.20	38.31	5.12	36.32	43.43	7.11	75
6H	40.70	50.21	8.16	48.86	58.37	9.51	100
7H	50.20	59.76	9.95	60.15	69.71	9.56	101
8H	59.70	66.51	9.67	69.37	76.18	6.81	72
9H	69.20	78.37	12.03	81.23	90.40	9.17	97
10H	78.70	88.54	13.26	91.96	101.80	9.84	104
11H	88.20	97.86	14.53	102.73	112.39	9.66	102
12H	97.70	107.37	17.37	115.07	124.74	9.67	102
13H	107.20	116.70	19.27	126.47	135.97	9.50	100
14H	116.70	126.38	21.29	137.99	147.67	9.68	102
15H	126.20	135.77	23.53	149.73	159.30	9.57	101
16H	135.70	145.40	25.00	160.70	170.40	9.70	102
17H	145.20	155.12	26.51	171.71	181.63	9.92	104
18H	154.70	164.39	28.21	182.91	192.60	9.69	102
19H	164.20	174.41	30.13	194.33	204.54	10.21	107
20H	173.70	183.08	31.43	205.13	214.51	9.38	99
21H	183.20	192.93	34.78	217.98	227.71	9.73	102
22H	192.70	201.89	37.45	230.15	239.34	9.19	97
23H	202.20	211.24	38.41	240.61	249.65	9.04	95
24H	211.70	221.15	40.92	252.60	262.05	9.45	99
25H	221.20	224.51	41.02	262.22	265.53	3.31	100
26H	224.50	234.09	40.49	264.99	274.58	9.59	101
27H	234.00	240.72	39.55	273.55	280.27	6.72	134
28H	239.00	248.38	42.01	281.01	290.39	9.38	99
29H	248.50	258.41	43.85	292.35	302.26	9.91	104
30H	258.00	267.40	45.49	303.49	312.89	9.40	99
31H	267.50	277.96	44.41	311.91	322.37	10.46	110
32H	277.00	286.27	45.42	322.42	331.69	9.27	98
323-U1344E-							
1H	0.00	5.34	0.28	0.28	5.62	5.34	101
2H	5.30	15.02	3.11	8.41	18.13	9.72	102
3H	14.80	24.85	4.15	18.95	29.00	10.05	106
4H	24.30	34.68	5.37	29.67	40.05	10.38	109
5H	33.80	43.82	7.31	41.11	51.13	10.02	105
6H	43.30	53.38	8.67	51.97	62.05	10.08	106
7H	52.80	62.10	11.33	64.13	73.43	9.30	98
8H	62.30	72.05	10.20	72.50	82.25	9.75	103
9H	71.80	81.37	11.98	83.78	93.35	9.57	101
10H	81.30	90.85	13.21	94.51	104.06	9.55	101
11D	90.80	90.80	13.21	104.01	104.01	—	0
12H	93.80	103.05	16.42	110.22	119.47	9.25	97
13H	103.30	112.90	18.56	121.86	131.46	9.60	101
14H	112.80	122.46	19.43	132.23	141.89	9.66	102

Table T24 (continued).

Core	Depth CSF (m)		Offset (m)	Depth CCSF-A (m)		Recovered (m)	Recovery (%)
	Top	Bottom		Top	Bottom		
15H	122.30	127.10	21.18	143.48	148.28	4.80	107
16H	126.80	136.51	23.44	150.24	159.95	9.71	102
17H	136.30	145.03	26.81	163.11	171.84	8.73	92
18H	145.80	155.49	26.81	172.61	182.30	9.69	102
19H	155.30	165.44	28.92	184.22	194.36	10.14	107
20H	164.80	174.28	30.74	195.54	205.02	9.48	100
21H	174.30	182.62	33.00	207.30	215.62	8.32	88
22H	183.80	193.85	34.87	218.67	228.72	10.05	106
23H	193.30	202.79	36.74	230.04	239.53	9.49	100

Note: — = not applicable.

Table T25. Splice table indicating tie points between holes, Site U1344. Sampling along the splice should be used to construct a continuous record.

Hole, core, section, interval (cm)	Depth (m)			Hole, core, section, interval (cm)	Depth (m)	
	CSF	CCSF-A			CSF	CCSF-A
323-				323-		
U1344A-1H-5, 121.33	7.21	7.22	Tie to	U1344D-2H-2, 79.99	5.00	7.22
U1344D-2H-6, 9.22	10.29	12.52	Tie to	U1344A-2H-2, 109.90	11.70	12.52
U1344A-2H-5, 71.84	15.82	16.63	Tie to	U1344D-3H-2, 4.45	13.74	16.63
U1344D-3H-6, 82.47	20.52	23.40	Tie to	U1344A-3H-2, 126.04	21.36	23.40
U1344A-3H-7, 51.63	28.12	30.13	Tie to	U1344E-4H-2, 5.77	24.75	30.13
U1344E-4H-7, 24.82	32.44	37.85	Tie to	U1344D-5H-1, 150.13	32.70	37.85
U1344D-5H-4, 114.59	36.85	41.97	Tie to	U1344E-5H-2, 44.01	34.62	41.97
U1344E-5H-6, 106.03	41.24	48.59	Tie to	U1344A-5H-5, 2.76	42.63	48.59
U1344A-5H-7, 40.44	46.01	51.99	Tie to	U1344D-6H-3, 79.88	43.80	51.99
U1344D-6H-5, 33.68	46.34	54.52	Tie to	U1344E-6H-2, 123.28	45.82	54.52
U1344E-6H-6, 112.47	51.71	60.40	Tie to	U1344A-6H-4, 122.06	52.74	60.40
U1344A-6H-6, 130.46	55.78	63.47	Tie to	U1344D-7H-3, 29.68	53.50	63.47
U1344D-7H-5, 79.51	56.90	66.88	Tie to	U1344A-7H-2, 135.75	59.06	66.88
U1344A-7H-7, 50.70	65.71	73.39	Tie to	U1344E-8H-2, 49.64	63.15	73.39
U1344E-8H-7, 80.85	70.89	81.09	Tie to	U1344A-8H-5, 74.41	71.69	81.09
U1344A-8H-7, 20.49	74.13	83.50	Tie to	U1344D-9H-3, 23.01	71.46	83.50
U1344D-9H-6, 66.49	76.32	88.37	Tie to	U1344E-9H-4, 72.99	76.38	88.37
U1344E-9H-6, 145.94	80.07	92.07	Tie to	U1344A-9H-4, 75.18	79.95	92.07
U1344A-9H-7, 3.43	83.70	95.85	Tie to	U1344D-10H-4, 27.91	82.55	95.85
U1344D-10H-7, 50.14	87.15	100.43	Tie to	U1344A-10H-2, 82.59	87.21	100.43
U1344A-10H-6, 108.77	93.44	106.68	Tie to	U1344D-11H-4, 42.03	92.12	106.68
U1344D-11H-6, 129.60	95.71	110.29	Tie to	U1344A-11H-2, 86.61	96.06	110.29
U1344A-11H-7, 23.38	102.78	117.05	Tie to	U1344D-12H-2, 67.00	99.65	117.05
U1344D-12H-6, 59.12	105.12	122.53	Tie to	U1344E-13H-1, 65.07	103.95	122.53
U1344E-13H-7, 1.89	111.45	130.01	Tie to	U1344D-13H-4, 26.69	110.74	130.01
U1344D-13H-7, 50.53	115.24	134.53	Tie to	U1344E-14H-3, 12.36	115.05	134.53
U1344E-14H-7, 10.92	120.97	140.43	Tie to	U1344D-14H-2, 136.02	119.10	140.43
U1344D-14H-6, 119.00	124.68	146.01	Tie to	U1344A-14H-2, 139.32	125.20	146.01
U1344A-14H-7, 56.55	131.65	152.48	Tie to	U1344E-16H-2, 123.47	129.00	152.48
U1344E-16H-8, 57.43	135.64	159.10	Tie to	U1344A-15H-3, 132.80	136.30	159.10
U1344A-15H-6, 129.75	140.70	163.52	Tie to	U1344D-16H-3, 85.11	138.50	163.52
U1344D-16H-6, 75.49	142.71	167.75	Tie to	U1344A-16H-2, 39.14	143.05	167.75
U1344A-16H-7, 81.04	150.80	175.52	Tie to	U1344D-17H-4, 15.34	149.00	175.52
U1344D-17H-7, 25.02	153.50	180.01	Tie to	U1344A-17H-3, 38.89	153.81	180.01
U1344A-17H-7, 100.98	160.26	186.48	Tie to	U1344E-19H-2, 127.63	157.55	186.48
U1344E-19H-6, 133.13	163.37	192.33	Tie to	U1344A-18H-3, 140.69	164.41	192.33
U1344A-18H-7, 64.02	169.54	197.46	Tie to	U1344D-19H-3, 101.71	167.31	197.46
U1344D-19H-8, 61.91	173.23	203.37	Tie to	U1344A-19H-3, 12.85	172.82	203.37
U1344A-19H-6, 115.76	178.24	208.76	Tie to	U1344E-21H-2, 3.94	175.74	208.76
U1344E-21H-5, 72.71	180.53	213.54	Tie to	U1344A-20H-1, 110.21	181.20	213.54
U1344A-20H-6, 99.00	188.25	220.55	Tie to	U1344E-22H-2, 131.14	185.65	220.55
U1344E-22H-6, 127.52	191.62	226.50	Tie to	U1344A-21H-2, 117.10	191.54	226.50
U1344A-21H-6, 103.40	197.02	231.80	Tie to	U1344D-22H-2, 89.09	194.30	231.80
U1344D-22H-6, 125.07	199.89	237.37	Tie to	U1344A-22H-3, 2.03	201.50	237.37
U1344A-22H-8, 22.57	208.14	244.02	Tie to	U1344D-23H-3, 43.77	205.60	244.02
U1344D-23H-6, 59.06	210.25	248.67	Tie to	U1344A-23H-1, 135.13	209.95	248.67
U1344A-23H-6, 91.28	216.76	255.48	Tie to	U1344D-24H-3, 64.01	214.54	255.48
U1344D-24H-7, 83.24	220.30	261.21	Tie to	U1344A-24H-4, 14.63	222.55	261.21
U1344A-24H-6, 2.46	225.42	264.08	Tie to	U1344D-25H-2, 33.66	223.04	264.08
U1344D-25H-3, 51.36	223.92	264.95	Tie to	U1344A-25H-1, 10.03	226.70	264.95
U1344A-25H-7, 43.57	235.48	273.69	Tie to	U1344D-27H-1, 10.03	234.10	273.69
U1344D-27H-5, 5.67	239.98	279.58	Tie to	U1344A-26H-3, 147.83	239.01	279.58
U1344A-26H-6, 148.94	243.50	284.06	Tie to	U1344D-28H-3, 113.04	242.04	284.06
U1344D-28H-7, 45.95	246.94	288.97	Tie to	U1344A-27H-2, 39.46	246.92	288.97
U1344A-27H-7, 59.24	253.85	295.93	Tie to	U1344D-29H-3, 55.10	252.05	295.93
U1344D-29H-6, 81.07	256.77	300.64	Tie to	U1344A-28X-2, 94.48	257.54	300.64
U1344A-28X-5, 122.21	262.32	305.40	Tie to	U1344D-30H-2, 40.71	259.91	305.40
U1344D-30H-6, 68.35	266.10	311.61	Tie to	U1344A-29X-3, 94.11	267.54	311.61
U1344A-29X-5, 41.09	269.56	313.64	Tie to	U1344D-31H-2, 86.58	269.20	313.64
U1344D-31H-7, 131.54	277.05	321.48	Tie to	U1344A-30X-5, 8.83	278.28	321.48
U1344A-30X-6, 17.28	279.66	322.86	Tie to	U1344D-32H-1, 40.05	277.40	322.86
U1344D-32H-7, 2.07	285.23	330.70	Tie to	U1344A-31X-4, 45.59	286.90	330.70
U1344A-31X-5, 49.99	288.24	332.02	Append to	U1344A-79X-CC, 31.00	746.59	790.37

Table T26. Sedimentation rates and their control points, Site U1344. (See table note.)

Age (Ma)	Depth (m)		Control point	Sedimentation rate (cm/k.y.)
	CSF	CCSF-A		
0.3	106.6	122.8	Average depth of LO *Spongodiscus* sp.	41
0.781	284.1	332.2	Hole U1344D depth of Brunhes bottom	44
0.998	348.4	394.8	Jaramillo top	29
1.072	373.0	419.4	Jaramillo bottom	33
1.173	412.6	459.0	Cobb Mountain top	39
1.185	423.2	469.6	Cobb Mountain bottom	89
1.778	669.9	716.3	Olduvai top	42
1.9	731.43	777.9	LO *Ammodochium rectangulare*	50

Note: LO = last occurrence.

Table T27. Datum events of radiolarians, diatoms, and silicoflagellates, Holes U1345A, U1345C, U1345D, and U1345E. (See table notes.)

Datum event	Taxon/ magnetics	Age (Ma)	Depth CSF (m)				Depth CCSF-A (m)			
			Hole U1345A	Hole U1345C	Hole U1345D	Hole U1345E	Hole U1345A	Hole U1345C	Hole U1345D	Hole U1345E
LO *Lychnocanoma nipponica sakaii*	Radiolarian	0.05	19.0	10.9	14.5	21.8	19.0	14.1	16.3	22.8
LO *Amphimelissa setosa*	Radiolarian	0.08–0.10	38.2	—	—	—	39.3	—	—	—
LO *Distephanus octonarius*	Silicoflagellate	0.2–0.3	75.9	—	—	—	81.4	—	—	—
LO *Spongodiscus* sp.	Radiolarian	0.28–0.32	84.5	77.4	78.4	80.0	91.4	85.5	87.1	88.0
LO *Axoprunum acquilonium*	Radiolarian	0.25–0.43	93.4	106.2	107.4	89.3	102.1	117.6	120.3	98.6
LO *Thalassirosira jouseae*	Diatom	0.3	84.5	—	—	80.0	91.4	—	—	88.0

Notes: For last occurrences (LO), the depth was estimated as the midpoint between the depth at which the species was last observed and the depth of the next sample above. — = not applicable.

Table T28. Affine table indicating the amount that each core in each hole needs to be offset in order to construct a continuous record, Site U1345. (**Continued on next page.**)

	Depth CSF (m)		Offset	Depth CCSF-A (m)		Recovered	Recovery
Core	Top	Bottom	(m)	Top	Bottom	(m)	(%)
323-U1345A-							
1H	0.00	4.39	0.00	0.00	4.39	4.39	100
2H	4.40	14.09	0.04	4.44	14.13	9.69	102
3H	13.90	23.92	0.01	13.91	23.93	10.02	105
4H	23.40	33.44	0.98	24.38	34.42	10.04	106
5H	32.90	42.95	1.49	34.39	44.44	10.05	106
6H	42.40	51.61	3.12	45.52	54.73	9.21	97
7H	51.90	61.84	3.81	55.71	65.65	9.94	105
8H	61.40	71.11	5.20	66.60	76.31	9.71	102
9H	70.90	80.64	5.79	76.69	86.43	9.74	103
10H	80.40	88.36	7.46	87.86	95.82	7.96	84
11H	89.90	98.49	9.57	99.47	108.06	8.59	90
12H	99.40	108.53	9.46	108.86	117.99	9.13	96
13H	108.90	118.98	11.20	120.10	130.18	10.08	106
14H	118.40	128.12	12.40	130.80	140.52	9.72	102
15H	127.90	138.09	13.68	141.58	151.77	10.19	107
16H	137.40	147.43	14.72	152.12	162.15	10.03	106
323-U1345B-							
1H	0.00	8.25	0.20	0.20	8.45	8.25	101
2H	8.20	17.99	0.21	8.41	18.20	9.79	103
3H	17.70	27.77	0.78	18.48	28.55	10.07	106
4H	27.20	37.33	1.27	28.47	38.60	10.13	107
323-U1345C-							
1H	0.00	5.96	0.09	0.09	6.05	5.96	99
2H	6.00	15.82	0.97	6.97	16.79	9.82	103
3H	15.50	25.66	2.03	17.53	27.69	10.16	107
4H	25.00	35.14	2.96	27.96	38.10	10.14	107
5H	34.50	44.04	3.41	37.91	47.45	9.54	100
6H	44.00	53.87	4.93	48.93	58.80	9.87	104
7H	53.50	63.21	6.08	59.58	69.29	9.71	102
8H	63.00	72.60	7.46	70.46	80.06	9.60	101
9H	72.50	82.14	8.55	81.05	90.69	9.64	101
10H	82.00	91.91	9.76	91.76	101.67	9.91	104
11H	91.50	101.33	10.67	102.17	112.00	9.83	103
12H	101.00	111.08	11.62	112.62	122.70	10.08	106
13H	110.50	119.16	12.86	123.36	132.02	8.66	91
14H	120.00	129.85	13.92	133.92	143.77	9.85	104
15H	129.50	140.05	15.53	145.03	155.58	10.55	111
16H	139.00	148.53	16.93	155.93	165.46	9.53	100
323-U1345D-							
1H	0.00	9.76	1.61	1.61	11.37	9.76	103
2H	9.50	19.23	2.28	11.78	21.51	9.73	102
3H	19.00	29.19	3.19	22.19	32.38	10.19	107
4H	28.50	38.69	3.80	32.30	42.49	10.18	107
5H	38.00	47.54	5.25	43.25	52.79	9.54	100
6H	47.50	56.72	6.63	54.13	63.35	9.22	97
7H	57.00	66.36	7.40	64.40	73.76	9.36	99
8H	66.50	73.32	7.27	73.77	80.59	6.82	91
9H	74.00	83.52	9.83	83.83	93.35	9.52	100
10H	83.50	93.47	10.36	93.86	103.83	9.97	105
11H	93.00	102.77	11.60	104.60	114.37	9.77	103
12H	102.50	112.03	13.04	115.54	125.07	9.53	100
13H	112.00	122.65	13.44	125.44	136.09	10.65	112
14H	121.50	131.81	14.64	136.14	146.45	10.31	109
15H	131.00	141.06	15.85	146.85	156.91	10.06	106
16H	140.50	150.51	17.49	157.99	168.00	10.01	105
323-U1345E-							
1H	0.00	8.27	–0.09	–0.09	8.18	8.27	101
2H	8.20	15.68	0.75	8.95	16.43	7.48	79
3H	17.70	27.86	1.47	19.17	29.33	10.16	107
4H	27.20	37.47	2.24	29.44	39.71	10.27	108
5H	36.70	46.59	3.27	39.97	49.86	9.89	104
6H	46.20	56.54	4.42	50.62	60.96	10.34	109
7H	55.70	65.08	5.86	61.56	70.94	9.38	99
8H	65.20	75.46	7.06	72.26	82.52	10.26	108
9H	74.70	84.55	8.70	83.40	93.25	9.85	104

Table T28 (continued).

Core	Depth CSF (m)		Offset (m)	Depth CCSF-A (m)		Recovered (m)	Recovery (%)
	Top	Bottom		Top	Bottom		
10H	84.20	93.99	9.12	93.32	103.11	9.79	103
11H	93.70	103.44	10.52	104.22	113.96	9.74	103
12H	103.20	113.19	11.29	114.49	124.48	9.99	105
13H	112.70	121.88	12.04	124.74	133.92	9.18	97
14H	122.20	132.14	13.56	135.76	145.70	9.94	105
15H	131.70	141.62	14.31	146.01	155.93	9.92	104
16H	141.20	150.89	15.15	156.35	166.04	9.69	110

Table T29. Splice table indicating tie points between holes, Site U1345. Sampling along the splice should be used to construct a continuous record.

Hole, core, section, interval (cm)	Depth (m)			Hole, core, section, interval (cm)	Depth (m)	
	CSF	CCSF-A			CSF	CCSF-A
323-				323-		
U1345A-1H-3, 28.71	3.29	3.31	Tie to	U1345D-1H-2, 19.76	1.70	3.31
U1345D-1H-6, 74.19	8.24	9.86	Tie to	U1345C-2H-2, 135.02	8.85	9.86
U1345C-2H-6, 36.13	13.86	14.83	Tie to	U1345D-2H-3, 24.64	12.51	14.83
U1345D-2H-6, 145.68	18.21	20.52	Tie to	U1345C-3H-3, 15.45	18.46	20.52
U1345C-3H-7, 55.33	24.85	26.90	Tie to	U1345A-4H-2, 120.31	25.90	26.90
U1345A-4H-7, 9.89	32.29	33.29	Tie to	U1345D-4H-1, 55.13	29.45	33.29
U1345D-4H-4, 129.43	34.75	38.55	Tie to	U1345A-5H-3, 112.96	37.03	38.55
U1345A-5H-6, 36.47	40.76	42.29	Tie to	U1345C-5H-3, 139.39	38.84	42.29
U1345C-5H-6, 60.04	42.60	46.01	Tie to	U1345A-6H-1, 50.05	42.85	46.01
U1345A-6H-6, 3.04	49.84	53.00	Tie to	U1345C-6H-4, 45.09	48.06	53.00
U1345C-6H-7, 26.38	52.37	57.30	Tie to	U1345D-6H-3, 21.74	50.67	57.31
U1345D-6H-6, 98.73	55.87	62.53	Tie to	U1345C-7H-3, 65.19	56.43	62.53
U1345C-7H-6, 19.55	60.40	66.47	Tie to	U1345D-7H-3, 2.23	59.04	66.47
U1345D-7H-6, 101.73	64.48	71.92	Tie to	U1345C-8H-2, 72.91	64.45	71.92
U1345C-8H-6, 143.70	71.13	78.60	Tie to	U1345A-9H-3, 1.34	72.80	78.60
U1345A-9H-7, 12.85	78.81	84.64	Tie to	U1345C-9H-3, 108.90	76.07	84.64
U1345C-9H-6, 81.76	80.27	88.82	Tie to	U1345D-9H-4, 142.50	78.94	88.82
U1345D-9H-6, 114.73	81.60	91.47	Tie to	U1345A-10H-3, 107.09	83.99	91.47
U1345A-10H-4, 49.99	85.54	93.02	Tie to	U1345C-10H-1, 100.18	83.24	93.02
U1345C-10H-3, 114.84	85.94	95.74	Tie to	U1345D-10H-2, 32.37	85.34	95.74
U1345D-10H-7, 58.44	92.89	103.28	Tie to	U1345A-11H-3, 115.37	93.70	103.28
U1345A-11H-6, 18.92	97.24	106.85	Tie to	U1345D-11H-2, 112.91	95.25	106.85
U1345D-11H-7, 4.87	101.57	113.18	Tie to	U1345A-12H-4, 89.90	103.72	113.18
U1345A-12H-6, 142.20	107.18	116.64	Tie to	U1345C-12H-3, 145.98	105.01	116.64
U1345C-12H-7, 65.28	110.04	121.68	Tie to	U1345A-13H-2, 71.65	110.46	121.68
U1345A-13H-4, 123.96	113.98	125.18	Tie to	U1345C-13H-2, 60.64	112.30	125.18
U1345C-13H-5, 114.79	117.32	130.20	Tie to	U1345D-13H-4, 92.72	116.76	130.20
U1345D-13H-6, 138.43	120.16	133.64	Tie to	U1345A-14H-3, 94.71	121.20	133.64
U1345A-14H-7, 95.97	127.21	139.65	Tie to	U1345D-14H-3, 65.89	125.00	139.65
U1345D-14H-6, 57.41	129.39	144.04	Tie to	U1345A-15H-3, 49.40	130.30	144.04
U1345A-15H-7, 94.28	136.75	150.49	Tie to	U1345D-15H-3, 55.26	134.60	150.49
U1345D-15H-6, 121.92	139.76	155.62	Tie to	U1345A-16H-3, 132.94	140.86	155.62
U1345A-16H-6, 58.70	144.39	159.15	Tie to	U1345C-16H-3, 114.68	142.18	159.15
U1345C-16H-5, 120.06	145.23	162.20	Tie to	U1345D-16H-4, 50.43	144.69	162.20

Table T30. Sedimentation rates and their control points, Site U1345. (**See table note.**)

Age (Ma)	Depth (m)		Control point	Sedimentation rate (cm/k.y.)
	CSF	CCSF-A		
0.05	16.5	18.0	Average depth of LO *Lychnocanoma nipponica sakaii*	32
0.28–0.32	80.1	88.0	Average depth of LO *Spongodiscus* sp.	28

Note: LO = last occurrence.

Figure F1. Map illustrating the seven sites drilled and cored during IODP Expedition 323 in the Bering Sea along with cross sections of the passes with volume transport (Sv) in the Aleutian Island arc and the Bering Strait. Note that the horizontal and vertical scales of the Bering Strait are twice that of the Aleutians (from Stabeno et al., 1999; Takahashi, 2005).

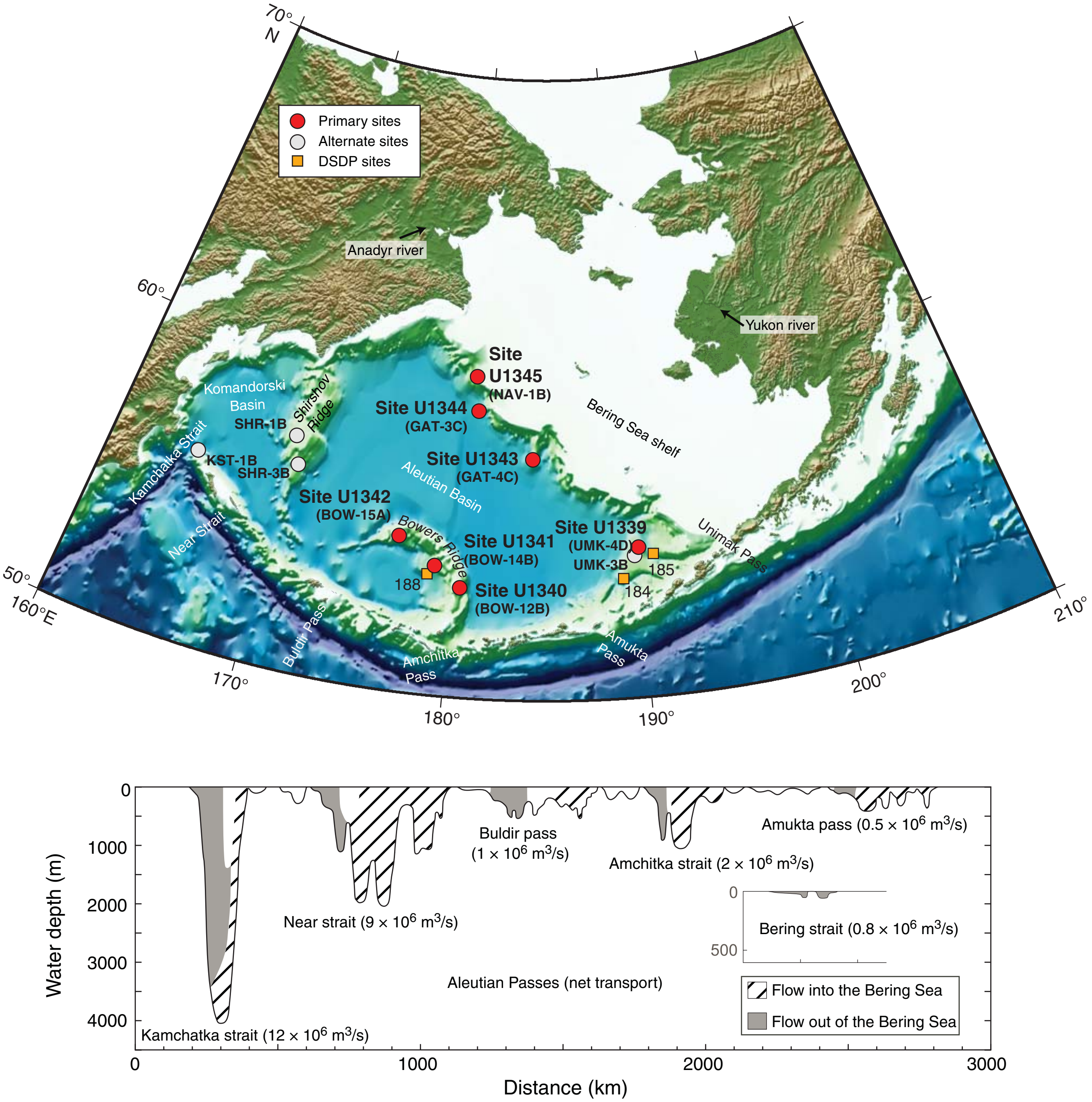

Figure F2. Map showing surface water circulation with the topography of the Bering Sea (from Stabeno et al., 1999). The Alaskan Stream, Kamchatka Current, Bering Slope Current (BSC), and Aleutian North Slope Current (ANSC) are indicated.

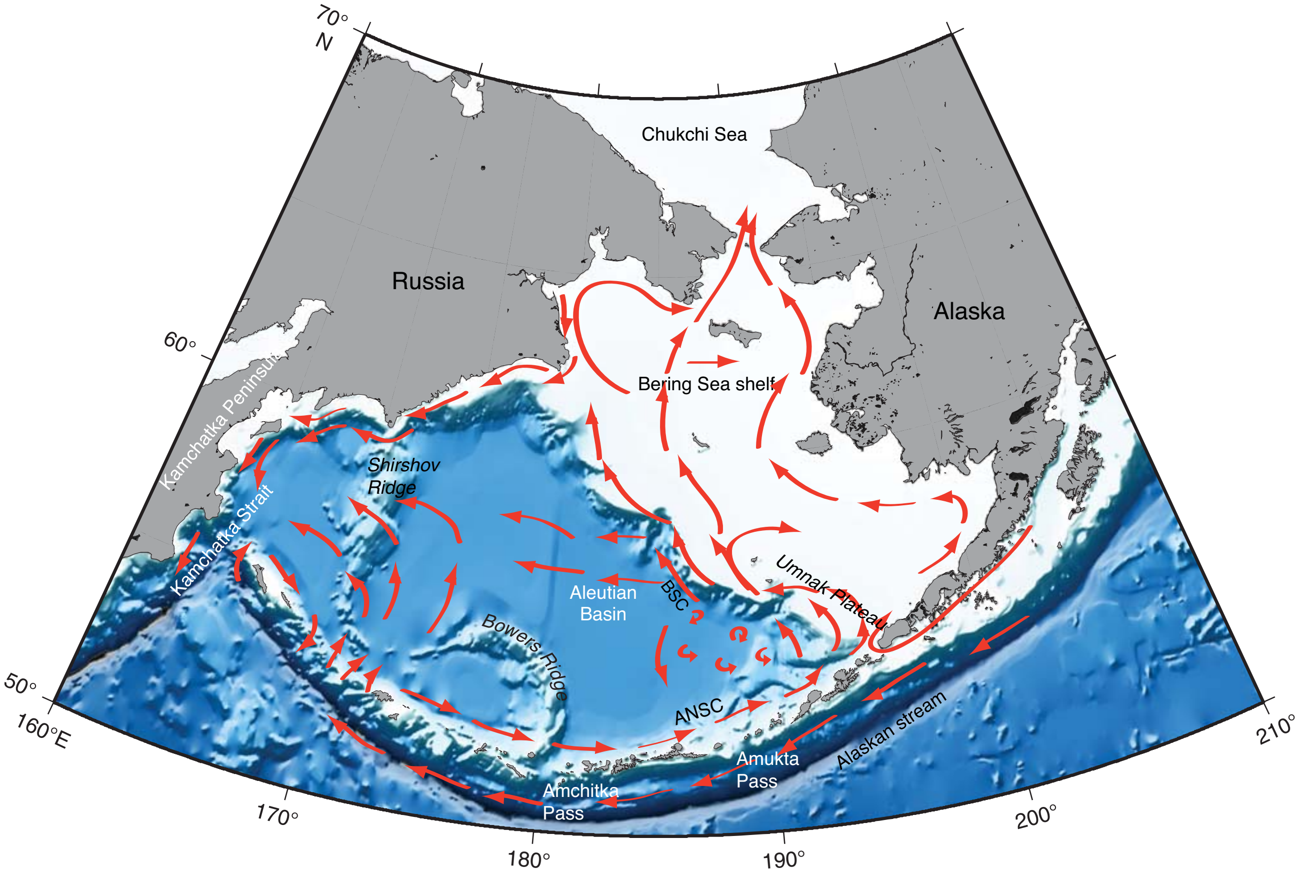

Figure F3. Map showing subsurface water circulation with the topography of the Bering Sea (from Stabeno et al., 1999).

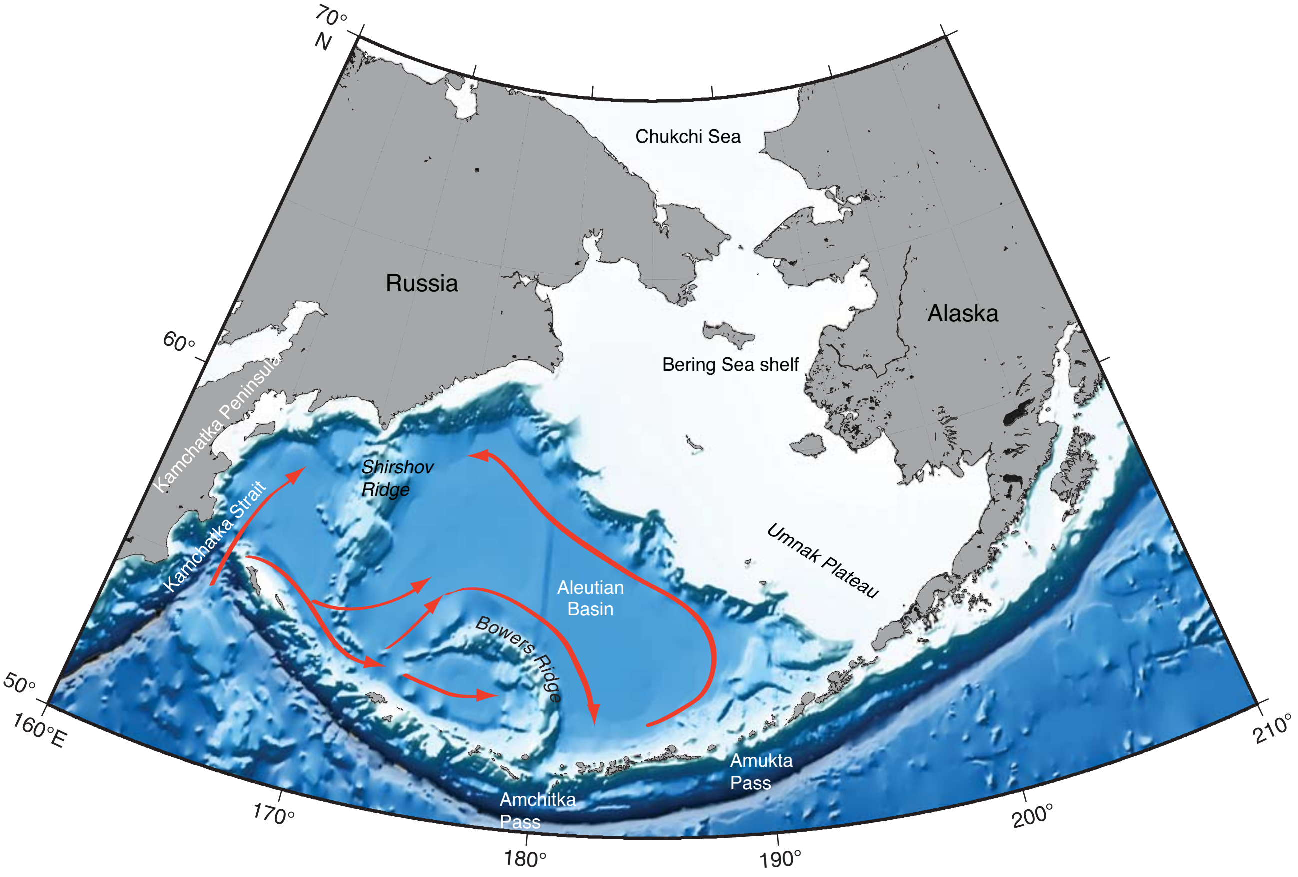

Figure F4. Vertical profiles of (**A**) temperature, (**B**) salinity, (**C**) dissolved oxygen, and (**D**) along the transect on 180° on the map of the Bering Sea (data from World Ocean Atlas [2005]; figures drawn by Ocean Data View).

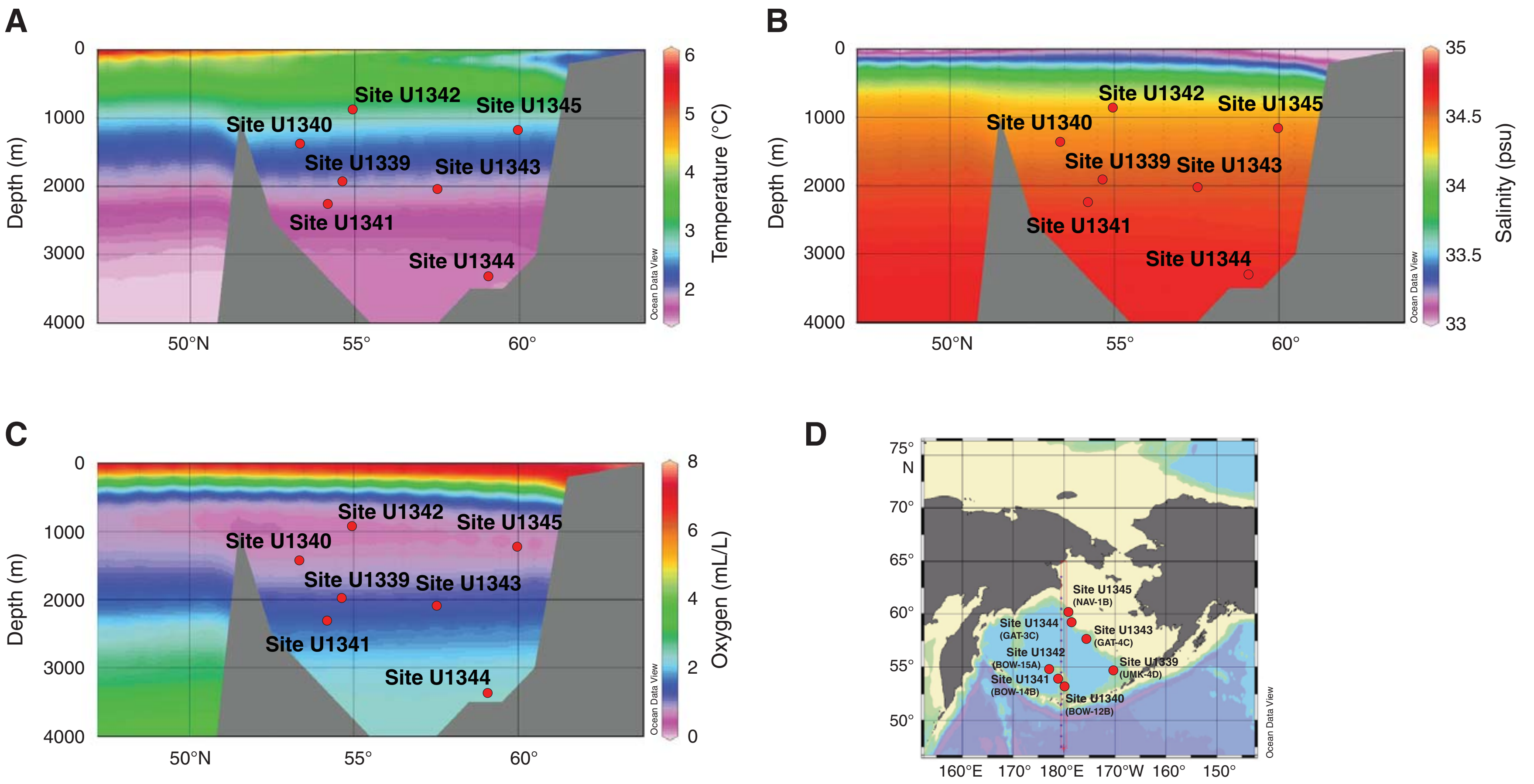

Figure F5. Sedimentation rates observed for all seven drill sites in the Bering Sea.

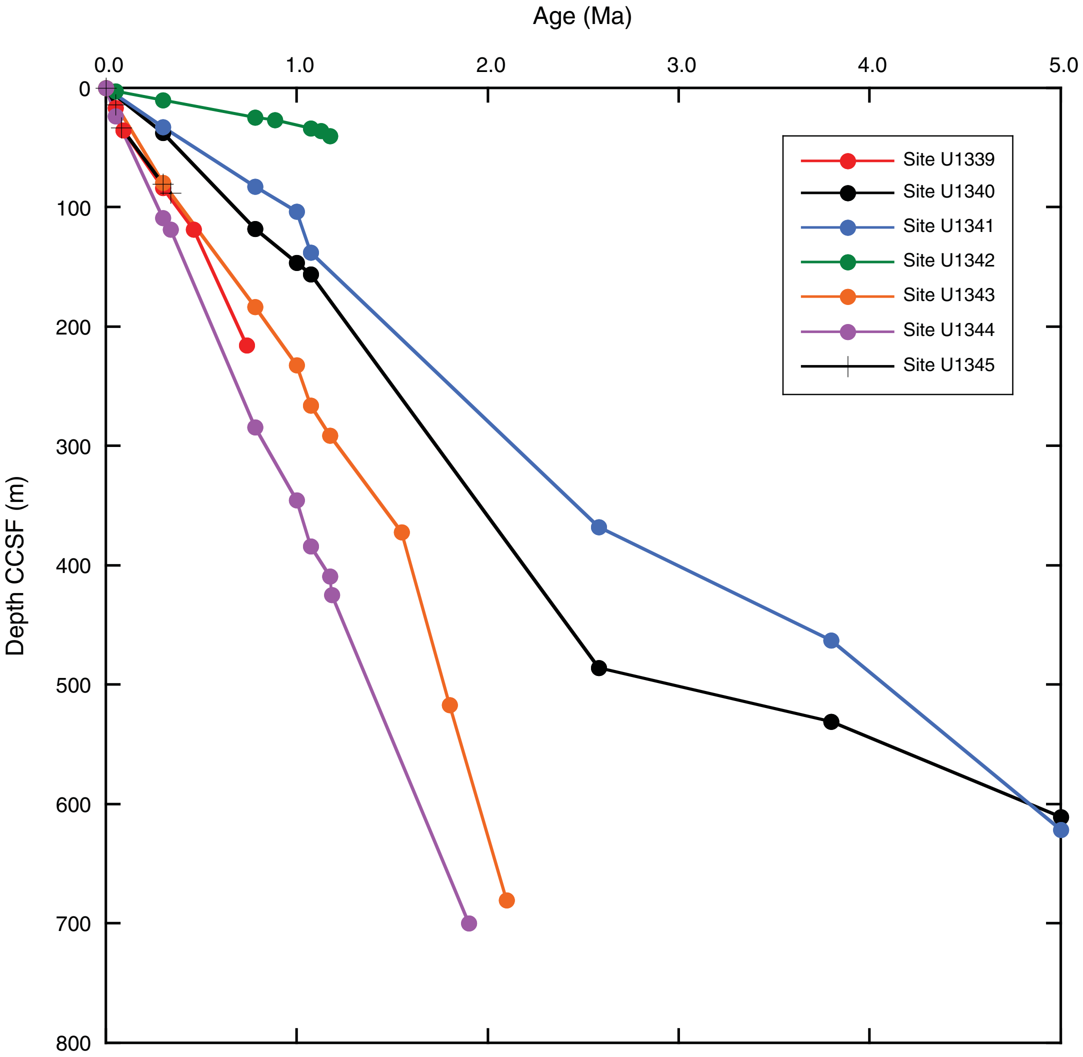

Figure F6. Lithostratigraphic summary of the seven drill sites in the Bering Sea. Natural gamma ray data are plotted along with lithology.

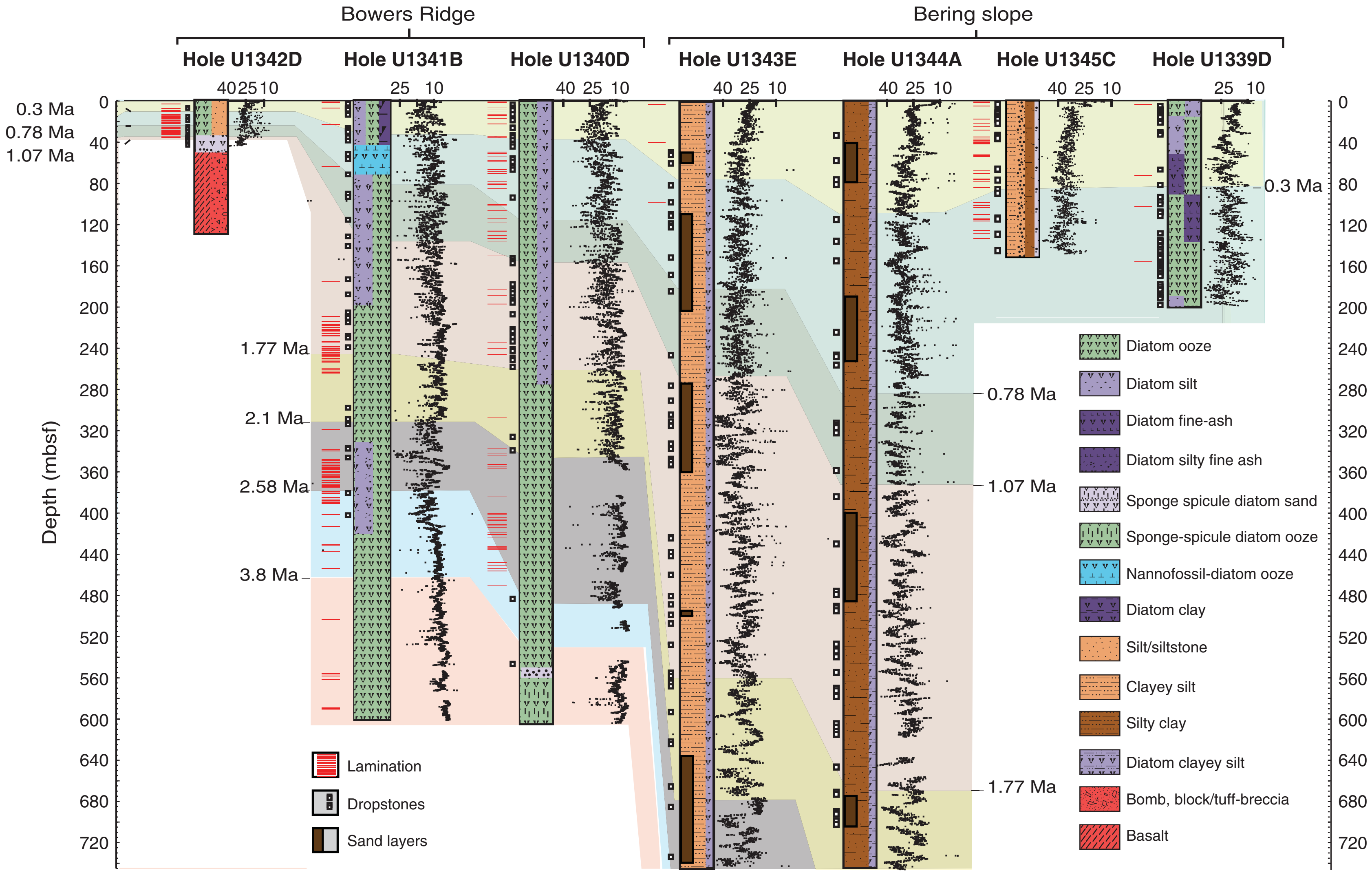

Figure F7. Variations in potassium content measured by downhole logging in Holes U1341B, U1343E, and U1344A, illustrating changes in frequency and amplitude. Biostratigraphic (black) and paleomagnetic (red) age estimates are also shown.

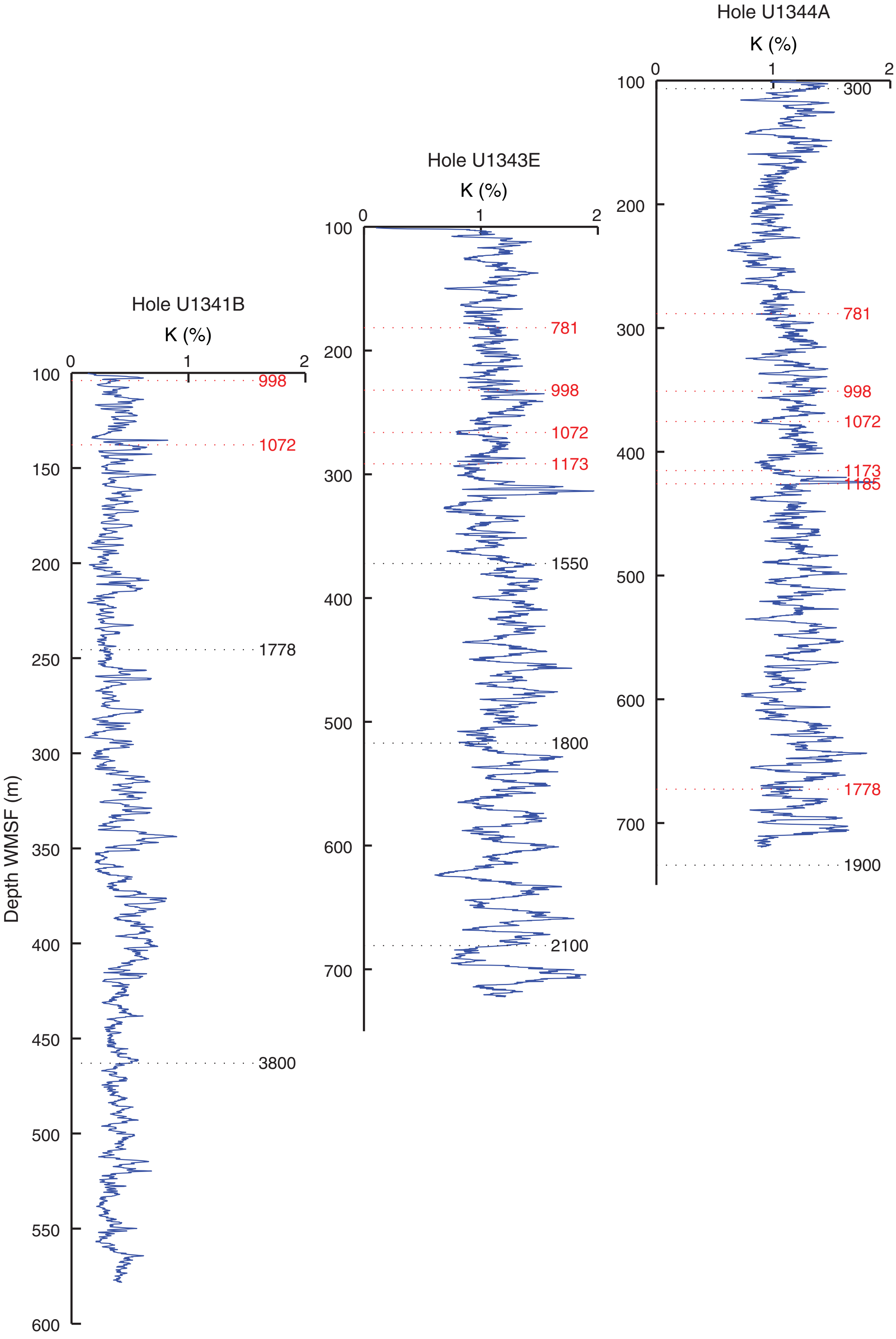

Figure F8. Variations in natural remanent magnetization/Chi (NRM/Chi) or relative paleointensity along with the biostratigraphic (black) and paleomagnetic (red) age estimates for the seven drill sites (from Tables T6, T10, T14, T18, T22, T26, and T30) in k.y.

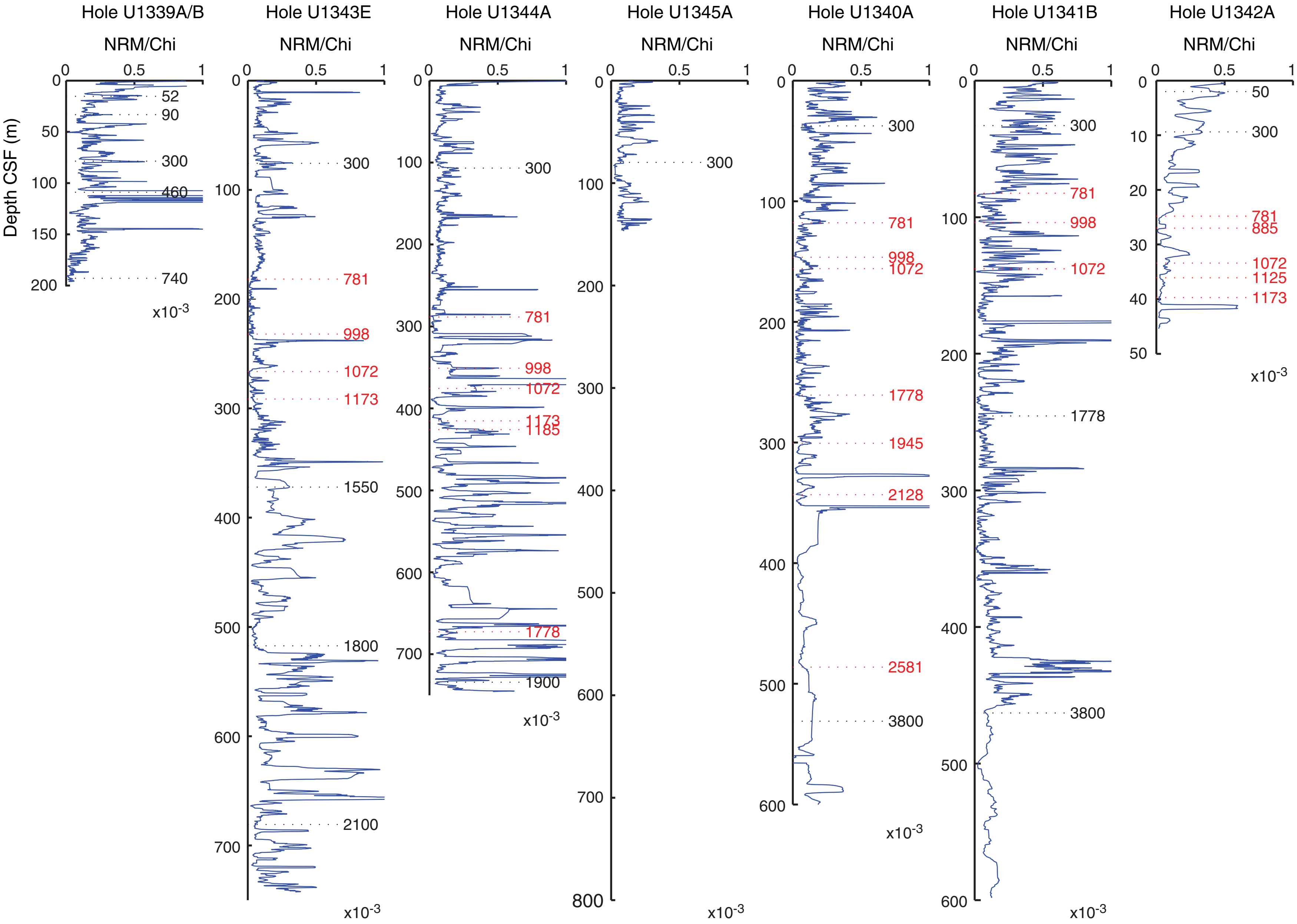

Figure F9. Changes in sea ice coverage derived from sea ice diatoms such as *Thalassiosira antarctica* spores and sea ice dinoflagellates (e.g., *Islandinium minutum)* at the seven drill sites.

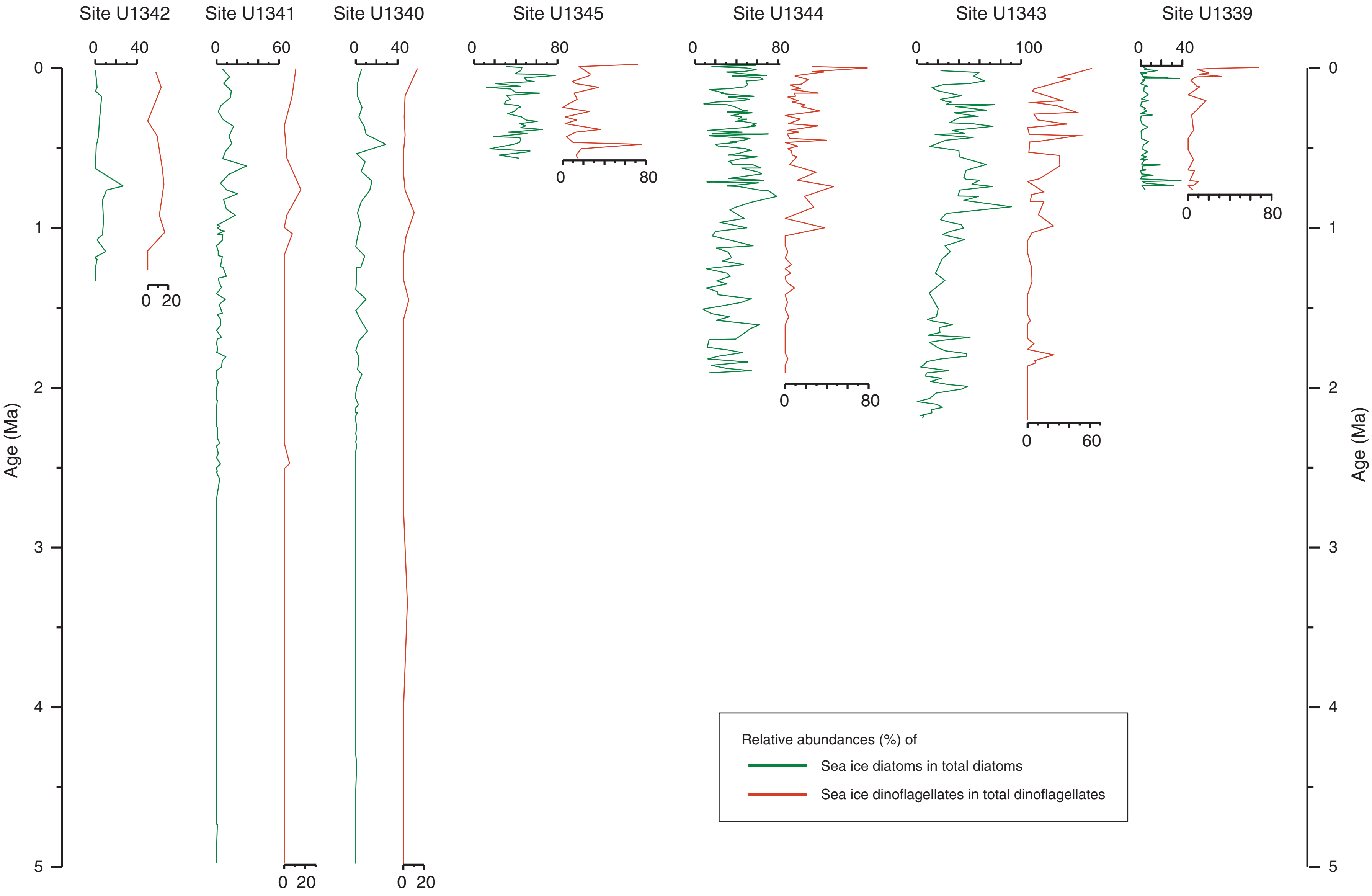

Figure F10. Changes in biological productivity and temperature depicted by variations in *Neodenticula* spp., *Actinocyclus* spp., *Coscinodiscus marginatus*, and heavily silicified *Pyxidicula* spp. at the seven drill sites.

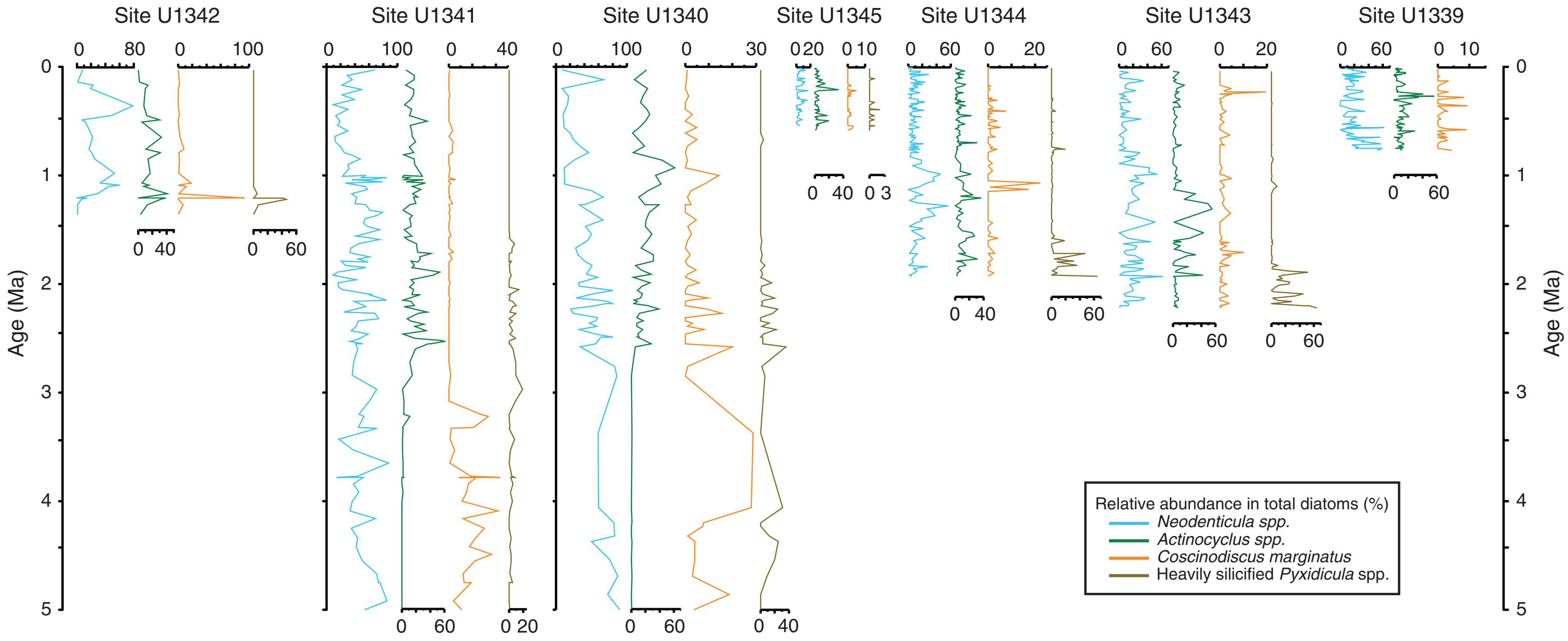

Figure F11. Changes in benthic foraminifers, which are related to low oxygen contents in bottom waters at the seven drill sites.

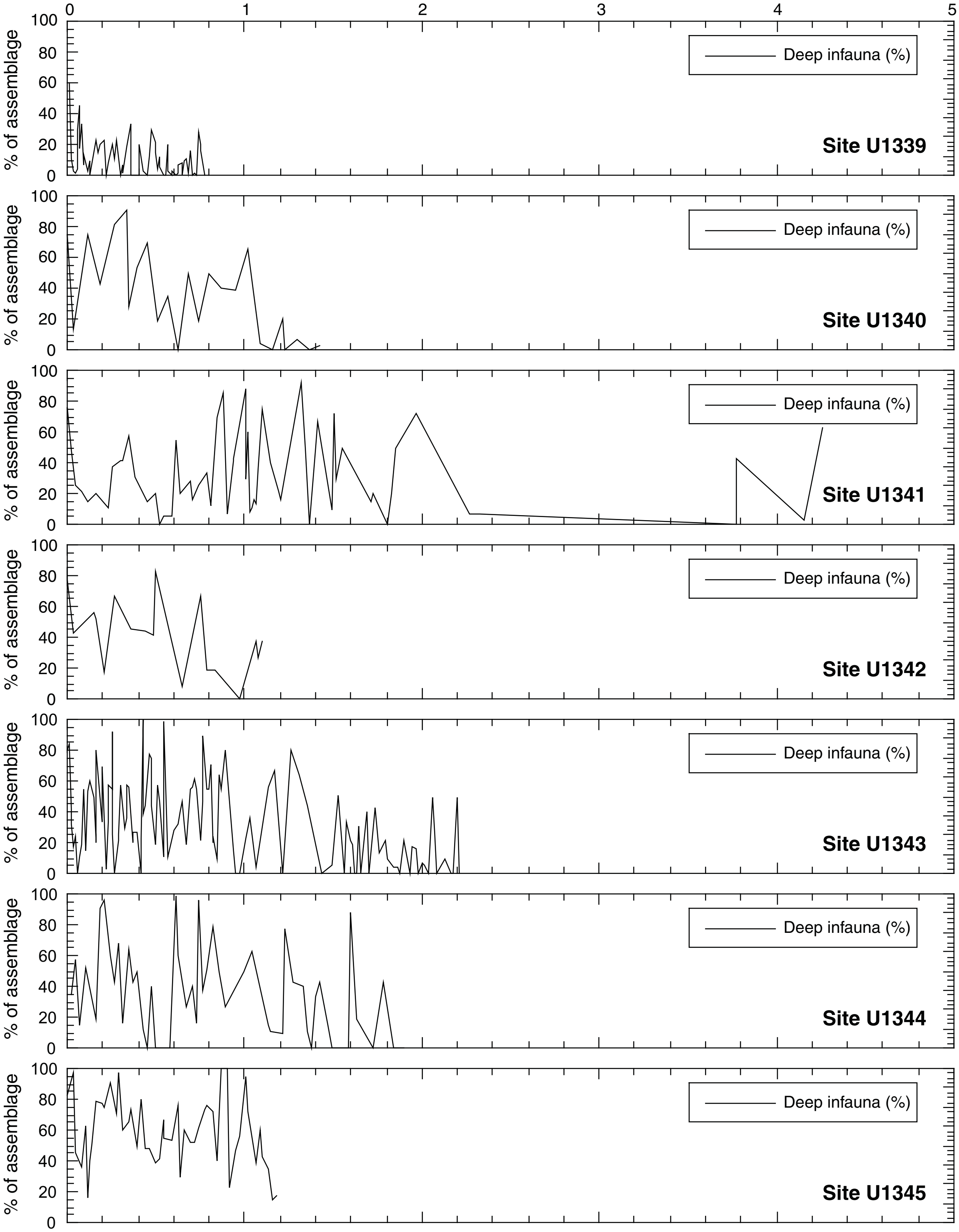

Figure F12. Changes in benthic foraminiferal deep infauna, *Eggerella bradyi*, *Martinottiella communis*, and intermediate water–dwelling radiolarian *Cycladophora davisiana* at Sites U1340 and U1341, indicating the bottom water ventilation history in the Bering Sea.

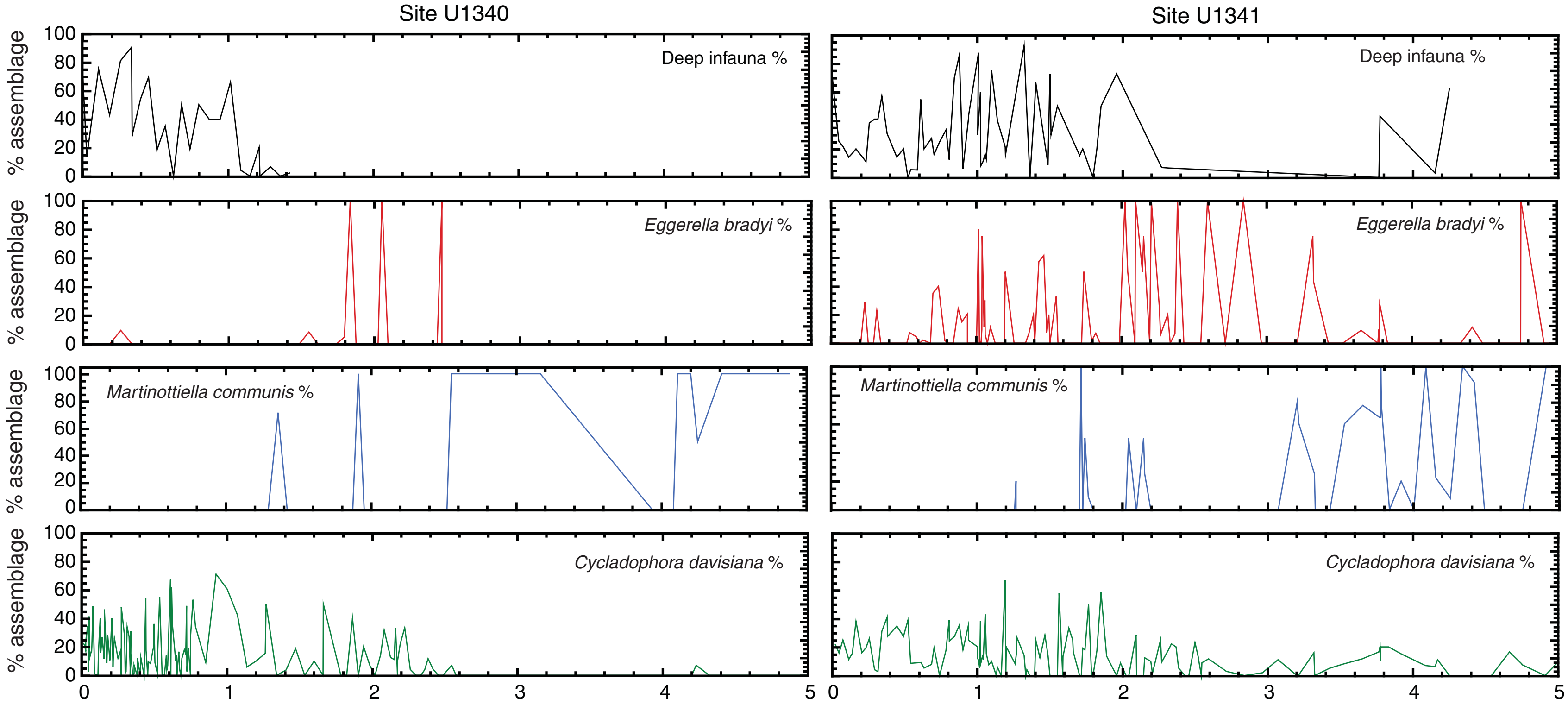

Figure F13. Depth variations in dissolved inorganic carbon (DIC), ammonium, sulfate, and sulfide, illustrating the depth locations of the sulfate–methane transition zone (SMTZ) at Sites U1339, U1342, U1343, U1344, and U1345.

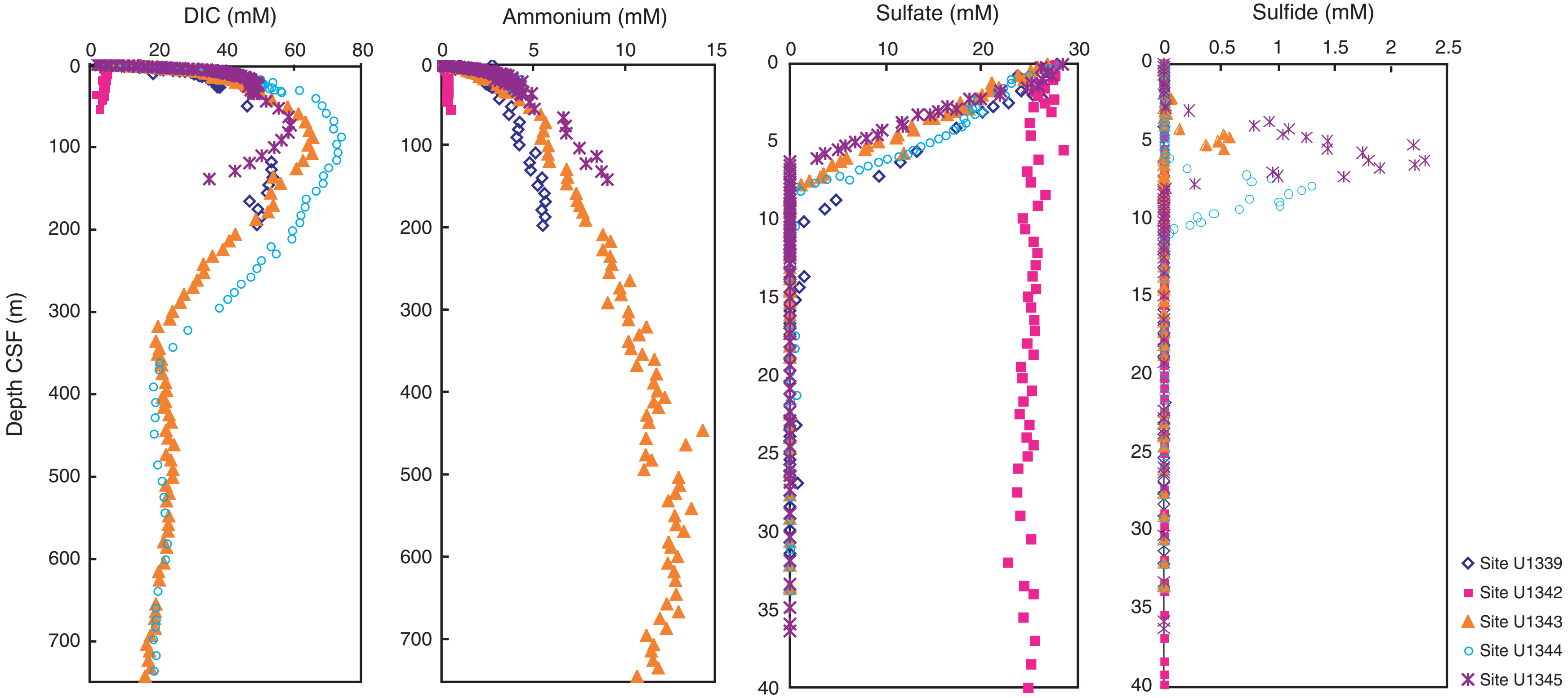

Figure F14. Location map for Site U1339 on Umnak Plateau showing seismic navigation lines.

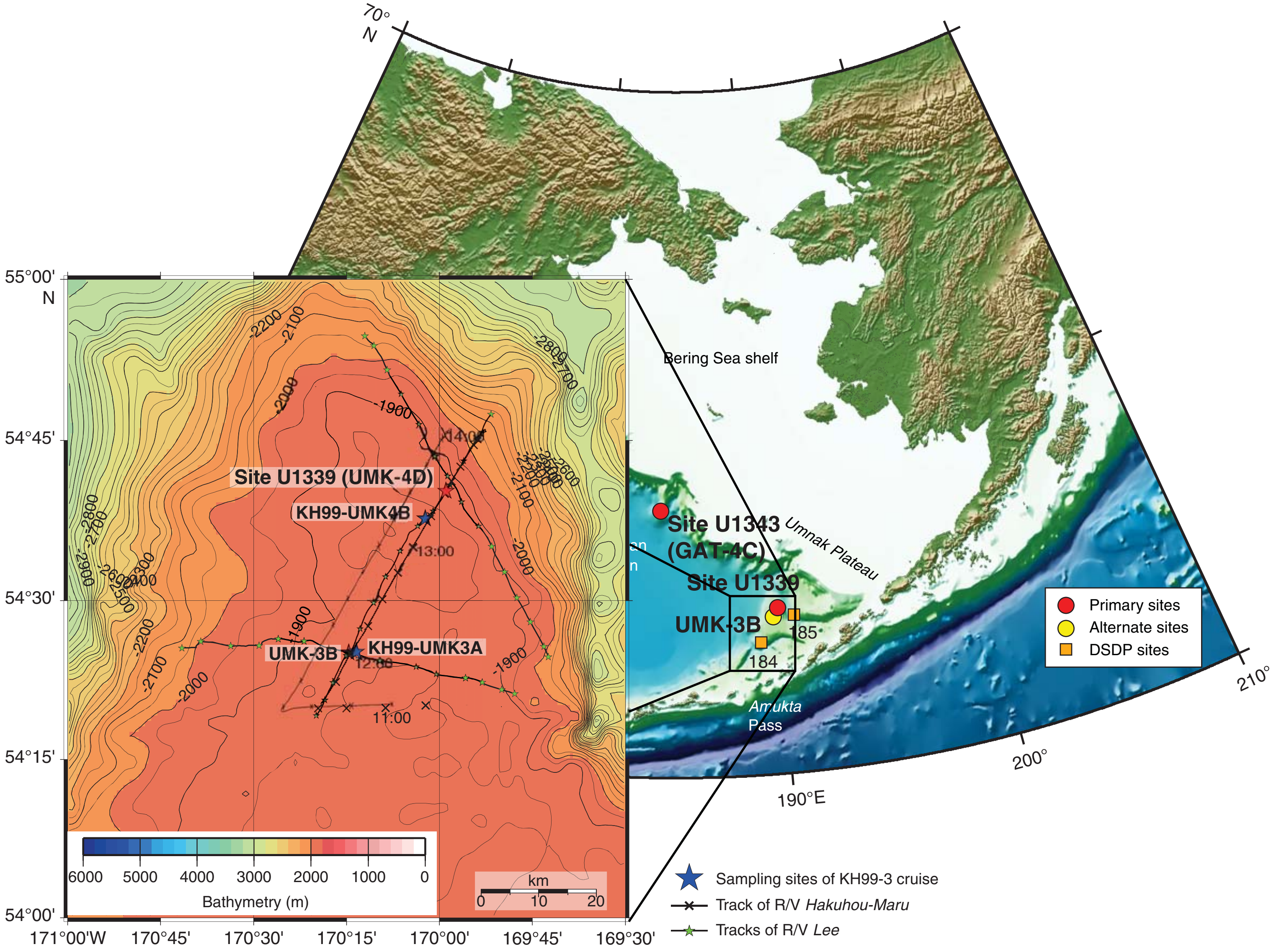

Figure F15. 3.5 kHz subbottom profile survey from *Hakuhou-Maru* Cruise KH99-3 around Site UMK-4D, the location of Site U1339. Horizontal axis of ship time corresponds to time annotation in swath bathymetric map along southwest–northeast line.

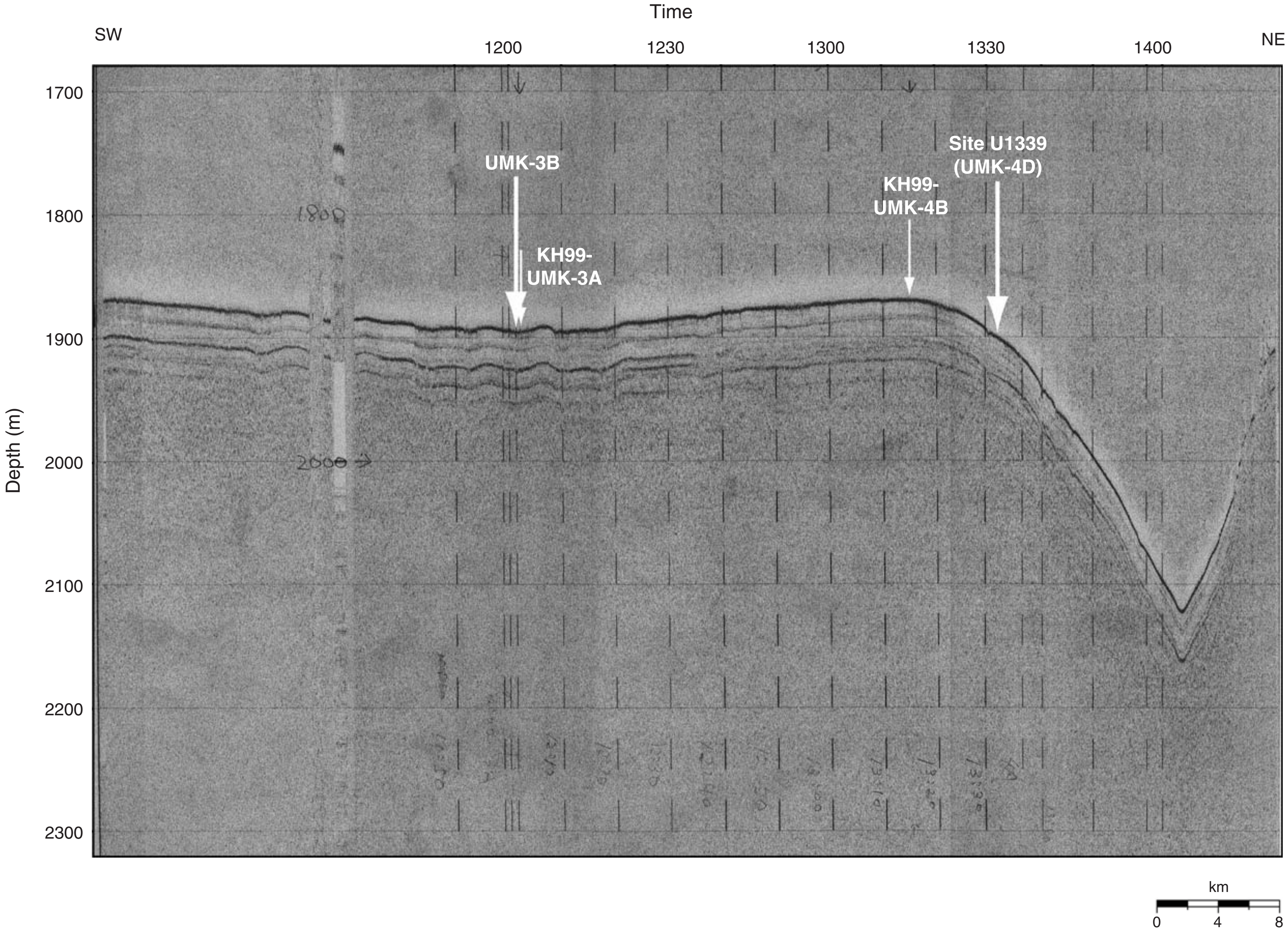

Figure F16. **A.** Close-up seismic profile of USGS *Lee* Cruise L6-80 Line 2, a southwest–northeast line across Site UMK-4D (Site U1339). **B.** Close-up seismic profile of USGS *Lee* Cruise L6-80 Line 5 near Site UMK-4D (Site U1339). CDP = common depth point.

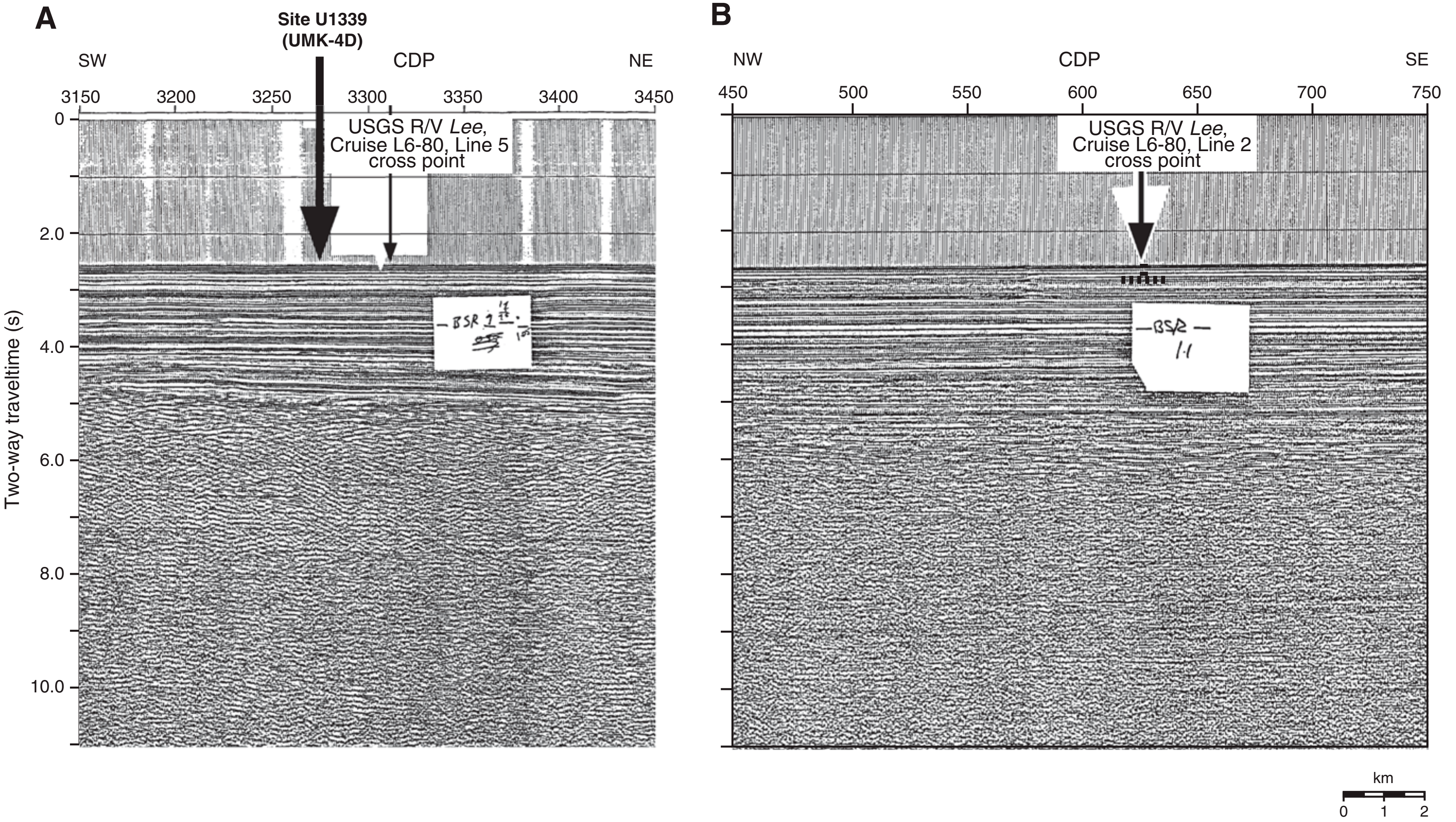

Figure F17. Summary of some shipboard analyses at Site U1339: core recovery, core image, lithology, lithologic units and subunits, age, paleomagnetic chronology, zone of biostratigraphically important radiolarians, diatoms, and silicoflagellates, and spliced records of natural gamma radiation (NGR), gamma ray attenuation (GRA) bulk density, magnetic susceptibility (MS), and the b* index of color reflectance.

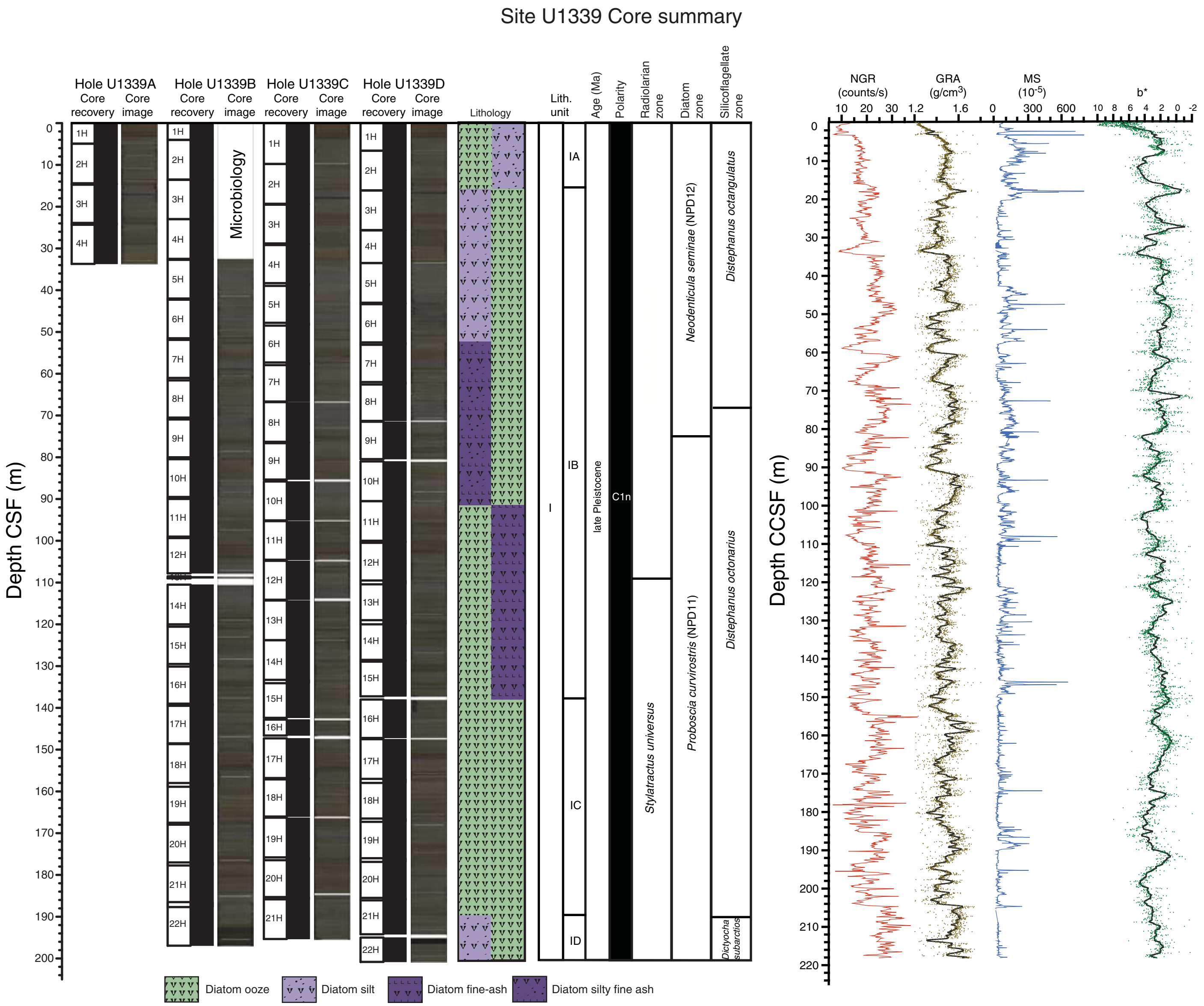

Figure F18. Interstitial water chemistry analyses for Hole U1339B: (**A**) sulfate, (**B**) methane, and (**C**) dissolved inorganic carbon (DIC).

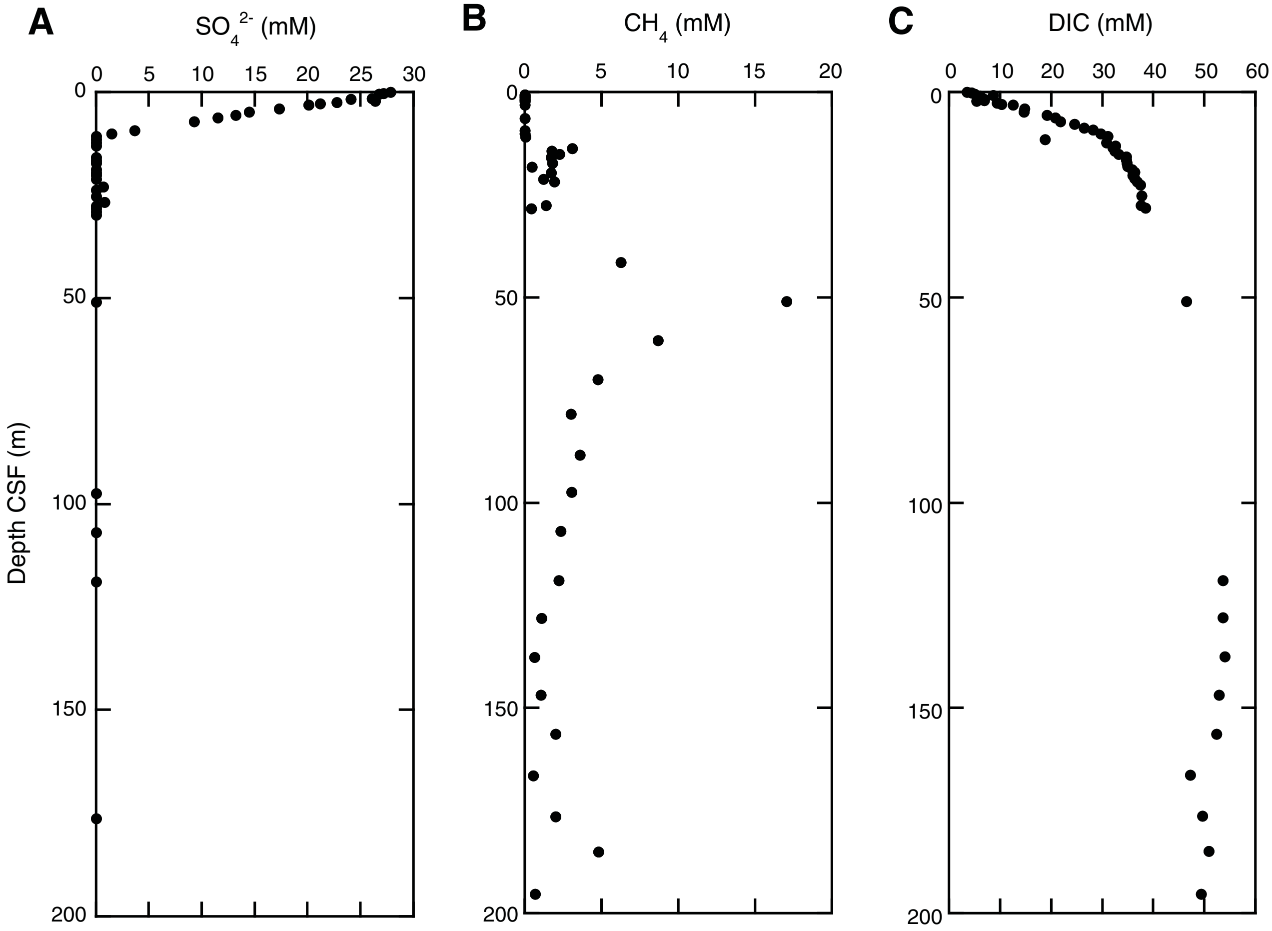

Figure F19. Age-depth plot, Site U1339. Note that the four radiolarian datum levels appear below the line of the interpreted sedimentation rates. This is due to unreliable datums caused by rare abundances of radiolarians *A. aquilonium* and *S. universus*, which occur extremely rarely in the samples.

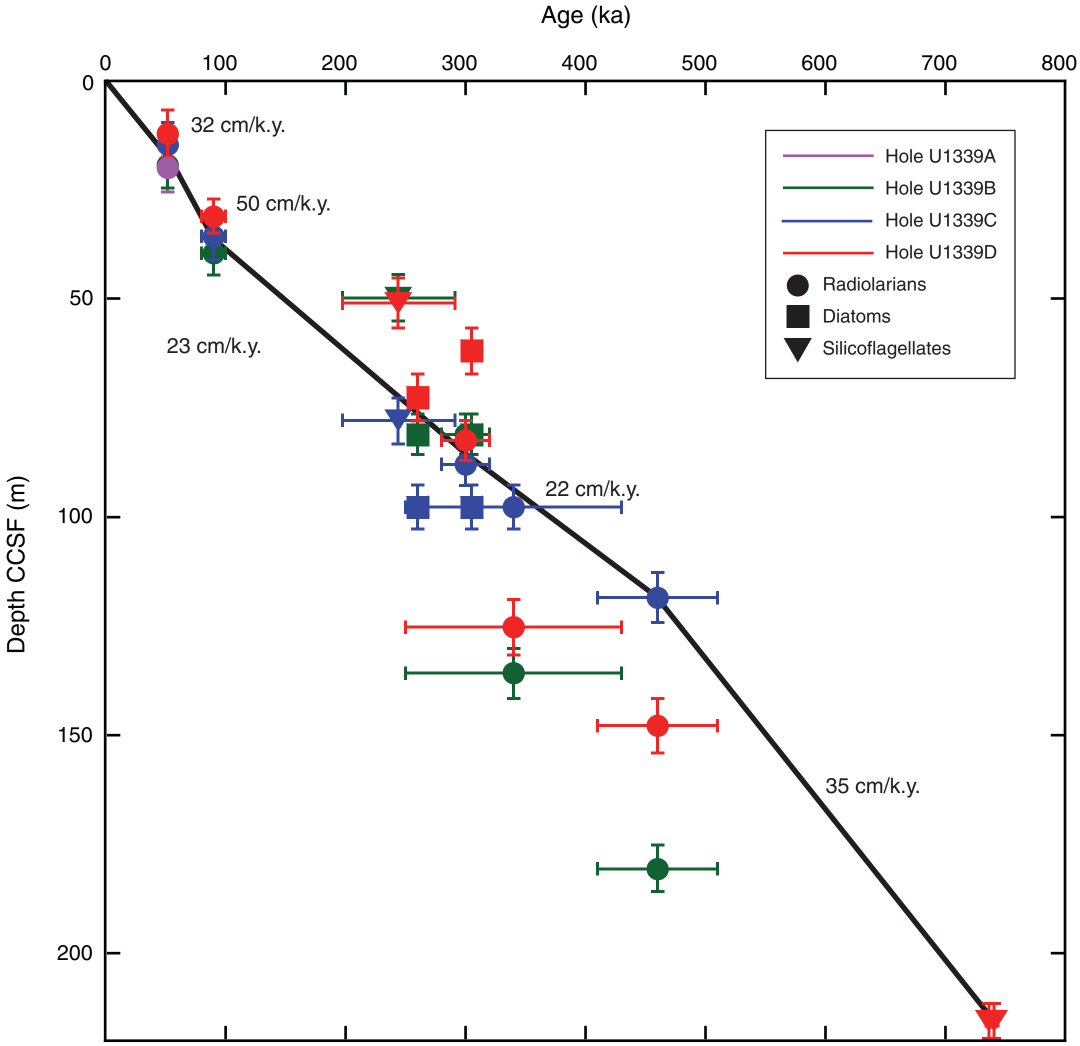

Figure F20. Location map for Site U1340 on Bowers Ridge. Sites U1341 and U1342 are also shown.

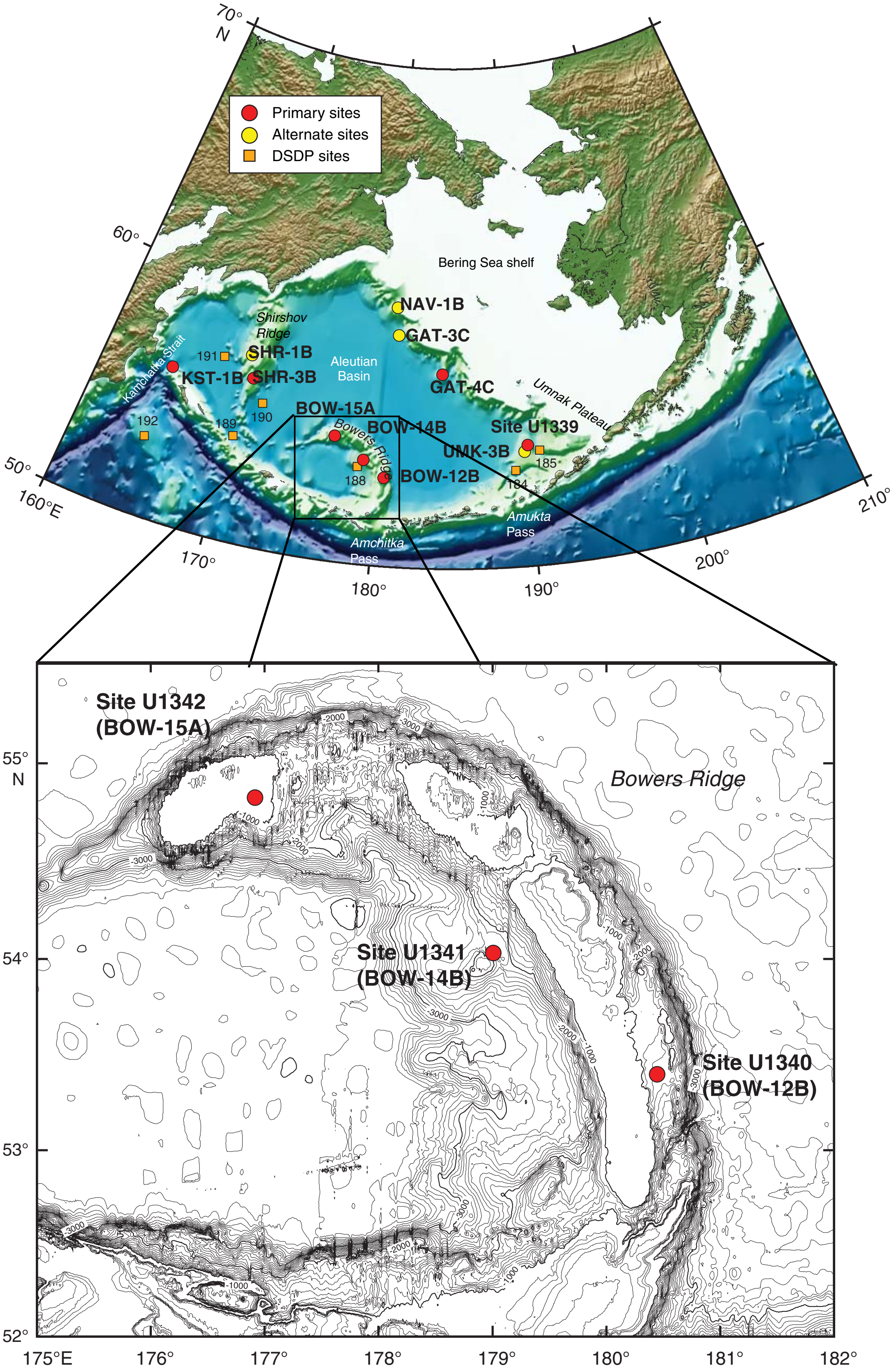

Figure F21. Seismic profile of *Hakuhou-Maru* Cruise KH99-3 Line Stk6-1 (west–east) with the location of Site U1340 shown.

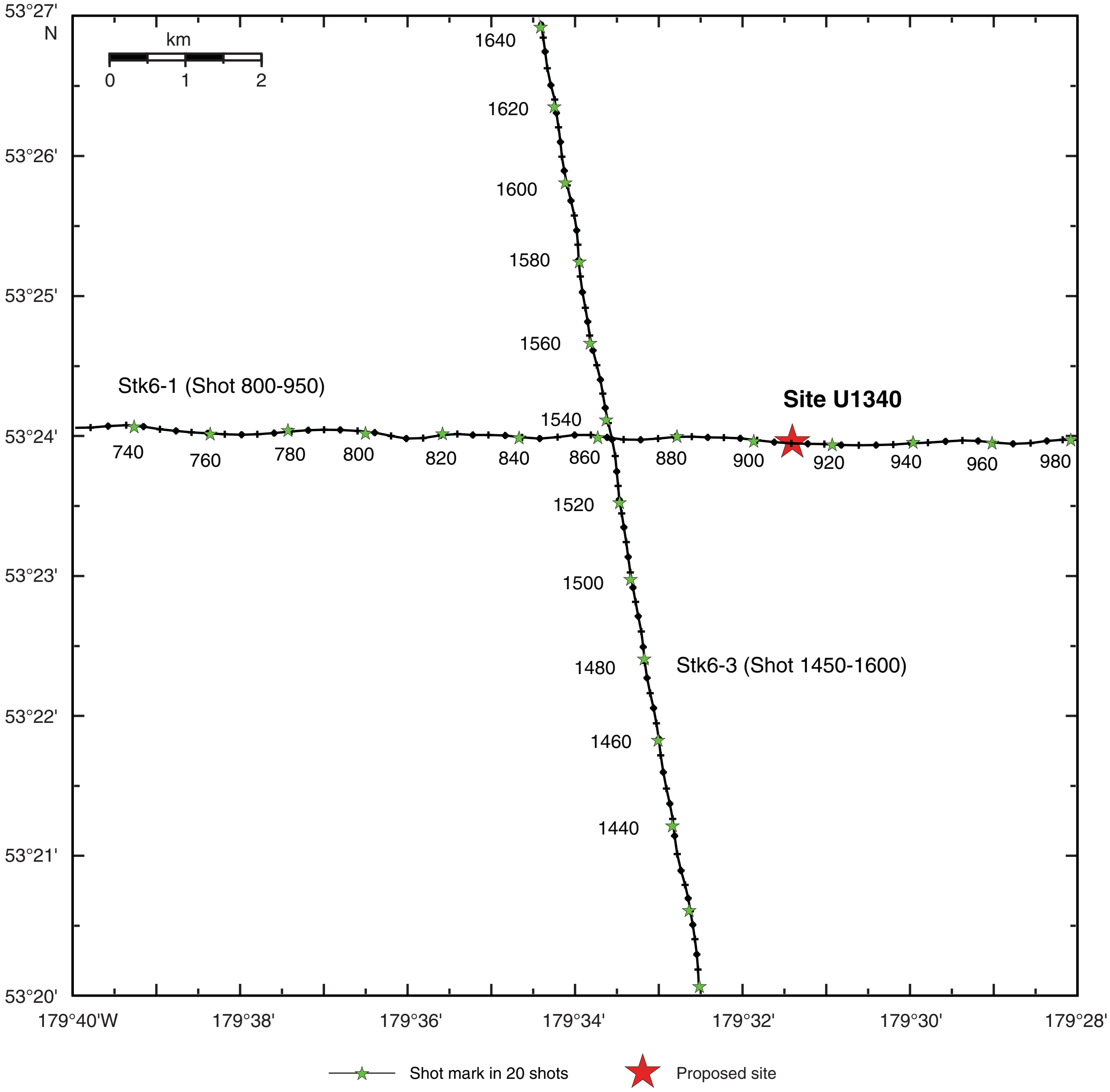

Figure F22. Navigation map of *Hakuhou-Maru* Cruise KH99-3 around Site U1340 for close-up seismic profiles found in Figures F23 and F24.

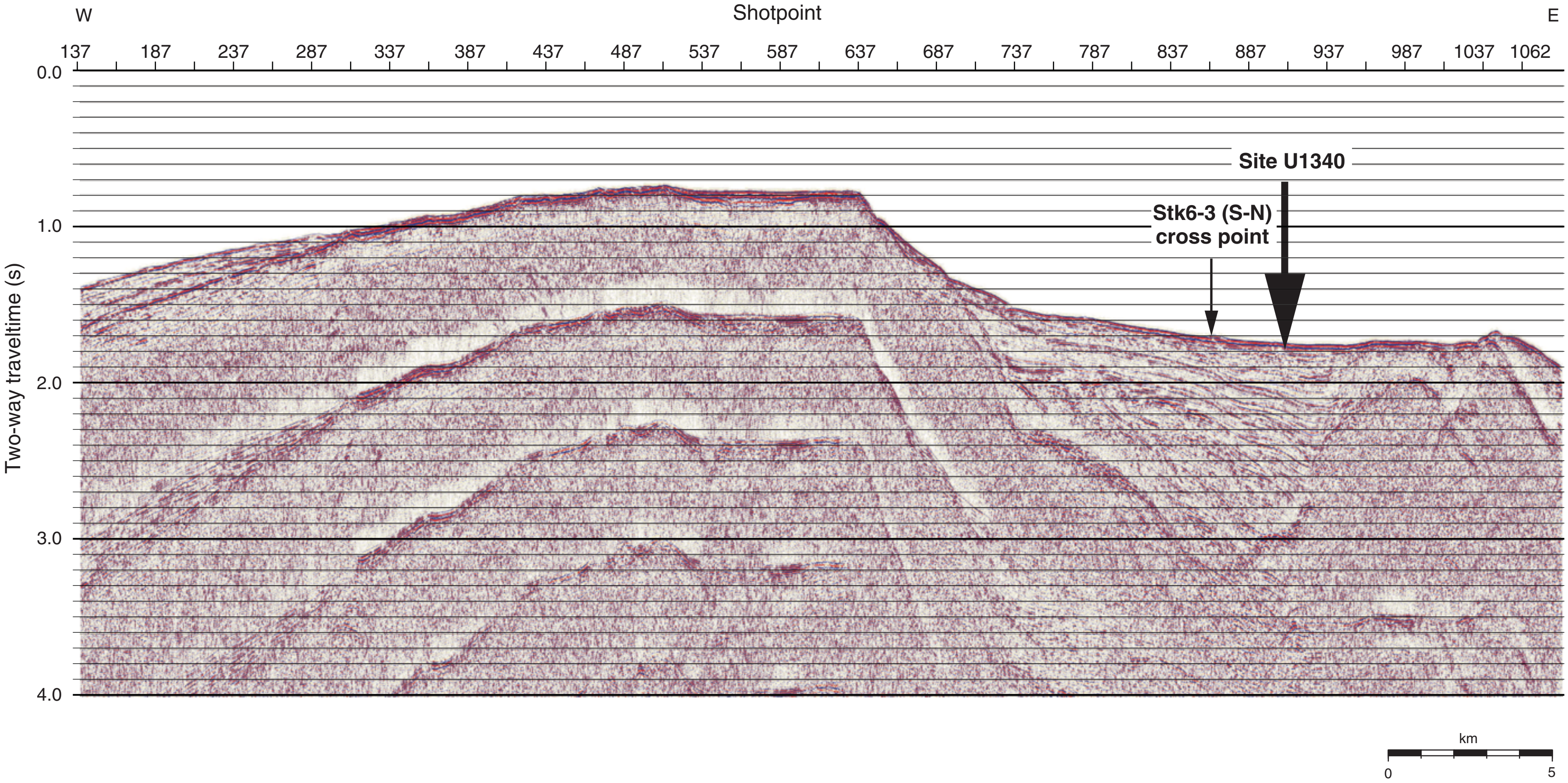

Figure F23. A. Close-up seismic profile of *Hakuhou-Maru* Cruise KH99-3 Line Stk6-1 (west–east) near Site U1340. Cross point with Line Stk6-2 (south–north) is at Shotpoint 863. **B.** Time-depth curve estimated from results of velocity analyses on Lines Stk6-1 and Stk6-3 around Site U1340.

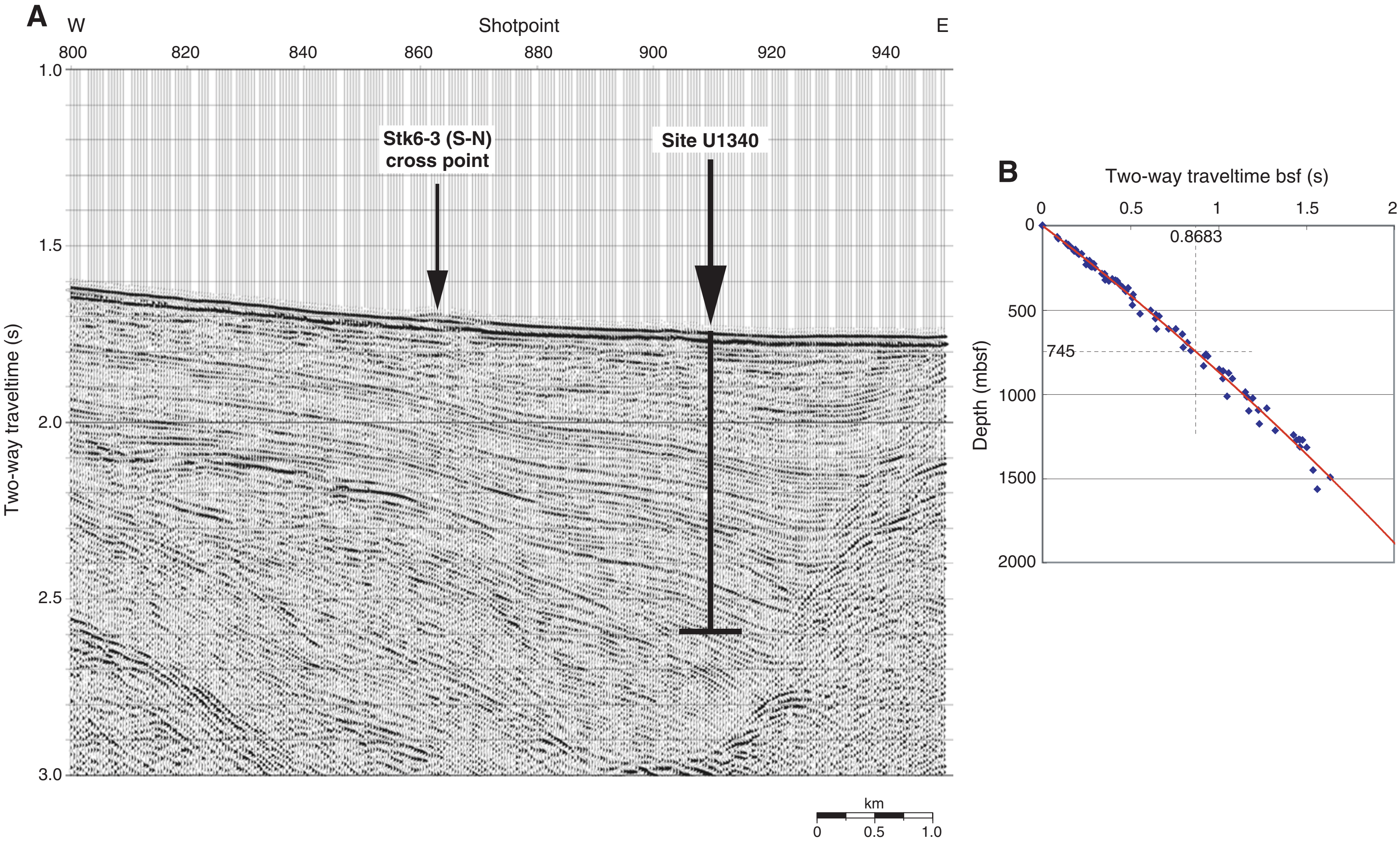

Figure F24. **A.** Close-up seismic profile of *Hakuhou-Maru* Cruise KH99-3 Line Stk6-3 (south–north) near Site U1340. Penetration depth of this site is projected from the east on the cross point (see Fig. F22). **B.** Time-depth curve estimated from results of velocity analyses on Lines Stk6-1 and Stk6-3 around Site U1340.

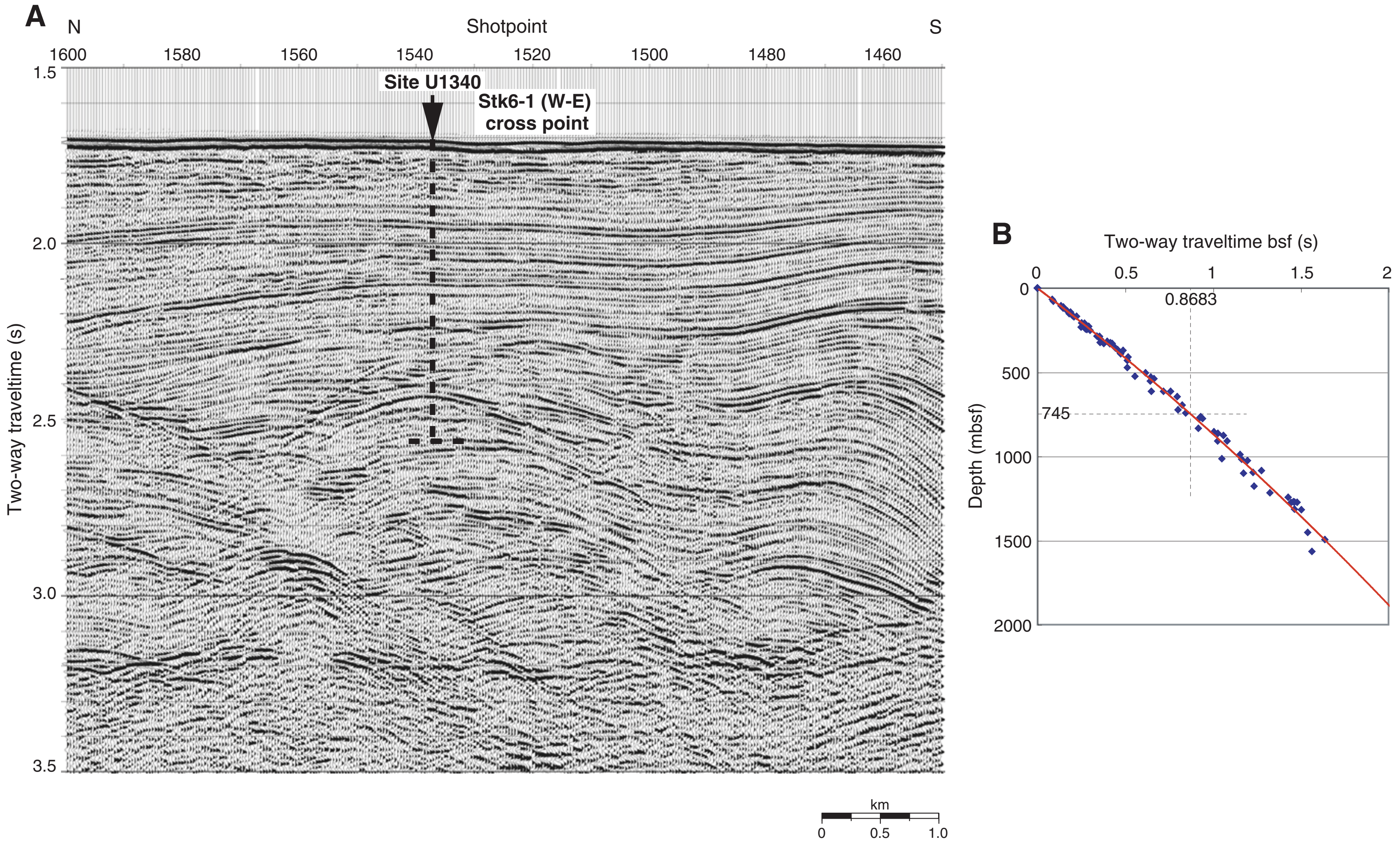

Figure F25. Summary of some shipboard analyses at Site U1340: core recovery, core images, lithology and lithologic units and subunits, age, paleomagnetic chronology, zone of biostratigraphically important radiolarians, diatoms, and silicoflagellates, and spliced records of natural gamma radiation (NGR), gamma ray attenuation (GRA) bulk density, magnetic susceptibility (MS), and the b* index of color reflectance.

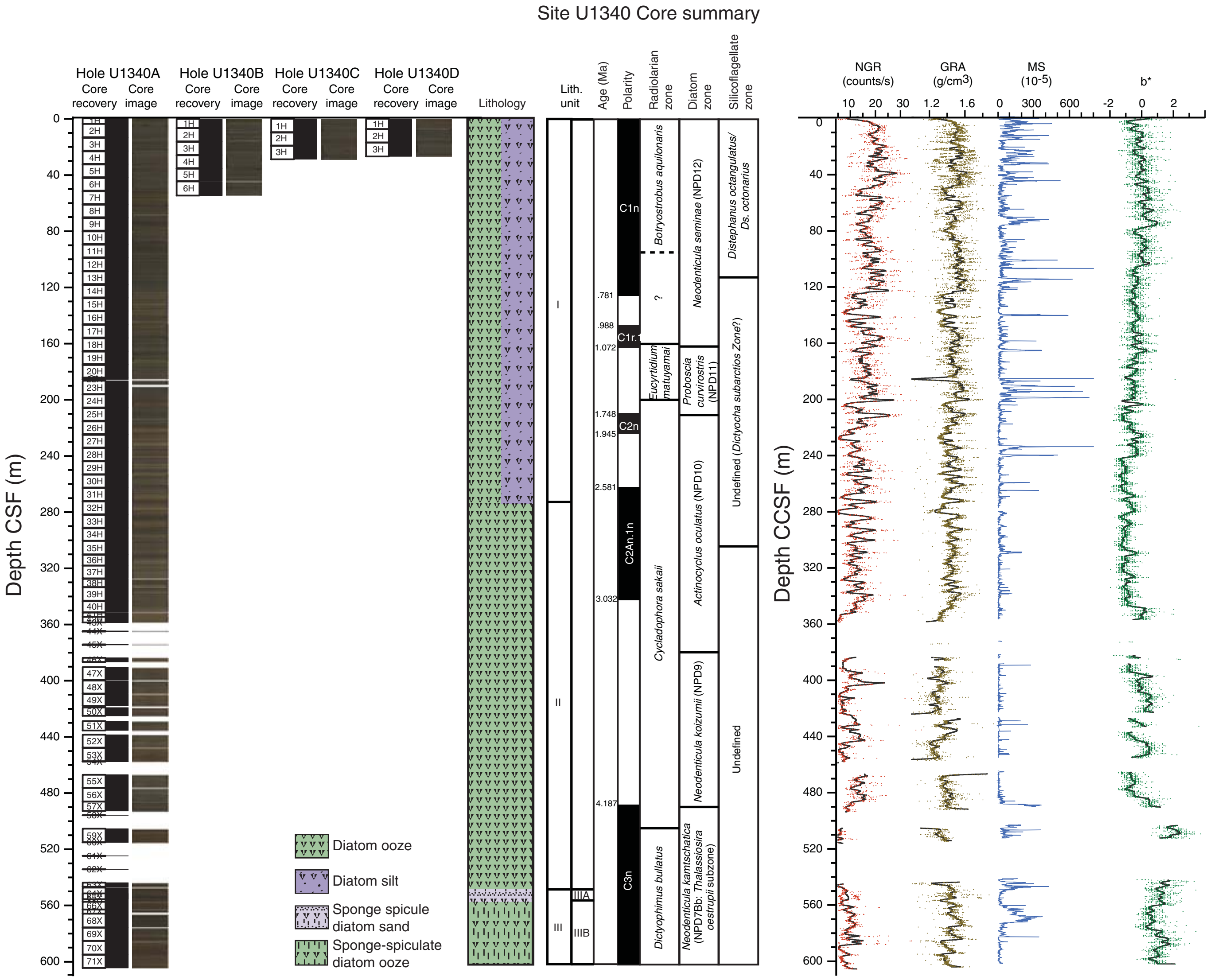

Figure F26. Age-depth plot for Hole U1340A, including all biostratigraphic and paleomagnetic datums listed in Table T7. Sedimentation rates are based only on paleomagnetic reversal data.

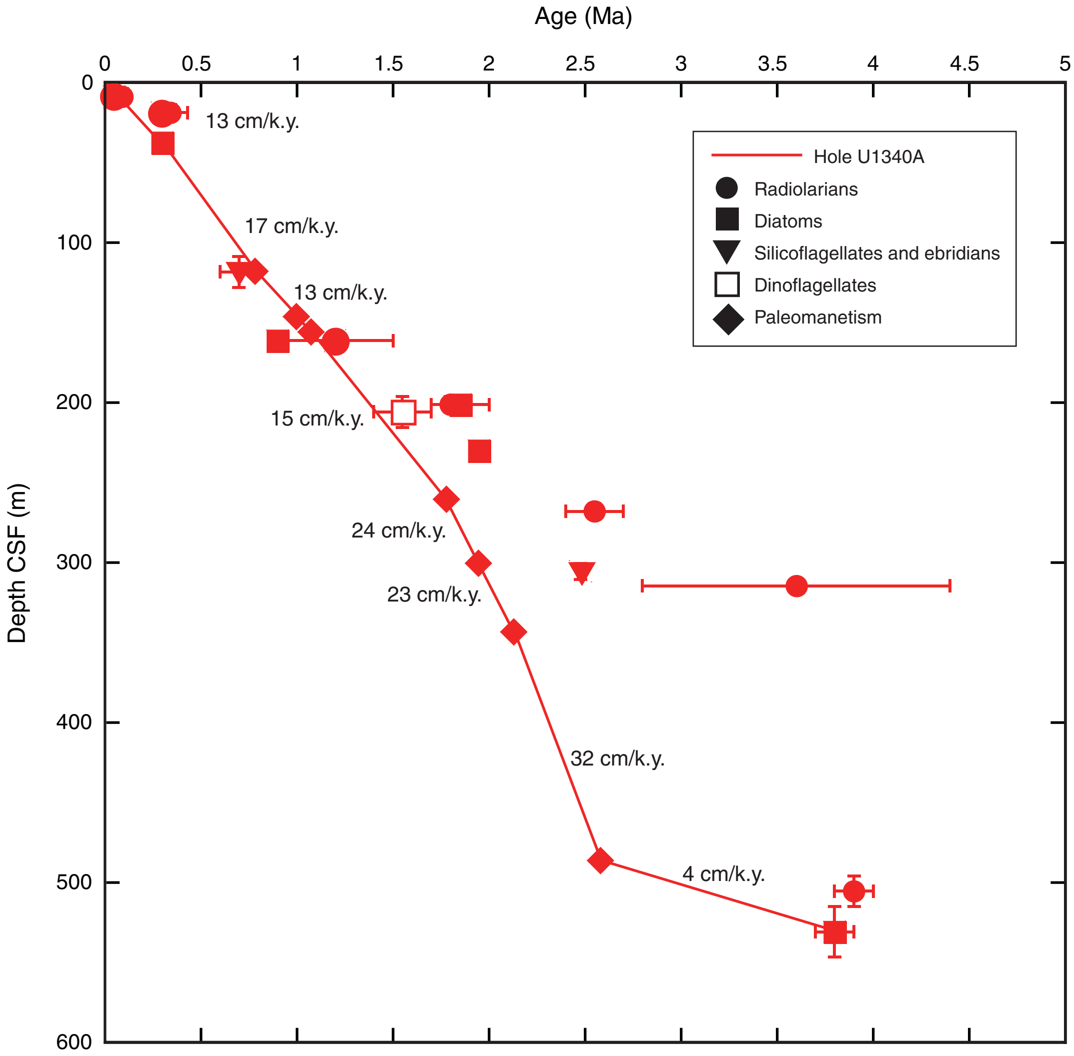

Figure F27. Seismic profile of *Hakuhou-Maru* Cruise KH99-3 Line Stk5-1 (west–east) at Site U1341.

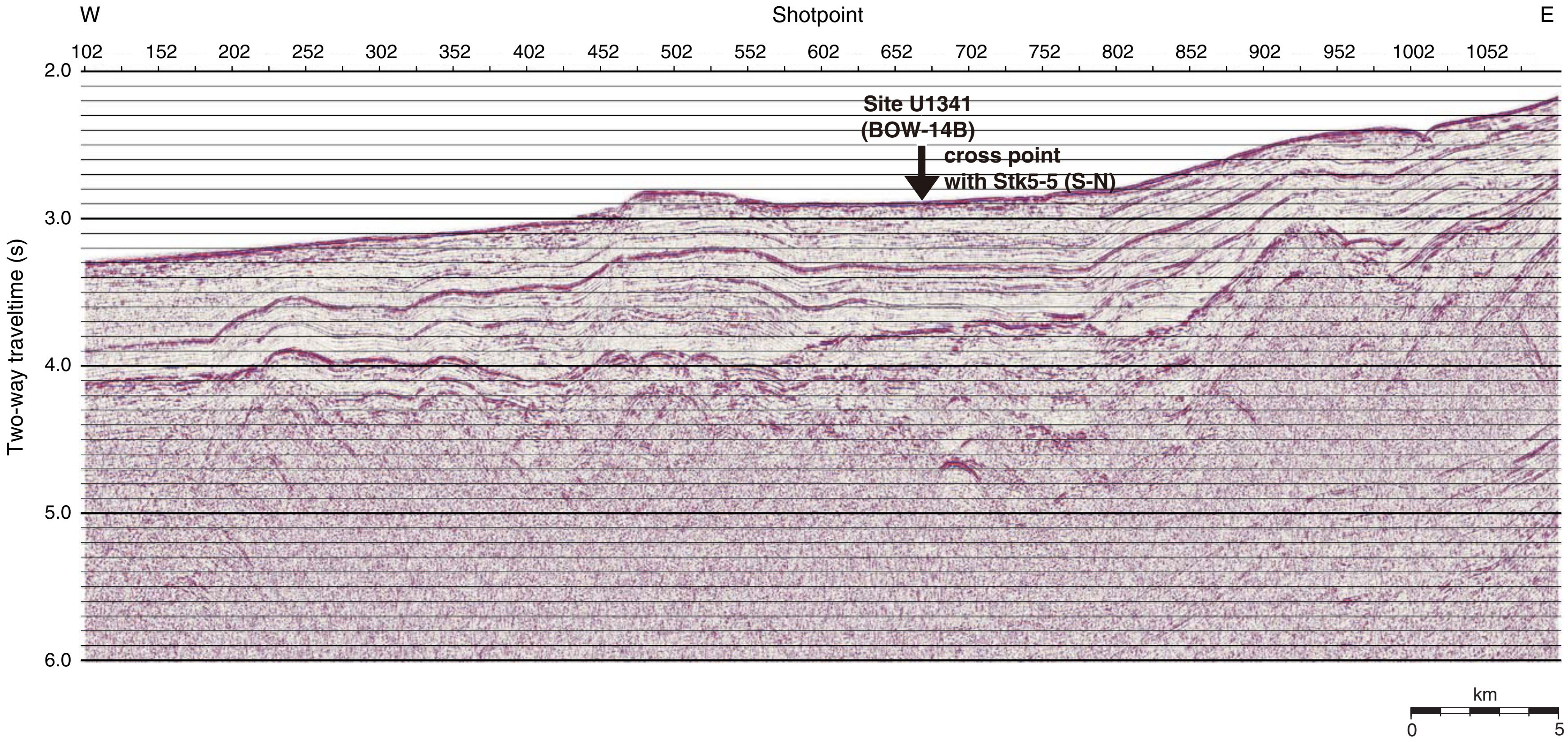

Figure F28. Navigation map of *Hakuhou-Maru* Cruise KH99-3 around Site U1341 for close-up seismic profiles found in Figures F29 and F30.

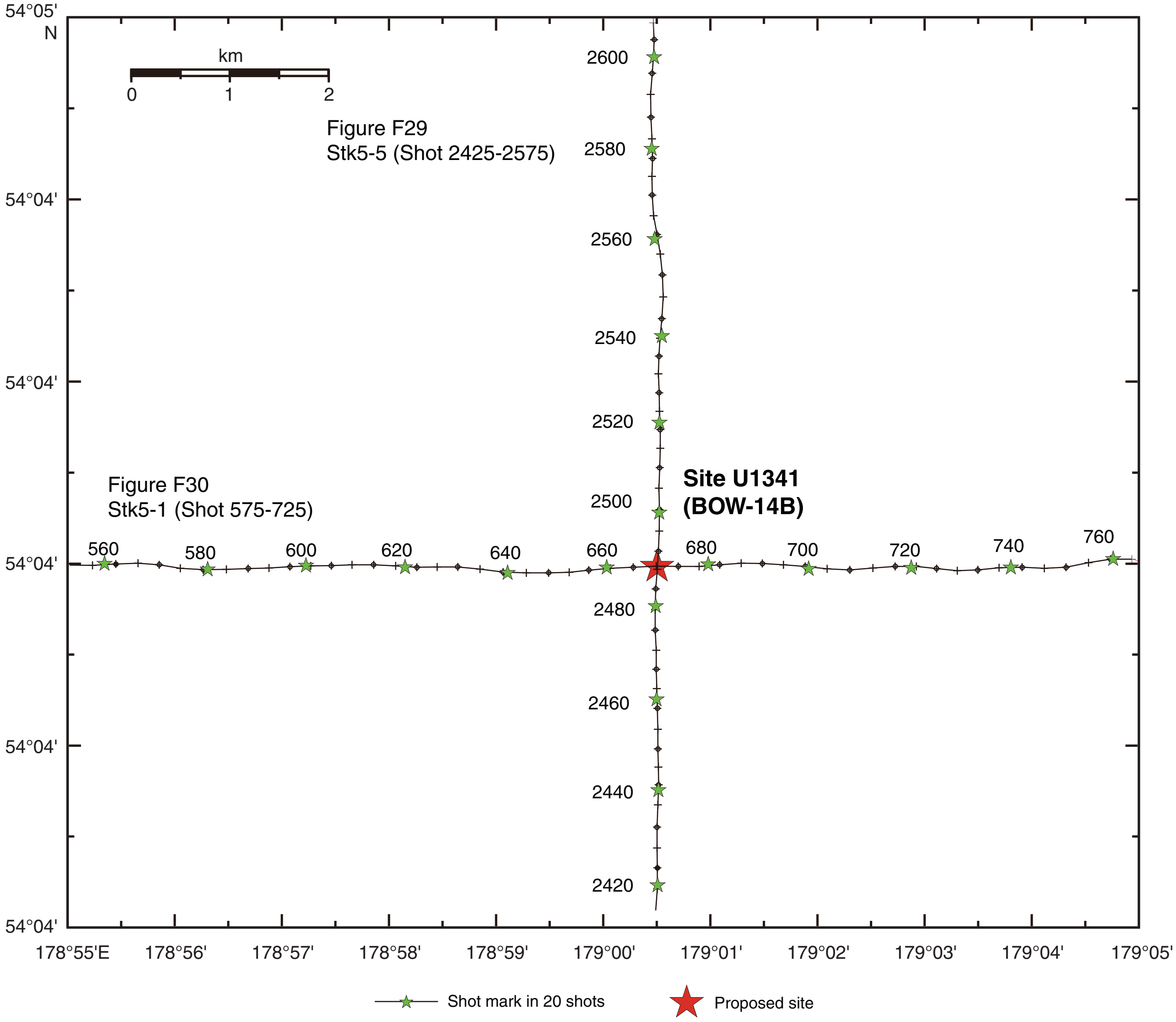

Figure F29. A. Close-up seismic profile of *Hakuhou-Maru* Cruise KH99-3 Line Stk5-1 (west–east) near Site U1341. Cross point with Line Stk5-5 (south–north) is at Shotpoint 670. **B.** Time-depth curve estimated from results of velocity analyses on Lines Stk5-1 and Stk5-5 around Site U1341.

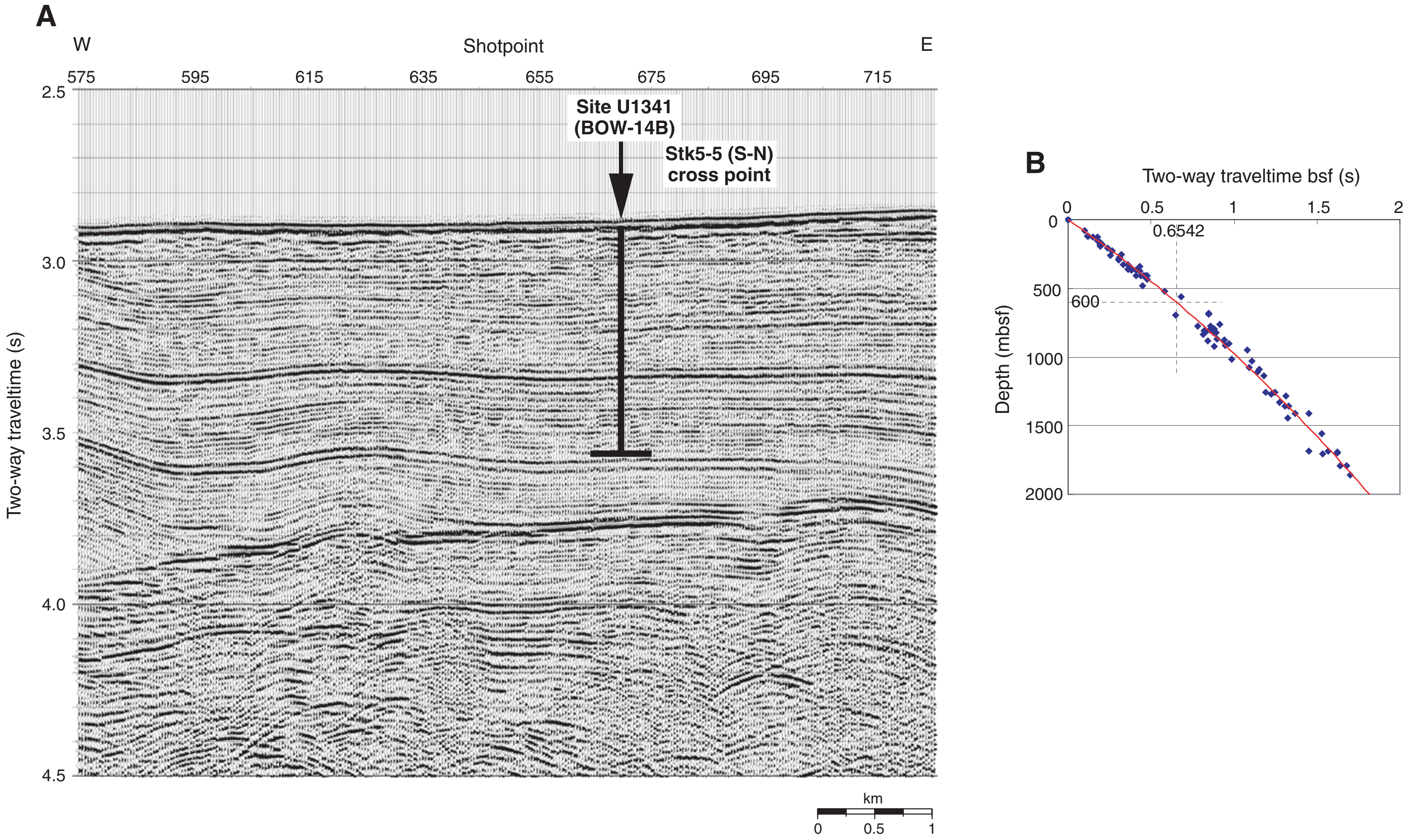

Figure F30. **A.** Close-up seismic profile of *Hakuhou-Maru* Cruise KH99-3 Line Stk5-5 (south–north) near Site U1341. Cross point with Line Stk5-1 (south–north) is at Shotpoint 2488. **B.** Time-depth curve estimated from results of velocity analyses on Lines Stk5-1 and Stk5-5 around Site U1341.

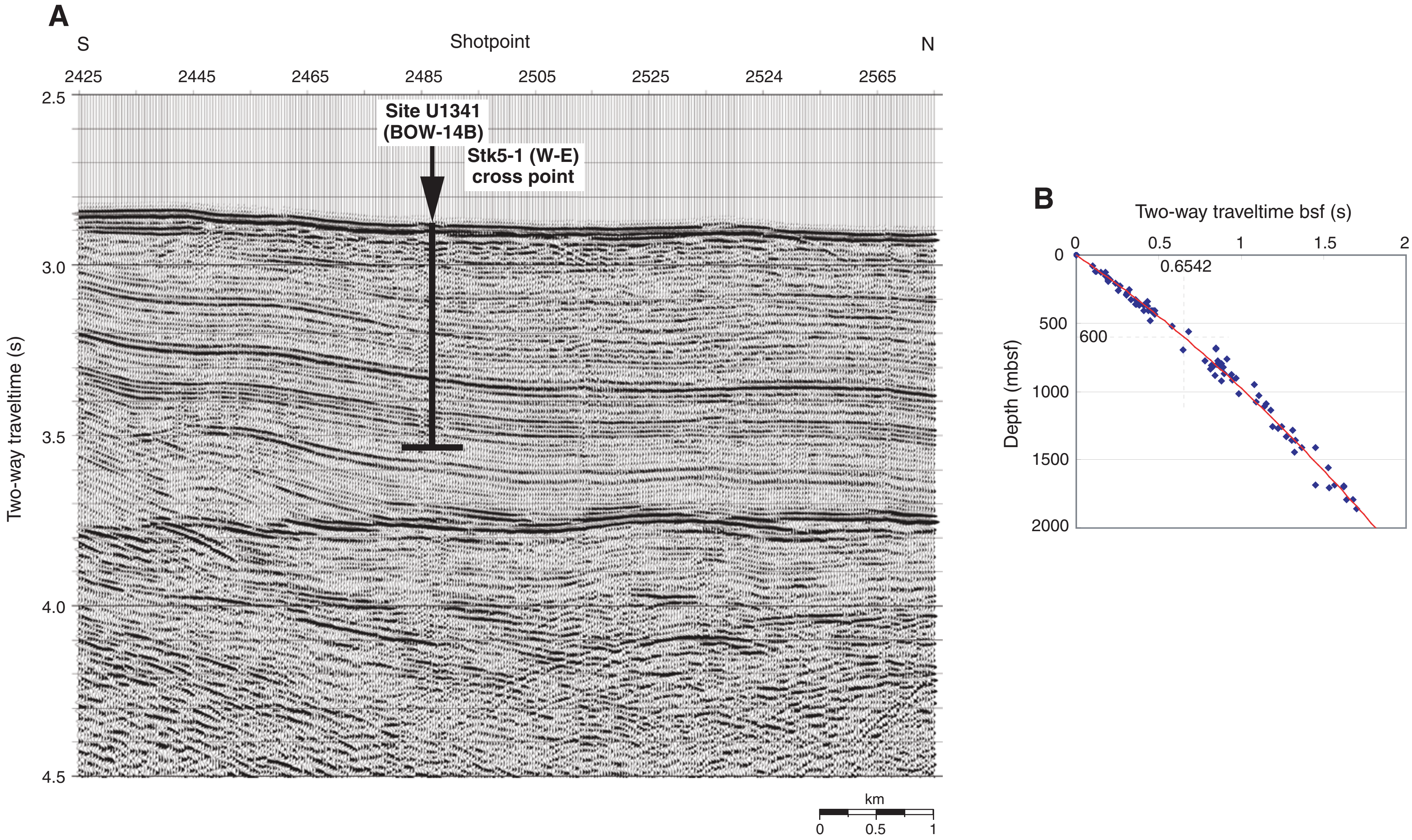

Figure F31. Summary of some shipboard analyses at Site U1341: core recovery, core images, lithology, lithologic units and subunits, age, paleomagnetic chronology, zone of biostratigraphically important radiolarians, diatoms, and silicoflagellates, and spliced records of natural gamma radiation (NGR), gamma ray attenuation (GRA) bulk density, magnetic susceptibility (MS), and the b* index of color reflectance.

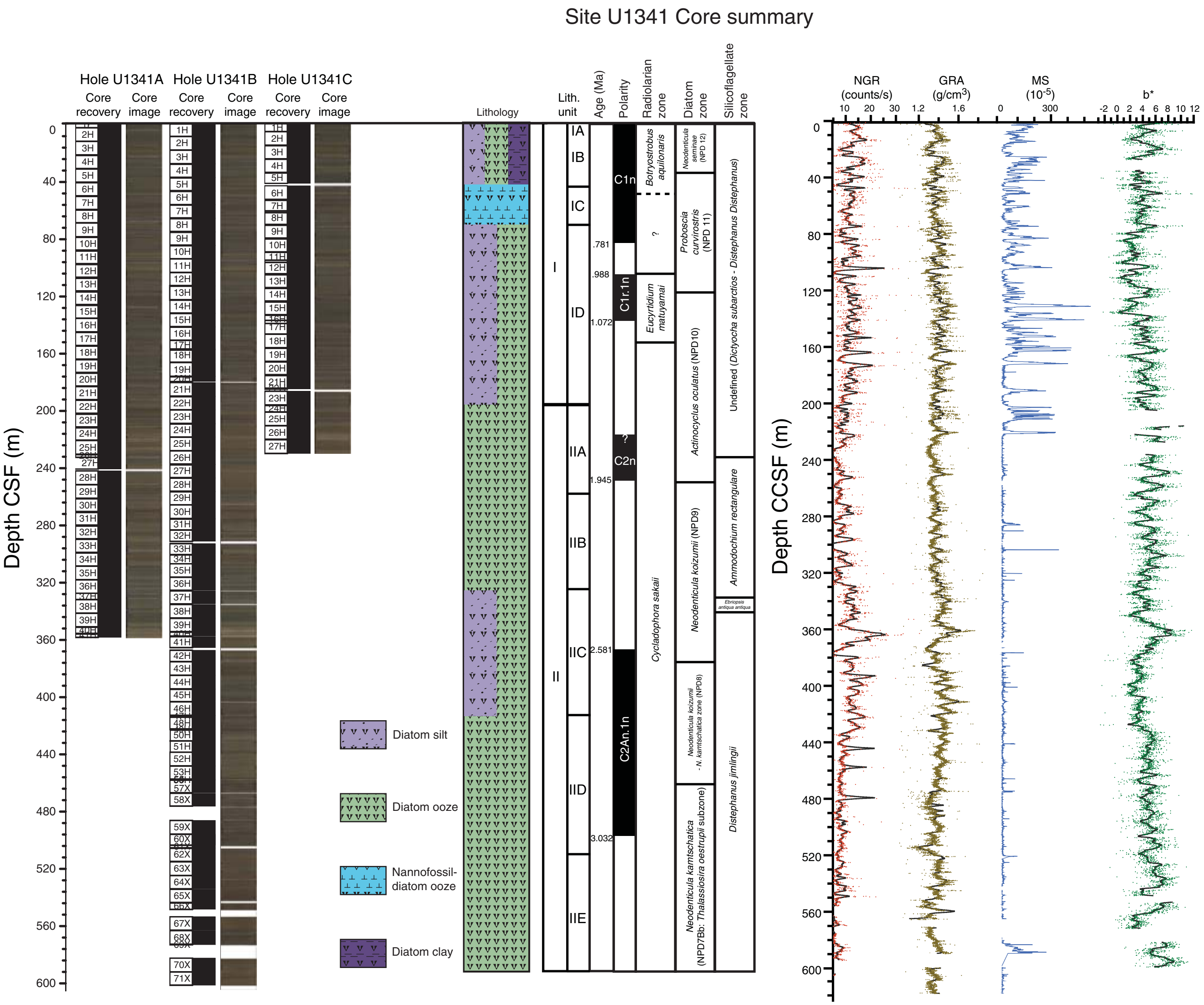

Figure F32. Combined profiles of concentrations of pore water constituents, Holes U1341A and U1341B: (**A**) DIC, (**B**) pH, (**C**) alkalinity, (**D**) sulfate, (**E**) sulfide, (**F**) methane, (**G**) phosphate, (**H**) ammonium, and (**I**) salinity.

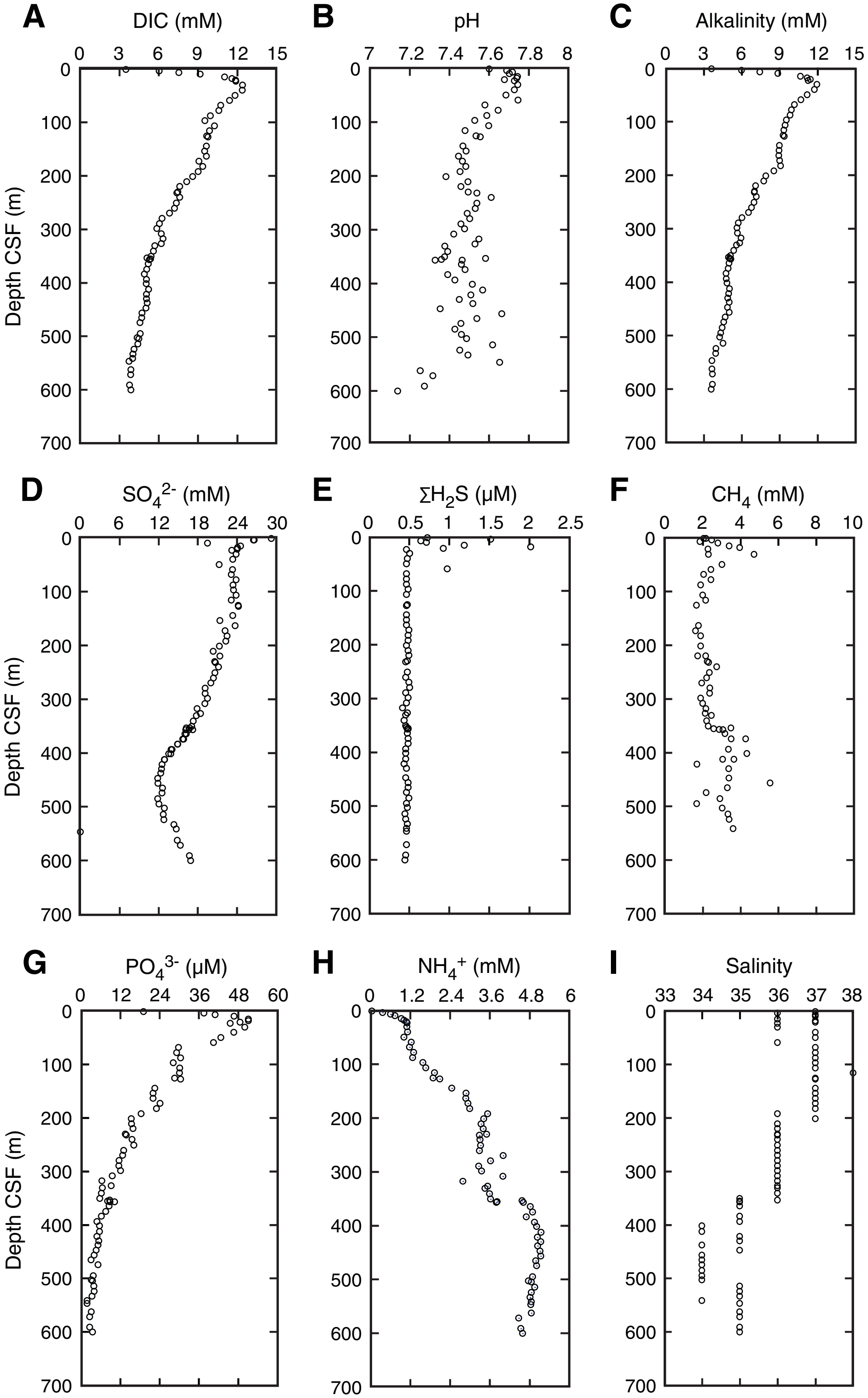

Figure F33. Summary of spectral natural gamma ray measurements in Hole U1341B.

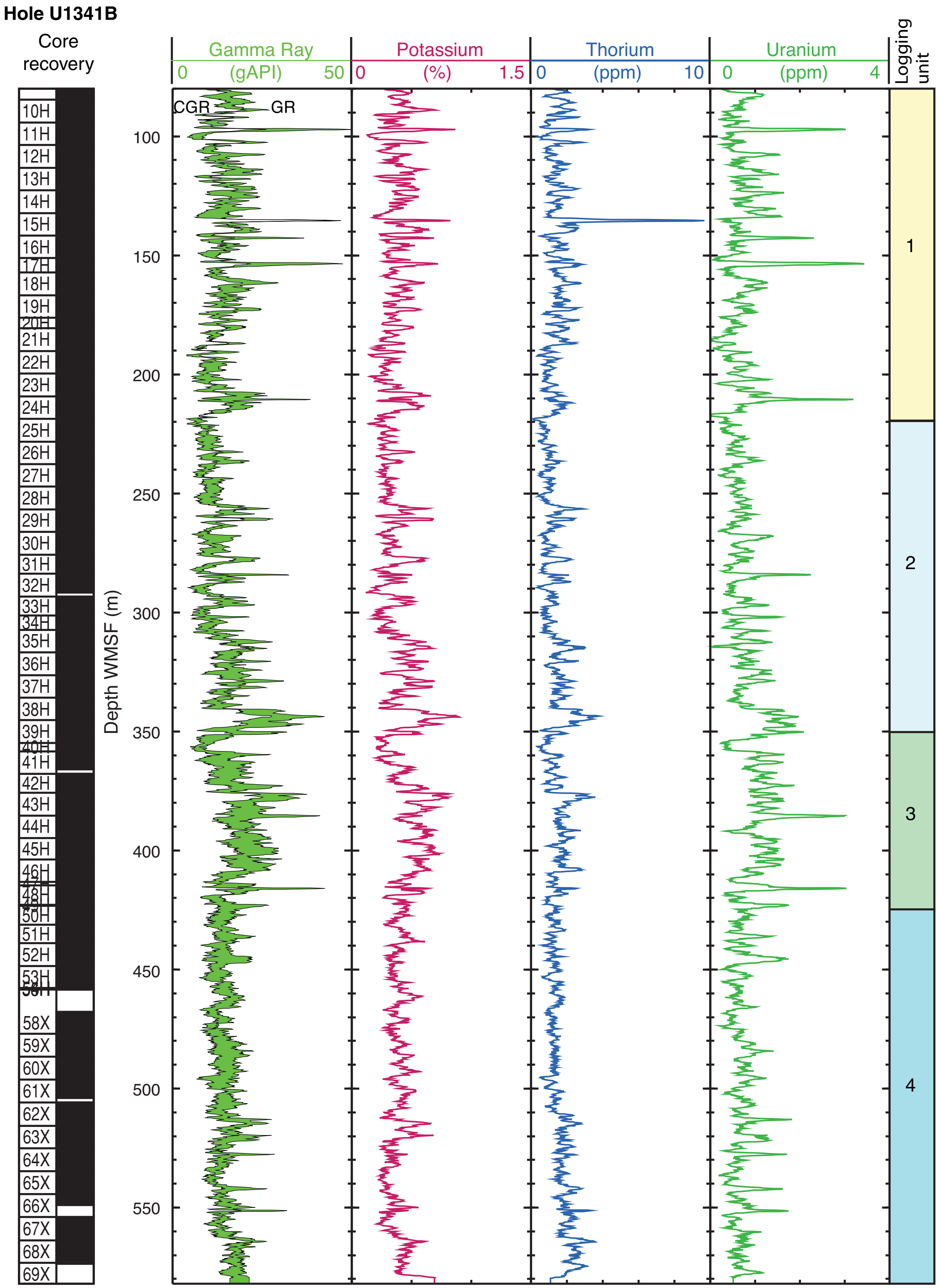

Figure F34. Percent changes of *Neodenticula seminae*, *Neodenticula kamtschatica*, and *Neodenticula koizumii* within total counts of three taxa belonging to genus *Neodenticula*, Holes U1340A and U1340B. Based on the rapid increases (RI) and decreases (RD) of each taxon, a clear assignment of tie points is accomplished. The RI of *N. koizumii* and RD of *N. kamtschatica* coincide with the top of Gauss at 2.581 Ma. The RD of *N. koizumii* and RI of *N. seminae* coincide with the top of Olduvai at 1.778 Ma.

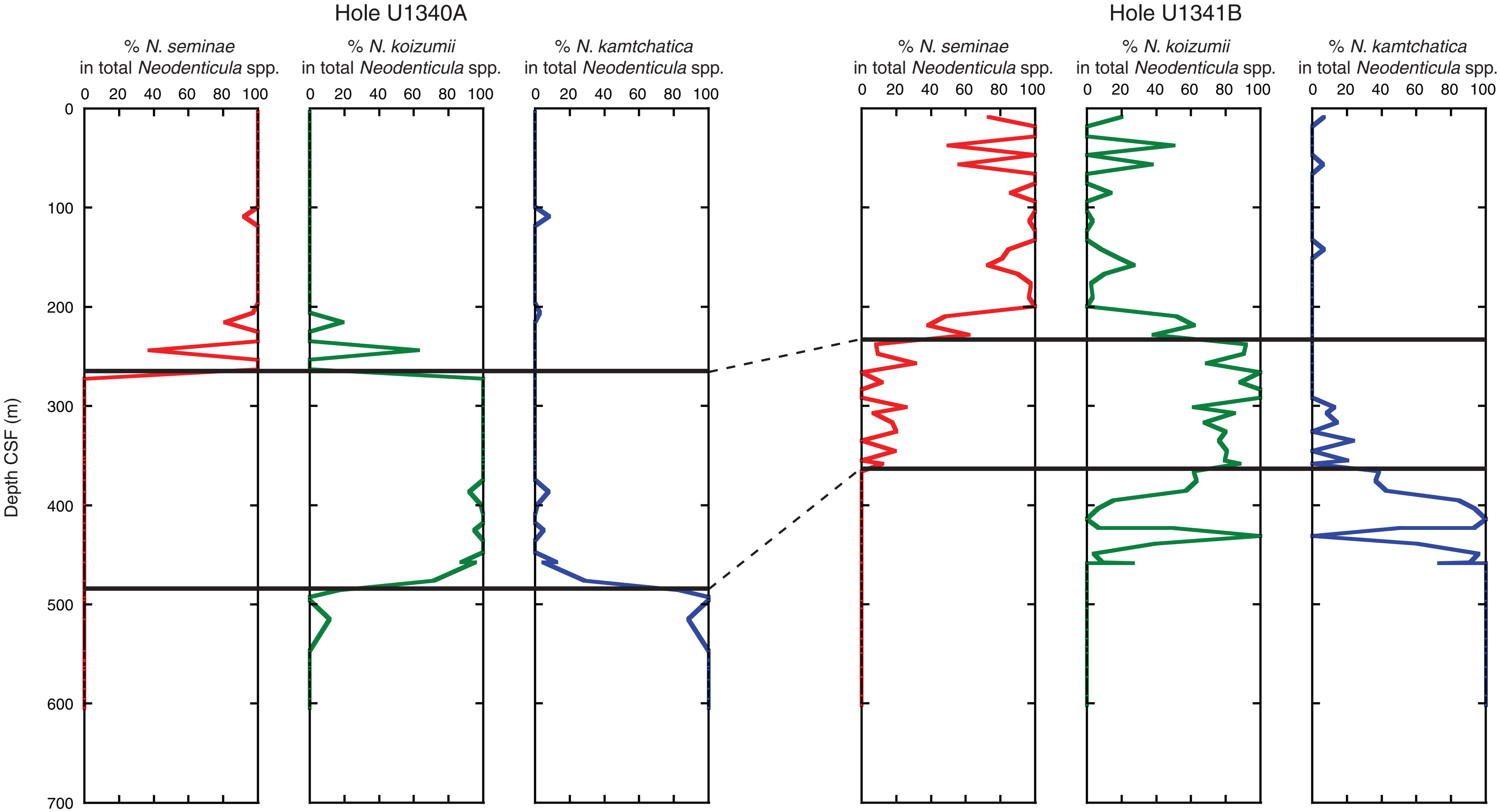

Figure F35. Percent changes of *Neodenticula seminae*, *Neodenticula kamtschatica*, and *Neodenticula koizumii* and tie points of relevant biostratigraphic and paleomagnetic datums between Holes U1340A and U1341B. With the exception of the LO of *E. antiqua antiqua*, whose abundance is low, the age assignment of each of the events fits well. T = top, B = bottom, APC= advanced piston corer, XCB = extended core barrel, FO = first occurrence, LO = last occurrence, BM = bench mark.

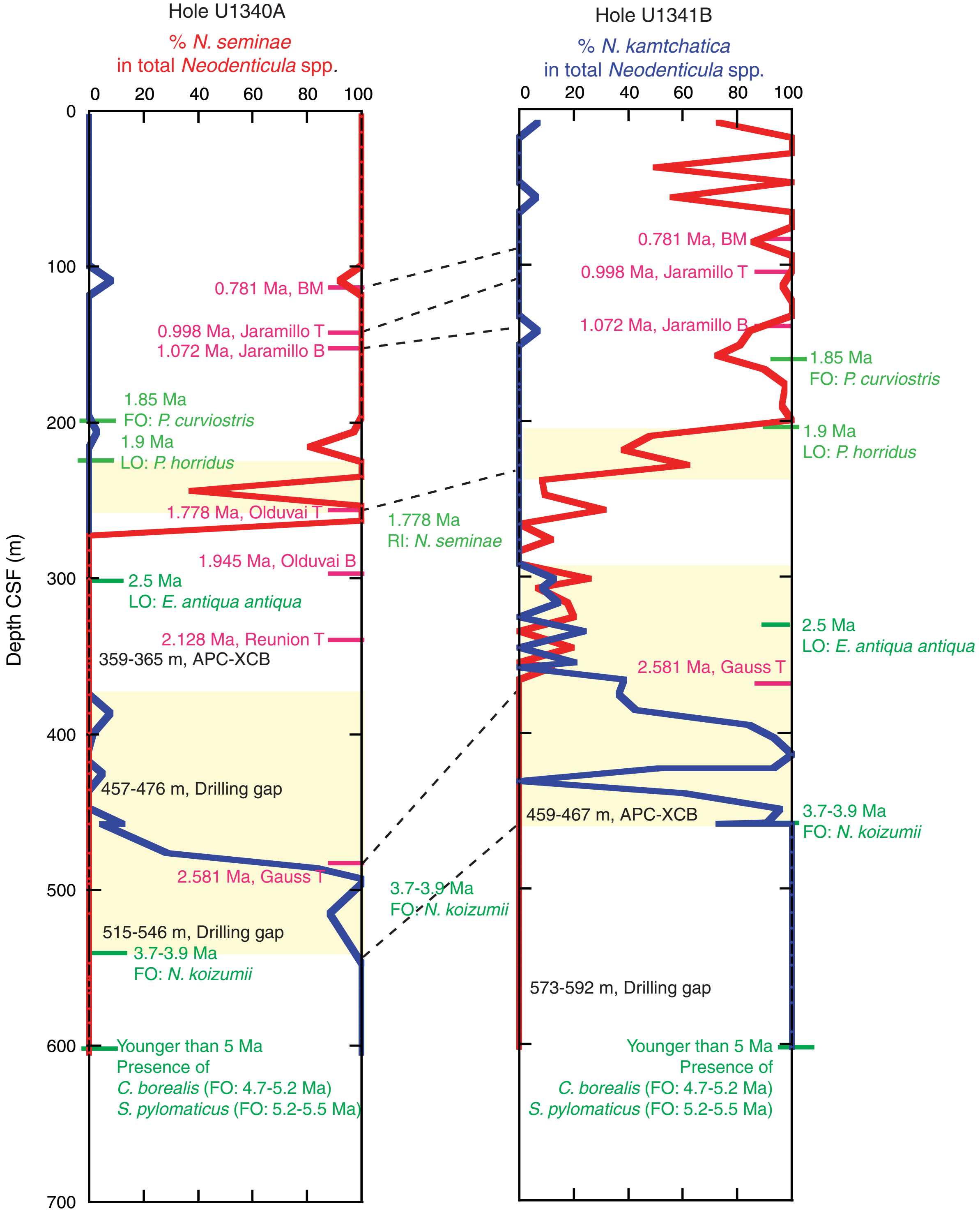

Figure F36. Age-depth plot for Site U1341, including all biostratigraphic and paleomagnetic datums listed in Table T11. Sedimentation rates are based on paleomagnetic reversal data and a few biostratigraphic datums.

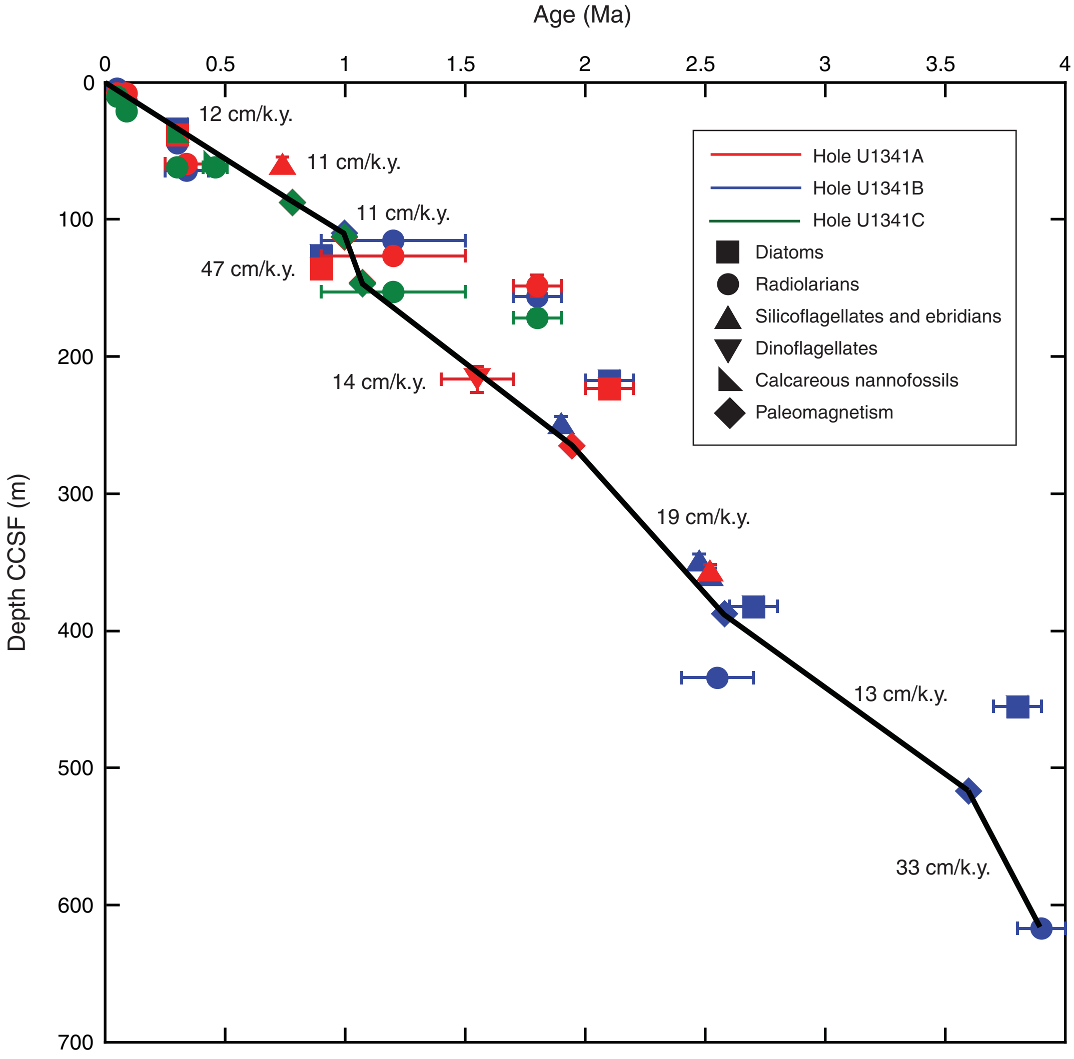

Figure F37. Seismic profile of *Hakuhou-Maru* Cruise KH99-3 Line Stk4-1 (north–south) at Site U1342 (BOW-15A).

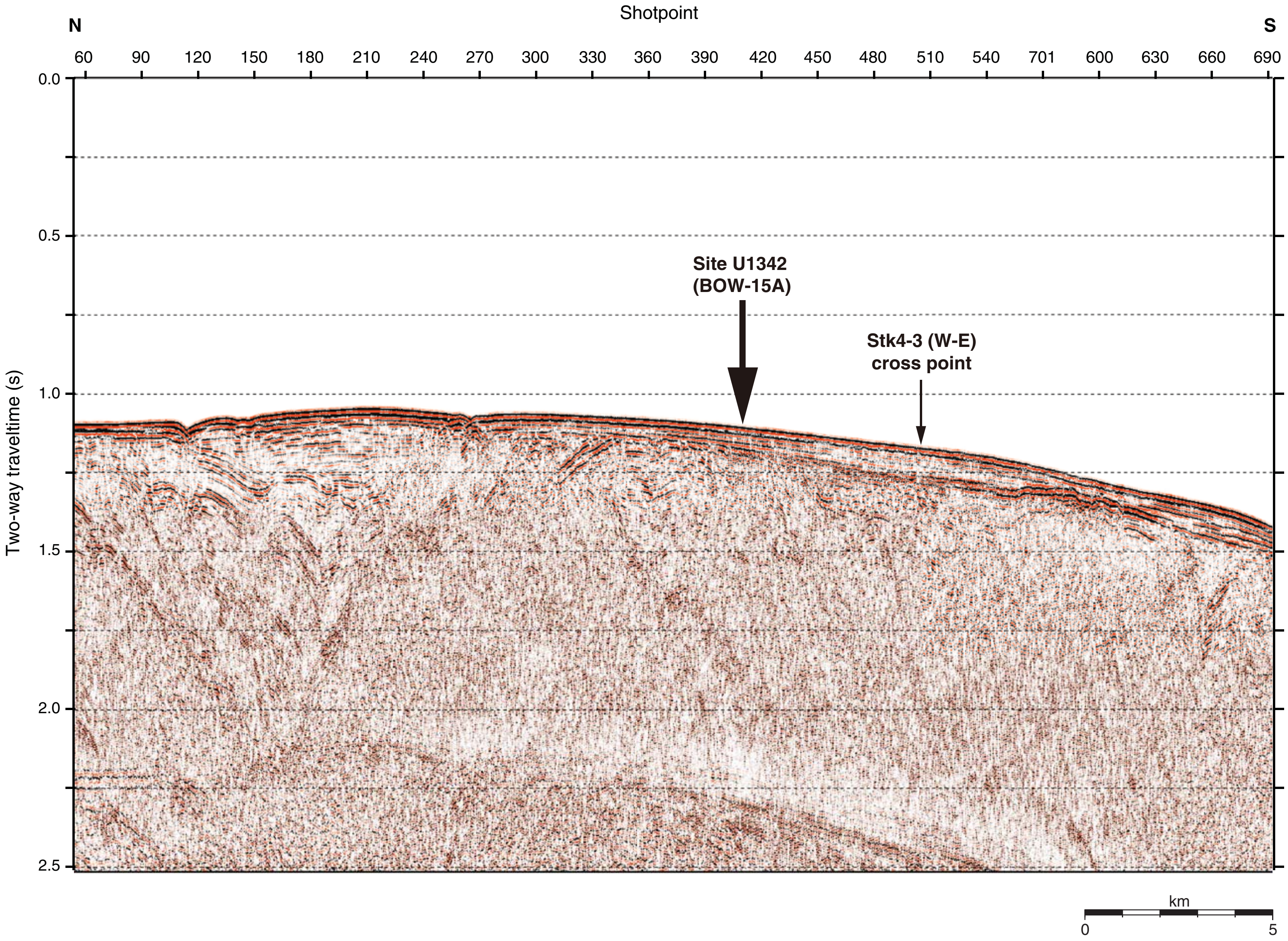

Figure F38. Navigation map of *Hakuhou-Maru* Cruise KH99-3 around Site U1342 (BOW-15A) for close-up seismic profiles found in Figures **F39** and **F40.**

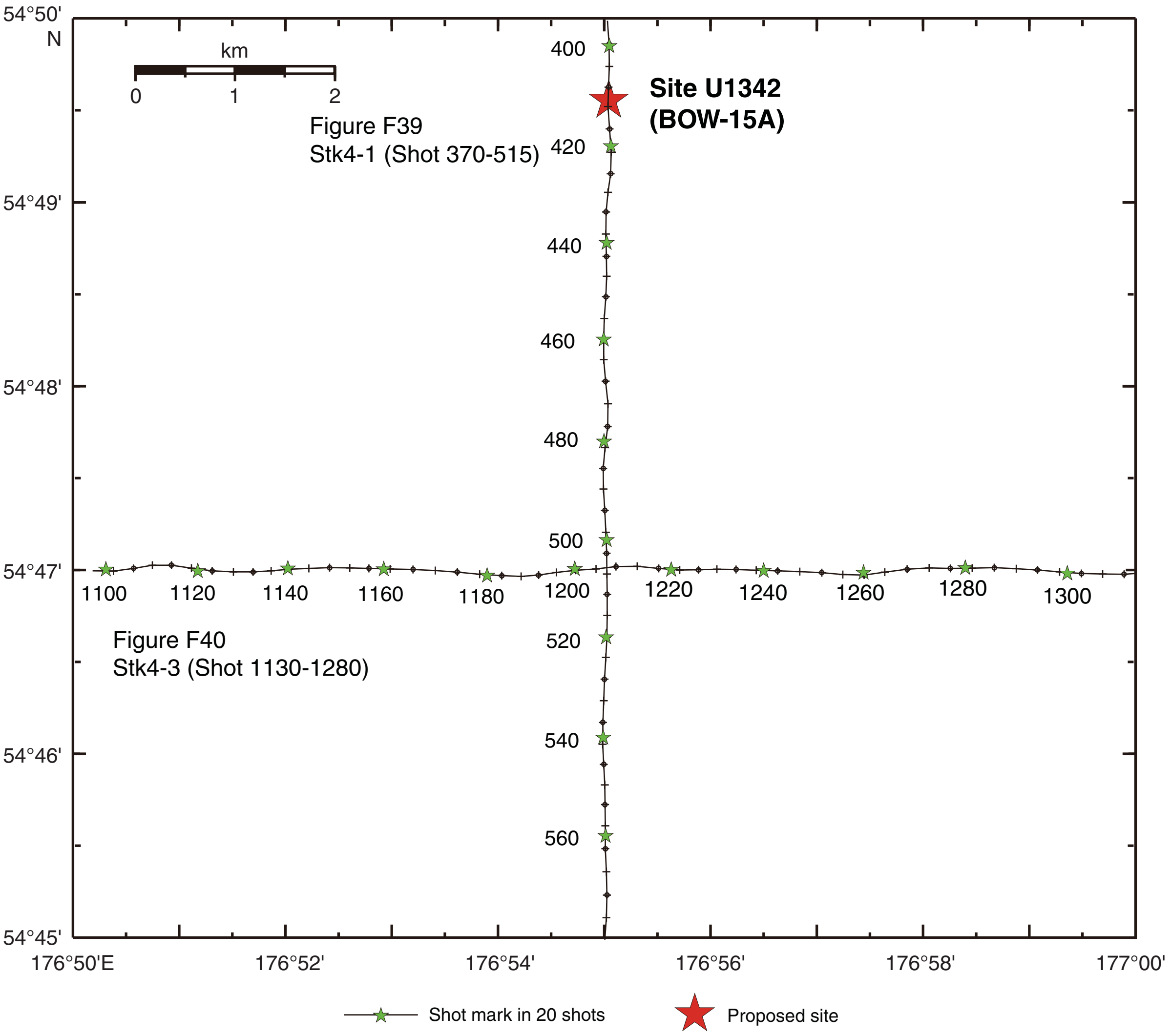

Figure F39. **A.** Close-up seismic profile of *Hakuhou-Maru* Cruise KH99-3 Line Stk4-1 (north–south) near Site U1342. Cross point with Line Stk4-3 (west–east) is at Shotpoint 505. **B.** Time-depth curve estimated from results of velocity analyses on Lines Stk4-1 and Stk4-3 around Site U1342.

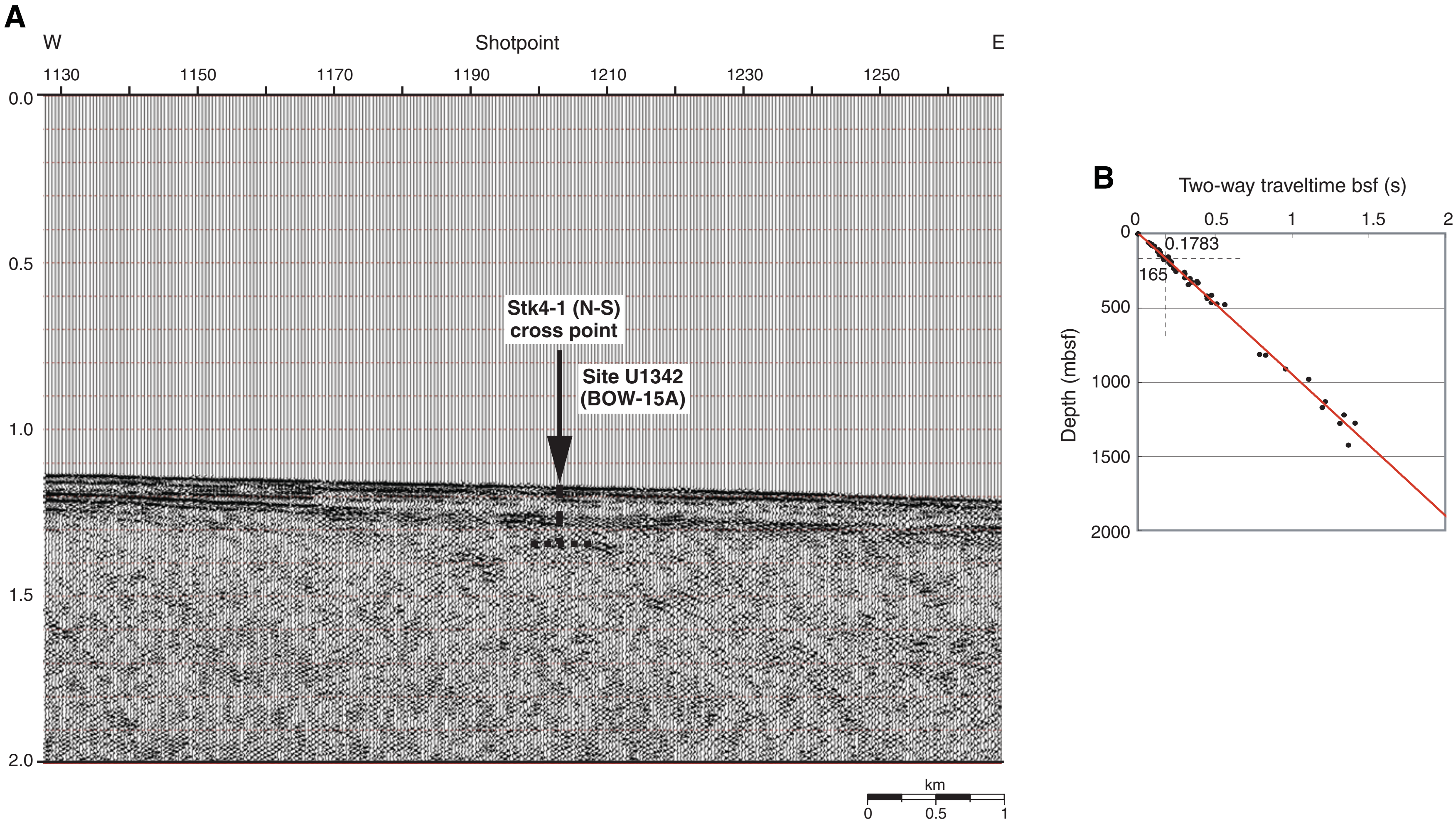

Figure F40. **A.** Close-up seismic profile of *Hakuhou-Maru* Cruise KH99-3 Line Stk4-3 (west–east) near Site U1342. Cross point with Line Stk4-1 (south–north) is at Shotpoint 1203. **B.** Time-depth curve estimated from results of velocity analyses on Lines Stk4-1 and Stk4-3 around Site U1342.

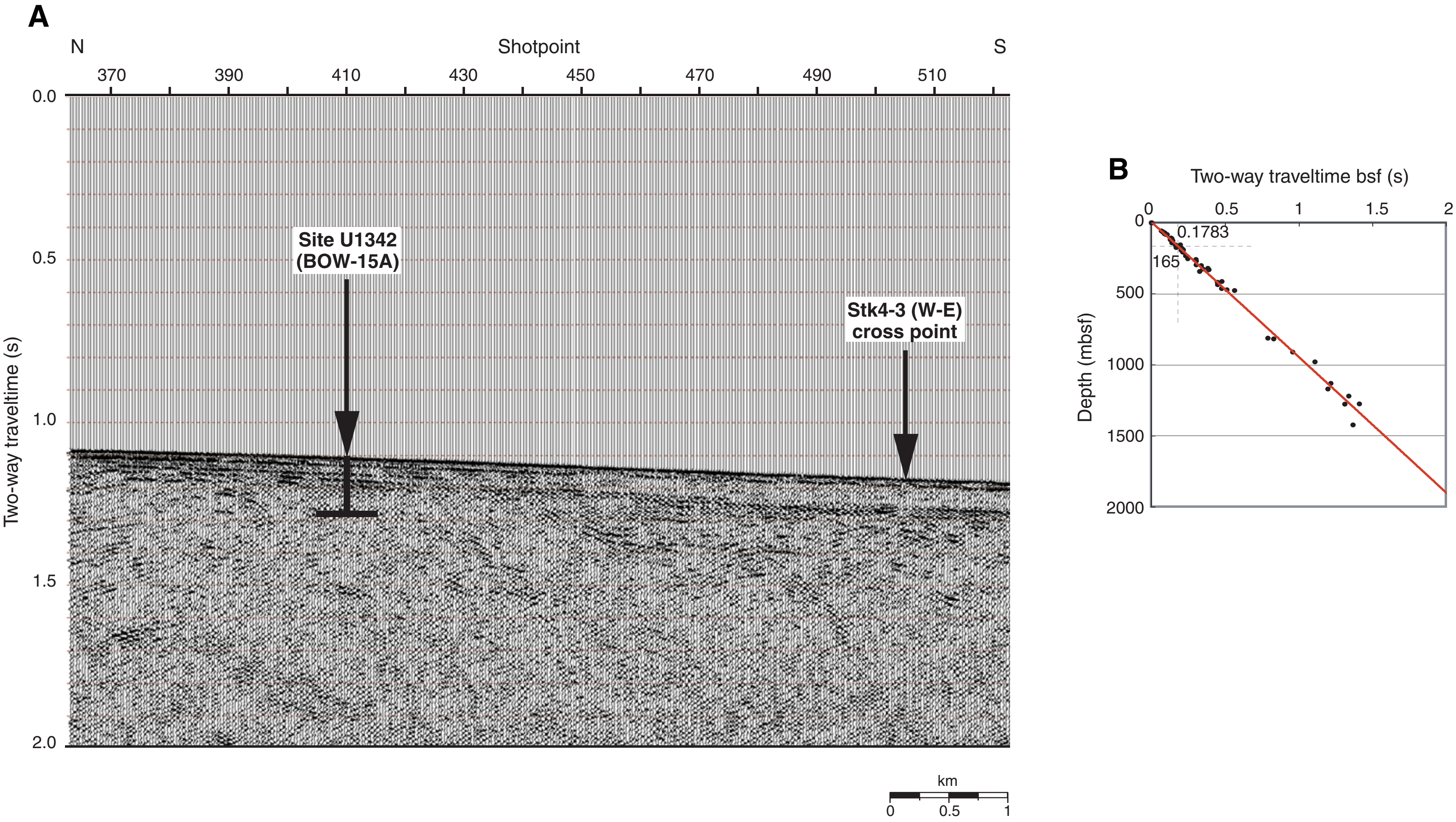

Figure F41. Summary of some shipboard analyses at Site U1342: core recovery, core images, lithology, lithologic units and subunits, age, paleomagnetic chronology, zone of biostratigraphically important radiolarians, diatoms, and silicoflagellates, and spliced records of natural gamma radiation (NGR), gamma ray attenuation (GRA) bulk density, magnetic susceptibility (MS), and the b* index of color reflectance.

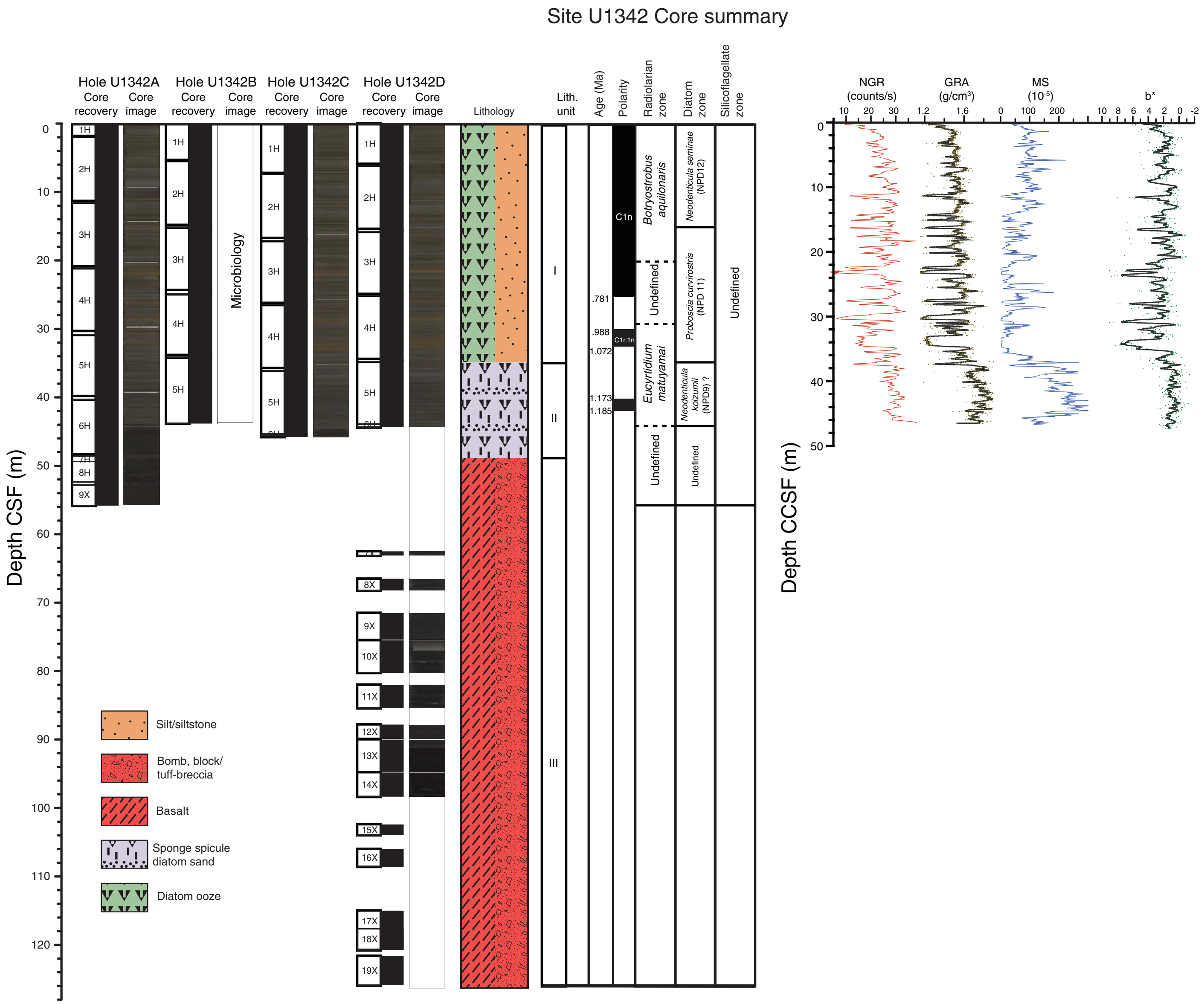

Figure F42. Combined profiles of concentrations of pore water constituents, Holes U1342A and U1342B: (**A**) DIC, (**B**) pH, (**C**) alkalinity, (**D**) sulfide, (**E**) sulfate, (**F**) methane, (**G**) chloride, (**H**) salinity, (**I**) phosphate, and (**J**) ammonium.

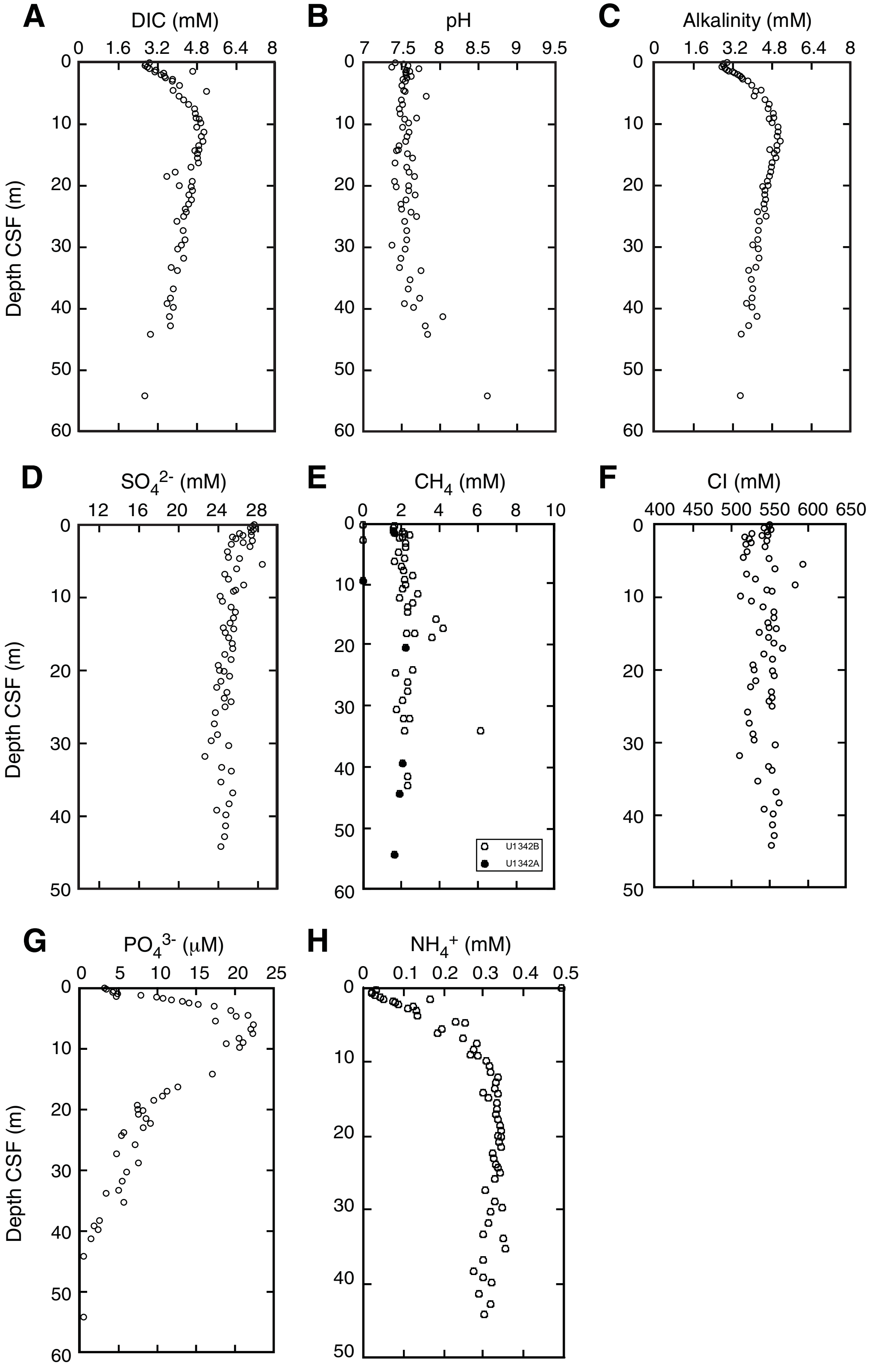

Figure F43. Age-depth plot for Site U1342, including all biostratigraphic and paleomagnetic datums listed in Table T15. Sedimentation rates are based on paleomagnetic reversal data and a few biostratigraphic datums.

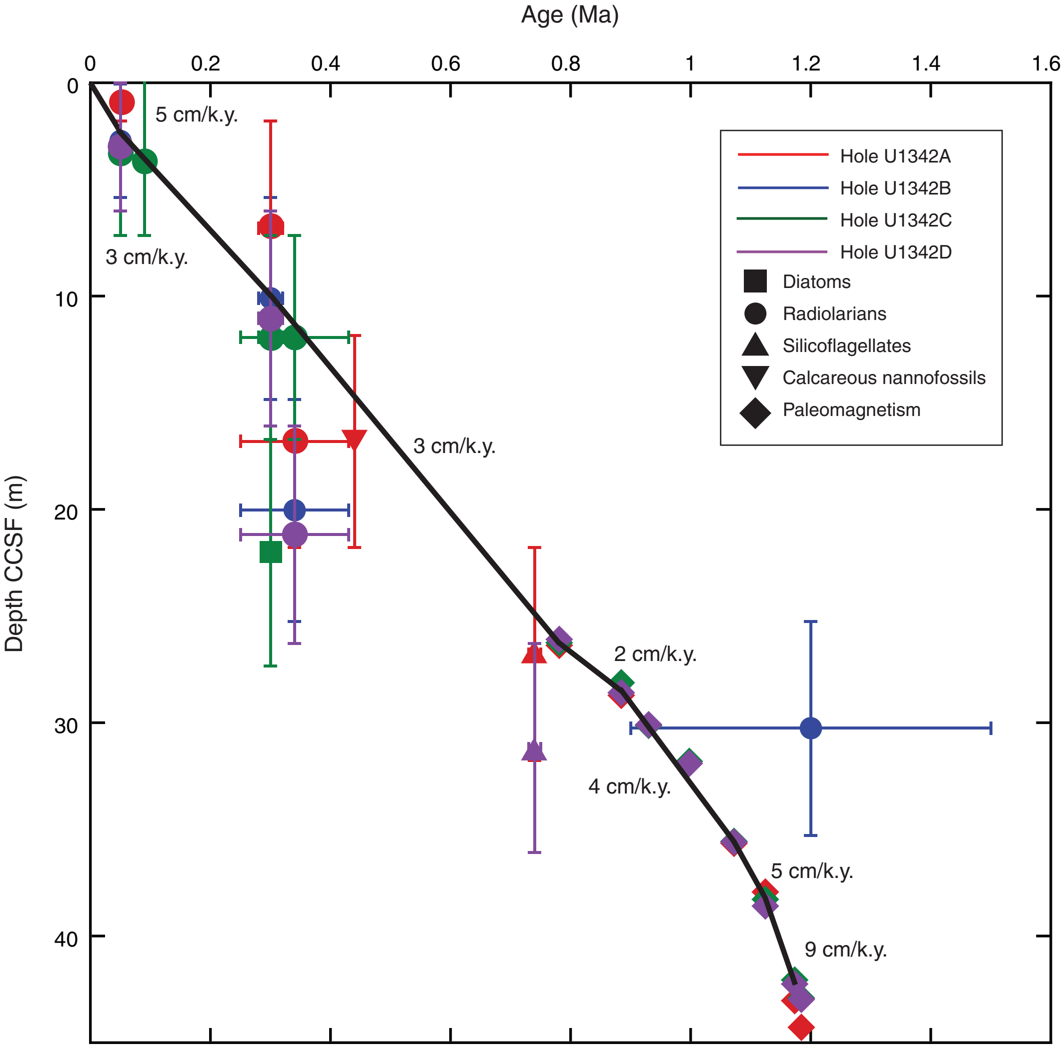

Figure F44. Location map showing Sites U1343, U1344, and U1345.

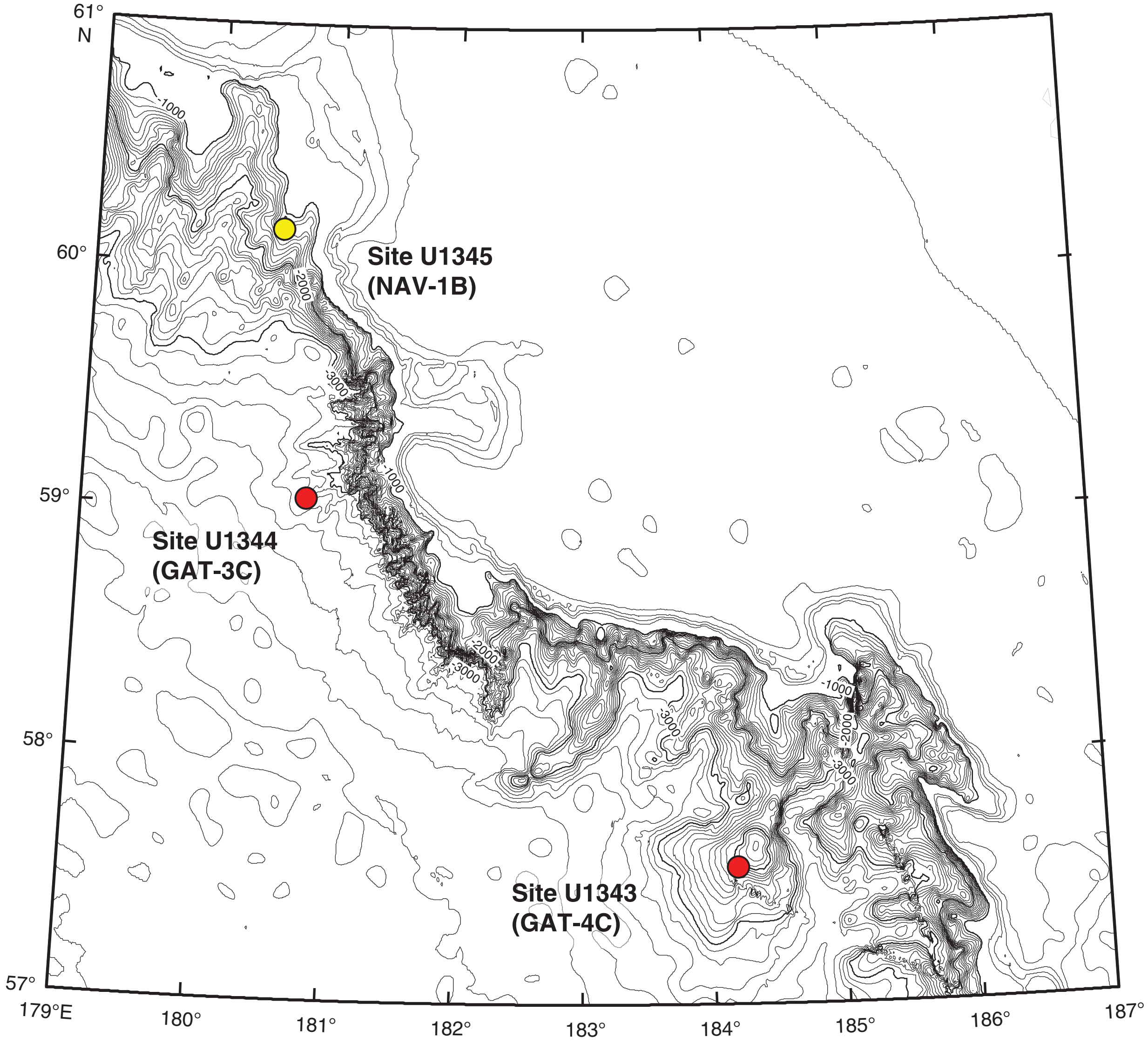

Figure F45. Navigation map of *Hakuhou-Maru* Cruise KH99-3 across Site U1343 for close-up seismic profiles in Figures F46 and F47.

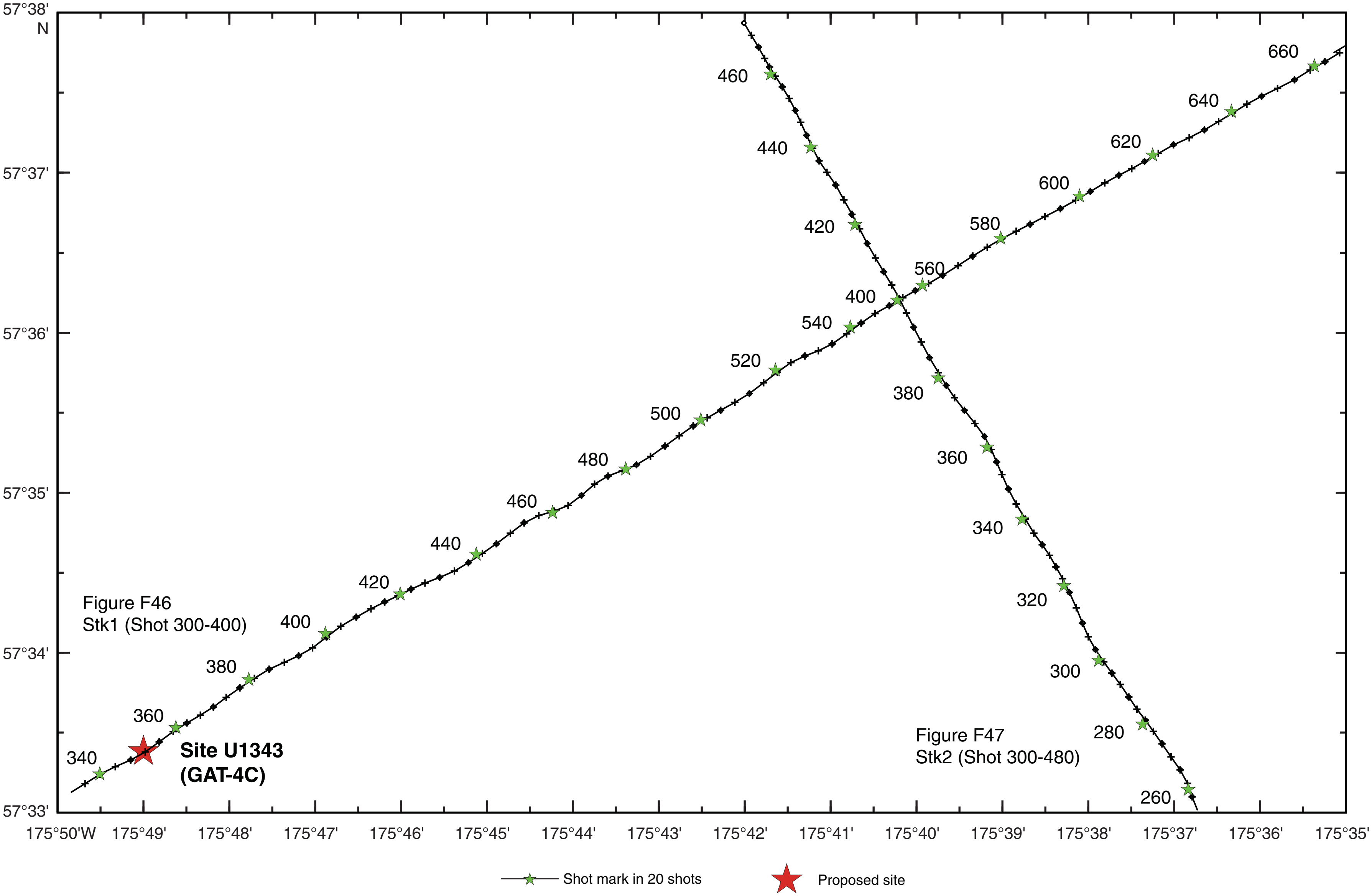

Figure F46. A. Close-up seismic profile of *Hakuhou-Maru* Cruise KH99-3 Line Stk-1 (southwest–northeast) near Site U1343. **B.** Time-depth curve estimated from results of velocity analyses near Site U1343.

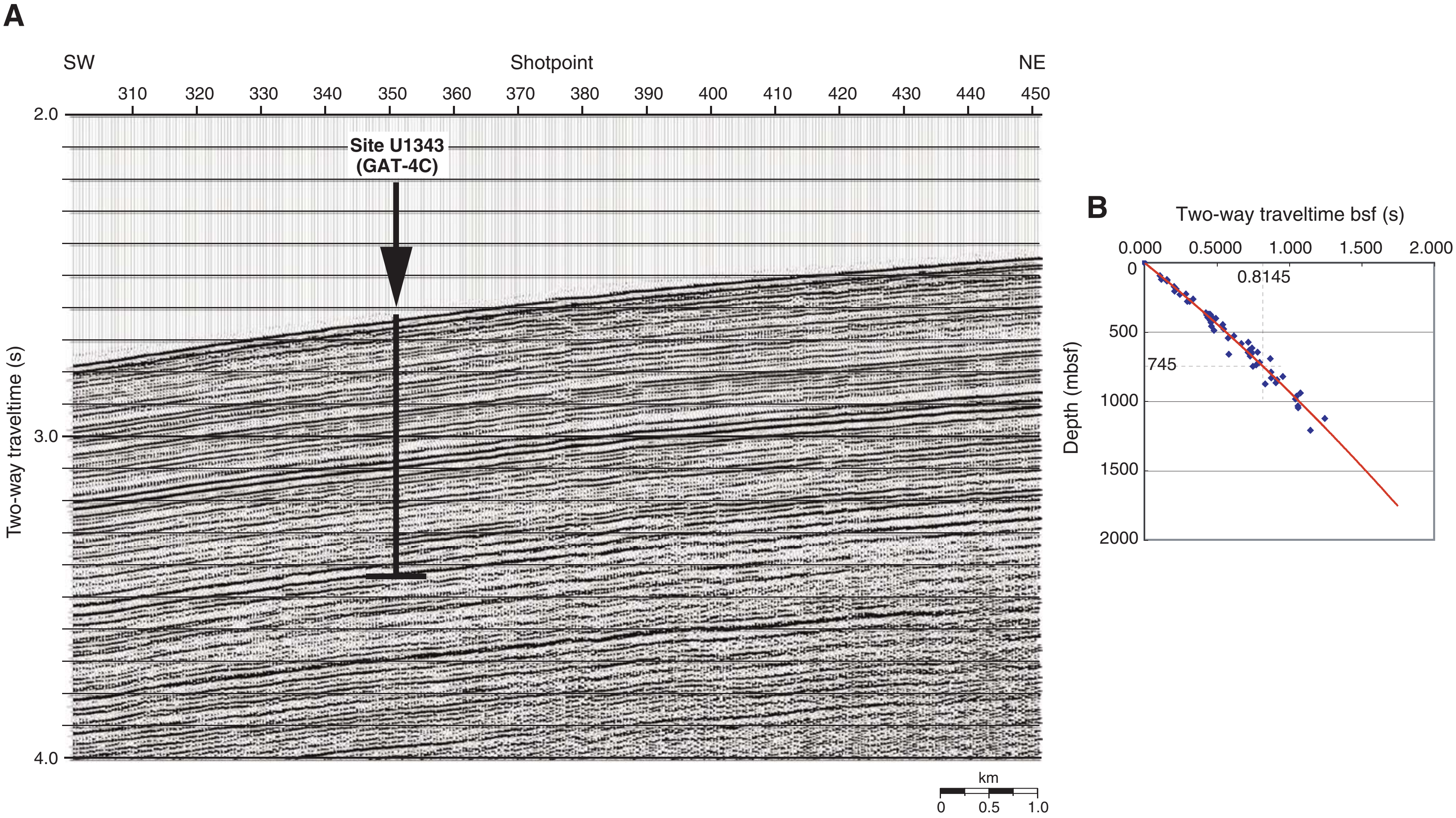

Figure F47. A. Close-up seismic profile of *Hakuhou-Maru* Cruise KH99-3 Line Stk-2 (southeast–northwest) near Site U1343. **B.** Time-depth curve estimated from results of velocity analyses near Site U1343.

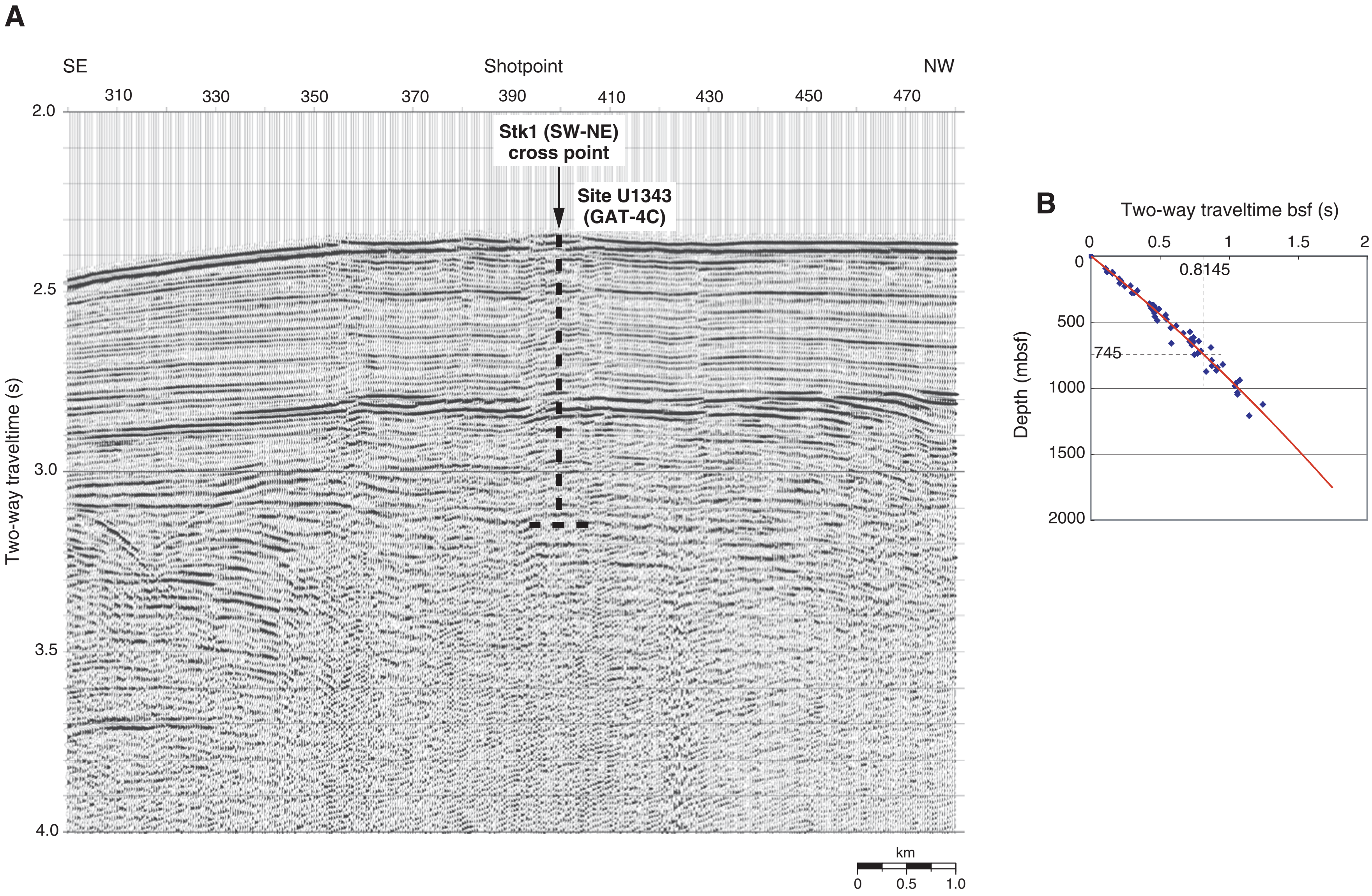

Figure F48. Seismic profile of *Hakuhou-Maru* Cruise KH99-3 Line Stk-1 at Site U1343.

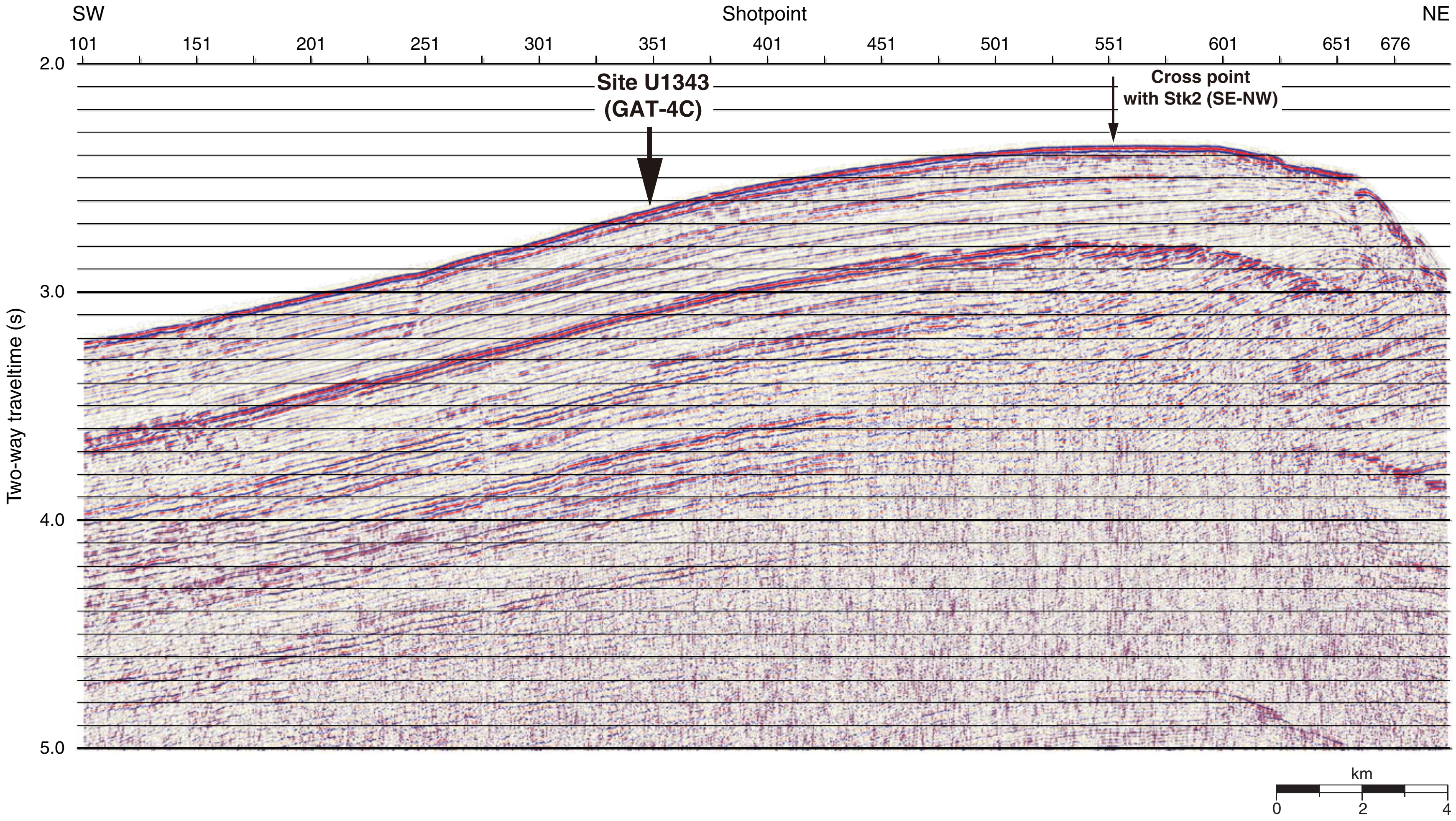

Figure F49. Summary of some shipboard analyses at Site U1343: core recovery, core images, lithology, lithologic units and subunits, age, paleomagnetic chronology, zone of biostratigraphically important radiolarians, diatoms, and silicoflagellates, and spliced records of natural gamma radiation (NGR), gamma ray attenuation (GRA) bulk density, magnetic susceptibility (MS), and the b* index of color reflectance.

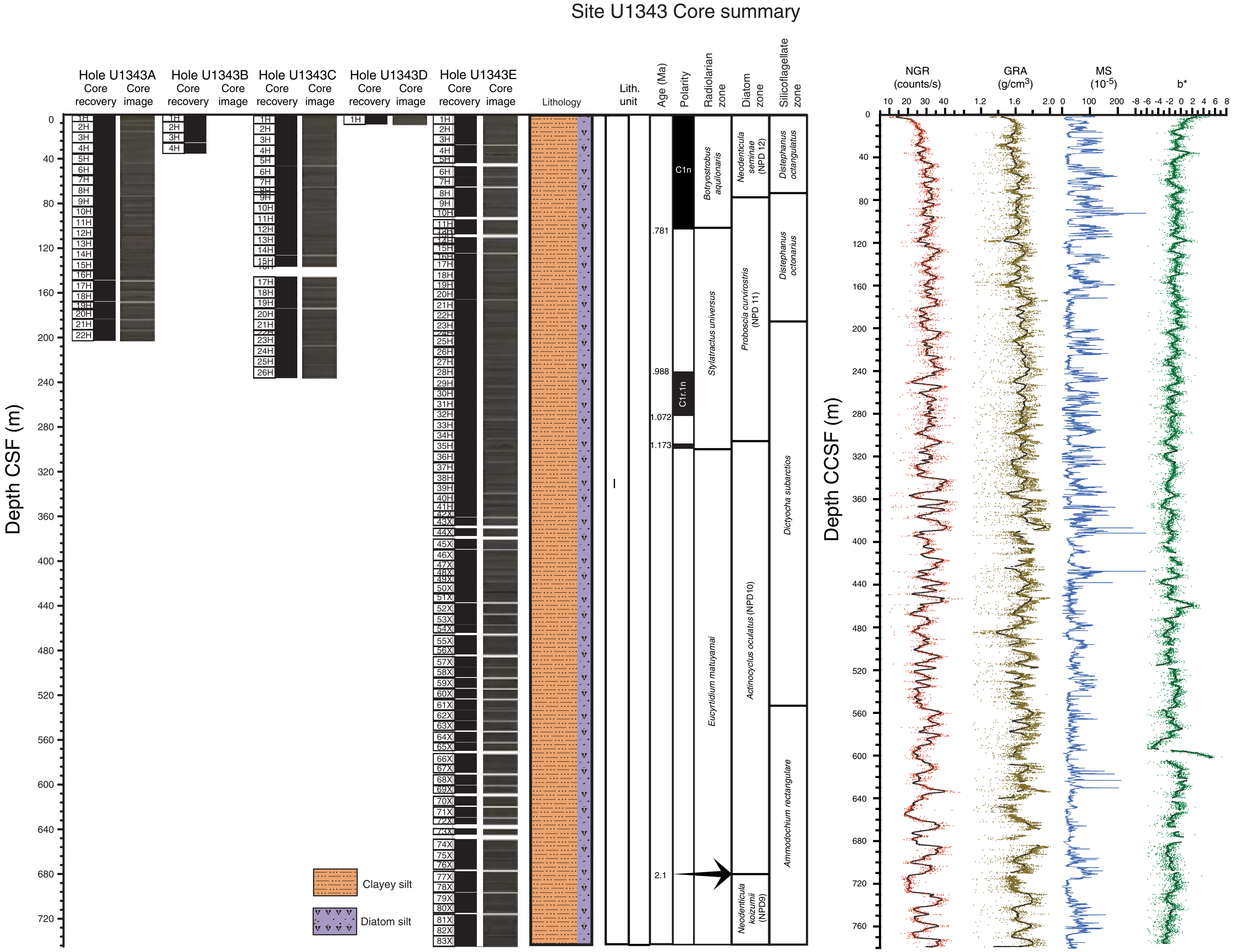

Figure F50. Pore water constituents, Site U1343: (**A**) DIC, (**B**) pH, (**C**) alkalinity, (**D**) sulfate, (**E**) methane, (**F**) sulfide, (**G**) phosphate, (**H**) ammonium, and (**I**) salinity.

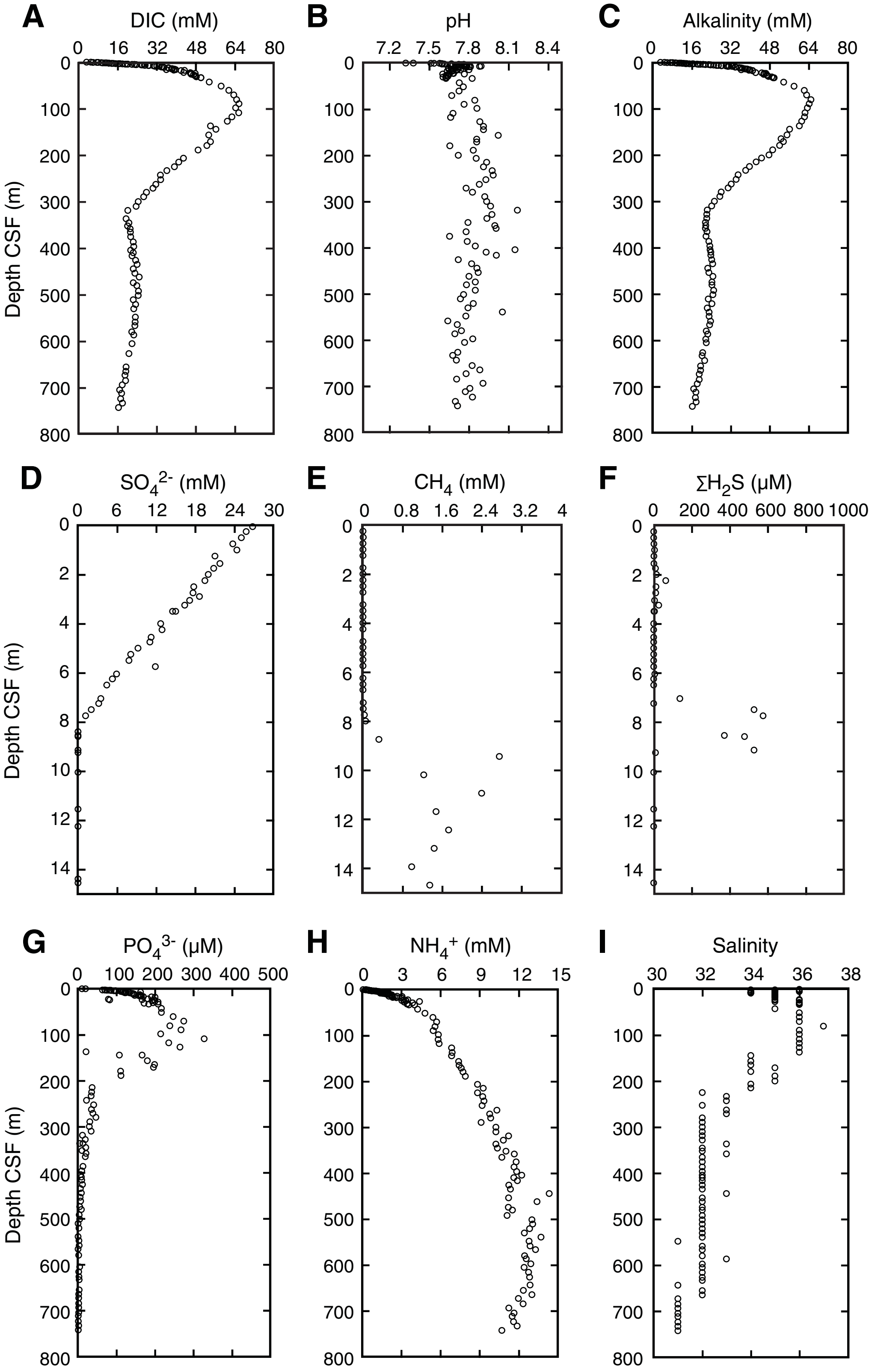

Figure F51. Age-depth plot for Site U1343, including biostratigraphic and paleomagnetic datums listed in Table T19.

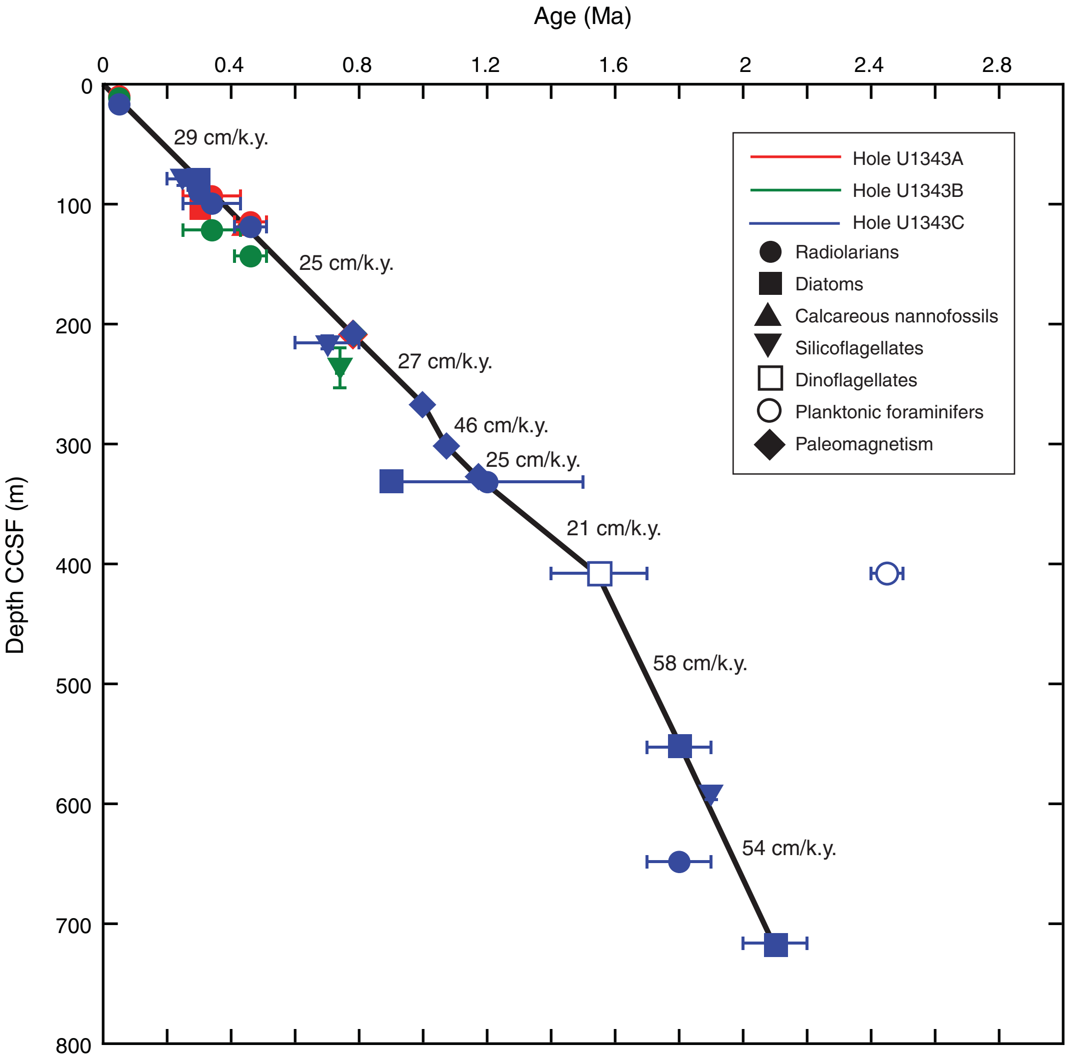

Figure F52. Navigation map of *Hakuhou-Maru* Cruise KH99-3 around Site U1344 (GAT-3C) for seismic profiles, including close-ups shown in Figures F53 and F54.

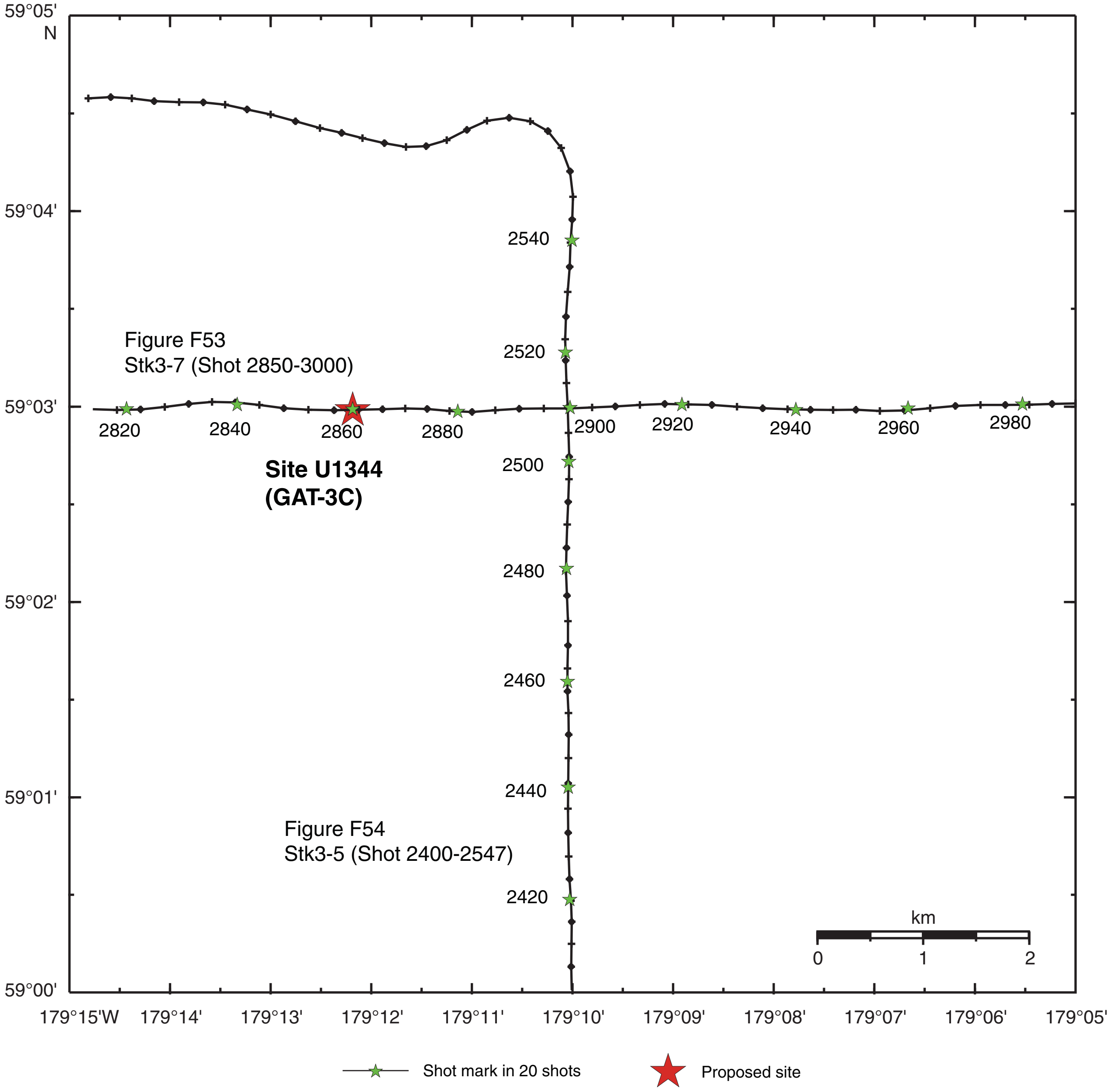

Figure F53. Seismic profile of *Hakuhou-Maru* Cruise KH99-3 Line Stk3-7 (west–east) at Site U1344 (GAT-3C). Cross point with Line Stk3-5 (south–north) is at Shotpoint 2510.

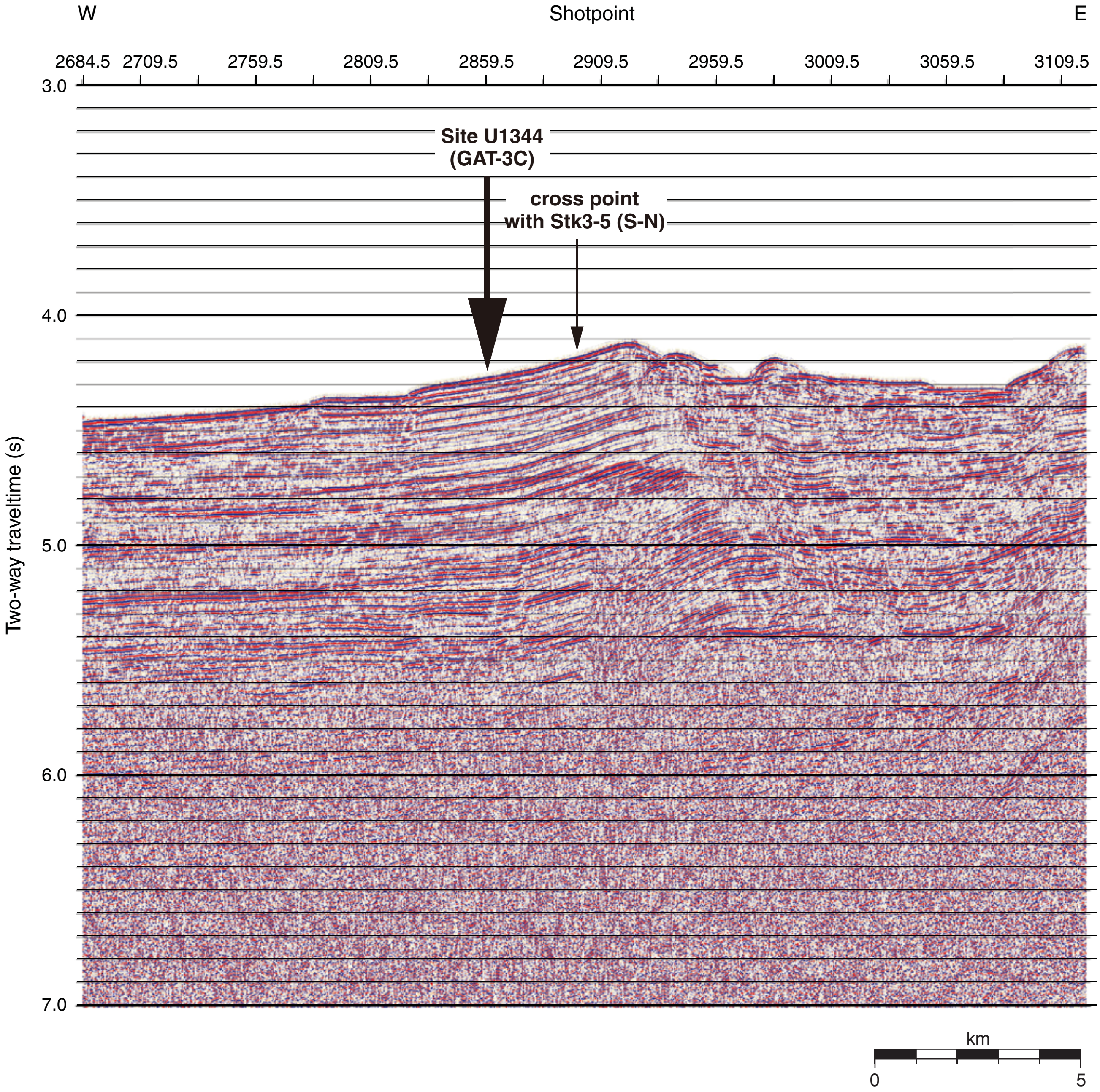

Figure F54. **A.** Close-up seismic profile of *Hakuhou-Maru* Cruise KH99-3 Line Stk3-7 (west–east) near Site U1344. **B.** Time-depth curve estimated from results of velocity analyses on Lines Stk3-7 and Stk3-5 around Site U1344.

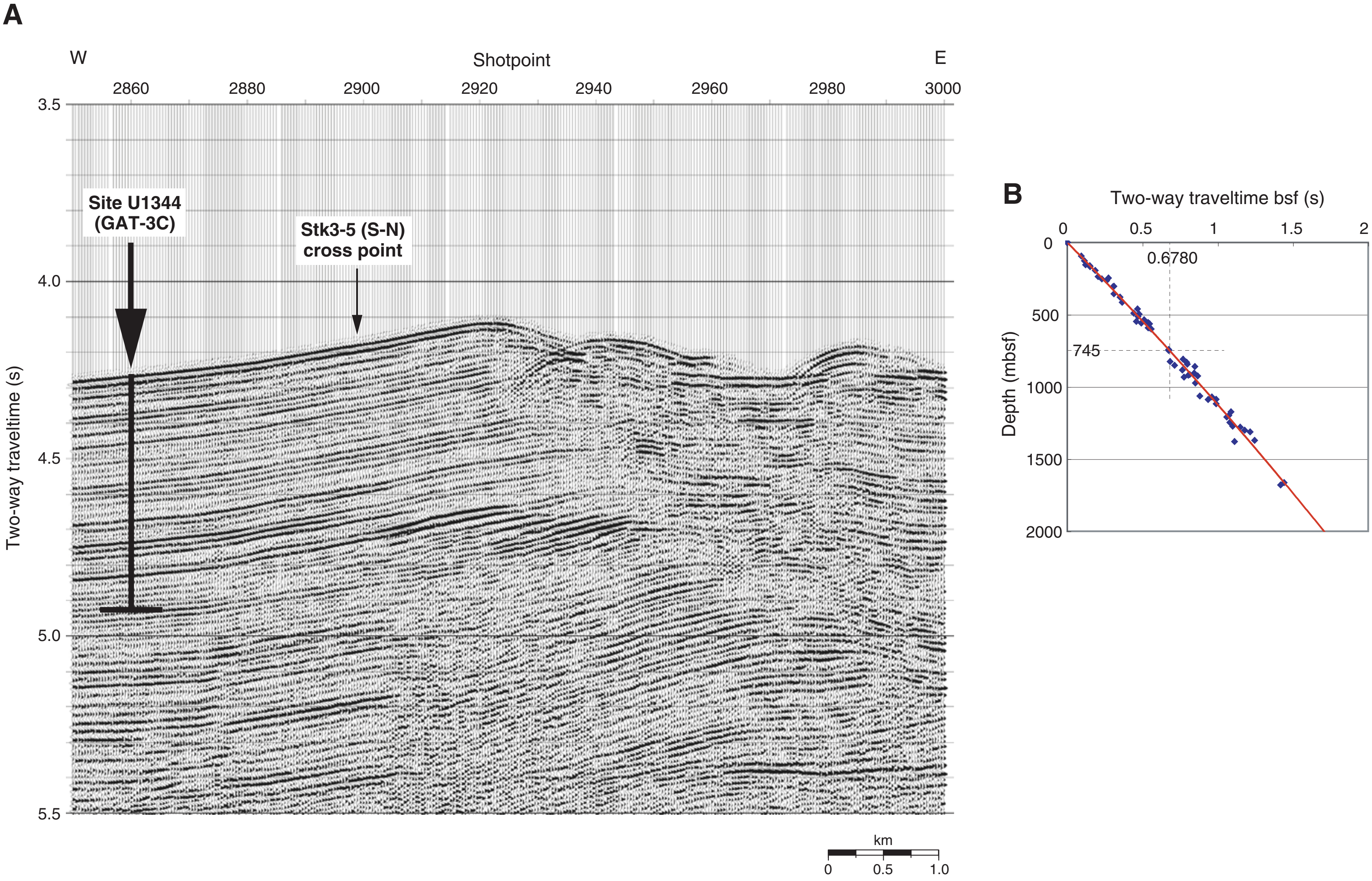

Figure F55. **A.** The projected drill penetration of Site U1344 (GAT-3C) is shown by the dashed line. Cross point with Stk3-7 (west–east) is at Shotpoint 2900. **B.** Time-depth curve estimated from results of velocity analyses on Lines Stk1 and Stk2 around Site U1343.

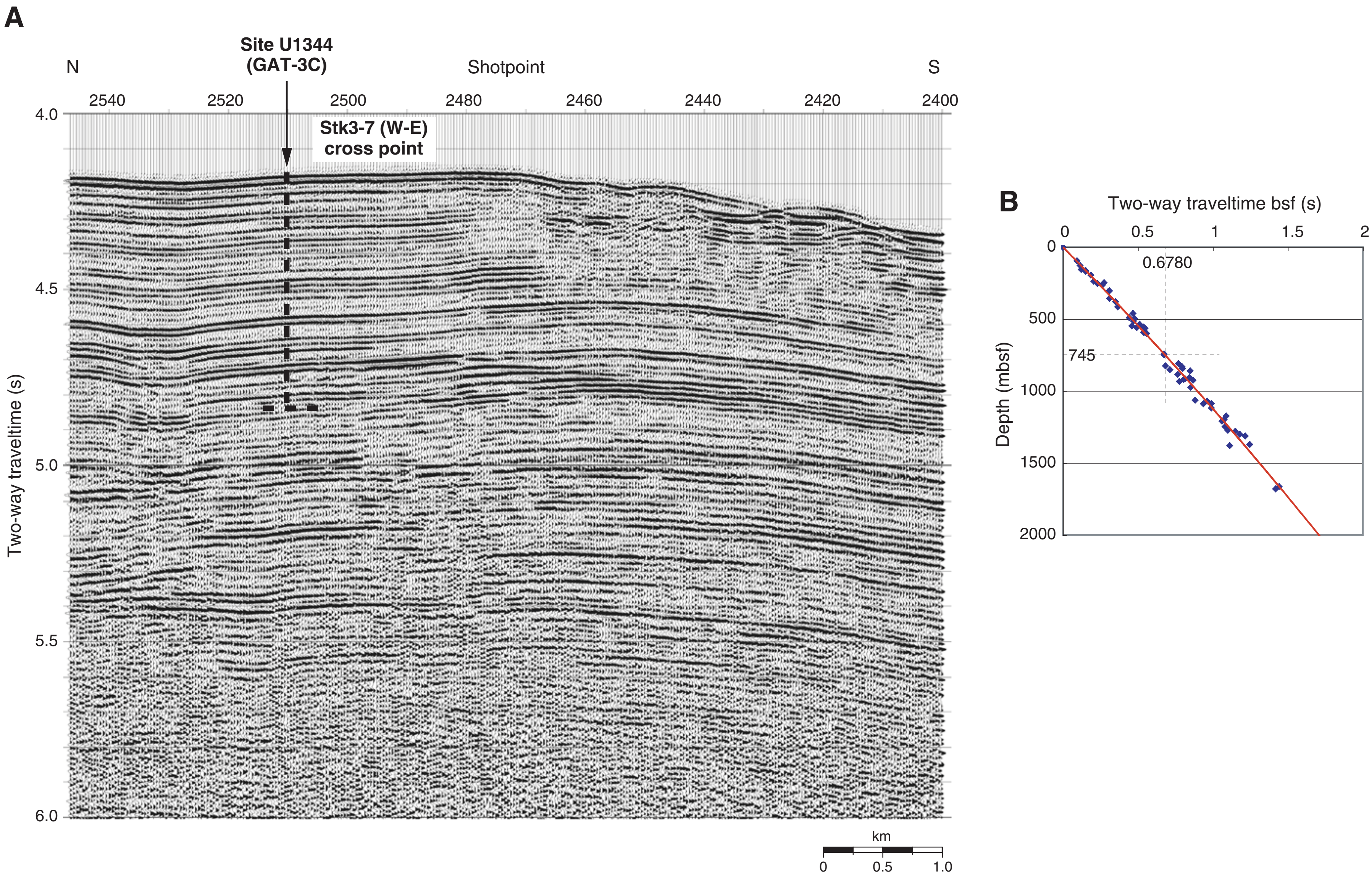

Figure F56. Summary of some shipboard analyses at Site U1344: core recovery, core images, lithology, lithologic units and subunits, age, paleomagnetic chronology, zone of biostratigraphically important radiolarians, diatoms, and silicoflagellates, and spliced records of natural gamma radiation (NGR), gamma ray attenuation (GRA) bulk density, magnetic susceptibility (MS), and the b* index of color reflectance.

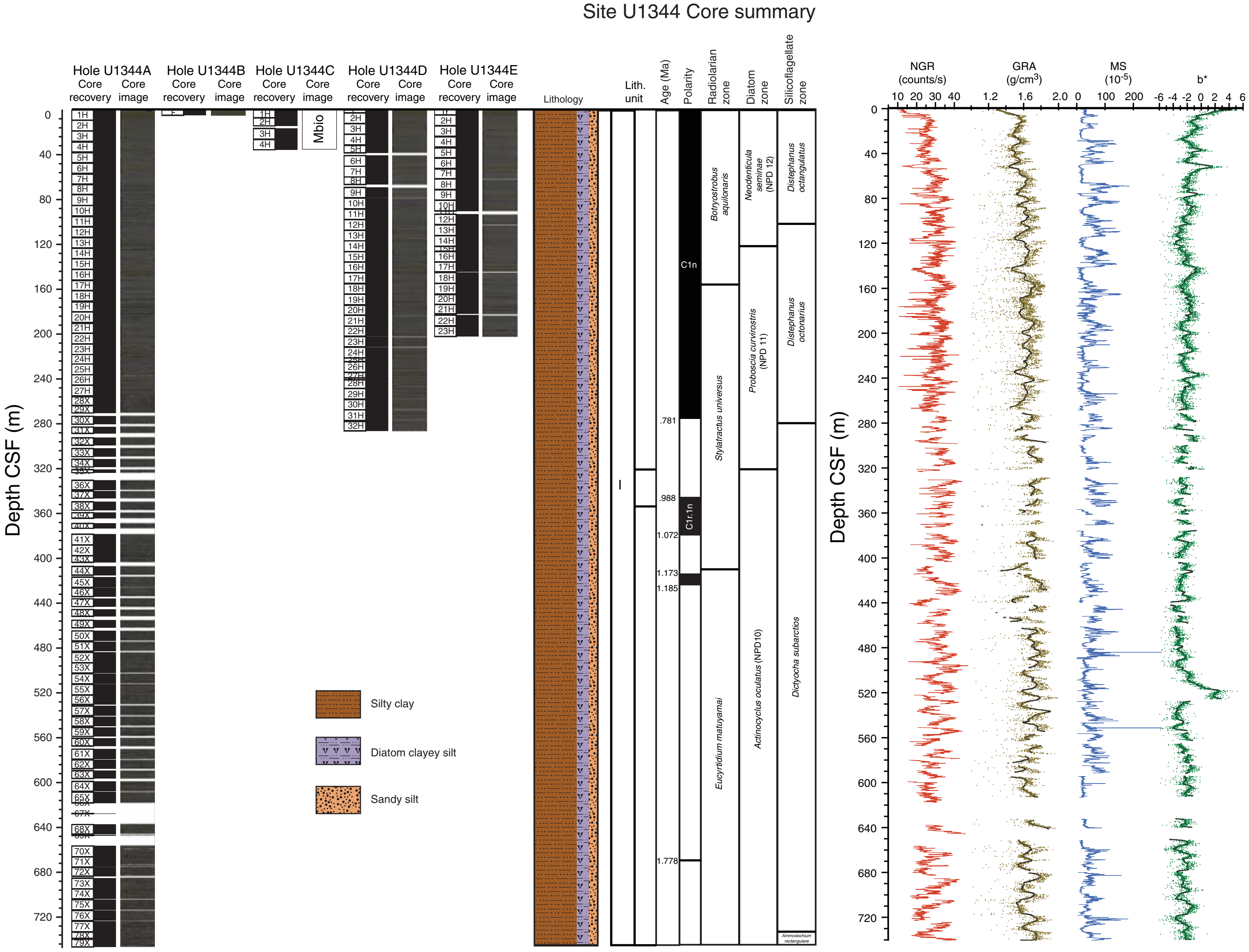

Figure F57. Combined profiles of concentrations of pore water constituents, Holes U1344A, U1344B, and U1344E: (**A**) DIC, (**B**) pH, (**C**) alkalinity, (**D**) sulfate, (**E**) methane, (**F**) sulfide, (**G**) phosphate, (**H**) ammonium, and (**I**) salinity.

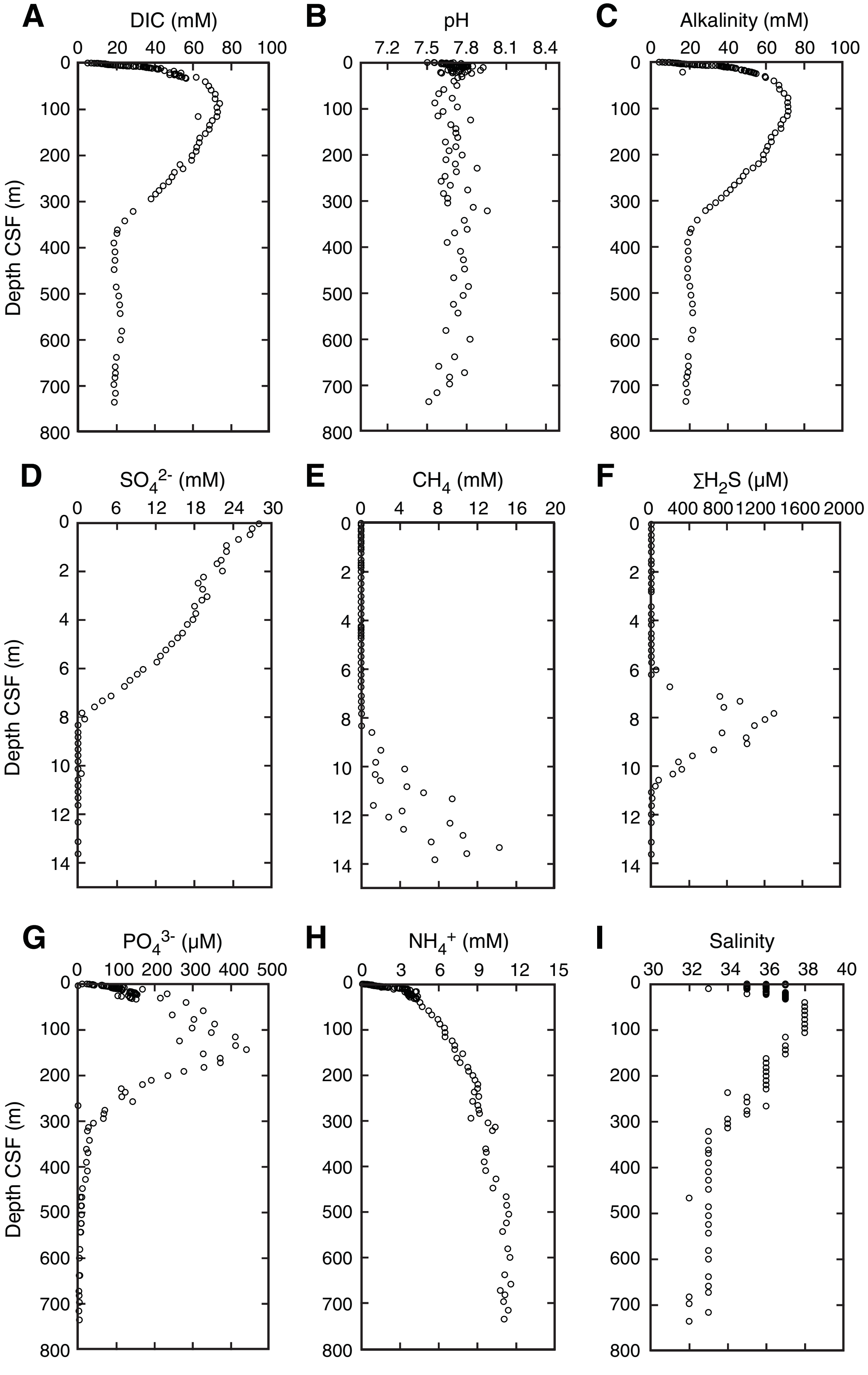

Figure F58. Age-depth plot for Site U1344, including all biostratigraphic and paleomagnetic datums listed in Table T23. Sedimentation rates are based on paleomagnetic reversal data and a few biostratigraphic datums.

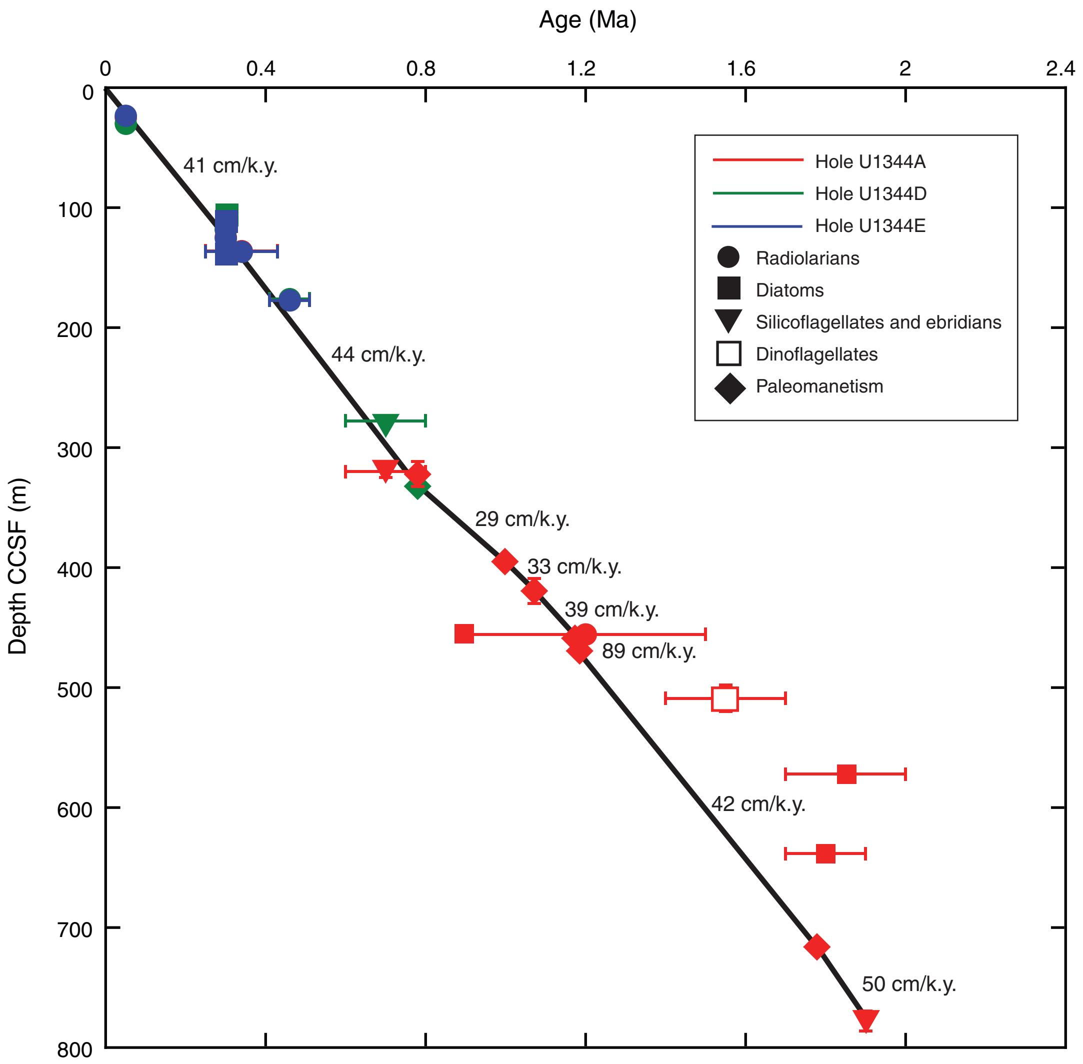

Figure F59. Navigation map for *Discoverer* 4-80-BS Line 18 and *Farnella* 2-86-BS Line 4A and around Site U1345 (NAV-1B) and HLY02-02-3JPC. CDP = common depth point.

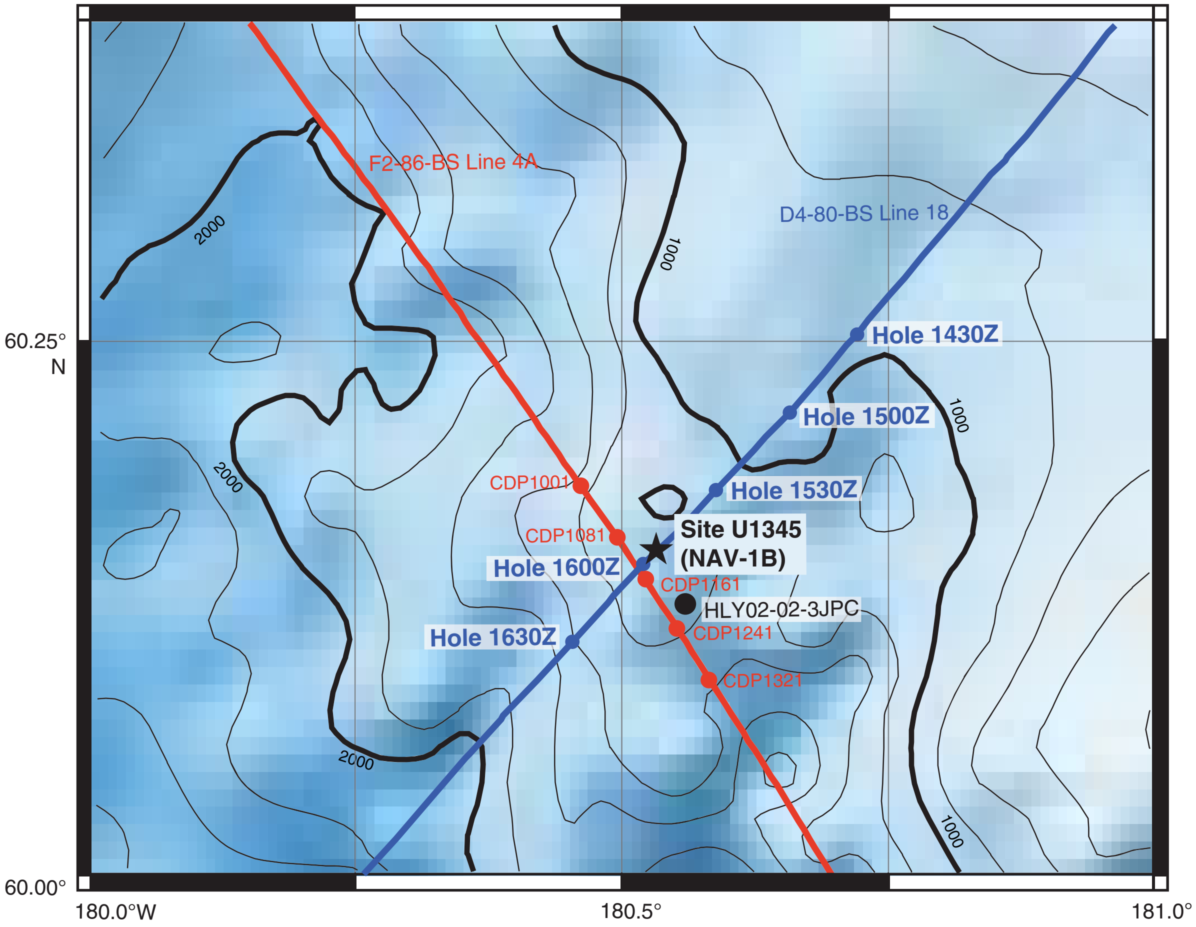

Figure F60. Seismic profile of *Farnella* 2-86-BS Line 4A (northwest–southeast) with the location of Site U1345 (NAV-1B) shown. CDP = common depth point.

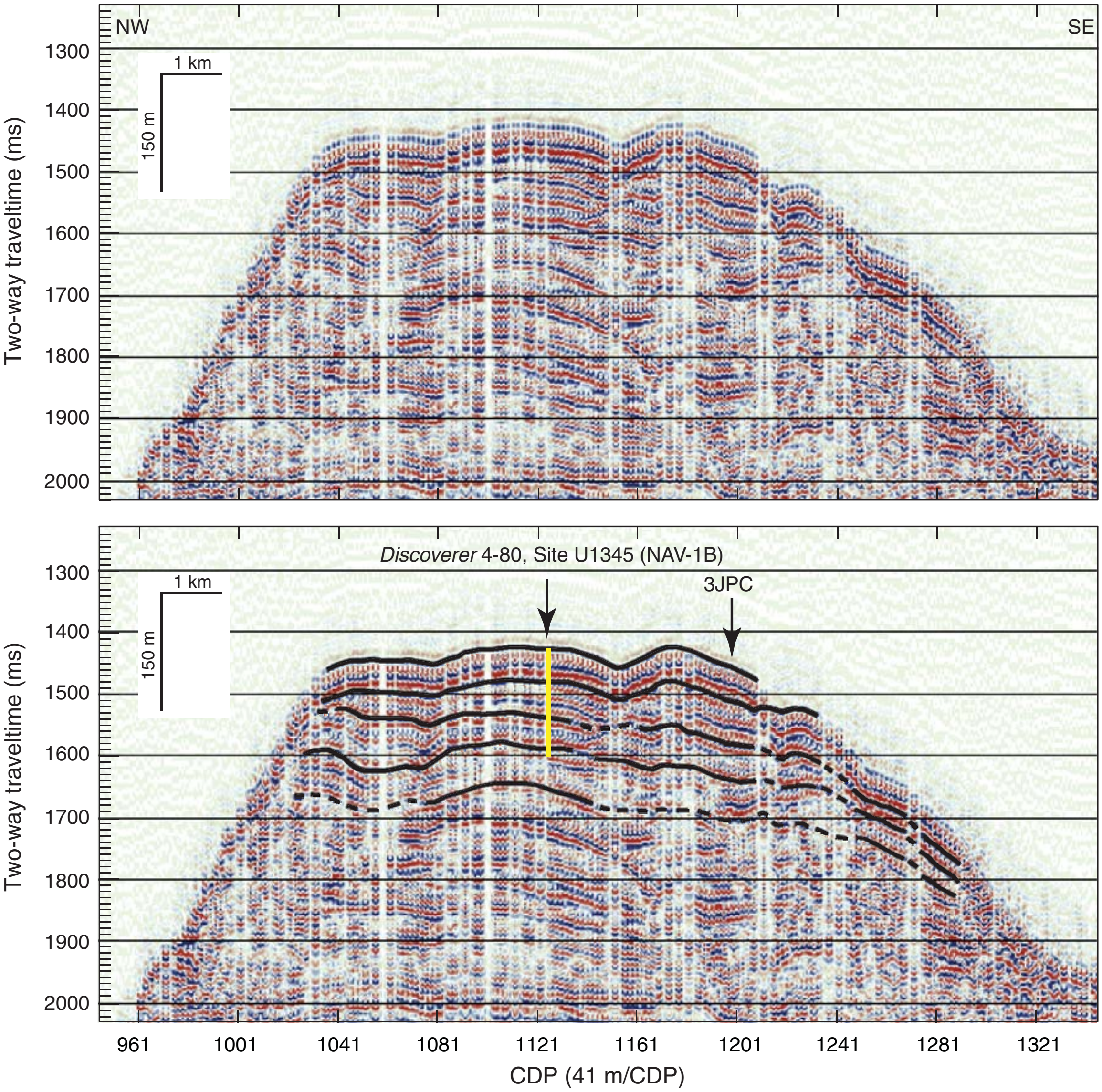

Figure F61. Seismic profile of *Discoverer* 4-80 BS Line 18 (northeast–southwest) with the location of Site U1345 (NAV-1B) shown.

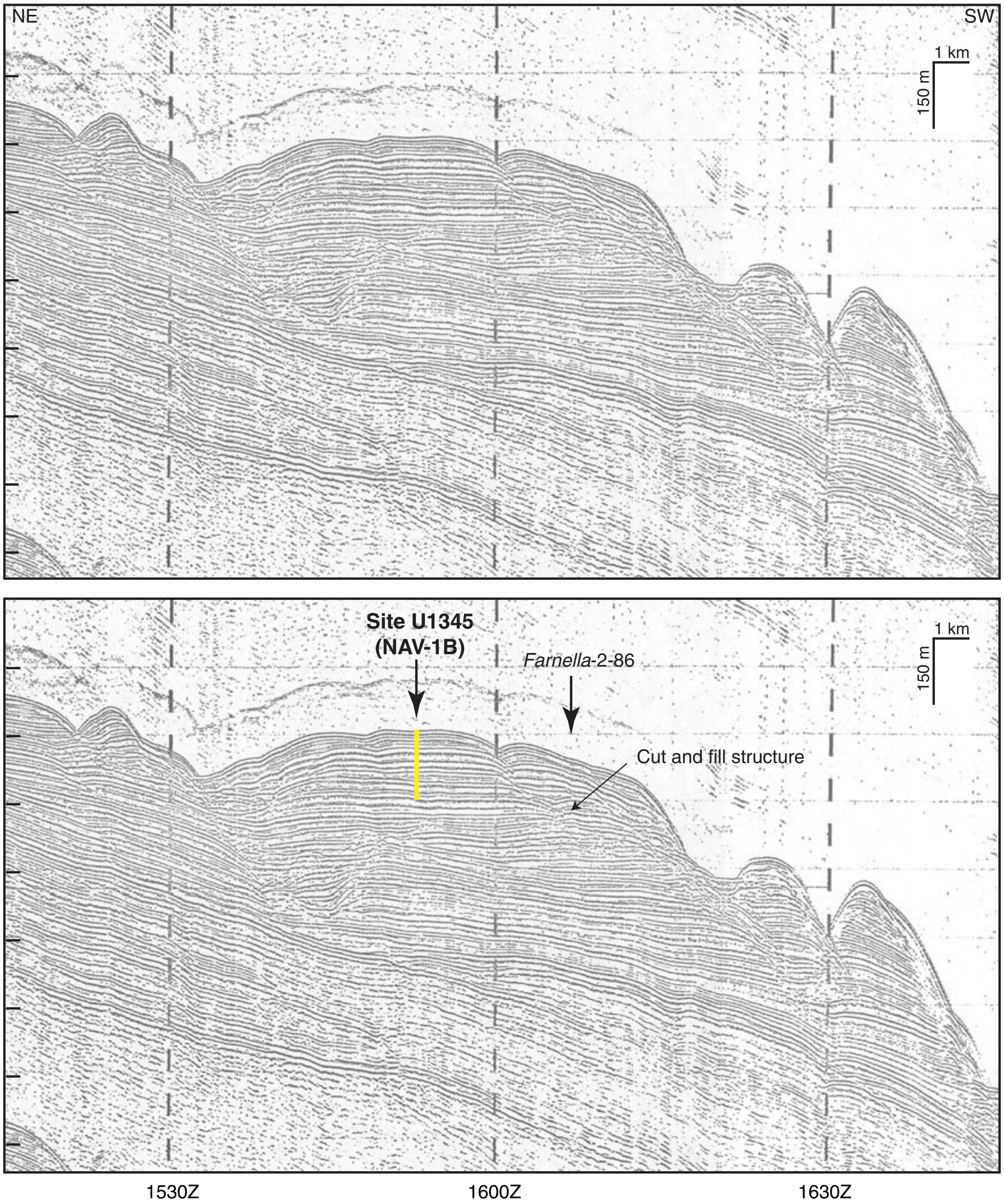

Figure F62. Minisparker profile of *Discoverer* 4-80-BS Line 18 (northeast–southwest) with the location of Site U1345 (NAV-1B) shown.

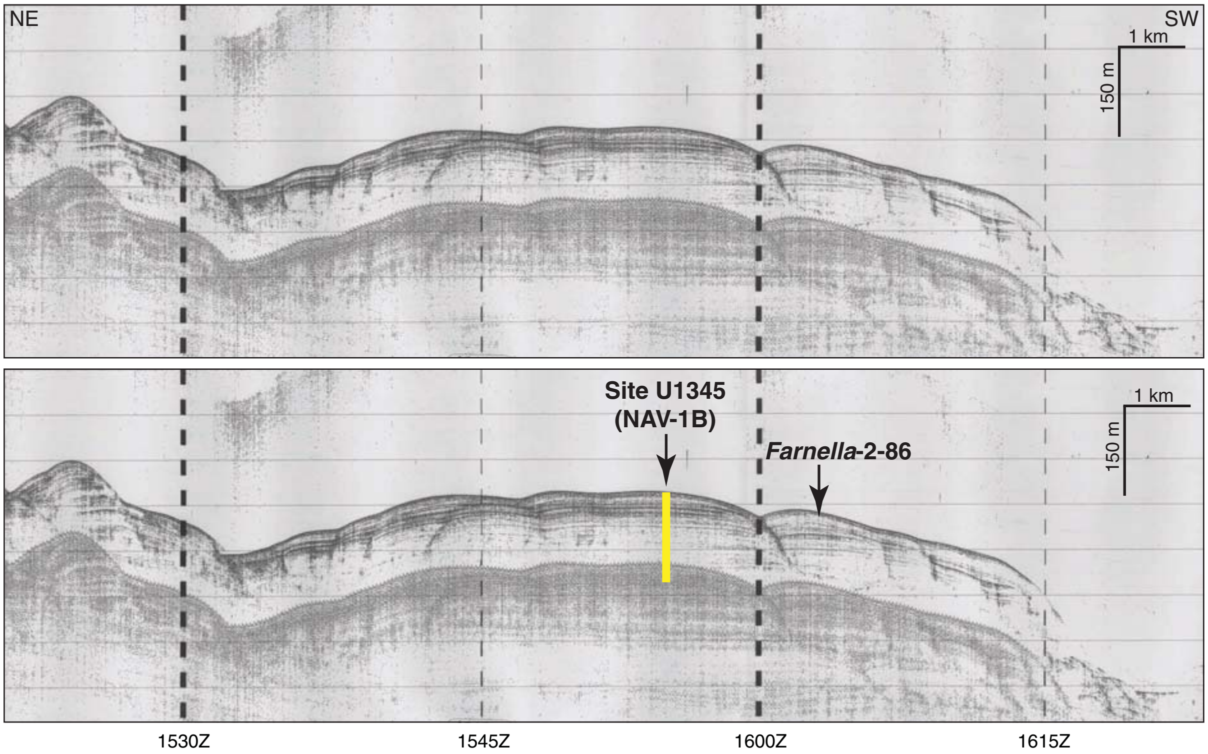

Figure F63. Summary of some shipboard analyses at Site U1345: core recovery, core images, lithology, lithologic units and subunits, age, paleomagnetic chronology, zone of biostratigraphically important radiolarians, diatoms, and silicoflagellates, and spliced records of natural gamma radiation (NGR), gamma ray attenuation (GRA) bulk density, magnetic susceptibility (MS), and the b* index of color reflectance.

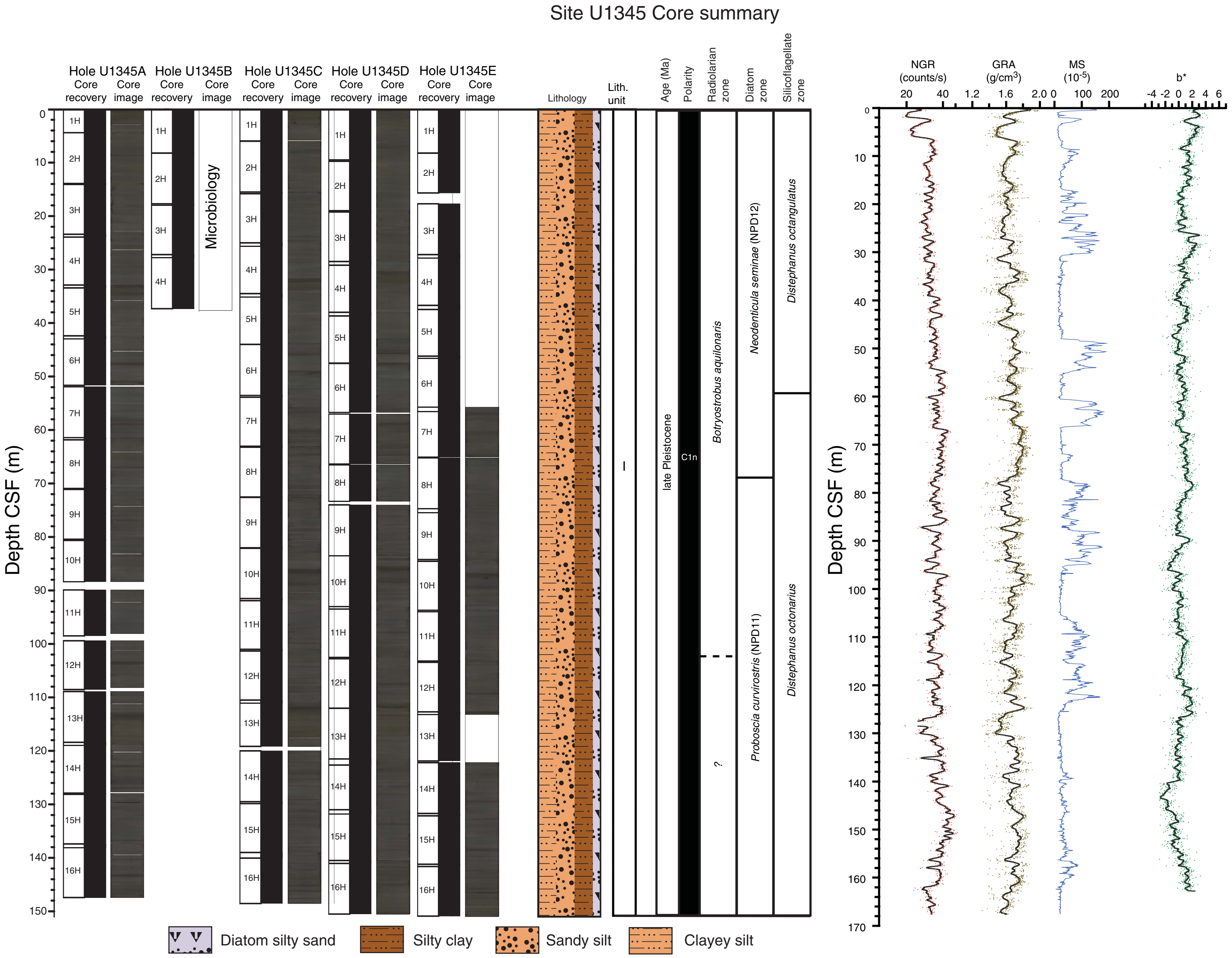

Figure F64. Combined profiles of concentrations of pore water constituents, Hole U1345A: (**A**) DIC, (**B**) pH, (**C**) alkalinity, (**D**) sulfate, (**E**) methane, (**F**) sulfide, (**G**) phosphate, (**H**) ammonium, and (**I**) salinity.

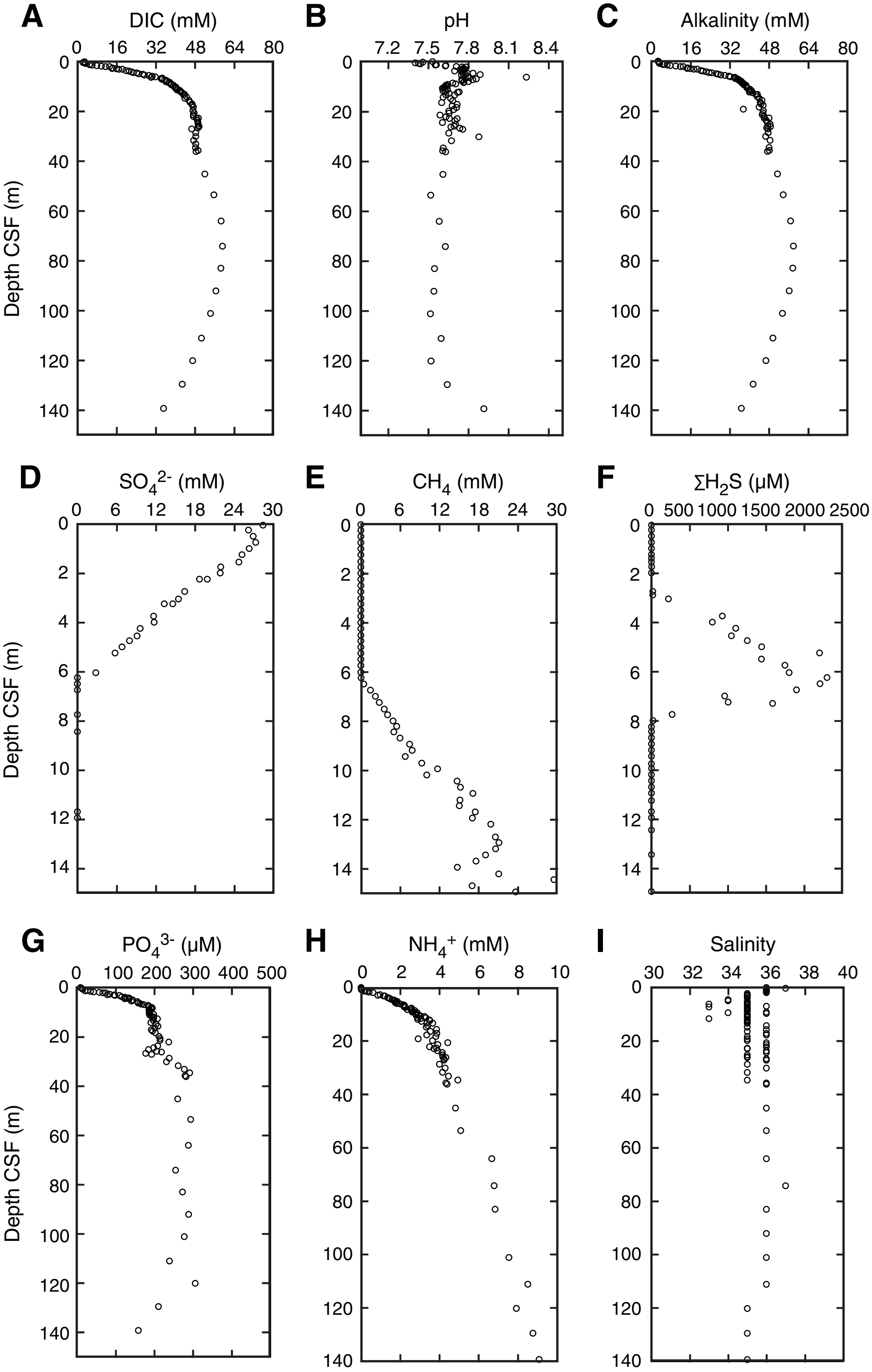

Figure F65. Age-depth plot for Site U1345, including all biostratigraphic and paleomagnetic datums listed in Table T27. Sedimentation rates are based on paleomagnetic reversal data and a few biostratigraphic datums.